Université de Lille

THÈSE DE DOCTORAT DE L'UNIVERSITÉ DE LILLE

Spécialité :

Sciences de la Matiére, du Rayonnement et de l'environnement

Présentée par

Marcos Herreras Giralda

pour obtenir de grade de

Docteur de l'Université de Lille

Développement d'un algorithme de restitution des propriétés des aérosols atmosphériques en utilisant la synergie du spectre solaire et infrarouge thermique

---

Jury composé de:

Cathy Clerbaux	Directrice de recherche	LATMOS IPSL, Paris	Rapportrice
Jeffrey Reid	Senior Scientist	Naval Research Laboratory, USA	Rapporteur
Gérard Brogniez	Professeur émérite	LOA, Université de Lille	Examinateur
René Preusker	Maître de conférences	Free University of Berlin	Examinateur
Roberto Román	Maître de conférences	GOA, University of Valladolid	Examinateur
Stéphane Victori	Docteur	CIMEL Electronique, France	Examinateur (invité)
Oleg Dubovik	Directeur de recherche	CNRS/Université de Lille	Directeur de thèse
Yevgeny Derimian	Chargé de recherche	LOA, CNRS/Université de Lille	Co-directeur de thèse
Pavel Litvinov	Docteur	GRASP SAS, France	Co-encadrant de thèse

Thèse soutenue le 28/04/2022

Laboratoire d'Optique Atmosphérique

LOA UMR 8518 CNRS / Université Lille

Bâtiment P5 - Université Lille - Sciences et Technologies

59655 Villeneuve d'Ascq Cedex

Développement d'un algorithme de restitution des propriétés des aérosols atmosphériques en utilisant la synergie du spectre solaire et infrarouge thermique

La connaissance et le suivi de la composition chimique des aérosols atmosphériques sont très importants pour la compréhension et l'évaluation du climat, des processus environnementaux et de la qualité de l'air. La composition des aérosols détermine l'efficacité des interactions avec les nuages, l'interaction directe avec le rayonnement, l'évaluation de « Particulate Matter » (PM) et l'impact sur l'écosystème marin suite au dépôt des aérosols. La poussière minérale représente la deuxième plus grande fraction des émissions des aérosols atmosphériques, après les aérosols marins. L'effet radiatif net de la poussière atmosphérique dépend de sa composition minéralogique. La grande variété de la minéralogie du sol détermine la variabilité de la composition des poussières atmosphériques, mais un lien direct entre les deux n'est pas évident. La composition minéralogique des cendres volcaniques est encore moins prévisible, pourtant elle a une importance majeure pour la sécurité aérienne. Enfin, la fraction des espèces hygroscopiques des aérosols est déterminante pour les interactions entre les nuages et les aérosols.

L'objectif de cette thèse est d'établir un cadre pour la restitution cohérente des propriétés optiques des aérosols atmosphériques et des composants des aérosols en utilisant la synergie des mesures solaires et infrarouges thermiques (TIR). L'implémentation de ce développement est faite dans le cadre de l'algorithme GRASP (Dubovik et al., 2021). La synergie entre les deux parties du spectre vise à améliorer la sensibilité aux propriétés microphysiques des aérosols et de caractériser plus finement les composants minéralogiques de la poussière, par exemple, en séparant les fractions de quartz et d'argile. Le développement présenté est une extension de l'approche GRASP/Component développée précédemment (Li et al., 2019). Une nouveauté importante réside dans l'intégration de l'émission Planck dans le schéma de transfert radiatif de Ordres Successifs de Diffusion qui est employé par l'algorithme GRASP. En outre, des méthodologies « line-by-line » et « K-Distribution » ont été implémentées pour intégrer les raies d'absorption de gaz et l'indice de réfraction très variable des aérosols minéraux dans le TIR a été pris en compte.

Des tests synthétiques ont été réalisés pour évaluer la précision i) de la méthodologie conçue pour les simulations de mesures d'un radiomètre infrarouge thermique et ii) de la paramétrisation réactualisée des composants de l'aérosol. De plus, une étude a été menée sur l'influence de l'information supposée a priori. Une amélioration de la sensibilité aux grosses particules, une caractérisation plus fine des composants de la poussière, la restitution de la hauteur moyenne de couche des aérosols à partir des mesures passives et enfin la restitution de la concentration totale dans la colonne atmosphérique de la vapeur d'eau ont été illustrées comme faisables en s'appuyant sur la synergie des mesures Solaire-TIR. Ainsi, le nouvel algorithme de restitution GRASP/Component combinant le spectre solaire-TIR a été appliqué aux mesures combinées du photomètre solaire AERONET (AErosol RObotic Network) (Holben et al., 1998) et du radiomètre infrarouge thermique CLIMAT (Legrand et al., 1999 , Brogniez et al., 2003) effectués par le Laboratoire d'optique atmosphérique au Sénégal.

Les observations réelles, obtenues entre novembre 2020 et avril 2021 sur le site de Dakar Bel Air, ont été sélectionnées pour l'application de l'algorithme GRASP/Components. Un accord important a été trouvé entre les valeurs restituées et les résultats correspondants du produit standard d'AERONET. De plus, il a été constaté que la vapeur d'eau totale dans la colonne atmosphérique et la hauteur moyenne de la couche d'aérosol peuvent être restituées simultanément avec les caractéristiques des aérosols. Les restitutions ont montré une bonne corrélation avec la vapeur d'eau dérivée indépendamment par l'algorithme AERONET et un accord qualitatif a été observé avec les mesures de profils d'aérosols par un système lidar. Les étapes suivantes du travail incluent une validation plus poussée des composants d'aérosol restitués. La perspective réside dans l'application de l'algorithme à une combinaison des capteurs 3MI et IASI-NG qui seront lancés à bord de la mission spatiale MetOp-SG A ou dans des missions similaires.

Development of an algorithm for retrievals of atmospheric aerosol properties using synergy of solar and thermal IR spectrum

Knowledge and monitoring of atmospheric aerosol chemical composition is highly important for the understanding and evaluation of Earth's climate, environmental processes and air quality. The aerosol composition drives the efficiency of interactions with clouds, direct interaction of radiation with the Particulate Matter, impact on marine ecosystem after the aerosol deposition, etc.. Mineral dust represents the second, after the marine aerosol, largest fraction of the global atmospheric aerosol emissions. The net radiative effect of the atmospheric dust depends on its mineralogical composition. The vast variety of soil mineralogy determines the variability of airborne dust composition, but direct link between them is not evident. Mineralogical composition of volcanic ash is even less predictable, while has an importance for aviation safety. Finally, the fraction of aerosol hygroscopic species is determinant for aerosol cloud interactions.

The objective of this thesis is to establish a framework for the combined and consistent retrieval of atmospheric aerosol optical properties and aerosol components using synergy of solar and Thermal Infrared (TIR) measurements. The implementation is done as part of the GRASP algorithm (Dubovik et al., 2021). Synergy between both parts of the spectra is expected to provide an enhanced sensitivity to aerosol microphysical properties as well as a finer characterization of the mineral dust components, e.g. Quartz and clays fractions separation. The presented development is an extension the of previously developed GRASP/Components approach (Li et al., 2019). An important update has been done on the incorporation of Planck emission into the Successive Orders of Scattering radiative transfer scheme that is employed in the GRASP algorithm. In addition, line-by-line and K-Distribution methodologies to integrate gas absorption lines and a methodology to deal with the highly varying aerosol refractive index in TIR was implemented in order to fulfill the objectives.

Synthetic tests were performed to evaluate the accuracy of (i) the designed methodology for the measurements simulation of a thermal infrared radiometer and (ii) the updated aerosol components parameterization. Furthermore, a synthetic study was conducted to evaluate the influence of a priori assumed information. An enhancement of the sensitivity to the coarse mode particles, a finer characterization of the dust components, the retrieval of the Aerosol Mean Height (AMH) from passive measurements and finally the retrieval of total column water vapor concentration was illustrated as possible based on the Solar-TIR measurements synergy. Namely, the new combined solar-TIR GRASP/Components retrieval algorithm was applied to the AERONET (AErosol RObotic Network) (Holben et al., 1998) sun photometer and the CLIMAT Thermal Infrared radiometer (Legrand et al., 1999, Brogniez et al., 2003) combined measurements conducted by LOA in Senegal.

The observations conducted between November 2020 to April 2021 at the Dakar Belair site were selected for the application of the Solar-TIR GRASP/Components retrieval. A high degree of agreement was found between the derived values and the corresponding standard AERONET retrievals. Moreover, it was found that the total column water vapor and AMH can be retrieved simultaneously with the aerosol characteristics. The retrievals showed good correlation with the independently derived AERONET precipitable water and a qualitative agreement with lidar aerosol profiles observations. The future steps of this work include a further validation of the retrieved aerosol components. The perspective is in the algorithm application to combined 3MI and IASI-NG sensors that will fly onboard of MetOp-SG A space mission or similar.

Acknowledgements

First of all, I want to express my deep and sincere thanks to my thesis supervisors Oleg Dubovik, Pavel Litvinov and Yevgeny Derimian for their continuous and invaluable support. They have always been available for sharing their knowledge and time which have made this period much easier. I also would like to remark that despite their excellent guidance, they have allowed me to work and perform my research in my own way, which has given me the opportunity to progress more, not only scientifically, but also in very different senses. I am going to specifically remark the support and the trustfulness that David Fuertes put on me to start this project and during the different phases and challenges that we encountered. All the GRASP team has incredibly helped me, directly or indirectly, with invaluable discussions and ideas, but also with relaxing and funny moments that help a lot to continue the hard work. All the people around GRASP are a huge source of inspiration and I feel extremely lucky to be part of this, it is really easy to work with all of you around. I would also like to thank all the members in LOA that have helped me to complete this phase. I highly appreciate your support and help that all of you gave me from the beginning to the end of this thesis.

The most important part of the time that I had in Lille, and also responsible for this thesis, are the very nice people that I have met and all the super cool things that we have done and will be done together. Thank you for the parties, the concerts, the basketball, the beer and all the fun that we had together. It has been a pleasure to be close to all of you and to know that I can count with you in every moment, the good ones and the bad ones.

Me gustaría agradecer también a Benja todo lo que me ha ayudado en este tiempo en Lille, en los primeros meses Ilaria y Benja literalmente me adoptaron. Las discusiones que hemos tenido sobre absolutamente todos los temas de la vida no tienen precio. Gracias por descubrirme el Cheval Blanc.

La gente del GOA tiene gran parte de la culpa de todo lo que ha pasado los últimos tres años. Siempre confiaron en mí y siempre me han ayudado en todo lo que les he pedido. Muchísimas gracias por hacerme sentir parte de la familia.

En estos últimos años, mi vida ha cambiado mucho en muchos aspectos, pero hay gente que ha estado ahí casi desde el principio y que estará hasta el final. A pesar de que últimamente no hemos estado tan en contacto como me gustaría, cuando estoy con vosotros es como volver a casa, gracias Ramón, Fernan, Victor e Iñigo.

Una parte fundamental de mi vida es el comando, sois parte de mi familia y os aprecio infinito a todos. Cada vez que estamos juntos es una aventura increíble, no solo por lo bien que lo pasamos, si no también por lo que aprendo de vosotros[1].

Si hay alguien al que le tengo que agradecer por todo lo que tengo y todo lo que soy es a mi familia, a mis tíos, a mis primos, a mi abuela Lupi, a mis padres Jesús y Begoña y a mi hermano Alberto. Muchas veces no estoy tan cerca de vosotros como debería y lo siento mucho. Aunque no os lo diga muy a menudo, os quiero mucho.

Finally, I feel really fortunate of all the incredible people that are around me, unfortunately I cannot thank each of you individually. If you have come here looking for your name, I really appreciate you, thank you very much!

[1] Si que se sobró

Contents

Introduction

General context

Aerosols can be defined as atmospheric particles in solid or liquid state which remain suspended in the air for a time long enough to be measured (Willeke et al. (1993), Kulkarni et al. (2011)). The size of these particles covers a radius range from 0.001 to 100 μm. In general, large water particles are excluded from this classification because they are identified as cloud droplets.

The aerosol particles influence numerous natural and environmental processes and human life. For example, in areas where the Particulate Matter concentration is elevated, aerosols have a crucial impact over human health (Wellenius et al. (2012), Ault and Axson (2017)). On the other hand, the influence of atmospheric aerosols on the Earth's radiative budget and some atmospheric processes plays a key role in global climate change. Aerosols contribute mainly in two processes (Bauer and Menon (2012), Szopa et al. (2021)): the "aerosol-radiation interaction", which consists in the direct aerosol scattering and absorption of the incoming solar and outgoing infrared radiation; and the "aerosol-cloud interaction", where aerosols act as cloud condensation and ice nuclei, influencing cloud properties, such as droplets size and cloud lifetime. Despite the significant efforts dedicated to studies of aerosol climatic impacts, the IPCC (Inter- governmental Panel on Climate Change) (Szopa et al., 2021) points out that aerosols are still one of the most unknown parts of the climate system. Figure 1 shows the effective radiative forcing contributions of some of the main atmospheric constituent emissions. The greenhouse gasses such as CO_2, methane or other CFC (Chlorofluorocarbons) species present by far the highest impact on the Earth's radiative budget. In contrast, aerosol contribution seems to be significantly lower. However, the uncertainty associated to this atmospheric component is, in relative and absolute terms, one of the largest of all.

The main reasons behind the aerosol radiative forcing uncertainty are: the high temporal and spa-

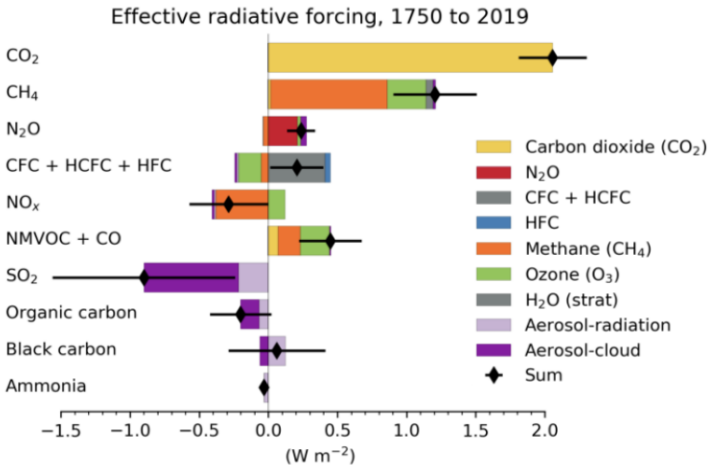

Figure 1: Effective radiative forcing contribution from atmospheric component emissions from 1750 to 2019 (extracted from Szopa et al. (2021)).

tial variability of aerosol properties and concentrations, the vast amount of aerosol origin sources and the extreme variability of the aerosol chemical composition. This is in contrast to the greenhouse gasses, which remain in the atmosphere for prolonged periods of time, which contributes to their homogeneity. CO_2 is a very well mixed greenhouse gas at global scale (Tans et al. (1990), Yokota et al. (2009)). Thus, a high degree of homogeneity of CO_2 concentration around the globe can be observed. Notwithstanding, other gaseous species such as SO_2 (Carn et al., 2017), mainly associated with volcanic activity, or NO_2 (Martin et al., 2003) and N_2O (Olivier et al., 1998) present a global distribution much more dependent on the local conditions.

In addition, aerosols present a varying nature and origins. The main components normally found in the atmospheric particles include: organic matter, water, insoluble components (as mineral dust and soot) and soluble inorganic species (e.g. salt, ammonium nitrate and sulfate). Their lifetime is much shorter in comparison with the gaseous components with typical values of 5 days for local to regional processes, but also hemispherical transports can spam until 20 days (Andreae, 2007). Furthermore, during these long range transport events, aerosol properties, such as size or composition, can significantly change (Prospero, 1999). For all these reasons, the monitoring of atmospheric aerosols all around the globe is a very determinant factor in order to achieve a proper understanding of the Earth system.

In principle, the in-situ methodologies, in which the atmospheric aerosols are directly analyzed to measure their different properties (e.g. Particle Size Distribution (PSD) (Porter and Clarke, 1997) or the chemical composition (Kavouras et al., 2012), seem to be the best alternative for aerosol monitoring because of its high accuracy. The optical, microphysical and chemical techniques employed in in-situ measurements provide precise characterisations and a high information content. However, these kind of techniques do not lack drawbacks. Despite its precision in comparison with other methodologies, in general, in-situ measurements present a very low spatial and often also low temporal resolution. Whereas most of the in-situ procedures are restricted to a single point on the surface, the aerosol load at elevated layers can present very different characteristics. The in-situ measurements based on radiosonde or aircraft profiling (Anderson et al. (2003), Volkamer et al. (2015)) partially solve the problem, but in order to have a proper spatio-temporal coverage another approach should be taken.

Remote sensing measurements offer a high temporal resolution, mainly in the case of ground based instruments (Holben et al. (1998), Tzortziou et al. (2012)), and a global coverage in the case of satellite on-board sensors (Remer et al. (2005), Chen et al. (2020)). However, remote sensing techniques offer a much lower or different degree of details about aerosol properties. In general, application of mathematical inversion procedures is required to link the radiance or irradiance measured by different sensors with the corresponding aerosol and atmospheric characteristics. As it will be discussed in detail hereafter, the inversion of remote sensing measurements is an ill posed problem, which jointly with the physical assumptions needed to model the atmosphere-surface system, reduce its precision in comparison with in-situ methodologies.

The main physical and mathematical basis necessary for the developed argumentations and the results presented in this thesis will be exposed in the corresponding chapters.

Motivation

The largest emissions of particulate matter into the troposphere come from oceans and arid regions. Between 6.3 to 10.1 and 1.2 to 1.8 Gigatons of PM10 soil dust and sea salt respectively are injected into the atmosphere each year (Gassó et al., 2010). The most active dust sources are the Sahara and Sahel regions in Northern Africa, followed by the Gobi and Taklamakan deserts in East Asia (Prospero et al. (2002), Ginoux et al. (2010); Querol et al. (2019)). Despite these high emissions rates, the deposition processes crucially affect the amount of large particles in the air. On average, approximately twenty million metric tons of dust aerosols are suspended in the atmosphere (Gassó et al., 2010). For comparison the mass of fine ash ejected by Mt. Pinatubo in 1991 almost exceeded this value only during the first day of the eruption (Guo et al., 2004). However, while these strong injection events have a more sporadic occurrence, the emission of dust is more homogeneous in temporal terms.

As it has been previously mentioned, aerosols present significant effects over the whole Earth system. In particular, airborne dust reduces global precipitation, because of the reduction of both the radiative heating of the underlying surface, and also the evaporative cooling of the surface (Stevens

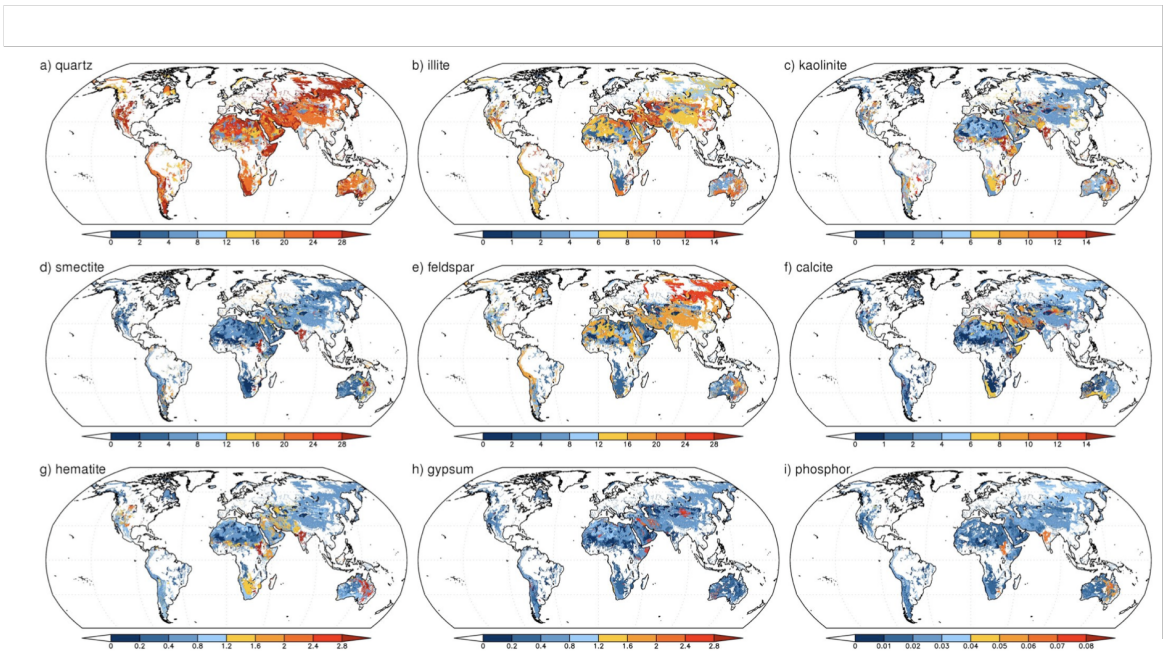

Figure 2: Global distribution of dust soils mineralogical composition expressed in percentage (extracted from Nickovic et al. (2012)).

and Feingold, 2009). However, aerosol mineral dust effect on radiative forcing is much more complex and depends on several factors (Liao and Seinfeld (1998), Claquin et al. (1999), Di Biagio et al. (2020)). In general, it can be established that the net effect of dust at the TOA is generally a warming over bright surfaces and a cooling over dark surfaces. However, for example, sunlight absorption is mainly driven by the location of the dust layer in the atmospheric column, significant differences can be found if the dust load is found above or at cloud levels.

The chemical and mineralogical composition of aerosol mineral dust have been pointed out as one of the key factors determining its radiative effect (Sokolik and Toon (1999), Gassó et al. (2010), Di Biagio et al. (2020)). Aerosol mineral dust is formed by a large varitety of species. Depending on the geographycal origin (Journet et al. (2014), Nickovic et al. (2012), see figure 2) and the weathering processes suffered by these particles the ratios between the different components can significantly differ (Formenti et al. (2014), Baldo et al. (2020)). The main species which form aerosol mineral dust are mainly grouped in: Silicates, like Quartz; clay materials, mainly Kaolinite, Illite and Montmorillonite; Iron oxides, as Goethite and Hematite; and Calcium rich materials, like Calcite and Gypsum (Sokolik et al. (1998); Claquin et al. (1999), Sokolik (2002), Scheuvens and Kandler (2014), Pye (2015), Shevchenko et al. (2021)). In particular, the amount of the Iron oxide mineral species (e.g. Hematite or Goethite) plays an important role in marine ecosystems (Gao et al., 2001) and in the net radiative forcing effect of these particles. Small variations in the volume fractions of these species can lead to a change from a cooling to a warming effect. Moreover, the changes in the soluble/insoluble fractions crucially affects particle hygroscopicity (Sullivan et al., 2009), which leads to important effects in the precipitation and cloud formation process.

The high climatic influence of the aerosol mineral composition, jointly with its vast variation around the globe, make global monitoring of aerosol composition a crucial factor to improve our understanding of the climate system.

Thanks to the high sensitivity of radiation at solar spectrum to particle microphysics, aerosol characterization from remote sensing measurements in this part of the spectra has been proven to be efficient and important progress has been done in this field, e.g., (Tanré et al. (1997), Kaufman et al. (1997), Dubovik and King (2000), Dubovik et al. (2002), Dubovik et al. (2019)). Recent progress in remote sensing has demonstrated the benefits of extended information content in advanced observations for the characterization of different atmospheric constituents. In particular, essential improvements in dust characterization are related to the extension of measurements from visible to Near Infrared

(NIR) and shortwave infrared (SWIR) spectral ranges (Zhou et al., 2020). Remote sensing at thermal infrared (TIR) presents specific advantages; for instance, observations are available both for daytime and nighttime, while active vertical sounders always give the possibility to derive aerosol layer altitude and dust detection is possible. In addition, TIR presents sensitivity to dust altitude (Vandenbussche et al., 2013), an enhanced monitoring of dust sources (Chomette et al., 1999) and new possibilities of dust and volcanic aerosol characterization (Klüser et al. (2012), Dubuisson et al. (2014)). All of this is among the main applications of remote sensing at TIR spectral bands. Besides, strong resonances can be observed for the complex refractive index of different volcanic and dust chemical components (Legrand et al. (2014), Klüser et al. (2015), Kostinski and Derimian (2020)). Thus, information about its mineralogical composition may be retrieved (Sokolik, 2002). However, the lack of a complete sensitivity of the TIR measurements (e.g.: sensitivity trades between particle size and aerosol composition or particle shape assumptions) raises the need to develop more sophisticated retrieval schemes in order to provide an improved aerosol characterization. In this regard a combination of VIS, NIR, SWIR and TIR measurements will present a proper sensitivity to both the particle microphysics and the composition of aerosol particles.

Hitherto, GRASP (Generalized Retrieval of Atmosphere and Surface Properties) (Dubovik et al. (2011), Dubovik et al. (2014) and Dubovik et al. (2021)) has been limited to work in spectral ranges where thermal emission is not important. In this thesis the development of the necessary tools to expand the application of GRASP to the full electromagnetic spectrum will be provided, jointly with a study of the possibilities and implications of a combined retrieval of solar and Thermal infrared measurements in GRASP. In particular, the AERONET (AErosol RObotic NETwork) sunphotometer (Holben et al., 1998) and the CLIMAT TIR radiometer (Legrand et al. (2000), Brogniez et al. (2003)) are the selected instruments for the real data application of the proposed retrieval scheme.

Objectives

This thesis is meant to provide a framework for the combination of solar and Thermal Infrared spectral measurements in GRASP algorithm in general, and for an enhanced retrieval of aerosol components in particular. This new aerosol components retrieval is built on the initial scheme developed for the solar spectrum only, as presented in Li et al. (2019). The synergic combination of measurements in both parts of the spectra aims to provide an increased sensitivity to previously retrieved parameters and introduces new characteristics such as the ability of a finer characterization of aerosol mineral dust; namely determination of fractions of Quartz and clays.

As GRASP code was not initially designed to handle measurements that include thermal emission, an adaptation and an extension of the GRASP forward model to work with the longwave part of the spectrum was one of the first objectives of this work. The main necessary developments include:

- A full radiative transfer scheme that accounts for Planck Thermal emission. Note that the original GRASP radiative transfer scheme is based on the Successive Orders of Scattering (SOS) approach (Lenoble et al., 2007), which is limited to the Solar spectral range.
- Gas absorption lines around visible wavelengths, in general, do not present a major problem in terms of simulation. Hitherto, the Gas Optical Depth (GOD) column integrated values used in GRASP have been proven useful for the required applications. However, in the TIR range a more precise methodology to account for gas absorption was necessary. Thus, line-by-line and K-distribution data have to be included as part of GRASP input.
- Aerosol optical properties at TIR spectral range significantly differ from what is observed at solar wavelengths. GRASP forward model has to be adapted to include both the huge spectral variability of aerosol properties in the longwave range and a much larger range of values of refractive index. The varying nature of aerosol optical characteristics at TIR will require excessive computer resources and computation time. Thus, it is required a sensitivity study to optimize the modeling of these characteristics without a significant loss of representativity.

In addition, whereas the CIMEL sunphotometer is a standard instrument inside the aerosol retrieval community, the possibilities of the CLIMAT TIR radiometer to retrieve aerosol information

has not been fully explored yet. One of the objectives of this thesis was therefore to revise the calibration protocol of CLIMAT aiming an evaluation and an adaptation of the accuracy requirements for the aerosol inversion. Once that the necessary tools have been developed and the TIR measurements count with a proper calibration for the purposes presented here, the real data application of the proposed retrieval scheme was planned using examples of the combined CIMEL sunphotometer and CLIMAT radiometer observations in a site operated by LOA (Laboratoire d'Optique Atmosphérique, Université de Lille) in Senegal.

Finally, the dust aerosol model in the retrieval of aerosol components (Li et al., 2019) had to be revised in order to provide more detailed dust mineralogy characterisation based on spectral resolution of CLIMAT radiometer. Distinguishing between quartz and clays was in the scope. Sensitivity to aerosol mean height and profiles of water vapor and temperature had to be evaluated. The sensitivity and accuracy limits of the retrieval scheme have to be characterized by means of synthetic tests. Then, the retrieved characteristics had to be validated against the reference inversion products of AERONET.

Thesis layout

This thesis is formed by eight chapters.

In the first chapter a general introduction, the motivation and the objectives of this work are exposed.

Second chapter is a methodological summary of some of the main aerosol retrieval algorithms, not based on GRASP, which operate in the solar, in the Thermal Infrared and with the combination of both spectra. The objective of this chapter is to provide a context to the assumptions and accuracy of the retrieval scheme presented here.

The third chapter is dedicated to the description of the technical details and measurement principles of the two instruments selected for the application of the retrieval scheme: the AERONET sunphotometer and the CLIMAT radiometer. Furthermore, an extension of the calibration protocol of CLIMAT instrument to fulfill the accuracy requirements for aerosol retrieval is presented.

In the fourth chapter, GRASP algorithm and some of its main applications are described. Moreover, specific details about some of the developments made for this thesis (like the subchannels approach or about K-Distribution) are also included here.

The development of the thermal inclusion in the SOS radiative transfer approach and its validation against DISORT code can be found in the fifth chapter.

Sixth chapter is dedicated to the study of aerosol optical modeling in TIR.

Seventh chapter is devoted to the enhanced dust retrieval using the synergy between solar and Thermal Infrared measurements. Sensitivity analysis and real data application to the Dakar Belair station and its validation can be found.

Finally, in the eighth chapter the conclusions and future perspectives can be found.

References

Anderson, T. L., Masonis, S. J., Covert, D. S., Ahlquist, N. C., Howell, S. G., Clarke, A. D., and McNaughton, C. S. (2003). Variability of aerosol optical properties derived from in situ aircraft measurements during ace-asia. *Journal of Geophysical Research: Atmospheres*, 108(D23).

Andreae, M. O. (2007). Atmospheric aerosols versus greenhouse gases in the twenty-first century. *Philosophical Transactions of the Royal Society A: Mathematical, Physical and Engineering Sciences*, 365(1856):1915–1923.

Ault, A. P. and Axson, J. L. (2017). Atmospheric aerosol chemistry: Spectroscopic and microscopic advances. *Analytical chemistry*, 89(1):430–452.

Baldo, C., Formenti, P., Nowak, S., Chevaillier, S., Cazaunau, M., Pangui, E., Di Biagio, C., Doussin, J.-F., Ignatyev, K., Dagsson-Waldhauserova, P., et al. (2020). Distinct chemical and mineralogical composition of icelandic dust compared to northern african and asian dust. *Atmospheric Chemistry and Physics*, 20(21):13521–13539.

Bauer, S. E. and Menon, S. (2012). Aerosol direct, indirect, semidirect, and surface albedo effects from sector contributions based on the ipcc ar5 emissions for preindustrial and present-day conditions. *Journal of Geophysical Research: Atmospheres*, 117(D1).

Brogniez, G., Pietras, C., Legrand, M., Dubuisson, P., and Haeffelin, M. (2003). A high-accuracy multiwavelength radiometer for in situ measurements in the thermal infrared. part ii: Behavior in field experiments. *Journal of Atmospheric and Oceanic Technology*, 20(7):1023–1033.

Carn, S., Fioletov, V., McLinden, C., Li, C., and Krotkov, N. (2017). A decade of global volcanic so2 emissions measured from space. *Scientific reports*, 7(1):1–12.

Chen, C., Dubovik, O., Fuertes, D., Litvinov, P., Lapyonok, T., Lopatin, A., Ducos, F., Derimian, Y., Herman, M., Tanré, D., et al. (2020). Validation of grasp algorithm product from polder/parasol data and assessment of multi-angular polarimetry potential for aerosol monitoring. *Earth System Science Data*, 12(4):3573–3620.

Chomette, O., Legrand, M., and Marticorena, B. (1999). Determination of the wind speed threshold for the emission of desert dust using satellite remote sensing in the thermal infrared. *Journal of Geophysical Research: Atmospheres*, 104(D24):31207–31215.

Claquin, T., Schulz, M., and Balkanski, Y. (1999). Modeling the mineralogy of atmospheric dust sources. *Journal of Geophysical Research: Atmospheres*, 104(D18):22243–22256.

Di Biagio, C., Balkanski, Y., Albani, S., Boucher, O., and Formenti, P. (2020). Direct radiative effect by mineral dust aerosols constrained by new microphysical and spectral optical data. *Geophysical Research Letters*, 47(2):e2019GL086186.

Dubovik, O., Fuertes, D., Litvinov, P., Lopatin, A., Lapyonok, T., Doubovik, I., Xu, F., Ducos, F., Chen, C., Torres, B., Derimian, Y., Li, L., Herreras-Giralda, M., Herrera, M., Karol, Y., Matar, C., Schuster, G. L., Espinosa, R., Puthukkudy, A., Li, Z., Fischer, J., Preusker, R., Cuesta, J., Kreuter, A., Cede, A., Aspetsberger, M., Marth, D., Bindreiter, L., Hangler, A., Lanzinger, V., Holter, C., and Federspiel, C. (2021). A comprehensive description of multi-term lsm for applying multiple a priori constraints in problems of atmospheric remote sensing: Grasp algorithm, concept, and applications. *Frontiers in Remote Sensing*, 2:23.

Dubovik, O., Herman, M., Holdak, A., Lapyonok, T., Tanré, D., Deuzé, J., Ducos, F., Sinyuk, A., and Lopatin, A. (2011). Statistically optimized inversion algorithm for enhanced retrieval of aerosol properties from spectral multi-angle polarimetric satellite observations. *Atmospheric Measurement Techniques*, 4(5):975–1018.

Dubovik, O., Holben, B., Eck, T. F., Smirnov, A., Kaufman, Y. J., King, M. D., Tanré, D., and Slutsker, I. (2002). Variability of absorption and optical properties of key aerosol types observed in worldwide locations. *Journal of the atmospheric sciences*, 59(3):590–608.

Dubovik, O. and King, M. D. (2000). A flexible inversion algorithm for retrieval of aerosol optical properties from sun and sky radiance measurements. *Journal of Geophysical Research: Atmospheres*, 105(D16):20673–20696.

Dubovik, O., Lapyonok, T., Litvinov, P., Herman, M., Fuertes, D., Ducos, F., Lopatin, A., Chaikovsky, A., Torres, B., Derimian, Y., et al. (2014). Grasp: a versatile algorithm for characterizing the atmosphere. *SPIE Newsroom*, 25.

Dubovik, O., Li, Z., Mishchenko, M. I., Tanre, D., Karol, Y., Bojkov, B., Cairns, B., Diner, D. J., Espinosa, W. R., Goloub, P., et al. (2019). Polarimetric remote sensing of atmospheric aerosols: Instruments, methodologies, results, and perspectives. *Journal of Quantitative Spectroscopy and Radiative Transfer*, 224:474–511.

Dubuisson, P., Herbin, H., Minvielle, F., Compiègne, M., Thieuleux, F., Parol, F., and Pelon, J. (2014). Remote sensing of volcanic ash plumes from thermal infrared: a case study analysis from seviri, modis and iasi instruments. *Atmospheric Measurement Techniques*, 7(2):359–371.

Formenti, P., Caquineau, S., Desboeufs, K., Klaver, A., Chevaillier, S., Journet, E., and Rajot, J.-L. (2014). Mapping the physico-chemical properties of mineral dust in western africa: mineralogical composition. *Atmospheric Chemistry and Physics*, 14(19):10663–10686.

Gao, Y., Kaufman, Y., Tanre, D., Kolber, D., and Falkowski, P. (2001). Seasonal distributions of aeolian iron fluxes to the global ocean. *Geophysical Research Letters*, 28(1):29–32.

Gassó, S., Grassian, V. H., and Miller, R. L. (2010). Interactions between mineral dust, climate, and ocean ecosystems. *Elements*, 6(4):247–252.

Ginoux, P., Garbuzov, D., and Hsu, N. C. (2010). Identification of anthropogenic and natural dust sources using moderate resolution imaging spectroradiometer (modis) deep blue level 2 data. *Journal of Geophysical Research: Atmospheres*, 115(D5).

Guo, S., Rose, W. I., Bluth, G. J., and Watson, I. M. (2004). Particles in the great pinatubo volcanic cloud of june 1991: The role of ice. *Geochemistry, Geophysics, Geosystems*, 5(5).

Holben, B. N., Eck, T. F., Slutsker, I. a., Tanre, D., Buis, J., Setzer, A., Vermote, E., Reagan, J. A., Kaufman, Y., Nakajima, T., et al. (1998). Aeronet—a federated instrument network and data archive for aerosol characterization. *Remote sensing of environment*, 66(1):1–16.

Journet, E., Balkanski, Y., and Harrison, S. P. (2014). A new data set of soil mineralogy for dust-cycle modeling. *Atmospheric Chemistry and Physics*, 14(8):3801–3816.

Kaufman, Y., Tanré, D., Remer, L. A., Vermote, E., Chu, A., and Holben, B. (1997). Operational remote sensing of tropospheric aerosol over land from eos moderate resolution imaging spectroradiometer. *Journal of Geophysical Research: Atmospheres*, 102(D14):17051–17067.

Kavouras, I. G., Nikolich, G., Etyemezian, V., DuBois, D. W., King, J., and Shafer, D. (2012). In situ observations of soil minerals and organic matter in the early phases of prescribed fires. *Journal of Geophysical Research: Atmospheres*, 117(D12).

Klüser, L., Banks, J., Martynenko, D., Bergemann, C., Brindley, H., and Holzer-Popp, T. (2015). Information content of space-borne hyperspectral infrared observations with respect to mineral dust properties. *Remote Sensing of Environment*, 156:294–309.

Klüser, L., Kleiber, P., Holzer-Popp, T., and Grassian, V. H. (2012). Desert dust observation from space–application of measured mineral component infrared extinction spectra. *Atmospheric environment*, 54:419–427.

Kostinski, A. B. and Derimian, Y. (2020). Minimum principles in electromagnetic scattering by small aspherical particles: Extension to differential cross-sections. *Journal of Quantitative Spectroscopy and Radiative Transfer*, 241:106720.

Kulkarni, P., Baron, P. A., and Willeke, K. (2011). *Aerosol measurement: principles, techniques, and applications*. John Wiley & Sons.

Legrand, M., Dubovik, O., Lapyonok, T., and Derimian, Y. (2014). Accounting for particle nonsphericity in modeling of mineral dust radiative properties in the thermal infrared. *Journal of Quantitative Spectroscopy and Radiative Transfer*, 149:219–240.

Legrand, M., Pietras, C., Brogniez, G., Haeffelin, M., Abuhassan, N. K., and Sicard, M. (2000). A high-accuracy multiwavelength radiometer for in situ measurements in the thermal infrared. part i: Characterization of the instrument. *Journal of atmospheric and oceanic technology*, 17(9):1203–1214.

Lenoble, J., Herman, M., Deuzé, J., Lafrance, B., Santer, R., and Tanré, D. (2007). A successive order of scattering code for solving the vector equation of transfer in the earth's atmosphere with aerosols. *Journal of Quantitative Spectroscopy and Radiative Transfer*, 107(3):479–507.

Li, L., Dubovik, O., Derimian, Y., Schuster, G. L., Lapyonok, T., Litvinov, P., Ducos, F., Fuertes, D., Chen, C., Li, Z., et al. (2019). Retrieval of aerosol components directly from satellite and ground-based measurements. *Atmospheric Chemistry and Physics*, 19(21):13409–13443.

Liao, H. and Seinfeld, J. (1998). Radiative forcing by mineral dust aerosols: sensitivity to key variables. *Journal of Geophysical Research: Atmospheres*, 103(D24):31637–31645.

Martin, R. V., Jacob, D. J., Chance, K., Kurosu, T. P., Palmer, P. I., and Evans, M. J. (2003). Global inventory of nitrogen oxide emissions constrained by space-based observations of no2 columns. *Journal of Geophysical Research: Atmospheres*, 108(D17).

Nickovic, S., Vukovic, A., Vujadinovic, M., Djurdjevic, V., and Pejanovic, G. (2012). High-resolution mineralogical database of dust-productive soils for atmospheric dust modeling. *Atmospheric Chemistry and Physics*, 12(2):845–855.

Olivier, J., Bouwman, A., Van der Hoek, K., and Berdowski, J. (1998). Global air emission inventories for anthropogenic sources of nox, nh3 and n2o in 1990. *Environmental Pollution*, 102(1):135–148.

Porter, J. N. and Clarke, A. D. (1997). Aerosol size distribution models based on in situ measurements. *Journal of Geophysical Research: Atmospheres*, 102(D5):6035–6045.

Prospero, J. M. (1999). Long-range transport of mineral dust in the global atmosphere: Impact of african dust on the environment of the southeastern united states. *Proceedings of the National Academy of Sciences*, 96(7):3396–3403.

Prospero, J. M., Ginoux, P., Torres, O., Nicholson, S. E., and Gill, T. E. (2002). Environmental characterization of global sources of atmospheric soil dust identified with the nimbus 7 total ozone mapping spectrometer (toms) absorbing aerosol product. *Reviews of geophysics*, 40(1):2–1.

Pye, K. (2015). *Aeolian dust and dust deposits*. Elsevier.

Querol, X., Tobías, A., Pérez, N., Karanasiou, A., Amato, F., Stafoggia, M., García-Pando, C. P., Ginoux, P., Forastiere, F., Gumy, S., et al. (2019). Monitoring the impact of desert dust outbreaks for air quality for health studies. *Environment International*, 130:104867.

Remer, L. A., Kaufman, Y., Tanré, D., Mattoo, S., Chu, D., Martins, J. V., Li, R.-R., Ichoku, C., Levy, R., Kleidman, R., et al. (2005). The modis aerosol algorithm, products, and validation. *Journal of the atmospheric sciences*, 62(4):947–973.

Scheuvens, D. and Kandler, K. (2014). On composition, morphology, and size distribution of airborne mineral dust. In *Mineral Dust*, pages 15–49. Springer.

Shevchenko, I., Engelbrecht, J. P., Mostamandi, S., and Stenchikov, G. (2021). Evaluation of minerals being deposited in the red sea using gravimetric, size distribution, and mineralogical analysis of dust deposition samples collected along the red sea coastal plain. *Aeolian Research*, 52:100717.

Sokolik, I. N. (2002). The spectral radiative signature of wind-blown mineral dust: Implications for remote sensing in the thermal ir region. *Geophysical Research Letters*, 29(24):7–1.

Sokolik, I. N. and Toon, O. B. (1999). Incorporation of mineralogical composition into models of the radiative properties of mineral aerosol from uv to ir wavelengths. *Journal of Geophysical Research: Atmospheres*, 104(D8):9423–9444.

Sokolik, I. N., Toon, O. B., and Bergstrom, R. W. (1998). Modeling the radiative characteristics of airborne mineral aerosols at infrared wavelengths. *Journal of Geophysical Research: Atmospheres*, 103(D8):8813–8826.

Stevens, B. and Feingold, G. (2009). Untangling aerosol effects on clouds and precipitation in a buffered system. *Nature*, 461(7264):607–613.

Sullivan, R., Moore, M., Petters, M., Kreidenweis, S., Roberts, G., and Prather, K. (2009). Effect of chemical mixing state on the hygroscopicity and cloud nucleation properties of calcium mineral dust particles. *Atmospheric Chemistry and Physics*, 9(10):3303–3316.

Szopa, S., V. Naik, B. A., Artaxo, P., Berntsen, T., Collins, W., Fuzzi, S., Gallardo, L., Scharr, A. K., Klimont, Z., Liao, H., Unger, N., and Zanis, P. (2021). *Short-Lived Climate Forcers. In Climate Change 2021: The Physical Science Basis. Contribution of Working Group I to the Sixth Assessment Report of the Intergovernmental Panel on Climate Change*. Cambridge University Press.

Tanré, D., Kaufman, Y., Herman, M., and Mattoo, S. (1997). Remote sensing of aerosol properties over oceans using the modis/eos spectral radiances. *Journal of Geophysical Research: Atmospheres*, 102(D14):16971–16988.

Tans, P., Fung, I., and Takahashi, T. (1990). Observational constraints on the global atmospheric co2 budget. *Science247*, pages 1431–1438.

Tzortziou, M., Herman, J. R., Cede, A., and Abuhassan, N. (2012). High precision, absolute total column ozone measurements from the pandora spectrometer system: Comparisons with data from a brewer double monochromator and aura omi. *Journal of Geophysical Research: Atmospheres*, 117(D16).

Vandenbussche, S., Kochenova, S., Vandaele, A. C., Kumps, N., and De Mazière, M. (2013). Retrieval of desert dust aerosol vertical profiles from iasi measurements in the tir atmospheric window. *Atmospheric Measurement Techniques*, 6(10):2577–2591.

Volkamer, R., Baidar, S., Campos, T. L., Coburn, S., DiGangi, J. P., Dix, B., Eloranta, E. W., Koenig, T. K., Morley, B., Ortega, I., et al. (2015). Aircraft measurements of bro, io, glyoxal, no 2, h 2 o, o 2–o 2 and aerosol extinction profiles in the tropics: Comparison with aircraft-/ship-based in situ and lidar measurements. *Atmospheric Measurement Techniques*, 8(5):2121–2148.

Wellenius, G. A., Burger, M. R., Coull, B. A., Schwartz, J., Suh, H. H., Koutrakis, P., Schlaug, G., Gold, D. R., and Mittleman, M. A. (2012). Ambient air pollution and the risk of acute ischemic stroke. *Archives of internal medicine*, 172(3):229–234.

Willeke, K., Baron, P. A., and Martonen, T. (1993). *Aerosol measurement: principles, techniques, and applications*, volume 876. Van Nostrand Reinhold New York.

Yokota, T., Yoshida, Y., Eguchi, N., Ota, Y., Tanaka, T., Watanabe, H., and Maksyutov, S. (2009). Global concentrations of co2 and ch4 retrieved from gosat: First preliminary results. *Sola*, 5:160–163.

Zhou, Y., Levy, R. C., Remer, L. A., Mattoo, S., Shi, Y., and Wang, C. (2020). Dust aerosol retrieval over the oceans with the modis/viirs dark-target algorithm: 1. dust detection. *Earth and Space Science*, 7(10):e2020EA001221.

Chapter 1

Methodological Review of aerosol retrieval algorithms

¿Puede traer la carta de postres?

Laura Ares Santos

This chapter is meant to provide a brief overview of the state of the art of some aerosol retrieval algorithms non based on GRASP that operate in solar, thermal infrared and with the combination of both spectra. The GRASP algorithm will be explained in detail in the following sections. The chapter provides a comparison of the input information, the assumptions, the key aspects for atmospheric/surface modelization, the available output products and the validation of the results. The algorithms are presented in chronological order. The intention of this chapter is to provide insights about how the main problems encountered in the different spectral ranges have been faced until now, and to provide a framework for a better understanding of the methodology proposed in this thesis.

1.1 Aerosol inversion methodologies in the solar spectrum

The aerosol retrieval techniques involving channels in the solar spectrum are by far the most popular inside the scientific literature. The atmospheric windows, nearly free of all gaseous absorption, or the low dependence on the aerosol vertical distribution can be taken as some of the main advantages of the solar spectrum. At the same time, the high angular dependence of the radiance measured in this spectral range, which translates in a high sensitivity to particle size distribution and surface BRDF (Bidirectional Reflectance Distribution Function), requires a special consideration to find a balance between the assumed simplifications and the sophistication of the retrieved products. Most of the algorithms rely on the fitting of a combination of parameters which define an aerosol and surface model to the radiance/reflectance in different channels. The complexity of these models will depend on the information content of the selected measurements and/or the amount of available ancillary data. Here, the selected algorithms cover some of the most popular instruments inside the scientific community such as MODIS, OMI or CALIPSO.

1.1.1 Tanré et al. (1997), Kaufman et al. (1997) and Remer et al. (2005): Aerosol retrieval with MODIS over land and ocean

The original works of Kaufman et al. (1997) and Tanré et al. (1997) show MODIS (Moderate Resolution Imaging Spectroradiometer) aerosol retrieval methodologies over land and ocean respectively. Remer et al. (2005) presents an update of both algorithms with some methodological differences and with an extended validation.

The algorithm presents a retrieval of aerosol optical depth and size distribution from MODIS radiances by employing a LUT (Look-Up-Table) fitting approach. The selected MODIS channels cover the spectral range between 0.415 and 2.33 μm. However, whereas in Tanré et al. (1997) the 0.47 μm channel has been excluded because of the large uncertainty introduced by the simplifications made to the ocean surface model, in Kaufman et al. (1997) and Remer et al. (2005) this channel is used as one of the references to discriminate the aerosol type.

Both land and ocean algorithms are based on the definition of a priori aerosol models with fixed optical and microphysical characteristics. In the case of the ocean algorithm of Tanré et al. (1997), the assumed models are more simple than in the land case where 5 and 6 aerosol models are used for fine and coarse modes, respectively. The real part of the refractive index ranges from 1.4 to 1.5 and the imaginary part of all of them is fixed to 0.0035. The particle size distributions of the aerosol models assumed are mono-modal lognormal, with different values for the effective radius and standard deviation (Tanré et al., 1997). It is noteworthy the fact that none of these models correspond to a mixture of sizes. Under the assumption that both size modes have the same absorption, the multiple scattering effects can be approximately reproduced by a weighted sum of the radiance calculated independently for each one (Wang and Gordon, 1994). This approximation extremely simplifies the LUT calculation because it is only necessary to perform the calculations for the 11 models and not for all 30 possible combinations. These LUT calculations were done using the radiative transfer code presented by Ahmad and Fraser (1982). In Remer et al. (2005), the number of selected aerosol models is 9, and a variability of the imaginary part of the refractive index is accounted for. Then, the LUT calculations are performed over all possible combinations because the different models do not count any more with similar absorption values.

In the case of the land algorithm, Kaufman et al. (1997) selects four different aerosol types. However, their definition is more sophisticated than in the previous case. Each model is defined by different aerosol types with its own size distributions and absorption characteristics. In Remer et al. (2005), the biomass burning model is divided in two: "Developing world-moderate absorption" and "Developing world-strong absorption".

The elements defining the LUT used for the retrieval are common to the three studies. These elements are the AOD (Aerosol Optical Depth) and the viewing geometrical angles which define MODIS measurements. The considered LUT AOD values range from a purely Rayleigh atmosphere (AOD=0.0), to a high turbid atmosphere (AOD=2.0 approximately). The ocean surface reflectance is modeled by a Cox and Munk (1954) model but wind speed is presented independently. On the other hand, an empirical relationship is used in Remer et al. (2005) which links the reflectance measured at TOA (Top of the Atmosphere) at 2.13 μm with the surface reflectance value at 0.47 and 0.66 μm.

As it has been mentioned, these retrievals are based on the fitting of the radiative transfer calculations previously stored in the LUT to the MODIS radiance. In Kaufman et al. (1997) the AOD and the corresponding total mass concentration are the only retrieved parameters. However in Tanré et al. (1997) and in the updated version of the land algorithm of Remer et al. (2005), in addition to the AOD, the fraction between the fine and coarse mode (η) is also retrieved. In Tanré et al. (1997) the real measurements are fitted with LUT calculations combining one aerosol model corresponding to coarse mode and another to the fine mode. Thus, η is used to obtain the total radiance from the calculation of each aerosol model associated to each aerosol size mode in the following way:

$$L_\lambda^T(\mu_s, \mu_v, \phi_v) = \eta L_\lambda^f(\mu_s, \mu_v, \phi_v) + (1-\eta) L_\lambda^c(\mu_s, \mu_v, \phi_v) \tag{1.1}$$

Where L_λ^T, L_λ^f and L_λ^c are correspondingly the total, fine and coarse mode radiances. On the other hand, in Remer et al. (2005) over land η is obtained from the following empirical relation:

$$\eta = 1 - \frac{\left[\dfrac{\rho_{o0.66}}{\rho_{o0.47} - 0.72}\right]}{0.90 - 0.1(\Theta - 150^\circ) - 0.72} \tag{1.2}$$

Where $\rho_{o0.66}$ and $\rho_{o0.47}$ represents the measured TOA reflectance at 0.66 and 0.47 μm and Θ is the corresponding scattering angle.

In the three works the magnitude to be minimized is the following:

$$\epsilon = \sqrt{\frac{1}{n}\sum_{k=1}^{n}\left(\frac{L_\lambda^m(\mu_s, \mu_v, \phi_v) - L_\lambda^c(\mu_s, \mu_v, \phi_v)}{L_\lambda^m(\mu_s, \mu_v, \phi_v) + 0.01}\right)^2} \tag{1.3}$$

Where n is the number of aerosol models, L_λ^m, ρ_o in the notation of Kaufman et al. (1997) and Remer et al. (2005), are the real measurements of MODIS; and L_λ^c, or ρ_{LUT}, are the corresponding calculated values with the LUTs.

There are two types of solutions, the combination of AOD and η that provides the smaller residual is called the optimal solution. However, it is possible that more than one of these combinations also provides an acceptable fitting. The average of all combinations of solutions with a $\epsilon < 3\%$ is called average solution.

In Tanré et al. (1997) extensive sensitivity tests were performed to analyze the limits and uncertainties of the algorithm. Synthetic scenarios were generated with the radiative transfer code in order to obtain reference radiance values to be retrieved and compared with the original values used for its calculation. On the one hand, some scenarios were created with parameters outside the limits of the LUT, for example: bigger or smaller particles, higher AOD and different wind speed or refractive index. On the other hand, synthetic radiance measurements were obtained inside the limit of the LUT but with the addition of noise emulating real conditions of the MODIS measurements. The results of these tests showed that the AOD is the most robust product and that the effective radius and the fraction between size modes can only be considered as an estimation and not as a retrieved product. The optimal solution is in general more accurate than the average one in almost all situations. The effect of measurement errors lead to the conclusion that whereas a random error in the channels does not produce a significant uncertainty in the retrieval, the possible bias plays a more important role.

The validation against AERONET data of the algorithm presented by Tanré et al. (1997) showed uncertainties of $\Delta\tau = \pm 0.05 \pm 0.5\tau$, (at 550nm), $\Delta r_{\text{eff}} = \pm 30\%$ and $\Delta\eta = \pm 0.25$. In the case of the validation provided by Kaufman et al. (1997) that was also done against AERONET products, the uncertainty of AOD was $\Delta\tau = \pm 0.05 \pm 0.2\tau$.

However, the improvements to both algorithms proposed by Remer et al. (2005) and the significantly more extensive validation, including 132 AERONET stations during two years, showed a $\Delta\tau = \pm 0.03 \pm 0.05\tau$ over ocean and $\Delta\tau = \pm 0.05 \pm 0.15\tau$ over land. An uncertainty of $\Delta r_{\text{eff}} = \pm 0.11 \mu m$ for the particle effective radius was also estimated. Thus, it is clear that the updated algorithms present a significantly better behavior in comparison with AERONET, especially over ocean.

1.1.2 Kim et al. (2007): Aerosol classification with MODIS/OMI

Here is presented the comparison of the results of two different algorithms for aerosol typing: MODIS-OMI Algorithm (MOA), which is based on MODIS and OMI (Ozone Monitoring Instrument) data; and the 4 channel algorithm 4CA, which uses the MODIS measurements only. Despite the nature and the main basis of both methodologies are different, the two algorithms distinguish four major aerosol types: dust, carbonaceous, sea salt and sulfate. Furthermore, a three-dimensional aerosol transport model, SPRINTARS (Takemura et al., 2002), is used for a better interpretation of the results and an enhancement of the comparisons.

MOA methodology uses two derived quantities to discern between fine/coarse absorbing and non-absorbing particles. The absorbing coarse mode model is identified with dust, non-absorbing coarse mode is sea salt, absorbing fine mode is carbonaceous and non-absorbing fine mode is identified with sulfate. This classification is based on the work of Higurashi and Nakajima (1999). The FMF, which is the ratio between the fine mode and the total AOD at 550 nm, is used for the size discrimination. On the other hand, the OMI AI, which is an index based on the logarithm of the ratio of the OMI radiance at 360 nm and the corresponding radiance calculation for a pure Rayleigh atmosphere, establishes the filter for absorbing or non-absorbing particles.

The 4CA methodology is more elaborated and is based on the calculation of a LUT of TOA reflectances based on a bimodal lognormal aerosol size distribution assuming absorbing or non-absorbing aerosol types. This LUT was made with the Rstar5b radiative transfer model by Nakajima and Tanaka (1986) for different geometries covering MODIS requirements, and for 11 cases of ratios between fine and coarse mode concentrations. The differences between the channels 410 nm and 440 nm provide information for distinguishing between absorbing and non-absorbing aerosol types. After the aerosol model identification, the MODIS reflectances are fitted by the corresponding LUT for finding the optimal aerosol model and for the retrieval of total AOD and the ratio between aerosol size modes.

Comparisons of the aerosol fractions over easter Asia showed a high degree of consistency between both aerosol typing algorithms and the transport model. The agreement of aerosol type classification for each aerosol type ranges from 32% to 81% depending on the type. The dust type detection frequency was almost the same for the two algorithms, while the frequency distribution of the fine mode particles showed larger differences. Furthermore, if a downsizing of the aerosol typing methodologies is performed to match the resolution of SPRINTARS model, also a high degree of agreement can be observed between the three.

1.1.3 Omar et al. (2009): CALIPSO lidar aerosol typing

The algorithm presented by Omar et al. (2009) is not based on radiance or irradiance calculations, but on the LIDAR signal of different channels of the Cloud-Aerosol Lidar and Infrared Pathfinder Satellite Observations (CALIPSO; Winker et al. (2013)). The objectives of this algorithm are to perform an aerosol typing classification and to obtain the corresponding lidar ratio with an uncertainty of less than 30%. Six different aerosol types are going to be considered: clean continental, clean marine, dust, polluted continental, polluted dust, and smoke. However, as the information content in CALIPSO vertical profiles is not enough, surface type from International Geosphere-Biosphere Programme (IGBP) was also taken as ancillary data to close the retrieval.

The definition of the six aerosol models has been done from a multiyear cluster analysis of AERONET data between 1993 and 2002. However, the lidar ratio corresponding to each of these models does not come directly from AERONET, but has been selected by taking into account also different measurement campaigns and databases for each of the aerosol types. Thus, the microphysical and optical model characteristics initially coming from AERONET have been slightly tuned to match with the lidar ratio values.

The case of clean marine aerosol is special. AERONET retrievals are scarce for this aerosol type, because AERONET stations are normally inland and only some of them are located in coastal areas or islands. Thus, the clean marine model data from Shoreline Environmental Aerosol Study (SEAS) experiment (Masonis et al., 2003) was used.

The retrieval of the aerosol typing is based on a series of complex criteria based on surface type, elevated layer altitude and threshold values for layer integrated attenuated backscatter and depolarization ratio. The latter is used to differ spherical from non-spherical particles, and the attenuated backscatter provides information about unusual high aerosol loads over regions where it is not expected. Each surface classification has a limited number of possible aerosols and not all combinations are allowed. However, the algorithm is designed in such a way that almost all possibilities are covered, and with the objective to make it as much as independent as possible to the geographical criteria. One of the examples of the lacks of this algorithm is the impossibility to find dust or smoke over polar areas.

Comparisons against Langley airborne high spectral resolution lidar (HSRL) shows that the bias of lidar ratio in comparison with this reference instrument is between -7.4 and -9.2 sr.

A sensitivity study for the selected thresholds of attenuated backscatter and depolarization ratio was done in order to analyze the effect of these limits in the final aerosol typing. A 25% variation was introduced in the defined thresholds. Smoke aerosols were unaffected, some of the dust cases were not identified as polluted dust, and some of the polluted dust cases were identified as smoke. In general these misclassifications are not crucial because the lidar ratio is close between them, but for the transition between dust and polluted dust. In this case an error of 47% is being committed in the lidar ratio calculation.

1.1.4 Lyapustin et al. (2018), Lyapustin et al. (2021) and Go et al. (2022): MAIAC algorithm

The MAIAC algorithm is an aerosol retrieval methodology systematically described by Lyapustin et al. (2018) where the AOD and land products are retrieved based on a LUT fitting approach for fixed aerosol models selected from climatological studies. In Lyapustin et al. (2021) an enhancement of this algorithm is presented by adding the aerosol absorption. Go et al. (2022) took a step further and showed a methodology, for some a priori known conditions, to infer the fractions of Hematite and Goethite from this additional absorption product.

Whereas in Lyapustin et al. (2018) the MAIAC algorithm is applied to the MODIS instrument, in Lyapustin et al. (2021) and in Go et al. (2022) this methodology is applied to the Earth Polychromatic Imaging Camera (EPIC) from the Deep Space Climate Observatory (DSCOVR). The look-up-tables used on the three methodologies have been calculated with the IPOL radiative transfer code (Emde et al. (2015), Korkin and Lyapustin (2019)).

The cloud mask algorithm used in these studies is a complex methodology based on four different criteria. The first one is called "Bright cloud test", it takes the shortest channel around 0.4 μm and the highest AOD in the LUT to establish a threshold of reflectance. The second criteria, "Cold (high) cloud test", is based on the comparison of brightness temperature difference at 11 μm and the maximal mesoscale climatology of this value. The "High cloud test" represents additional thresholds for the measured reflectance at 1.38 μm and the brightness temperature differences at 11 μm. Finally, a spatial variability test is applied to ensure homogeneity over grids of 2x2 pixels of 500 meters.

The dust/smoke detection algorithm is based on the ratios of the estimated aerosol reflectance at 0.412, 0.47 and 0.646 μm, compared with simulated theoretical thresholds which are geometrically dependent.

The surface is also an important part of this retrieval algorithm. The MAIAC radiative transfer model uses a semi-empirical Ross-thick Li-sparse BRDF model Lucht et al. (2000), whose reflectance can be expressed as follows:

$$\rho(\mu_0, \mu, \phi) = k^l + k^G f_G(\mu_0, \mu, \phi) + k^V f_V(\mu_0, \mu, \phi) \tag{1.4}$$

Where k^l, k_G and k_V are part of the weighting kernels, and f_G and f_V are predefined geometric functions. In order to perform the retrieval, a separation between the effects of surface and aerosol is necessary. Thus, it is more convenient to work with a Lambertian Equivalent Reflector (LER) function:

$$R(\mu_0, \mu, \phi) \cong R^A(\mu_0, \mu, \phi) + \frac{\rho(\mu_0, \mu, \phi) T^d(\mu_0) T^u(\mu)}{1 - s\rho(\mu_0, \mu, \phi)} \tag{1.5}$$

Where R^A stands for reflectance from wind-ruffled ocean surfaces, T^d and T^u are the downward and upward atmospheric transmittances and s is the spherical albedo of the atmosphere.

In the MAIAC algorithm version presented in Lyapustin et al. (2018) 8 different aerosol models, based on the climatologies of Dubovik et al. (2006) were selected to represent the different geographical areas. These models are defined by a bimodal lognormal size distribution, the fraction of spherical properties and the refractive index. However, the imaginary part of the refractive index does not follow Dubovik et al. (2006), it is modeled according to a power law:

$$\begin{aligned} k(\lambda) &= k(\lambda_0) \left(\frac{\lambda}{\lambda_0} \right)^{-b}, \quad \forall \quad \lambda < \lambda_0 = 0.66 \mu m \\ k(\lambda) &= k(\lambda_0) \qquad\qquad\quad \forall \quad \lambda > \lambda_0 \end{aligned} \tag{1.6}$$

Where the exponent b can be directly related to the Absorption Angstrom Exponent (AAE): $b \approx \text{AAE} - 1$. The generated LUT covers all possible measurement geometries of MODIS and it counts with 12 AOD values from 0.05 to 4 for each aerosol model. The LUT is calculated for a constant water vapor column of 0.5 cm.

In the approach presented by Lyapustin et al. (2021) only two aerosol models are considered. Once the smoke/dust detection filtering has been applied, the model based on Solar Village values of Dubovik et al. (2006) is applied in the regions identified as dust, and the rest of the cloud free pixels are treated as smoke. The necessary calculations for the creation of the LUT now are different. There are only two aerosol models and in this updated version the aerosol absorption is retrieved, therefore $k(\lambda_0)$ and b are also part of the LUT grid. Furthermore, in comparison with the previous version, the maximum value of the AOD has been extended to 6.

Go et al. (2022) only applied MAIAC to dust scenarios. This restriction enabled a more sophisticated dust aerosol model. This aerosol model is based on a Maxwell-Garnett internal mixture to represent each mode, and an external mixture is performed between aerosol particles of different size modes. All dust chemical components are considered to be part of the host and only the iron oxides (Hematite and Goethite) are considered to be inclusions. In these models it is considered that the absorption comes only from the iron oxide components, the rest of the elements conforming aerosol particles are considered to have an imaginary part of the refractive index equal to zero.

The cost function to be minimized in the fitting of Lyapustin et al. (2018) is:

$$F(\tau^a) = \omega_1 \left(1 - \frac{R^T_{0.47}(\tau^a)}{R^M_{0.47}}\right)^2 + \omega_2 \left(1 - \frac{\left[\frac{\rho_{0.47}(\tau^a)}{\rho_{0.55}(\tau^a)}\right]}{b_{34}}\right)^2 \tag{1.7}$$

Where τ^a is the AOD considered in the actual iteration, $R^T_{0.47}$ represents the calculated reflectance at TOA at 0.47 um, $R^0_{0.47}$ represents the measured reflectance at TOA at 0.47 μm, ρ represents the LER at different wavelengths and b_{34} is the LER ratio between wavelengths 0.47 and 2.13 μm. The weights ω_1 and ω_2 are adjusted as a function of the "AOD uncertainty". This "AOD uncertainty" is a threshold value established by the difference between the expected theoretical clear sky and the measured TOA reflectance.

In Lyapustin et al. (2021) and Go et al. (2022) the cost function is different:

$$F^2 = \frac{1}{N} \sum \left[\frac{L^m_\lambda - L^t_\lambda}{L^m_\lambda}\right] = \min\{\text{AOD}_{443}, k_0, b\} \tag{1.8}$$

Where L^m_λ and L^t_λ are correspondingly the measured and theoretical values of the TOA reflectance. In Lyapustin et al. (2021) this fitting is performed with two LUT's in the case of smoke, with effective aerosol heights of 1 and 4 km, but only one for the case of dust. In the former scenario it is considered that aerosol mineral dust is restricted to the planetary boundary layer. However, in the case of Go et al. (2022), two different aerosol heights are considered for the dust conditions.

For the additional aerosol component retrieval of Go et al. (2022) the cost function to be minimized is:

$$\chi^2 = \sum_{j=1}^{4} \left[\frac{k_{\text{rtr}}(\lambda_j) - k_{\text{mix}}(\lambda_j)}{k_{\text{rtr}}(\lambda_j)}\right] \rightarrow \min \tag{1.9}$$

Where the index j represents the wavelengths: 0.34, 0.388, 0.443, and 0.68 μm; k_{rtr} is the imaginary part retrieved in the previous step of the inversion, and k_{mix} is the imaginary part of the mixing following the Maxwell-Garnett rule for the fractions of Hematite and Goethite that are being retrieved in this step.

The validation against globally distributed AERONET stations provided by Lyapustin et al. (2018) shows that 66% of retrievals agree with AERONET within $\pm 0.05 \pm 0.1$ AOD. However, Lyapustin et al. (2021) showed an AOD correlation coefficient between 0.5 and 0.8 in the case of smoke scenarios over North America and dust cases over North Africa and Middle East. The comparisons of the SSA at 0.443 μm are within a range of uncertainty of 0.03 with respect to the AERONET reference for this magnitude.

1.2 Aerosol inversion methodologies in the thermal infrared spectrum

The common assumptions of horizontal homogeneity of the atmosphere and surface in the atmospheric aerosol retrieval community imply almost no azimuth dependence of radiance in this spectral range. This reduced directionality of TIR radiance and the lower sensitivity to the particle size enable some simplifications in the aerosol modeling which are not possible in the solar range. Furthermore, this low directionality also simplifies the surface models, which are mainly described by its temperatures and a lambertian value of albedo. On the other hand, there are other kind of challenges which were not so crucial in the algorithms working between UV (UltraViolet) and SWIR. For example, the influence of the aerosol height, the crucial importance in some cases of the atmospheric temperature profile, the stronger gas absorption lines and the increased computation time derived from their calculation. In general, most of the algorithms restricted to work only in the TIR are mainly focused on aerosol type detection, whereas the retrieval of microphysical and optical aerosol properties is less common.

1.2.1 Turner (2008): MIXed-phase Cloud Retrieval Algorithm (MIXCRA) to aerosol dust

The study of Turner (2008) presents an adaptation of the MIXed-phase Cloud Retrieval Algorithm (MIXCRA) algorithm (Turner, 2005) to the retrieval of aerosol mineral dust. MIXCRA algorithm was originally developed for the retrieval of optical depth and effective radius of the liquid and ice parts of mixed-phase clouds. In this case, the two phases of water in clouds have been substituted by three aerosol dust components: Kaolinite, Gypsum and Quartz. The selection of these components is motivated by their different spectral signature in the spectral range of the instrument selected for this study, the AERI TIR radiometer.

The AERI (Knuteson et al. (2004a), Knuteson et al. (2004b)) TIR radiometer is the instrument selected to perform the retrievals. AERI provides zenith radiances between 3.3 and 19.0 μm with a spectral resolution of 0.1 cm^{-1}. However, MIXCRA has been applied only to 19 channels between 8.0 and 13.0 μm. In order to provide additional information to the atmospheric modeling required for the retrieval, radiosonde profiles from Vaisala RS92 and water vapor values from a microwave radiometer (MWR) were also used.

The core of the retrieval is based on an optimal estimation method (Rodgers, 2000) in which simulated radiances of AERI are fitted to a vector parameter state formed by the optical depth and the effective radius. The selected radiative transfer code is LBLDIS (Turner, 2005), which is a combination of the line-by-line radiative transfer model (LBLRTM) and the Discrete Ordinates Radiative Transfer solver (DISORT) (Stamnes et al., 1988). This retrieval scheme can be applied in single-component or in dual-component configuration. For these two possible configurations of the retrieval, aerosols are represented by a monomodal log-normal particle size distribution with a fixed standard deviation of 0.7 μm and an effective radii range from 0.02 to 12 μm. In the bi-component configuration an independent PSD is associated with each dust component and an external mixture procedure is applied to obtain the total scattering properties. Dust particles are assumed to be spherical, therefore all calculations are performed under the Mie theory. The vertical distribution of dust is not retrieved, it is assumed to be an homogeneous layer spanning from 0 to 1.5 km. Although this representation of the aerosol profile may not be realistic, its impact was evaluated as relatively weak for optical depths smaller than 1. In order to analyze the sensitivity to the effective aerosol temperature, a 0.2 K uncertainty was artificially introduced in the retrieval. This temperature uncertainty was propagated to the AOD as an uncertainty of 0.02, which is quite reasonable.

The methodology presented above is applied separately 6 times for all possible combinations of each dust component in the single-component retrieval (Kaolinite-only, Gypsum-only, Quartz-only) and also for the bi-component configurations (Kaolinite + Gypsum, Kaolinite + Quartz, Gypsum + Quartz). Then, the combination with the smallest residual is selected as the final result.

Simulated radiance calculations show an AOD accuracy around 1% and an uncertainty to separate between dust elements in a dual-component configuration of less than 5%. A real data validation was performed comparing the AOD of an AERI instrument operating in Namey (Nigeria) with the measurements of an AERONET sunphotometer in Banizoumbou. This comparison has been made by scaling the AERONET AOD at 1.02 μm by log(11.0 μm/1.02 μm). A high correlation and similar trends can be observed in both datasets. Furthermore, if no scaling factor is applied to the AERONET AOD a correlation of r^2 = 0.913 is obtained. The analysis of a large data set of retrievals showed that the quality of the AOD decreases for atmospheric scenarios of large water vapor content and low aerosol load.

1.2.2 Thomas and Gautier (2009): TIR dust optical depth from FTIR measurements

A Fourier Transform Infrared Radiometer (FTIR) called PIRATE is used in Thomas and Gautier (2009) to obtain dust optical depth. Jointly with these radiometric measurements the Santa Barbara Disort Atmospheric Radiative Transfer (SBDART) (Ricchiazzi et al., 1998), aerosol ancillary data from an AERONET sunphotometer and ozone column concentration from OMI (Dobber et al., 2008) are used to complete the input of the algorithm. The vertical temperature profiles were taken from climatological situations corresponding to midlatitude summer and tropical scenarios.

PIRATE is a FTIR with a spectral range of operation from 3 to 13 μm with a resolution of 4 cm^{-1}.

It is mounted on a robotic arm with a sun tracking device to follow the sun to measure the solar irradiance, the magnitude that will be used to obtain dust AOD. However, the methodology presented here is restricted from 8 to 13 μm. This spectral range was selected because of its high atmospheric transmissivity (despite ozone bands) and the increased signal-to-noise ratio of these channels.

The two main challenges faced by this algorithm are: the calculation of the Solar irradiance in clear atmospheric conditions and the filtering of the radiation coming from the detector itself. This AOD retrieval is based on three main points: the instrument calibration against reference blackbodies at different temperatures, the assumption of linear response of the FTIR sensor in different Brightness temperature ranges and simulations of clear atmospheric scenarios with the SBDART model.

The PIRATE sensor is considered to behave linearly in two ranges of brightness temperature of the measured target: between 55° to 75°C and between 125° to 200°C. These temperature ranges may seem quite high in comparison with the cold sky temperatures normally expected to be measured. However, it is important to note that this instrument is designed to perform direct sun measurements.

Reference measurements to blackbodies at two different controlled temperatures (75°C and 125°C) are used to establish the slope between the instrument counts and the measured irradiance:

$$\frac{dl}{dC_{\text{open}}} = \frac{I_{125\text{C}} - I_{75\text{C}}}{C_{125\text{C}} - C_{75\text{C}}} \tag{1.10}$$

The offset corresponding to each temperature range of this fitting contains the irradiance coming from all instrument parts but the aperture. The ratio of the irradiance coming from the aperture and just by the reference blackbody is considered to be constant. Thus, it is also possible to obtain this magnitude from the calibration measurements. Therefore, it is established the relation between the digital counts of the FTIR and the corresponding target irradiance for both linear regimes.

In order to get the AOD some further steps are necessary. The ancillary data already mentioned coming from AERONET, OMI and climatological temperature profiles with the SBDART model are used to calculate the irradiance of the clean atmosphere without dust. The total irradiance coming from the instrument is obtained considering the optical head as a perfect blackbody at 35°C. Thus, in the clean atmospheric scenario all atmospheric elements are accounted for but mineral dust. Then, the Beer-Bougert-Lambert attenuation formula can be inverted to obtain dust AOD:

$$\tau_d = (\ln(I_c - I_E) - \ln(I_D - I_E))\, cos(\theta) \tag{1.11}$$

Where τ_d is the dust AOD, I_c is the clean irradiance, I_E the self emission term and θ the solar zenith angle.

According to the results obtained in MBOUR 2006, the AOD at 10 μm presents a correlation with the AERONET AOD at 670 nm of r^2=0.98 for events with a visible AOD over 0.36. For lower values of AOD not enough sensitivity was found in these TIR measurements.

In this work some Mie calculations were made to try to fit the measured AOD spectra both in the visible and in TIR. Refractive index values from Volz (1973) and Fouquart et al. (1987) were used jointly with two size distributions from AERONET and also from from Volz (1973). The results present a reasonable degree of agreement in the TIR part. However, neither of the models studied here correctly matched this optical magnitude both in solar and TIR spectra.

1.2.3 Pierangelo et al. (2004): Dust from AIRS

The aim of this study was to obtain the AOD at 10 μm and the height of aerosol Saharan dust by means of the fit of TIR AIRS radiance measurements. The method does not work with the radiance itself measured by the sensor, but with the information content of the brightness temperature differences obtained from some specific channel combinations.

Through the study of synthetic tests, eight different channels were selected in the spectral range between 8 and 12 μm and four additional ones near 4 μm. There were two main reasons which led to the election of these channels: the maximization of the sensitivity to aerosol dust and the minimization of the effect of Ozone and water vapor absorption. In the case of Ozone, it is possible to work with bands totally unaffected by the absorption of this gas. However, the effect of water vapor cannot be completely avoided in any band of this spectral range.

The main basis of this algorithm consists in the use of a look-up-table (based on the methodology proposed by Tanré et al. (1997)) with precalculated radiance values for the 12 selected channels to fit the previously mentioned brightness temperature differences between these channels. This look-up-table was calculated for each channel and for different atmospheric conditions which try to cover as much as possible the dust scenarios occurring in the real atmosphere. As these precalculated radiative transfer calculations are not done "on the fly", the necessary simplifications lead to a very simple aerosol and atmospheric model. The aerosol optical and microphysical properties are fixed and correspond to the model MITR (MIneral TRansported) by Hess et al. (1998) which can be found in OPAC database. The relatively small sensitivity to the size distribution in this spectral range and the fact that this algorithm was meant to retrieve only Saharan dust support the selection of this fixed aerosol model. It is assumed that all atmospheric dust content is restricted to be in a single layer. Thus, the aerosol height product that this algorithm provides as output is the altitude at which half of the dust optical depth is below and half of the dust optical depth is above. This means that if two aerosol layers are present, the algorithm will provide an infrared optical equivalent of the average of both.

As it has been said, this algorithm is restricted to work only with a dust model. However, the possible contamination of different aerosol types does not suppose a major limitation because most of them correspond mainly to fine mode, which are quite invisible for the longwave channels.

The AOD validation of this methodology has been done against MODIS. A high correlation coefficient can be found for the complete considered dataset. On the other hand, the aerosol height product does not count with a direct validation. However, the visual inspection of the data is according to the expected results, and the interseasonal tendencies are in agreement with the results obtained in other works.

1.2.4 DeSouza-Machado et al. (2010): Dust with A-Train

The algorithm presented in this study shares a lot of characteristics with the previous one, mainly because the input (AIRS radiance) and the output of both algorithms (AOD at TIR wavelengths and aerosol height) are the same. However, despite these common points the algorithm by DeSouza-Machado et al. (2010) is much more sophisticated in terms of atmospheric modeling and the employed mathematical tools to perform the numerical inversion. Furthermore, the validation of the obtained results is much more extensive, because not only a direct comparison of the AOD is made but also a direct validation of the aerosol height against CALIPSO measurements is done.

The algorithm is divided into two main steps. First of all a very simple algorithm based on fixed thresholds of brightness temperature differences is applied to detect the regions not only free of clouds, but also containing aerosol dust. Once again, the channels to calculate the brightness temperature differences have been chosen to maximize the dust information and minimize the gas absorption. In this case no quantitative information can be extracted. The main goal of this first step is to optimize the computation time required to screen out pixels which are not eligible to apply the more sophisticated second step. The noise levels of AIRS channels enable the detection of dust plumes with an AOD over 0.2.

The second step of the retrieval is based on a minimization process in which a full radiative transfer code (AIRS-RTA) is linearize to fit with a Newton-Raphson iteration method the radiance of 25 channels spanning the 10.2-12.82 μm range, seven channels spanning 8.85-9.26 μm, and four channels located at 3.82, 3.84, 8.12 and 8.14 μm. This inversion procedure becomes inestable if the amount, size, height and refractive index defining the aerosol are retrieved at the same time. Thus, some simplifications are necessary to assure convergence.

Particles are considered pure spheres with a fixed uni-modal lognormal size distribution. The refractive index of the aerosol load is also fixed and corresponds to the measurements of Volz (1973). A comparison of this aerosol model against the MITR aerosol model used by Pierangelo et al. (2004) showed significant differences. On the other hand, the vertical extension of the dust layer is also not retrieved. The width of this layer was fixed to be less than 1 km thick. The election of this value attends to the correlation of the final results with the source of validation. Therefore, with these fixed aerosol conditions, a minimizing process based on Newton-Raphson tries to fit the selected radiance channels varying the total dust concentration. The result and the residual is stored and the procedure is repeated for a different value of aerosol height. This procedure is applied for 20 different pressure levels distributed between 1 and 6 km. The combination of AOD and height that produces the smallest

residual is taken as the final solution.

The interpretation of aerosol height that has to be associated with the output of this product is different than in the previous case. For the algorithm presented by DeSouza-Machado et al. (2010) the aerosol height is the top boundary of the dust layer and not the middle height as it was for Pierangelo et al. (2004).

The validation of the aerosol height (or top height) against the analogous product offered by CALIPSO presents a very high degree of correlation. In the case of the AOD validation, the results present a good correlation for thick dust storms. But also, in general, close values to other algorithms operating in visible, such as OMI or MODIS, can be found. However, these comparisons are not very strict because they are done assuming that the relation between TIR AOD and visible AOD are linked by a linear proportional factor of 4.

1.2.5 Klüser et al. (2011), Klüser et al. (2012) and Klüser et al. (2015): Dust from IASI

The main principle of Klüser et al. (2011) is to perform a dust retrieval of IASI measurements with the minimum amount of a priori assumptions (e.g. the atmospheric state). The algorithm shown here has a higher degree of complexity by presenting three steps: cloud screening, dust detection and aerosol retrieval based on Single Vector Decomposition (SVD). The use of this decomposition technique of equivalent optical depth spectra rather than on radiative transfer modeling and look- up-tables is the key to achieve more independence on the non retrieved atmospheric parameters.

The SVD technique is a mathematical procedure which provides non-correlated vectors of state parameters (surface emissivity, water vapor, ozone, temperature, dust..) in which the IASI measurements can be expanded. These vectors can be taken as "eigenvectors" of the system. However, one of the major problems of this type of mathematical procedure is that the vectors of this new base are not formed by a unique type of input parameters, but by a combination of them. These combinations sometimes can lead to results which are difficult to interpret.

The SVD-based methodology was performed within several days over a wide geographical region over western Sahara in order to cover the maximum variability as possible. As a result, the two first vectors of the uncorrelated base can be mainly associated with surface and ozone and water vapor absorption, and from the third to the fifth a high relation with the aerosol dust can be found. Here the aerosol dust is not going to be represented by one, but by four different dust models of the OPAC database: MIAM, MINM, MITR and MICM.

In order to optimize the amount of information that can be extracted from this methodology, not all IASI channels are part of the retrieval. IASI channels between 8 and 12 μm have been grouped in 42 bins equidistant in wavenumber space. Each of these bins contain 10 channels, the highest brightness temperature is selected as the representative of each bin in order to minimize the effects of strong gas absorption lines.

Then, for each of this selected spectral bins the equivalent optical depth is calculated as follow:

$$L_{\text{obs}}(\lambda) = e^{-\tau_{\text{eqv}}/\cos(\Theta_v)} B_\lambda(T_{\text{base}}) \tag{1.12}$$

Where T_{base} is the corresponding brightness temperature of the complete atmospheric slant path observed by IASI. The next step is to weight τ_{eqv} by the weights of the uncorrelated vectors of SVD corresponding to aerosol dust information. Then, a projection of the AOD (escalated at $\text{AOD}_{10\mu m}$ = 0.25) of the different OPAC models is made over this new base. This projection is made because the angle between the two vectors (spectral renormalised τ_{eqv} and AOD_{opac}) can be considered as the weight of each aerosol model in the original IASI spectrum. Then, these weights can be used to recover the total AOD with the weighted sum of all OPAC models. This AOD is used to invert equation 1.12 to obtain the dust temperature. Finally, a second iteration of this process is made with this corrected temperature value to improve the obtained AOD. The physical interpretation of this two step methodology consists in ignoring the dust emission in the first iteration and correcting it in the second step. The weights obtained for the AOD can also be used to weight the size distributions of the OPAC models and also provide an indirect retrieval product of particle effective radius.

The transfer coefficients to convert the TIR AOD to the visible to enable a direct comparison with

AERONET are similar to the one used by DeSouza-Machado et al. (2010)e, but in this case the AOD corresponding to each model has a specific weight obtained by Thomas and Gautier (2009).

This methodology has been applied to the Bodélé Depression in Northern Chad and to Rhub-al-Khali in Southern Saudi-Arabia. The linear correlation between AERONET observations and IASI retrieved dust AOD is r^2=0.623 with a negative bias of -0.18. The 64% of all IASI derived AOD values are within a band of coarse mode $\text{AOD}_{\text{AERONET}} \pm 0.2$.

In Klüser et al. (2012) the authors presented an improvement of the algorithm, extending the physical content of the models used to describe aerosol dust and performing a more sophisticated methodology to transform TIR AOD to visible.

Instead of the 4 OPAC dust mixtures, six pure dust extinction spectra are used as the aerosol input parameters in the SVD calculation. The selected species were: Quartz, Illite, Kaolinite, Montmorillonite, Calcite and Feldspar. This methodology enables a higher flexibility and a broader range of application. The transition to visible for the validation against AERONET is done both with a Mie code and also with the mineral composition extinction spectra. The transfer functions presented by Dufresne et al. (2002) were used to convert the selected extinction spectra into visible AOD. Furthermore, other improvements were added as a more flexible limit of cloud screening or a more accurate dust detection algorithm.

The improved version of the algorithm was applied over a wide geographical area covering 32 AERONET stations. In this case the correlation with AERONET improved with respect to the previous version of the methodology, for the $\text{AOD}_{0.5\mu m}$ for all 32 stations a r^2 of 0.757 was obtained with a bias of 0.003. For these comparisons, 80% of IASI observations lie within AOD± 0.2 of AERONET. It was found that the results corresponding to transition to visible made by the extinction spectra of the models, instead of using Mie calculations, had a higher agreement with the AERONET data. The improvement might be associated with the non-spherical characteristics contained in the models and the higher mineralogical information of this procedure.

The next development of the algorithm can be found in Klüser et al. (2015). The equivalent optical depth is not calculated any more as a rough approximation just based on the slant path view of the satellite radiance measurement, but with a two stream radiative transfer approximation. Moreover, the averaging kernels used in the SVD are calculated with a more sophisticated set of scenarios including: dust temperature varying between 220 K and 285 K, eight AOD values (varying between 0.01 and 1.0) and eight different aerosol models for eight possible sizes distributions. This more complex representation leads to a larger base of uncorrelated states containing significant information about aerosol dust formed by 35 vectors instead of the three previously used. In this new algorithm version, the best fitting dust spectrum is not projected in the AOD_{opac} base but directly in the spectrum of the selected IASI bins, 15 in this case.

The results were compared to eight AERONET stations in the western Sahara, covering a period from June 2011 to June 2012. The values of correlation with AOD at 500 nm did not improve significantly from the previous work. However, about 85% of IASI observations are within ± 0.2 of AERONET coarse mode AOD.

1.2.6 Vandenbussche et al. (2013): Desert dust vertical profiling using IASI

The method presented by Vandenbussche et al. (2013) is focused on the retrieval of the aerosol profile. The complex refractive index, the PSD, the surface emissivity and temperature, and the atmospheric state (except aerosols) are supposed to be known. As it has been seen in the previous works, the vertical distribution of aerosol is a very important characteristic in the thermal infrared. While in the solar spectrum the effect of the aerosol layer height or its shape have a minor importance, in the case of the thermal radiation the aerosol vertical distribution is a crucial element in terms of its influence in the radiative forcing introduced by the aerosols. A significant change in the altitude of an aerosol layer can change the sign of its impact in the net balance of energy.

This algorithm is also designed to work purely with desert dust. Then, the first step is to establish a criteria to filter the pixels which are mainly influenced by aerosol mineral dust. The mean brightness temperature corresponding to the IASI channels between 8.62-8.66 μm and 9.2-9.24 μm spectral bands have been selected to establish the next criteria for dust identification:

$$\text{BT}_{1085} + 0.76K < \text{BT}_{1158} \tag{1.13}$$

Dust is the only aerosol component expected to be found in the atmosphere. Thus, these authors take a fixed model of aerosol mineral dust corresponding to Volz (1972), Volz (1973) and Shettle and Fenn (1979). The sensitivity of IASI measurements to the PSD was studied here. It was found that the sensitivity to the AOD (i.e. the aerosol concentration) is one order of magnitude higher than the sensitivity associated with the size of the particles. Thus, the fixed microphysical model taken by these authors can be considered as reasonable.

The mathematical principles of the algorithm presented here are based on the application of the optimal estimation method (Rodgers, 2000) jointly with LIDORT radiative transfer (Spurr, 2008) and the SPHER Mie code (Mishchenko et al., 1999) to the IASI channels located in two spectral windows: 8.89-9.13 and 10.8-11.1 μm. The only retrieved parameter is the aerosol concentration vertical profile formed by 6 points distributed from 0 to 5 km. The important influence of the initial guess of this profile led to the split of the retrieval in two steps.

In the first step an area of 100 km is selected around the pixel to be retrieved. The retrieval methodology is applied to the average radiance of this area with a high variance to enable as much freedom as possible to the inversion. This wide geographical average is also made to significantly reduce the radiometric noise of the measurements. Then, the vertical profile obtained in the first step is used as the initial guess of the second inversion which is applied only over the pixel that is the target of the retrieval. However, in this case, the allowed variance in the vertical profile is reduced in one order of magnitude. The final product of the retrieval is formed by the shape of the profile of the first step renormalised by the integral of the profile of the second inversion.

The results of this method present a better convergence over ocean because of the higher inhomogeneity expected for land surfaces in terms of emissivity and temperature. A high degree of agreement can be found in the visual comparisons of the AOD at 10 μm obtained with this method with AOD at 500 nm of MODIS, or with the Aerosol Absorption Index of GOME-2 and OMI. The comparisons of aerosol height with CALIPSO in situations of moderate or high aerosol load also are quite satisfying. However, problems are encountered in situations of low turbidity.

1.2.7 Clarisse et al. (2013): Aerosol type specification with IASI

The methodology presented by Clarisse et al. (2013) aims to identify the following five aerosol types: volcanic ash, windblown sand, sulfuric acid droplets, ammonium sulfate and smoke particles. This algorithm can be tuned in order to adapt it for the detection of each of the components separately. However, this aerosol typing is restricted to provide only qualitative information, and no quantitative data can be extracted from it. In order to optimize the results in terms of information content and computation time, 100 channels of IASI instrument have been selected from a window covering the spectral range between 8.0 and 13.3 μm in brightness temperature space.

The mathematical basis of this retrieval algorithm start from a two class discrimination rule, which is a special class of the so-called Fischer discriminant analysis. The two classes to be defined are: the clear atmosphere and an atmospheric situation loaded with a specific aerosol type. These classes are also defined by additional characteristics which mark their validity and range of application. Each class corresponds to a fixed atmospheric condition in terms of plume altitude, thermal contrast and atmospheric temperature. Thus, the algorithm must be applied to measurements in a reasonable degree of coherence with these conditions. The aerosol properties of each class are also fixed, therefore the changes introduced by the different optical or mycrophysical aerosol properties are not taken into account. The last condition is related to the opacity of the aerosol plume. Certain degree of linearity between the parameters defining the classes and their effect over the measurements is assumed. Thus, in conditions of extreme aerosol load the validity of this linear behaviour can disappear.

Once the measurement channels and the parameters defining the atmosphere are selected, the covariance matrix between them is calculated assuming that the same matrix is valid for both classes, loaded and clear. Under the assumption of a normal gaussian behaviour for all accounted measurements and parameters, following the maximum likelihood method, a modified Mahalanobis distance with respect to the clear case is defined for each class. The Jacobian calculations needed for this Mahalanobis distance are obtained with a radiative transfer model and Mie theory. If these Jacobians are not available, they can be substituted by the difference of mean observations collected from a large enough number of both aerosol loaded and clear observations. The collection of these representative observations from each class is made by the use of more simple detection algorithms such as the BTD

(Brightness temperature difference) method.

The class with the smaller modified Mahalanobis distance is taken as the aerosol type corresponding to the retrieved spectra. However, as the aerosol classes are predefined and their characteristics are fixed and restricted to work under Mie theory, not all possibilities and cases encountered in the real atmosphere are properly covered. Thus, an extra criteria which establishes an absolute threshold of this distance is introduced to screen out possible outliers in the predefined aerosol conditions.

This method is applied to different situations where a predominant aerosol class is expected. As it is, between other examples, the case of Nyamuragira (D.R. Congo) in November and December of 2011 or Kilauea (Hawaii), where high concentrations of sulfuric acid aerosol can be found. In the case of mineral dust, a bigger region was selected because different sand aerosols could be identified in the northern hemisphere on 23 March 2010. A qualitative analysis of agreement between aerosol typing and other products such as MODIS AOD$_{0.55\mu m}$, OMI SO_2 or OMI absorption aerosol optical depth shows a high degree of correlation.

1.2.8 Pugnaghi et al. (2013): Simultaneous ash and SO2 retrieval with MODIS

The volcanic plume removal (VPR) procedure presented by Pugnaghi et al. (2013) is a quick retrieval method to simultaneously obtain aerosol ash properties and SO_2 concentration. The input measurements correspond to the radiance of TIR-MODIS bands 29, 31, and 32 (8.6, 11.0 and 12.0 μm), only two additional input parameters are needed: the average plume altitude and temperature. Another kind of parameters to perform corrections as atmospheric profiles or surface emissivity are not needed. The aerosol properties are fixed and correspond to the model presented by Volz (1973). However, it can be easily adapted to other ash properties. The tools to link the retrieval output parameters and the input information are look-up-tables calculated for climatological atmospheric conditions of the region of study, and empirical relationships derived from these climatologies.

The VPR methodology is based on the separation of the radiance coming from the ash plume and the corresponding to the rest of the atmosphere and surface. From the plume transmittance obtained for the MODIS channels, the effective ash particle radius and aerosol optical depth at 550 nm (AOD$_{550nm}$) can be computed. The MODIS bands 31 and 32 are almost transparent to SO_2 absorption. Thus, a higher sensitivity to the aerosol properties is obtained from these channels. The relationship between bans 31 and 29 enables the estimation of the SO_2 amount.

The horizontal extension of the ash plume is established attending at the significant decrease of radiance that the aerosol produces in the aforementioned MODIS channels. Thus, the pixels in which a smooth horizontal behaviour of the radiance can be observed are selected as the plume limits. A linear interpolation between these two limits is performed to assign the result of this interpolation to the corresponding atmosphere that would have taken place in the absence of the plume. A clear graphical representation of this procedure can be seen in figure 1. of Pugnaghi et al. (2013). The reliability of this method is based on the assumption of a high horizontal homogeneity below the plume, like the situations found over ocean or when the plume is located over a thick cloud.

MODTRAN radiative transfer simulations fed with climatological values of a selected geographical region were used to establish an empirical relationship between the altitude and the temperature of the plume with the brightness temperature of the atmospheric column. With this temperature and the separated radiances of the plume and the rest of the atmosphere it is possible to obtain the transmittance of the plume using a simplified radiative transfer equation. Then, as a second step, MODTRAN radiative transfer was used to obtain the plume transmittance for a wide range of possible plume characteristics. Synthetic scenarios were used to obtain a third order polynomial fit between the original transmittance of these scenarios (obtained with the full radiative transfer) and the transmittance obtained with the method shown here. This fit introduces corrections to aspects not adequately retained by the simple radiative transfer approximation considered in the first step. This procedure is applied to the bands 31 and 32. Thus, the AOD can be directly obtained from the transmittance if only aerosol contribution is supposed.

On the other hand, the SO_2 transmittance can be obtained with another fitting using MODTRAN simulations of the bands 31 and 29. In this case, channel 29 is supposed to be affected mainly by SO2. Thus, the transmittance of this gas can be also obtained, MODTRAN can be used to obtain an empirical relationship between SO2 extinction cross section and its corresponding concentration.

The SO_2 flux obtained with VPR method and with a LUT approach were compared in Mt. Etna for measurements corresponding to different days of 2006 and 2011 with a high degree of agreement.

1.3 Aerosol inversion methodologies combining solar and thermal infrared spectrum

Hitherto, the aerosol retrievals combining spectral ranges from UV to TIR have not been extensively explored. In general it is not common to find instruments which cover this broad spectrum, thus a combination of more than one instrument is necessary. In the scientific literature it is possible to find a lot of algorithms which base their aerosol type detection on measurements in one part of the spectrum and the aerosol microphysical and optical characteristics retrieval in the other. However, a combination of both spectra directly in the same retrieval scheme is not common. Nevertheless, two algorithms which take advantage of the full spectrum in the complete retrieval strategy were identified and are presented hereafter.

1.3.1 Zhou et al. (2020b) and Zhou et al. (2020a): MODIS/VIIRS Dust detection and AOD retrieval

Zhou et al. (2020b) and Zhou et al. (2020a) present an update of the MODIS Dark Target dust AOD retrieval method. As in some of the previously presented studies , this methodology is divided into two steps: dust detection and aerosol properties retrieval. The core of the aerosol retrieval is based on a LUT approach where TOA reflectance radiances are associated with the corresponding AOD. The radiative transfer methodology of Ahmad and Fraser (1982) was used to obtain the LUT. The combination of solar and thermal infrared spectrum in this case is only used in the first step, the dust AOD is retrieved at one wavelength (550 nm).

The algorithm validation is performed by a comparison of the results against the previous version of this algorithm and against AERONET Maritime Aerosol Network (MAN) stations (Smirnov et al. (2009) and Smirnov et al. (2011)). This algorithm is designed to work over land dark surfaces or the ocean. However, the majority of AERONET stations are inland and only a few of them are in coastal areas. Thus, to maximize the amount of data to perform a direct comparison these AERONET MAN stations were selected. Furthermore, the first detection step is validated against the aerosol typing algorithm from the CALIPSO instrument (Winker et al., 2013).

Because the algorithm aims for global universality, the selection of a dust aerosol model representative enough of all possible atmospheric situations is crucial. For the size distribution, a bimodal log-normal PSD was taken from the previous MODIS Dark target dust model with a slightly smaller mean radius for coarse mode. However, one of the main updates from this previous model is the inclusion of particle non-sphericity. After some sensitivity tests and comparisons between different shapes distributions, the fine mode was still considered as spherical, because of the lack of variability in the aerosol scattering properties under the changes in shape. However, a spheroidal shape distribution (Dubovik et al., 2006) was chosen for the coarse mode.

Because of the lack of ground reference data for the validation of the dust detection, a set of 19 visually identifiable scenarios were selected to test the dust detection. These scenarios include dust conditions over different seasons and regions, but also some smoke and mixed cloud cases are accounted for to explore the limits of detection. Different dust detection methods already used in the previous literature were tested for MODIS under these reference conditions. These methodologies include algorithms based on very different principles such as: only in visible, only in TIR, monochannel approaches, BTD... However, all of them are lacking in some aspects. There are algorithms with a very good performance on the detection of thick dust plumes but with problems to detect less turbid events; but also, the opposite case is possible to be found. Other big challenges are the detection of cirrus clouds or the separation of dust from big ash particles. The improved algorithm presented by these authors groups some of the main characteristics of all of them including spectral variations between visible an TIR channels and also the horizontal interpixel low variability attributed to aerosols.

A summary of the different criteria of this algorithm can be found below:

$$
\begin{aligned}
&9 - \text{pixelstdev}(R_{0.86}) < 0.02 \\
&0.06 < R_{0.41} < 0.35; \quad \text{if} \quad \frac{R_{0.47}}{R_{0.65}} < 0.9 \Rightarrow \text{dust} \\
&\quad \text{if} \frac{R_{0.47}}{R_{0.65}} < 0.9 \quad \text{then} \\
&\qquad \text{if} \quad \frac{R_{0.65}}{R_{0.55}} \geq 1.15 \quad \text{and} \quad \frac{R_{0.55}}{R_{0.47}} \geq 1.15 \Rightarrow \text{dust} \\
&\qquad \text{NDAI} > -2.8 \quad \text{or} \\
&\qquad -10 < \text{NDAI} < -2.8 \quad \text{and} \quad -3.5 < \text{BTD}8.6 - 11 < 1.0 \Rightarrow \text{dust}
\end{aligned} \tag{1.14}
$$

Where R_x represents the Reflectance at TOA in the different MODIS channels, BTD stands for Brightness Temperature Difference and NDAI is defined as follows:

$$
\text{NDAI} = -10\log_{10}\left(\frac{R_{0.41}}{R_{2.13}}\right) \tag{1.15}
$$

The comparison of the results with AERONET and CALIPSO dusty pixels reveals an approximate detection rate 30% of dusty pixels in weak aerosol conditions and above 80% of pixels with a high dust turbidity.

A fit of the observed TOA reflectance in six wavelengths (0.55, 0.65, 0.86, 1.2, 1.6 and 2.11 μm) to the AOD at 550 nm is done to find the optimal value. As it has been previously mentioned, this fit is performed by the use of a LUT. The input parameters used to make these calculations in addition to the AOD (which is the only one that is retrieved) are the observation geometry and the surface wind speed.

The improvements in the MODIS Dark Target algorithm provided by the new dust detection methodology and the inclusion of the non-spherical aerosol dust model lead to a reduction of the observed AOD bias from 0.06 to 0.02.

1.3.2 Zheng et al. (2022): CALIPSO + IIR

The passive infrared instrument selected for this study is the Infrared Imaging Radiometer (IIR) (Garnier et al., 2012). This instrument provides radiances for the channels centered at 8.65, 10.6, and 12.05 μm with a spectral resolution o f 0.9, 0.6, and 1.0 μm, respectively. The objective is to retrieve the Dust Aerosol Optical Depth in the TIR spectral range (DAOD_{TIR}) at 10.6 μm with a methodology based on a BTD method and a fit to a look-up-table approach. The channel around 10.6 μm was selected for its higher atmospheric transmissivity. The vertical lidar profiles provided by the Cloud-Aerosol Lidar with Orthogonal Polarization (CALIOP) onboard CALIPSO (Hunt et al. (2009), Vaughan et al. (2009)) were also used as input. This combination of measurements coming from different instruments reduces the uncertainty introduced by the assumptions normally done to make the corresponding radiative transfer calculations to obtain the look-up-tables. The operational measurement routine of the CALIPSO lidar and the higher complexity derived from pixels over land lead to the application of this algorithm exclusively at nighttime and over ocean pixels. The information content of dust in this spectral range also limits the results to pixels where CALIOP DAOD is higher than 0.05 at 532 nm.

Among other advantages of the combination of these two instruments operating in the TIR and solar parts of the spectra, it is remarkable the high capability to perform a cloud screening. The high spatial resolution of IIR and CALIPSO instruments makes it possible to detect the subpixel clouds which sometimes can contaminate the measurements of other sensors with a coarser spatial resolution, as IASI for example. On the other hand the broad channels of IIR makes it much more sensitive to uncertainties in the aerosol vertical distribution.

The selected aerosol model for this methodology is fixed for each pixel, which means that the refractive index, PSD or sphericity (among other factors) are not going to be part of the retrieval. The aerosol modeling presents also an additional degree of complexity by assuming a refractive index for each pixel based on the database of Di Biagio et al. (2017) and transport models of Griffin (2007) and Querol et al. (2019) and to divide the world ocean in seven different regions. There are two possible

particle size distributions to be used in this algorithm: one based on the work of Dubovik et al. (2002) at Cape Verde, the other distribution corresponds to the Fennec field campaign during June 2011 over the eastern Atlantic Ocean. The main difference between them is that the distribution of the Fennec campaign is centered around 10 μm, while the corresponding to Cape Verde presents its maximum around 3 μm.

As it has been said the methodology presented in this study relies on BTD at 10.6 μm. Thus, the first step after the cloud screening is to obtain the radiance corresponding to clear sky situations. The FAST radiative transfer code with the Discrete Ordinate Method (FASDOM) developed by Dubuisson et al. (2005) with instantaneous assimilated atmospheric profiles and surface temperature from Version 2 Modern-Era Retrospective analysis for Research and Applications (MERRA-2) have been used to obtain reference values to calculate the brightness temperature of this clear atmospheric situations at TOA, BT_{clear}.

The depolarization vertical profiles of CALIPSO are taken to obtain the dust vertical distribution. CALIPSO profiles are not referred just to dust, but for all aerosol present in the atmospheric column. To make this separation between dust and the rest of the atmospheric components the following formula is applied:

$$f_d(z) = \frac{(\delta(z) - \delta_{nd})(1 - \delta_d)}{(1 + \delta(z))(\delta_d - \delta_{nd})} \tag{1.16}$$

Where $\delta(z)$ is the Particle Depolarization Ratio at 532 nm and the values for dust (δ_d) and non dust (δ_{nd}) are taken from climatological studies. However, this is an optical magnitude in the solar spectral range and cannot be directly transferred to the TIR. Thus, only the shape of the obtained profile in the former equation is used as input for the LUT calculations. Once all aerosol conditions are defined, BT_{dust}-LUT from look-up-tables for different $DAOD_{TIR}$ values can be obtained at 10.6 μm. Therefore, the BT_{dust}-LUT results are compared with the BTD corresponding to the real measurements of IIR (BT_{dust}-LUT = BT_{TIR} - BT_{clear}) to find the $DAOD_{TIR}$ value that better fits the observations.

An analysis of the effect in the retrieval of the different assumptions shows that at 10.6 μm the $DAOD_{TIR}$ is more sensitive to the changes introduced by the two different PSD models than to the use of different dust refractive indexes. Only the 10% of the uncertainty can be directly associated to the refractive index in the methodology presented here. The rest corresponds to instrumental noise, atmospheric assumptions, and radiative simulations. Globally the BTclean calculations of FASDOM in comparison to the IIR bands marked as clean lie within $\pm$ 2.0 K. However, for the dusty pixels the annual mean differences are within $\pm$ 0.1 K.

The comparison of the results obtained here with two IASI DAOD products show good correlations on the seasonal dust transport variations, especially for the calculations corresponding to the Fennec campaign PSD. Furthermore, a validation against AERONET coarse AOD product is also shown, with a correlation coefficient between $DAOD_{10.6\mu m}$ and AOD_{500nm} of 0.754.

1.4 References

Ahmad, Z. and Fraser, R. S. (1982). An iterative radiative transfer code for ocean-atmosphere systems. *Journal of Atmospheric Sciences*, 39(3):656–665.

Clarisse, L., Coheur, P.-F., Prata, F., Hadji-Lazaro, J., Hurtmans, D., and Clerbaux, C. (2013). A unified approach to infrared aerosol remote sensing and type specification. *Atmospheric Chemistry and Physics*, 13(4):2195–2221.

Cox, C. and Munk, W. (1954). Measurement of the roughness of the sea surface from photographs of the sun's glitter. *Josa*, 44(11):838–850.

DeSouza-Machado, S., Strow, L., Imbiriba, B., McCann, K., Hoff, R., Hannon, S., Martins, J., Tanré, D., Deuzé, J., Ducos, F., et al. (2010). Infrared retrievals of dust using airs: Comparisons of optical depths and heights derived for a north african dust storm to other collocated eos a-train and surface observations. *Journal of Geophysical Research: Atmospheres*, 115(D15).

Di Biagio, C., Formenti, P., Balkanski, Y., Caponi, L., Cazaunau, M., Pangui, E., Journet, E., Nowak, S., Caquineau, S., Andreae, M. O., et al. (2017). Global scale variability of the mineral dust long-wave refractive index: a new dataset of in situ measurements for climate modeling and remote sensing. *Atmospheric Chemistry and Physics*, 17(3):1901–1929.

Dobber, M., Kleipool, Q., Dirksen, R., Levelt, P., Jaross, G., Taylor, S., Kelly, T., Flynn, L., Leppelmeier, G., and Rozemeijer, N. (2008). Validation of ozone monitoring instrument level 1b data products. *Journal of Geophysical Research: Atmospheres*, 113(D15).

Dubovik, O., Holben, B., Eck, T. F., Smirnov, A., Kaufman, Y. J., King, M. D., Tanré, D., and Slutsker, I. (2002). Variability of absorption and optical properties of key aerosol types observed in worldwide locations. *Journal of the atmospheric sciences*, 59(3):590–608.

Dubovik, O., Sinyuk, A., Lapyonok, T., Holben, B. N., Mishchenko, M., Yang, P., Eck, T. F., Volten, H., Munoz, O., Veihelmann, B., et al. (2006). Application of spheroid models to account for aerosol particle nonsphericity in remote sensing of desert dust. *Journal of Geophysical Research: Atmospheres*, 111(D11).

Dubuisson, P., Giraud, V., Chomette, O., Chepfer, H., and Pelon, J. (2005). Fast radiative transfer modeling for infrared imaging radiometry. *Journal of Quantitative Spectroscopy and Radiative Transfer*, 95(2):201–220.

Dufresne, J.-L., Gautier, C., Ricchiazzi, P., and Fouquart, Y. (2002). Longwave scattering effects of mineral aerosols. *Journal of the Atmospheric Sciences*, 59(12):1959–1966.

Emde, C., Barlakas, V., Cornet, C., Evans, F., Korkin, S., Ota, Y., Labonnote, L. C., Lyapustin, A., Macke, A., Mayer, B., et al. (2015). Iprt polarized radiative transfer model intercomparison project–phase a. *Journal of Quantitative Spectroscopy and Radiative Transfer*, 164:8–36.

Fouquart, Y., Bonnel, B., Roquai, M. C., Santer, R., and Cerf, A. (1987). Observations of saharan aerosols: Results of eclats field experiment. part i: Optical thicknesses and aerosol size distributions. *Journal of Applied Meteorology and Climatology*, 26(1):28–37.

Garnier, A., Pelon, J., Dubuisson, P., Faivre, M., Chomette, O., Pascal, N., and Kratz, D. P. (2012). Retrieval of cloud properties using calipso imaging infrared radiometer. part i: effective emissivity and optical depth. *Journal of Applied Meteorology and Climatology*, 51(7):1407–1425.

Go, S., Lyapustin, A., Schuster, G. L., Choi, M., Ginoux, P., Chin, M., Kalashnikova, O., Dubovik, O., Kim, J., da Silva, A., et al. (2022). Inferring iron-oxide species content in atmospheric mineral dust from dscovr epic observations. *Atmospheric Chemistry and Physics*, 22(2):1395–1423.

Griffin, D. W. (2007). Atmospheric movement of microorganisms in clouds of desert dust and implications for human health. *Clinical microbiology reviews*, 20(3):459–477.

Hess, M., Koepke, P., and Schult, I. (1998). Optical properties of aerosols and clouds: The software package opac. *Bulletin of the American meteorological society*, 79(5):831–844.

Higurashi, A. and Nakajima, T. (1999). Development of a two-channel aerosol retrieval algorithm on a global scale using noaa avhrr. *Journal of the Atmospheric Sciences*, 56(7):924–941.

Hunt, W. H., Winker, D. M., Vaughan, M. A., Powell, K. A., Lucker, P. L., and Weimer, C. (2009). Calipso lidar description and performance assessment. *Journal of Atmospheric and Oceanic Technology*, 26(7):1214–1228.

Kaufman, Y., Tanré, D., Remer, L. A., Vermote, E., Chu, A., and Holben, B. (1997). Operational remote sensing of tropospheric aerosol over land from eos moderate resolution imaging spectroradiometer. *Journal of Geophysical Research: Atmospheres*, 102(D14):17051–17067.

Kim, J., Lee, J., Lee, H. C., Higurashi, A., Takemura, T., and Song, C. H. (2007). Consistency of the aerosol type classification from satellite remote sensing during the atmospheric brown cloud–east asia regional experiment campaign. *Journal of Geophysical Research: Atmospheres*, 112(D22).

Klüser, L., Banks, J., Martynenko, D., Bergemann, C., Brindley, H., and Holzer-Popp, T. (2015). Information content of space-borne hyperspectral infrared observations with respect to mineral dust properties. *Remote Sensing of Environment*, 156:294–309.

Klüser, L., Kleiber, P., Holzer-Popp, T., and Grassian, V. H. (2012). Desert dust observation from space–application of measured mineral component infrared extinction spectra. *Atmospheric environment*, 54:419–427.

Klüser, L., Martynenko, D., and Holzer-Popp, T. (2011). Thermal infrared remote sensing of mineral dust over land and ocean: a spectral svd based retrieval approach for iasi. *Atmospheric Measurement Techniques*, 4(5):757–773.

Knuteson, R., Revercomb, H., Best, F., Ciganovich, N., Dedecker, R., Dirkx, T., Ellington, S., Feltz, W., Garcia, R., Howell, H., et al. (2004a). Atmospheric emitted radiance interferometer. part i: Instrument design. *Journal of Atmospheric and Oceanic Technology*, 21(12):1763–1776.

Knuteson, R., Revercomb, H., Best, F., Ciganovich, N., Dedecker, R., Dirkx, T., Ellington, S., Feltz, W., Garcia, R., Howell, H., et al. (2004b). Atmospheric emitted radiance interferometer. part ii: Instrument performance. *Journal of Atmospheric and Oceanic Technology*, 21(12):1777–1789.

Korkin, S. and Lyapustin, A. (2019). Matrix exponential in c/c++ version of vector radiative transfer code ipol. *Journal of Quantitative Spectroscopy and Radiative Transfer*, 227:106–110.

Lucht, W., Schaaf, C. B., and Strahler, A. H. (2000). An algorithm for the retrieval of albedo from space using semiempirical brdf models. *IEEE Transactions on Geoscience and Remote sensing*, 38(2):977–998.

Lyapustin, A., Go, S., Korkin, S., Wang, Y., Torres, O., Jethva, H., and Marshak, A. (2021). Retrievals of aerosol optical depth and spectral absorption from dscovr epic. *Frontiers in Remote Sensing*, 2:7.

Lyapustin, A., Wang, Y., Korkin, S., and Huang, D. (2018). Modis collection 6 maiac algorithm. *Atmospheric Measurement Techniques*, 11(10):5741–5765.

Masonis, S. J., Anderson, T. L., Covert, D. S., Kapustin, V., Clarke, A. D., Howell, S., and Moore, K. (2003). A study of the extinction-to-backscatter ratio of marine aerosol during the shoreline environment aerosol study. *Journal of Atmospheric and Oceanic Technology*, 20(10):1388–1402.

Mishchenko, M. I., Dlugach, J. M., Yanovitskij, E. G., and Zakharova, N. T. (1999). Bidirectional reflectance of flat, optically thick particulate layers: an efficient radiative transfer solution and applications to snow and soil surfaces. *Journal of Quantitative Spectroscopy and Radiative Transfer*, 63(2-6):409–432.

Nakajima, T. and Tanaka, M. (1986). Matrix formulations for the transfer of solar radiation in a plane-parallel scattering atmosphere. *Journal of Quantitative Spectroscopy and Radiative Transfer*, 35(1):13–21.

Omar, A. H., Winker, D. M., Vaughan, M. A., Hu, Y., Trepte, C. R., Ferrare, R. A., Lee, K.-P., Hostetler, C. A., Kittaka, C., Rogers, R. R., et al. (2009). The calipso automated aerosol classification and lidar ratio selection algorithm. *Journal of Atmospheric and Oceanic Technology*, 26(10):1994–2014.

Pierangelo, C., Chédin, A., Heilliette, S., Jacquinet-Husson, N., and Armante, R. (2004). Dust altitude and infrared optical depth from airs. *Atmospheric Chemistry and Physics*, 4(7):1813–1822.

Pugnaghi, S., Guerrieri, L., Corradini, S., Merucci, L., and Arvani, B. (2013). A new simplified approach for simultaneous retrieval of so 2 and ash content of tropospheric volcanic clouds: an application to the mt etna volcano. *Atmospheric Measurement Techniques*, 6(5):1315–1327.

Querol, X., Tobías, A., Pérez, N., Karanasiou, A., Amato, F., Stafoggia, M., García-Pando, C. P., Ginoux, P., Forastiere, F., Gumy, S., et al. (2019). Monitoring the impact of desert dust outbreaks for air quality for health studies. *Environment International*, 130:104867.

Remer, L. A., Kaufman, Y., Tanré, D., Mattoo, S., Chu, D., Martins, J. V., Li, R.-R., Ichoku, C., Levy, R., Kleidman, R., et al. (2005). The modis aerosol algorithm, products, and validation. *Journal of the atmospheric sciences*, 62(4):947–973.

Ricchiazzi, P., Yang, S., Gautier, C., and Sowle, D. (1998). Sbdart: A research and teaching software tool for plane-parallel radiative transfer in the earth's atmosphere. *Bulletin of the American Meteorological Society*, 79(10):2101–2114.

Rodgers, C. D. (2000). *Inverse methods for atmospheric sounding: theory and practice*, volume 2. World scientific.

Shettle, E. P. and Fenn, R. W. (1979). *Models for the aerosols of the lower atmosphere and the effects of humidity variations on their optical properties*, volume 79. Air Force Geophysics Laboratory, Air Force Systems Command, United States ....

Smirnov, A., Holben, B., Giles, D., Slutsker, I., O'Neill, N., Eck, T., Macke, A., Croot, P., Courcoux, Y., Sakerin, S., et al. (2011). Maritime aerosol network as a component of aeronet–first results and comparison with global aerosol models and satellite retrievals. *Atmospheric Measurement Techniques*, 4(3):583–597.

Smirnov, A., Holben, B., Slutsker, I., Giles, D., McClain, C., Eck, T., Sakerin, S., Macke, A., Croot, P., Zibordi, G., et al. (2009). Maritime aerosol network as a component of aerosol robotic network. *Journal of Geophysical Research: Atmospheres*, 114(D6).

Spurr, R. (2008). Lidort and vlidort: Linearized pseudo-spherical scalar and vector discrete ordinate radiative transfer models for use in remote sensing retrieval problems. In *Light Scattering Reviews 3*, pages 229–275. Springer.

Stamnes, K., Tsay, S.-C., Wiscombe, W., and Jayaweera, K. (1988). Numerically stable algorithm for discrete-ordinate-method radiative transfer in multiple scattering and emitting layered media. *Applied optics*, 27(12):2502–2509.

Takemura, T., Uno, I., Nakajima, T., Higurashi, A., and Sano, I. (2002). Modeling study of long-range transport of asian dust and anthropogenic aerosols from east asia. *Geophysical Research Letters*, 29(24):11–1.

Tanré, D., Kaufman, Y., Herman, M., and Mattoo, S. (1997). Remote sensing of aerosol properties over oceans using the modis/eos spectral radiances. *Journal of Geophysical Research: Atmospheres*, 102(D14):16971–16988.

Thomas, M. and Gautier, C. (2009). Investigations of the march 2006 african dust storm using ground-based column-integrated high spectral resolution infrared (8–13 μm) and visible aerosol optical thickness measurements: 2. mineral aerosol mixture analyses. *Journal of Geophysical Research: Atmospheres*, 114(D14).

Turner, D. (2008). Ground-based infrared retrievals of optical depth, effective radius, and composition of airborne mineral dust above the sahel. *Journal of Geophysical Research: Atmospheres*, 113(D13).

Turner, D. D. (2005). Arctic mixed-phase cloud properties from aeri lidar observations: Algorithm and results from sheba. *Journal of Applied Meteorology*, 44(4):427–444.

Vandenbussche, S., Kochenova, S., Vandaele, A. C., Kumps, N., and De Mazière, M. (2013). Retrieval of desert dust aerosol vertical profiles from iasi measurements in the tir atmospheric window. *Atmospheric Measurement Techniques*, 6(10):2577–2591.

Vaughan, M. A., Powell, K. A., Winker, D. M., Hostetler, C. A., Kuehn, R. E., Hunt, W. H., Getzewich, B. J., Young, S. A., Liu, Z., and McGill, M. J. (2009). Fully automated detection of cloud and aerosol layers in the calipso lidar measurements. *Journal of Atmospheric and Oceanic Technology*, 26(10):2034–2050.

Volz, F. E. (1972). Infrared refractive index of atmospheric aerosol substances. *Applied Optics*, 11(4):755–759.

Volz, F. E. (1973). Infrared optical constants of ammonium sulfate, sahara dust, volcanic pumice, and flyash. *Applied Optics*, 12(3):564–568.

Wang, M. and Gordon, H. R. (1994). Radiance reflected from the ocean–atmosphere system: synthesis from individual components of the aerosol size distribution. *Applied Optics*, 33(30):7088–7095.

Winker, D., Tackett, J., Getzewich, B., Liu, Z., Vaughan, M., and Rogers, R. (2013). The global 3-d distribution of tropospheric aerosols as characterized by caliop. *Atmospheric Chemistry and Physics*, 13(6):3345–3361.

Zheng, J., Zhang, Z., Garnier, A., Yu, H., Song, Q., Wang, C., Dubuisson, P., and Di Biagio, C. (2022). The thermal infrared optical depth of mineral dust retrieved from integrated caliop and iir observations. *Remote Sensing of Environment*, 270:112841.

Zhou, Y., Levy, R., Remer, L., Mattoo, S., and Espinosa, W. R. (2020a). Dust aerosol retrieval over the oceans with the modis/viirs dark target algorithm. part ii: Non-spherical dust model. *Earth and Space Science Open Archive ESSOAr*.

Zhou, Y., Levy, R. C., Remer, L. A., Mattoo, S., Shi, Y., and Wang, C. (2020b). Dust aerosol retrieval over the oceans with the modis/viirs dark-target algorithm: 1. dust detection. *Earth and Space Science*, 7(10):e2020EA001221.

Chapter 2

Instrumentation: CLIMAT Thermal infrared radiometer and CIMEL sunphotometer

¿Y los cinco se llaman Raúl?

Víctor Antonio Docampo Morate

This chapter is focused on the two instruments selected to demonstrate the application of the developments presented in this thesis. First is the CIMEL sunphotometer as the provider of measurements in the solar spectrum, and the second is the CLIMAT radiometer as the instrument measuring at the thermal infrared spectral range. The sunphotometer is a well established instrument in the scientific community. Thus, a description of the technical specifications and the calibration procedure will be exposed here only in order to recall the principles. However, the use of the CLIMAT radiometer for aerosol inversion purposes is rather new and has not been explored in detail. It should be mentioned that a significant part of the developments of this thesis has been focused on the adaptation of the calibration and data processing of the CLIMAT radiometer measurements to adapt the instrument data to the pursued objectives. The changes introduced in the previous methodology applied to CLIMAT have been made taking as reference the AERONET calibration process for sunphotometer. The efforts on the CLIMAT calibration were focused on the evaluation of radiance values and not Brightness temperature as in the majority of previous applications. The results shown in this chapter correspond to a radiometer which has been measuring in MBour and Dakar since 2018, the name of the instrument is PROTO.

2.1 CIMEL Sunphotometer

2.1.1 Technical description and measurement routines

The Cimel-318 is an automatic portable sunphotometer fabricated by CIMEL Electronique company (https://www.cimel.fr/), designed to measure the Sun irradiance and the sky radiance at different wavelengths and angles. The latest version is able to measure direct Moon irradiance too.

The Cimel-318 set up is formed by an optical head mounted over a robotic arm to perform measurements at different azimuth and zenith angles with an accuracy of 0.05°. Two collimators collocated in the aperture of the optical head enable this instrument to keep a reasonably narrow Field of View (FOV) of about 1.2°. The rest of the optical elements are situated inside the optical head to protect them from any weather condition. The most recent version of this instrument counts with two detectors: silicon and InGaAs. With these two different sensors the instrument is able to measure from 340 to 1640 nm. There is a spectral overlap between both detectors in the channel corresponding to 1020 nm, which constitutes a valuable source of information to evaluate and monitor the perfor-

mance of the detectors. A filter wheel is used to perform spectral measurements at 9 different channels with an approximated FWHM (Full Width at Half Maximum) of 10 nm. The head also counts with a temperature monitoring device which enables a temperature correction of the detector responsivity.

The design of the instrument is meant to be as independent as possible, robust and to successfully operate under a wide range of weather conditions. It counts with a battery pack which can be connected to a solar panel, which increases its independence. The measurement routine can be programmed with the control box and the data can be monitored remotely. Thus, there is no need for a constant presence of human control in the measurement site.

Figure 2.1: CIMEL sunphotometer set up during a sky measurement where the robot arm and the optical head can be appreciated. Photography source: GOA-UVa.

The Cimel-318 is the standard instrument for AERONET (AErosol RObotic NETwork, Holben et al. (1998); https://aeronet.gsfc.nasa.gov/). AERONET, funded by NASA, groups several passive ground-based aerosol networks all over the world as PHOTONS, RIMA, Aerocan, etc. The objective of AERONET is the creation of a continuum database of optical, radiative and microphysical properties of atmospheric aerosols for the calibration and validation of satellite-borne sensors, and for the research and characterization of aerosols at a climate scale. AERONET establishes the calibration, standardization and processing of the instruments within all the instruments belonging to the network. Furthermore, some of the institutions responsible for the calibration and maintenance of the instruments count with systems which monitor and control instruments in real time to detect as soon as possible electronic malfunctions, obstructions in the optical path or power problems. One example of this systemes is CÆLIS (Fuertes et al., 2018).

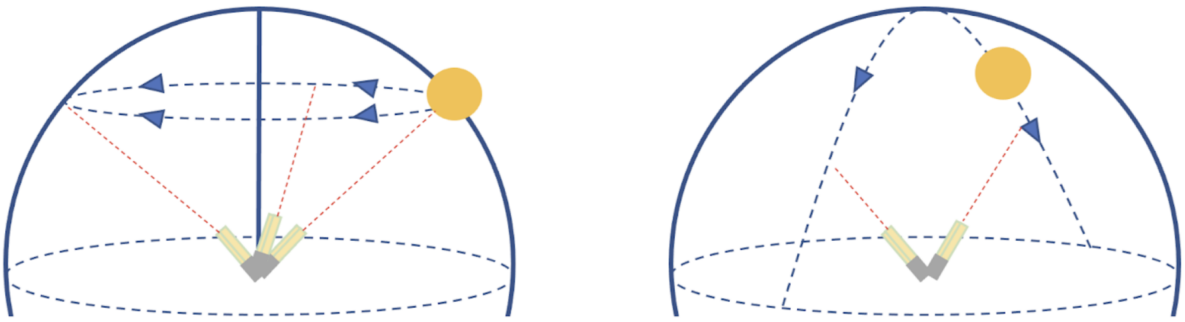

Figure 2.2: Scheme of Almucantar (left figure) and Principal Plane (right figure) of the CIMEL sunphotometer.

There are four main measurement routines of the CIMEL sunphotometer: the direct sun irradiance, the almucantar scenario, the principal plane and the hybrid measurements. In the case of the direct Sun irradiance, thanks to a 4-quadrant sensor and the GPS coordinates of the instrument, the robot arm points the optical head to the Sun (same azimuth and zenith angle) and three consecutive measurements for each channel are performed. This “triplet” measurement is used by the cloud screening algorithm, which is based on the faster temporal variability of clouds in comparison with

the more stable behavior of aerosols. The direct measurements of a triplet are performed within 60 seconds.

The Almucantar routine is formed by a series of measurements where the optical head of the CIMEL sun photometer is pointed to the sky with the same zenith angle as the Sun, but covering the full azimuth angle range. These measurements are performed in two branches: starting at the Sun and covering 180° in the clockwise direction, then the optical head is moved back to the Sun to perform the other 180° in a counterclockwise direction. From the comparison of the variability of both branches it is possible to filter out measurements corresponding to horizontally inhomogeneous atmospheric components which are normally related to clouds. This measurement geometry provides information about a wide range of scattering angles for large solar zenith angles (>50 degrees). Thus, it is very valuable in terms of content information for aerosol retrieval algorithms.

In the case of the principle plane measurements, the optical head of the sunphotometer is pointed to the same azimuth angle of the Sun covering all possible zenith angles. There is also a high amount of information in this measurement routine. However, it is less robust in terms of filtering out cloud contamination. Thus, it is normally less used for aerosol inversion purposes.

The Hybrid scenario is somehow a combination of the previous two measurement routines. The sequence of measurements to the sky starts from the Sun position, two branches covering the full azimuth range are performed as in the case of the almucantar. However, in this case the zenith angle of the optical head is also changing during the process covering from the sun to a certain bottom limit close to the horizon.

2.1.2 Calibration protocol

As it has been mentioned, the calibration protocol is standard for all CIMEL sunphotometers belonging to AERONET. The general protocol for the regular instruments dedicated to measure in the different sites is divided in four phases. The instruments are assumed to be able to measure with a proper accuracy in normal conditions for about one year. After that time, the instrument is sent to one of the calibration facilities that the network has around the world (Goddard Calibration Facility, LOA-PHOTONS or GOA-UVa among others). Then, a "Post calibration" is performed, which means to make a full calibration protocol without any manipulation/cleaning of the instrument. The result of this calibration is propagated back to the last period of measurement of the sunphotometer. Once this first calibration is done, the corresponding instrument maintenance is done. This procedure includes: cleaning of the different optical elements, replacement of damaged filters and electronic components, alignment of collimators, etc. Then, with the instrument in perfect condition to take measurements, the calibration protocol is performed again, which is called a "Pre calibration". The results obtained from this calibration will be applied to the next deployment of the instrument. In regular conditions around 4-6 weeks are needed for the full process from the beginning of the Post calibration to the end of the Pre calibration.

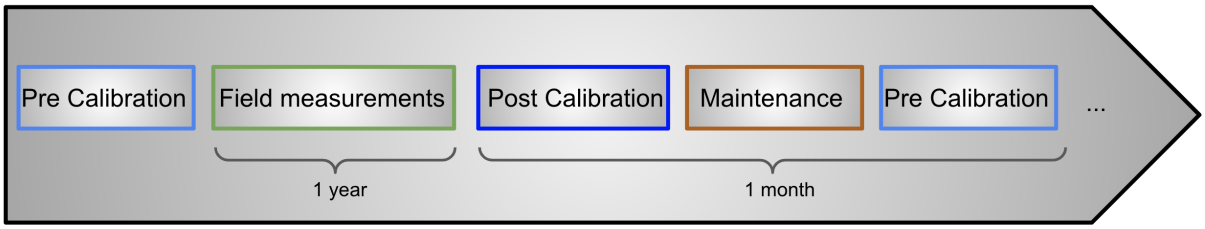

Figure 2.3: Standard measurement and calibration routine for AERONET sunphotometer.

The Pre and Post calibration processes are totally analogous and are formed by two main steps: the SUN and the SKY. The SUN calibration is performed as a direct comparison between the AOD measured by the sunphotometers considered as masters and the instrument that is being calibrated. Both instruments measure in parallel in the observation platform of the calibration facility until there is enough data corresponding to clear conditions and a low aerosol loading. This procedure offers between 1% and 2% percent of error in the calibration constant, and an uncertainty of 0.01-0.02 in the AOD. However, the uncertainties in the AOD are also explained by the uncertainties in the assumed ancillary information for its retrieval, such as the gas optical depth or the pressure at the measurement

site. On the other hand, the sky calibration is performed in the laboratory facing the instrument to a lamp with an spectral irradiance precisely characterized. The lamp is placed inside an integrating Ulbricht sphere. The inner part of these spheres are made of a very reflective material. Thus, all the light coming out of the lamp is integrated and emitted by the aperture where the instrument is located. Therefore, with this configuration the field of view of our photometer is filled with uniform radiance. This radiance is known thanks to a traveling master circulated from NASA to all calibration facilities of AERONET.

Each time that one sensor or filter of an instrument has to be replaced, in addition to the calibration protocol described above, a thermal characterization of the sunphotometer responsivity is performed. In this case the instrument is also placed in front of an integrating sphere, but the optical head is inside a thermal chamber which will vary the temperature between -40°C and 50°C in order to cover the full range of temperature conditions which the instrument could suffer in the field.

2.2 Thermal Infrared Radiometer

2.2.1 Technical description and measurement routines

The infrared radiometer CLIMAT (Conveyable Low-noise Infrared radiometer for Measurements of Atmosphere and Ground surface Targets) (Legrand et al. (2000), Brogniez et al. (2003)) is a Kohler design temperature controlled instrument, which provides brightness temperature and radiances at the thermal infrared range from 8 to 14 μm. The optical head is mounted over a moving robot arm to perform measurements at different zenith angles of the sky, and to the reference blackbody on the field. This reference blackbody, whose temperature is also continuously monitored, is collocated with the instrument to keep tracking of the performance of the instrument during the day. An example of the CLIMAT measurement setup on site is shown in figure 2.4.

Figure 2.4: CLIMAT measuring set up in the field, where the reference blackbody, the robot arm and the optical head can be appreciated.

The optical head of CLIMAT is at a temperature different from 0 K. Thus, the radiation coming from the instrument itself impinges also into the detector. Therefore, the optical and electronic design of CLIMAT, as well as its measurement routine, are meant to get rid of this undesired source of radiance. A high portability and a low power consumption were also two main factors which were addressed in the conception of the instrument.

The CLIMAT optical design, which can be seen in the figure 2.5, is based on three main elements: a conveyable golden mirror with a reflectivity of 99.74%, a filter wheel and a thermopile which acts as the detector.

The conveyable golden mirror is the first element of the instrument optics. It is mounted over a motor wheel to enable two configurations: completely obstructing the instrument aperture, which blocks all outer radiance to measure the thermal emission coming from the instrument itself; and to let open the FOV, to measure the radiance coming from the target in addition to the self-instrument emission.

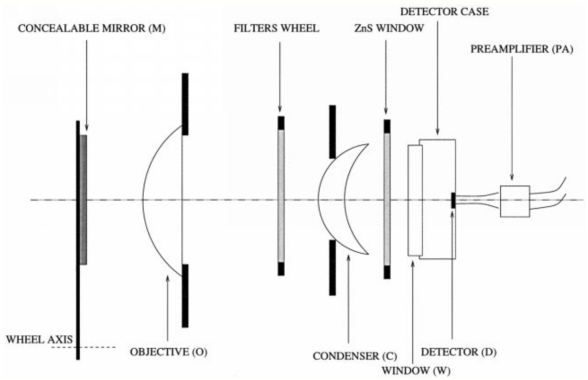

Figure 2.5: CLIMAT optical design. Figure from Legrand et al. (2000).

The combination of the objective and the condenser enables to homogeneously illuminate the filter wheel, which is in between them, and to focus the radiation over the detector. The radius and distance between the objective and the condenser establish the FOV of the instrument, which is approximately 10°. Over the rotating filter wheel, in the model used for this thesis, three different filters are mounted: N8.7 (8.2–9.2 μm), N11 (10.5–11.5 μm), and N12 (11.5–12.5 μm). In addition, if a position of the filter wheel without any filter is selected, the rest of the optics (objective, condenser and ZnS window) act as a Broadband filter, W (8-14 μm). The original transmissivity of the filters of the PROTO CLIMAT instrument can be seen in figure 2.6. However, the shape of the filter functions is likely to change with the time and the lower calibration accuracy derived from the assumption of these filter function shapes required a correction. It has to be clarified that in general, the calibration procedure accounts for the filter transmissivity degradation, but the change of the shape of the filter functions also has an influence. Different correction methods were suggested and an assumption of flat square filters of a FWHM of 1 μm was found as providing the more consistent calibration result. Note that the same approach is used in following the AERONET methodology.

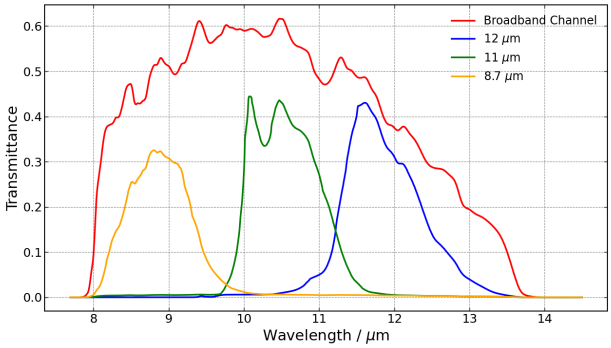

Figure 2.6: Original spectral filter transmissivity of CLIMAT PROTO filters measured in the year 1996.

The CLIMAT detector is a thermopile. The measured voltage by this detector is based on the temperature difference between the hot junction and the cold junction. In this case, the hot junction is heated by the radiation which reaches the detector, and the cold one corresponds to the substrate of the thermopile, which is indeed the temperature of the optical cavity. There are several advantages in the use of a thermopile: it is not necessary to be cooled, it has a wavelength independent response and a weak temperature dependence of the responsivity. However, as it will be shown, some correction which accounts for the temperature of the detector is needed in order to improve the accuracy of the measurements. On the other hand, one of the main drawbacks of this kind of detector is the proportionality of the signal to noise ratio to the measurement time, which is not desirable.

As it has been said, the temperature of the optical head is controlled, which means that the thermodynamic temperature of the detector is always monitored. However, this does not mean that this temperature is regulated. Thus, in the field, despite the thermal isolation of the cavity, the optical head temperature is highly influenced by the ambient conditions.

A summary of the technical characteristics of CLIMAT thermopile can be found in the table below:

Active area	(0.6x0.6)mm^2
Number of junctions	40
Resistor	60kΩ
Voltage noise	31.3 nV Hz$^{-1/2}$
Responsivity	120 V W^{-1}
Responsivity temperature coefficient α	-0.15%K^{-1}
Noise equivalent power (NEP)	0.26 nW Hz$^{-1/2}$
D*	2.3x10^8 cm W^{-1} Hz$^{-1/2}$
Time constant	12 ms
Field of view	80°
Germanium window with nonreflective coating	8-14μm

Table 2.1: CLIMAT thermopile characteristics at 296 K (Legrand et al., 2000).

Measurement principle

The radiance measured by CLIMAT radiometer ($L_i(T)$) corresponds to the convolution of the emission Planck function and the spectral filters (τ_i) of the instrument:

$$L_i(T) = \int_{\Delta_i \lambda} B_\lambda(T)\tau_i(\lambda)d\lambda \tag{2.1}$$

In the following section different approaches to represent this spectral weighting will be shown.

As it has been mentioned, the radiance impinging in the detector does not exclusively come from the measurement target (ex.: the sky or reference black body), but also from the optical head cavity. Thus, in order to isolate the radiance of the desired target, each measurement is formed by a first recording of the digital counts corresponding to the cavity $c_i(T_d)$, which means that the golden mirror is closing the aperture, and then a recording of the counts corresponding to the open configuration $c_i(T)$. Assuming that the cavity is a perfect black body, whose radiance is perfectly defined by the Planck function and the monitored temperature ($L_i(T_d)$), from the difference in counts of both configurations and the calculated radiance coming from the cavity, the radiance of the target ($L_{T,i}(T)$) can be obtained as follows:

$$\Delta L_i = S_i \Delta c_i \tag{2.2}$$

Where i represents the different instrument channels, $\Delta c_i = c_i(T) - c_i(T_d)$, $\Delta L_i = L_{T,i}(T) - L_i(T_d)$ and S_i is the calibration coefficient. Thus:

$$L_{T,i}(T) = \Delta c_i S_i + L_i(T_d) \tag{2.3}$$

The linearity between the difference in counts and the difference in radiance is extremely high, especially when the optical head cavity is around 20°C. However, as it would be shown, significant non-linear effects appear when this temperature rises over 30°C. These non-linear effects are not the only change in the behavior of the radiometer when the detector is warmed up. There is also a change in the sensitivity (calibration constant) which depends on the difference of temperature of the cavity during the calibration ($T_{d,\text{cal}}$) and the temperature of the cavity during the measurement (T_d). This change can be accounted for by the following correction in the calibration coefficient:

$$S_i' = S_i \exp(\alpha \Delta T_d) \tag{2.4}$$

Where $\Delta T_d = T_d - T_{d,\text{cal}}$ and α is the responsivity temperature coefficient, whose approximate value can be seen in table 2.1.

2.2.2 Calibration Principle

The calibration of CLIMAT radiometer is formed by a series of measurements in the laboratory taken to a reference source of radiation. As it has been shown in the case of the CIMEL sunphotometer, and for most of the instruments measuring at solar wavelengths, the reference source of radiation is a lamp, whose irradiance is well known, and an integrating sphere. However, in the case of this thermal

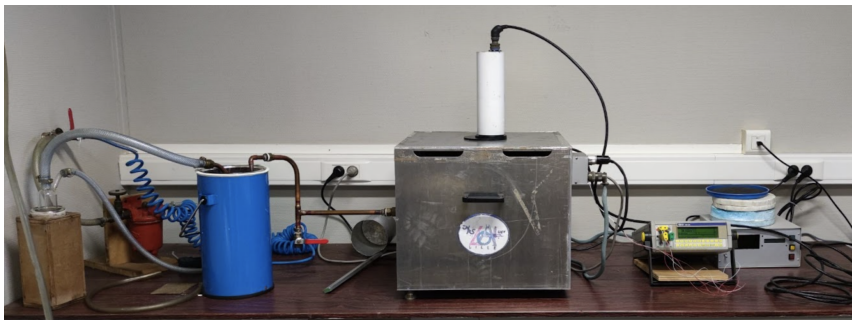

Figure 2.7: CLIMAT calibration set up at LOA facilities. The optical head is positioned looking to the reference blackbody.

infrared instrument, the reference for the calibration is a blackbody whose temperature is constantly monitored.

The CLIMAT optical head is faced to the blackbody, which counts with a system based on liquid nitrogen to cool down its temperature until -80°C, and a heating system device to warm it up to 40°C. The regular procedure consists in cooling the blackbody until the limit temperature of -80°C, and then perform measurements progressively, each 5-10°C approx., while the temperature of this reference rises to the laboratory temperature. Once the blackbody approaches the ambient temperature, the heating device is connected to complete the final range of temperature up to 40°C. It is important to note that the temperature of the optical head should be as stable as possible during this procedure. Thus, in between the measurements, the optical head is stored in a thermal incubator which allows to keep its temperature constant. In order to characterize the responsivity temperature coefficient, this procedure has to be repeated for different temperatures of the optical head.

As the temperature of the reference blackbody is known, the equation 2.2 can be used to perform a linear regression of the difference in counts between the open and closed configuration of CLIMAT during the calibration, and the difference in radiance between theoretical Planck radiance of the black body ($L_{\text{BB},i}(T)$) and the corresponding to the optical cavity ($L_i(T_d)$), both weighted by the CLIMAT filter functions. The slope of this regression is identified as the calibration coefficient:

$$\Delta L_i = L_{\text{BB},i}(T) - L_i(T_d) = S_i \Delta c_i \tag{2.5}$$

Finally, it is important to note that the knowledge of all the involved temperatures in the calibration is necessary to obtain the corresponding radiance values. However, according to equation 2.1, the spectral shape of the filters (τ_i) is also necessary to complete the calculations. There are different strategies to mathematically represent the CLIMAT filters to pass from $B_\lambda(T)$ to $L_i(T)$. However, the measurement principle and the main assumptions about CLIMAT behavior are common to all of them.

Hitherto, CLIMAT instrument was focused on observations of the Brightness temperature of the target and the radiance values were used less often, specially for the aerosol retrievals procedure and the accuracy it may require. Thus, as it will be shown, the parametrizations performed of Planck radiance enables its inversion into the corresponding temperature. The use of Brightness temperature to represent the radiance presents obvious advantages for measurement interpretation. However, in this thesis the measurements of CLIMAT have to be used as input of the GRASP inversion procedure (Dubovik et al., 2021) that operates in terms of radiances. Thus, it is necessary to work with the radiance value, as well as to assume a known filter shape in order to consistently introduce these measurements also for the corresponding computations of gas absorption. Therefore, the methodology selected for the calibration of the data used in this thesis is to assume the square filter shapes, with a FWHM of 1 μm, previously mentioned. This filter function is also used for convolution with the Planck function without any parametrization.

Other strategies: Direct and DLSQ (Damping Least SQuare) methods

Different strategies exist to represent the radiance measured by CLIMAT instrument which account for both the filter shape and the Planck radiation at the same time. On the one hand, the direct method consists in performing a multiparameter fit of the theoretical radiance obtained from convolving a filter shape by the corresponding Planck function at a certain temperature. This means that the integral

in equation 2.1 is replaced by:

$$L(T) \approx \frac{a}{\exp\left(\frac{b}{T^g} - d\right)} \tag{2.6}$$

Thus, a,b,g and d now represent the filter transmission function. Therefore once the measurement is performed the calculation of the corresponding brightness temperature is immediate:

$$T_i = \left(\frac{b}{R}\right)^{1/g} \qquad \text{with} \qquad R = \ln\left(\frac{a}{L_i} + d\right) \tag{2.7}$$

On the other hand, the Damping Least SQuare (DLSQ) method does not assume the filter shape. In this case, the equation 2.1 is parametrized in the following way:

$$D(T) = \exp\left(\frac{\beta}{T^{\mathcal{Y}}}\right) - \delta \tag{2.8}$$

Thus, equation 2.5 becomes:

$$\frac{1}{D(T_{\text{BB}})} - \frac{1}{D(T^{\circ}_{\text{cav}})} = \frac{\Delta C}{S_{\circ}} \tag{2.9}$$

The principle of the method consists in the combination of equations 2.8 ad 2.9 to obtain a function which depends on 3 variables (T_{BB}, T_{cav} and Δc) and 4 parameters ($S_{\circ}$, β, $\mathcal{Y}$ and δ). By an iterative procedure (Levenberg method) it is determined the best adjustment of the 4 parameters which satisfies the set of measurements, which are the N points of calibration of T_{BB}, T_{cav} and Δc. Thus, the spectral coefficients and the calibration coefficient $S_{\circ}$ are then determined at the same time without the knowledge of the spectral shape of the transmissivity of the channel.

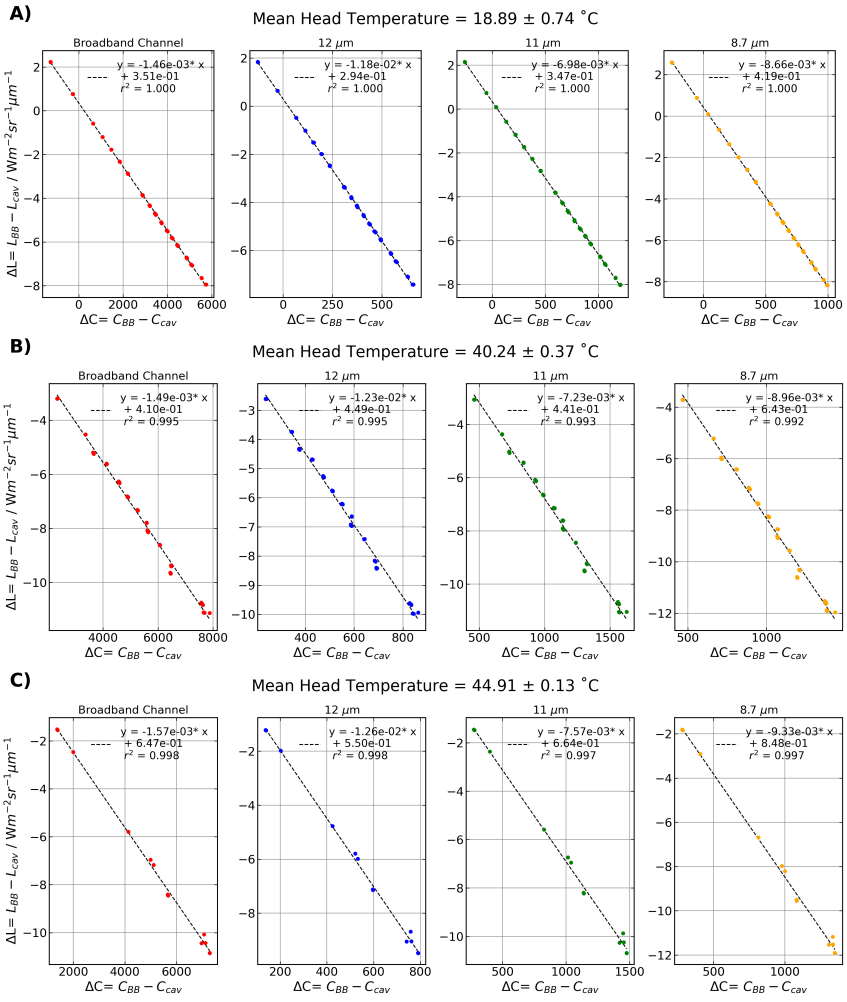

Figure 2.8: CLIMAT calibration curves for the Post-Calibration performed in November 2021. The panels (A, B and C) correspond to different optical head temperatures.

2.2.3 PROTO instrument Calibration

Once the basic calibration principle of CLIMAT radiometer has been shown, this section is devoted to the analysis of the calibration procedure made for the PROTO instrument. This radiometer was one of the first instruments built. It has been measuring in different stations, including recent measurements in Israel, Senegal and north of France (Lille). In this work, the measurements employed are from Dakar (Senegal), because it represents the desert dust environment and it is the last site where the instrument was operating before the calibration made for this thesis.

The previous calibration protocol was slightly enhanced for the use of the CLIMAT measurements for the purpose of this thesis and accuracy required for aerosol inversion.

A comparison of the Post and Pre calibrations is shown here.

Figure 2.8 shows the calibration curve for the Post calibration of CLIMAT made in November of 2021 upon the return of the instrument from the field. The procedure was performed three times for different temperatures of the optical head: around 20°C (Panel A), 40°C (Panel B) and 45°C (Panel C). The curves presented in this figure have been already filtered to exclude the outliers and the points out of the expected linear behavior. Note that for the calibration at ambient temperature the filtering was not necessary, all the points were in a high agreement with the expected linear dependence. On the other hand, when the temperature of the optical head was risen over 30°C noticeable non linear effects appeared. A mean difference in the calibration constant for the different optical head temperatures of 3% was obtained for the ensemble of the four CLIMAT channels, with a maximum difference of 8% in the 8.7 μm channel.

Once this calibration procedure was done, the maintenance of the instrument was performed. The golden mirror and the external part of the optical head were cleaned. Then, as previously described, the calibration procedure was repeated but this time only in ambient temperature conditions (around 24°C). The corresponding calibration curves of the Pre calibration are shown in figure 2.9, where a change of radiance around 6% in all channels can be appreciated after the maintenance of the radiometer.

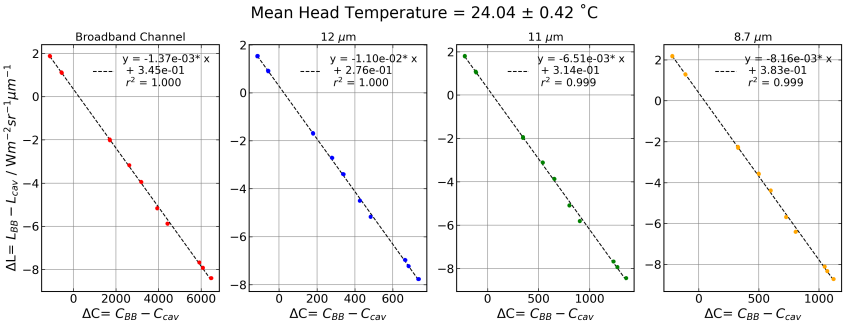

Figure 2.9: CLIMAT calibration curves for the Pre-Calibration performed in November 2021.

In order to characterize the validity of the obtained calibration constants, for the Post calibration data set with an optical head temperature of 18.89°C, the difference between the measured radiance of the laboratory reference black body and its theoretical Plank radiance as a function of the temperature of the black body was done, as it is shown in figure 2.10. The parameter α was empirically adjusted to find the best possible agreement between the measured radiance and the theoretical values, the best performance was found for α = 0.0037. As it can be seen, an agreement better than 1% is achieved for the temperature range covering from 35°C to -50°C, where no special spectral behavior is observed. However, from -50°C to -80°C the quality of the calibration is noticeably degraded. In this temperature range, all the channels present a growing bias that reaches uncertainties of around 5%. Whereas the 8.7 μm channel in this lowest temperature range has a negative uncertainty of -5% of difference for the coldest temperature, the broadband channel presents a positive difference with the theoretical values of approximately 7.5%. An important factor to take into account to correctly interpret these results is that the Planck emission is smaller for lower temperatures. Thus, as these results are expressed in relative terms, an increase of the relative uncertainty for this temperature range is expected.

On average, the sky brightness temperatures in the CLIMAT channels for aerosol observations (clouds free, but with aerosol loading conditions) oscillate between -20°C and -40°C. Thus, in prin-

ciple the uncertainties of the calibration in the lower temperature (clear sky, no dust) ranges are not crucial for the pursued objectives of this thesis.

Thanks to the presence of a reference blackbody in the field, it is possible to make comparisons of the quality of the measurements and calibration data acquired out of the laboratory conditions. Figure 2.11 shows the relative difference in percent of the measured radiance of the reference blackbody in the field and the theoretical Plack radiance of the same blackbody. Four different days spanning in a time period longer than a year in the Dakar station were selected in order to understand the temporal limit of application of the Post calibration constants. The continuous lines refers to the radiance obtained including the α correction, which accounts for the changes in sensitivity when the temperature of the optical head changes with respect to the calibration conditions; and the dashed line indicates the difference if this correction is omitted.

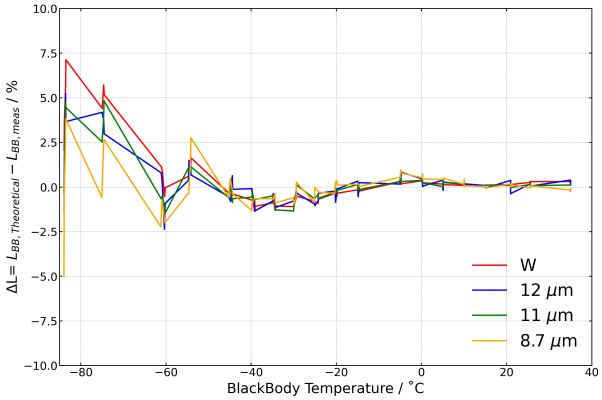

Figure 2.10: Relative difference of the theoretical Planck black body radiance and the CLIMAT radiance obtained for the Post calibration data set obtained for an optical head temperature of 18.89°C as a function of the black body temperature.

As it can be appreciated, the differences when the head temperature correction is not applied are clearly biased to negative values, ranging from -0.6% to -1.1%. The maximum difference can be found in the 8.7 μm channel with a relative MBE (Mean Bias Error), for the four days, of -1.1%. On the other hand, the broadband channel presents the lowest differences with a relative MBE of -0.6%.

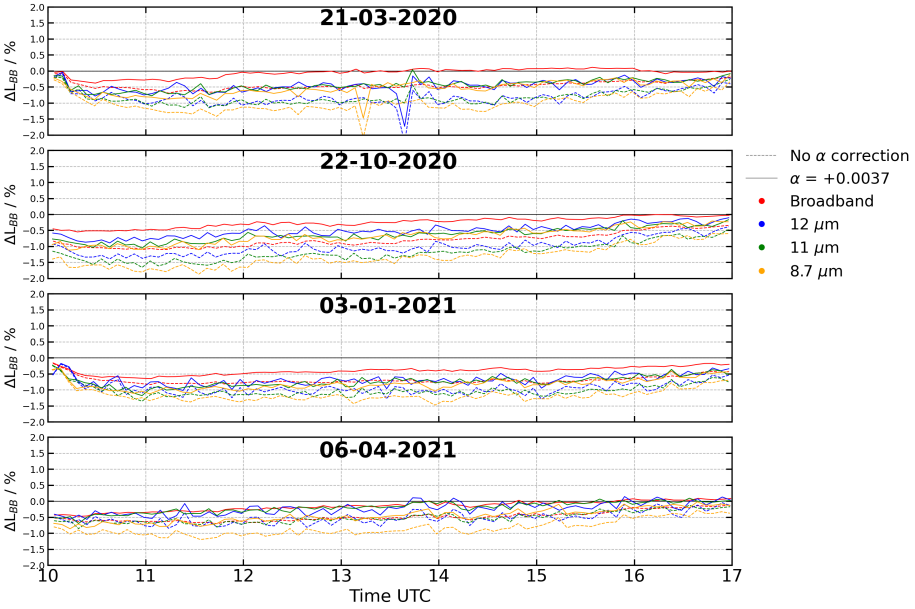

Figure 2.11: Relative radiance difference of the measured CLIMAT radiance of the reference black body in the field and its theoretical Plack radiance for four different days. The different colors in each panel correspond to the four CLIMAT channels. The dashed lines correspond to the calculation of the radiance without the correction to the temperature variations of the optical head, and the continuous lines to the radiance values already corrected by α.

The α correction reduces this bias. In this case, the best MBE can be found at the broadband channel with a value of -0.2%, and the worst corresponds to the 8.7 μm channel with a value of -0.7%. Thus, it is clear that the correction to the difference in the optical head temperature during the laboratory calibration and in field measurements is necessary, and it provides a higher agreement with the field reference black body.

The comparisons with the reference black body in the field provided until now correspond only to daylight time, because these are the conditions of the combined retrieval of the CIMEL sunphotometer and CLIMAT radiometer employed in this thesis work.

The results obtained here not only provide a proper calibration to obtain the radiance for the different channels of CLIMAT radiometer. But also the different comparisons and statistical analysis provide a highly valuable source of information to perform aerosol retrievals, as for example the expected range of uncertainty of each channel. In general, the channels corresponding to 11 and 12 μm present a higher stability and higher performance than the channel situated around 8.7 μm.

2.3 References

Brogniez, G., Pietras, C., Legrand, M., Dubuisson, P., and Haeffelin, M. (2003). A high-accuracy multiwavelength radiometer for in situ measurements in the thermal infrared. part ii: Behavior in field experiments. *Journal of Atmospheric and Oceanic Technology*, 20(7):1023–1033.

Dubovik, O., Fuertes, D., Litvinov, P., Lopatin, A., Lapyonok, T., Doubovik, I., Xu, F., Ducos, F., Chen, C., Torres, B., Derimian, Y., Li, L., Herreras-Giralda, M., Herrera, M., Karol, Y., Matar, C., Schuster, G. L., Espinosa, R., Puthukkudy, A., Li, Z., Fischer, J., Preusker, R., Cuesta, J., Kreuter, A., Cede, A., Aspetsberger, M., Marth, D., Bindreiter, L., Hangler, A., Lanzinger, V., Holter, C., and Federspiel, C. (2021). A comprehensive description of multi-term lsm for applying multiple a priori constraints in problems of atmospheric remote sensing: Grasp algorithm, concept, and applications. *Frontiers in Remote Sensing*, 2:23.

Fuertes, D., Toledano, C., González, R., Berjón, A., Torres, B., Cachorro, V. E., and de Frutos, Á. M. (2018). Cælis: Software for assimilation, management and processing data of an atmospheric measurement network. *Geoscientific Instrumentation, Methods and Data Systems*, 7(1):67–81.

Holben, B. N., Eck, T. F., Slutsker, I. a., Tanre, D., Buis, J., Setzer, A., Vermote, E., Reagan, J. A., Kaufman, Y., Nakajima, T., et al. (1998). Aeronet—a federated instrument network and data archive for aerosol characterization. *Remote sensing of environment*, 66(1):1–16.

Legrand, M., Pietras, C., Brogniez, G., Haeffelin, M., Abuhassan, N. K., and Sicard, M. (2000). A high-accuracy multiwavelength radiometer for in situ measurements in the thermal infrared. part i: Characterization of the instrument. *Journal of atmospheric and oceanic technology*, 17(9):1203–1214.

Chapter 3

GRASP algorithm

Venga, tú dale "unchi" "unchi" "unchi" con ritmo.

Luis Cantalapiedra Conde

This chapter is devoted to the description of the algorithm used for the retrieval of the dust properties from the selected input measurements, GRASP (Generalized Retrieval of Atmosphere and Surface Properties). The general framework of the algorithm, the main mathematical basis, the simulation features and some of the main applications are going to be exposed here. In order to provide a proper context to the specific methodology developed for this thesis, it is important to describe the fundamental mathematical concepts of the inversion in which it is based, and the already developed functionalities of GRASP code. No specific modifications to the inversion module have been done for this thesis. However, for the correct understanding of ideas and methods presented in the following chapters it is necessary to know the core fundamentals of the retrieval module. On the other hand, the new developments of the forward model (thermal emission inclusion in the radiative transfer, the gas absorption lines and the subchannels approach) cannot be properly understood without their context in the algorithm.

3.1 What is GRASP?

GRASP, which stands for Generalized Retrieval of Atmosphere and Surface Properties (Dubovik et al., 2011)(Dubovik et al., 2014)(Dubovik et al., 2021) , is an open source (https://www.grasp-open.com/) modular retrieval algorithm based on a Multi-term (Multi-Source) Least Square Method (LSM).

The generalized nature of the algorithm arises from two main facts: the inversion algorithm has been designed without any specific objective in mind, and from its modular structure. GRASP is divided into two main modules: the forward model and the inversion, which are totally independent. At the same time, the forward model is also divided into smaller independent modules which represent the different elements and processes involved in the interactions between the radiation and the Atmosphere-Surface system. Some examples of these forward model modules, which are going to be described later, are: radiative transfer, aerosol single scattering properties, surface models, gas absorption lines...

The total independence among the different modules enables a huge flexibility to adapt GRASP to any objective. GRASP code can be used as an inversion algorithm, which will retrieve the atmospheric and Surface properties from the input data sets (measurements and a priori knowledge). GRASP is also a forward model which will simulate the measurements corresponding to a given atmospheric scenario. Furthermore, all atmospheric and surface modeling modules can be ignored and GRASP can be set as a pure radiative transfer code based on the Successive Orders of Scattering Scheme proposed by (Lenoble et al., 2007). Thus, the GRASP package can be considered as a platform for developing, testing, and refining novel retrieval concepts and their utilization in operational processing environments.

The inversion module, which is based on the Method of Maximum Likelihood (MML) and in the end on a LSM fit, does not rely on any input or output fixed assumptions, but on the Central Limit

Theorem (CLT) for the errors/noise distributions of the input data sets. The retrieval scheme is exclusively constructed over statistical estimation theory with direct physical interpretation. This general and independent nature of the inversion allows the possibility of performing any retrieval with the only limitations of the information content available in the input, and the developed features of the forward model. However, the inversion has not only been designed to achieve a fully generalized structure, but also to provide the best behaved solution in statistical terms, as it will be shown later. The main problems faced by the multi-term LSM strategy are: forward model non-linearity, accounting for the non-negativity nature of measured and retrieved characteristics, dealing with the redundancy of observations, assuring consistency of multiple constraints and estimating retrieval errors.

The basic idea of GRASP can be described as an iterative process in which starting from the definition of the input measurements and the a priori constraints, synthetic measurements generated by the forward model are fitted to the real measurements. After some iterations between the numerical inversion and the forward model the residual of the fitting reaches a desirable value, which means that the simulated measurements and the real ones are close enough. Thus, the parameters which define the forward model of the final iteration are identified as the values of the real atmosphere. A representation of this iterative scheme can be seen in the figure below:

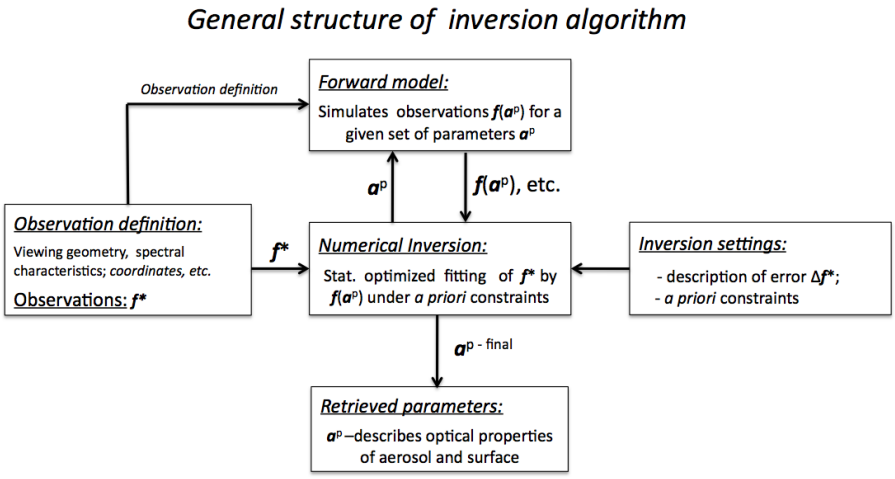

The flexibility of GRASP design enables the possibility to overcome the limitations introduced by the information content of the input data sets in different ways. Formally the balance of the lack of information content is achieved by reducing the available solution space. However, this reduction can be done by means of an increase of the a priori constraints, the reduction of retrieved parameters by fixing them to a constant value assumed as true, or by the simplification of these retrieved parameters by representing them with models that require a smaller amount of variables. At the same time, these trade-offs can be used to increase the retrieval speed by the price of reducing completeness of retrieval to adapt GRASP for processing large amounts of observations in a timely manner, for example as required for Near-Real-Time calculations.

GRASP input data sets have two different origins: measurements and constraints. However, there is no formal distinction between them as it will be shown later. It is possible to apply GRASP to a vast variety of measurements covering different geometries, channel configurations, polarization or atmospheric profiling techniques. Among other examples, GRASP has been used for retrievals of space-borne sensors as MODIS, POLDER, MISR or 3MI; ground-based photometers as CIMEL or PFR, spectrometers as Pandora and PSR, different lidar instruments belonging to EARLINET or LALINET, ceilometers, all-sky cameras...

The constraints retain the a priori knowledge from the retrieved parameters and help to deal with the non-uniqueness nature of the solution of the remote sensing inversion. There are two main types of constraints in GRASP: single-pixel and multi-pixel. The single pixel constraints are divided in two: smoothness, which are related to the functional expected shape of the parameters, and a priori, which are directly related to the parameter value. The multipixel constraints limit the spatial and temporal variability of input datasets corresponding to different spatial points or timestamps. These constraints are designed to retain information like the well known high horizontal spatial homogeneity of aerosols,

or the slow temporal variations of the surface.

There are different available options for each module of GRASP forward model in order to properly adapt it to any situation. The surface is represented as a BRDM (Bi-directional Reflectance Distribution Matrix) that includes Bidirectional Reflectance Distribution Function (BRDF) and Bidirectional Polarization Distribution Function (BPDF). However, there are different available models to represent BRDF and BPDF over land and ocean. The complexity of aerosol models is also a key point in the optimization of the inversion. The optical and microphysical particle properties can be accounted directly as the size distribution, sphericity, complex refractive index... However other approaches can be used such as the retrieval of chemical Componentes (Li et al., 2019), the use of predefined external mixtures (Lopatin et al., 2021) or the simplified representation of the particle size distribution (Torres et al., 2017) among many others. In addition, GRASP is designed for the calculation of Broadband fluxes and radiative forcing using retrieved parameters (Derimian et al., 2016).

The main principles of the methodology exposed above and different scientific applications of it are going to be discussed in this chapter. The section number 3.2 is devoted to the description of the inverse module. The section 3.3 is focused on the different characteristics of the forward model, especially to the new features developed for this thesis. And finally, in section 3.4 a brief summary of some of the main applications of GRASP until now will be presented.

3.2 Inversion

Inversion can be seen as the methodology which establishes the link from measurement space (here $\boldsymbol{f}$ represents the vector of measurements) to the space of physical parameters ($\mathbf{a}$ represents the vector of retrieved parameters). Generally, this projection from measurement space to the solution space is an ill-posed problem. There are infinite combinations of $\mathbf{a}$ which reproduce the input set of measurements and the solution is non-unique. Thus, the main challenge faced by an inversion methodology consists in identifying the correct solution. The chosen approach of statistical optimization discussed here is based on the assumption that the forward model is accurate enough in the modeling of the observations and the main uncertainties come from errors in measurements. If these conditions are not fulfilled, it might be not possible to fit the observations or the solution might have strong systematic errors.

The statistical optimization is based on the fact that the fitting becomes sensitive to the presence of random measurement errors if the number of measurements (Nf) exceeds the number of retrieved characteristics (Na):

$$\mathrm{Nf} > \mathrm{Na} \tag{3.1}$$

Indeed, under above condition, even fully accurate forward model cannot perfectly reproduce all measurements if they are contaminated by the random noise. In contrast, all measurements can be fitted fully accurately even if they are affected by random or even some systematic noise, if the number of measurements (Nf) is equal to the number of retrieved characteristics (Na). In this regard, the Multi-Source LSM approach employed and developed in the GRASP algorithm is aimed on making overdetermined systems (as in eq. 3.1) by adding additional equations using ancillary measurements and a priori knowledge to initial equations system formulated for the observations to be inverted. For example, as will be discussed below in details, GRASP often solves the equations as the follows:

$$\begin{cases} \boldsymbol{f}^* = & \boldsymbol{f}(\mathbf{a}) + \Delta\boldsymbol{f}^* \\ \mathbf{0}^* = & \mathbf{S}_m + \Delta(\Delta^m\mathbf{a})^* \\ \mathbf{a}^* = & \mathbf{a} + \Delta\mathbf{a}^* \end{cases} \tag{3.2}$$

Here, the first line represents the measurements to be inverted, while the second and third lines represent the measurements, smoothness and a priori estimated constraints that are added from a priori knowledge to improve the final solution. It should be noted that even in absence of any random and systematic errors the solution may not have unique solution and adding additional equations as shown in eq. 3.2 helps to achieving the uniqueness of the solution.

It should be emphasized that the three equations in eq. 3.2 are considered equally independent of their origin. As will be shown below, only the information of the included data accuracy (such as covariance matrix of errors) determines the overall impact of added equations.

Thus, GRASP can improve the solution by combining the information from different sources in the inversion using Multi-Term LSM approach that is also considered Multi-Source data inversion concept (**?**).

3.2.1 Input measurements and inversion problem definition

Accounting for the measurement noise is a fundamental problem. The real measurements ($\boldsymbol{f}^*$) include two parts: the true values of measured characteristic ($\boldsymbol{f}(\mathbf{a})$), and the noise ($\Delta\boldsymbol{f}^*$):

$$\boldsymbol{f}^* = \boldsymbol{f}(\mathbf{a}) + \Delta\boldsymbol{f}^* \tag{3.3}$$

The noise distribution is assumed to be known, and the forward model, capable to accurately reproduce the measurements, is assumed to be linear:

$$\boldsymbol{f}^* = \mathbf{Ka} \tag{3.4}$$

where **K**, represents the matrix of coefficients and can be considered as a Jacobian matrix defined as $\{\mathbf{K}_{ji}\} = \frac{\partial f_j(\mathbf{a})}{\partial a_i}$.

Without even rigorous considerations one can state that eq.3.4 can be inverted just taking into consideration that Nf>Na, multiplying both sides by the transpose of **K** ($\mathbf{K}^T$):

$$(\mathbf{K}^T\boldsymbol{f}^*) = (\mathbf{K}^T\mathbf{K})\hat{\mathbf{a}} \tag{3.5}$$

Thus, the solution of the system can be expressed as:

$$\hat{\mathbf{a}} = (\mathbf{K}^T\mathbf{K})^{-1}(\mathbf{K}^T\boldsymbol{f}^*) \tag{3.6}$$

While this equation can be derived nearly intuitively, as shown above, it represents the classical equation of LSM that also can be formally derived from the Method of Maximum likelihood. Moreover, while the above simple formulation was derived under the assumption that the measured characteristic is linearly related with the sought parameters, it is also highly relevant to non-linear cases. Indeed, any non-linear forward model can be represented using Taylor series, where **K** is the first element:

$$\boldsymbol{f}(\mathbf{a'}) = \boldsymbol{f}(\hat{\mathbf{a}}) + \mathbf{K}_{\hat{\mathbf{a}}}(\mathbf{a'} - \hat{\mathbf{a}}) + o(\mathbf{a'} - \hat{\mathbf{a}})^2 + ... \tag{3.7}$$

Assuming that measurement errors are rather small and the first term is dominant. Therefore, eq. 3.6 can be used to estimate error propagation even in non-liner cases.

3.2.2 Method of Maximum Likelihood (MML) Least Square Method (LSM)

The Method of Maximum likelihood (MML) is based on finding the solution with the most probable noise occurrence. The Probability Distribution Function (PDF) of the measurement errors is defined as:

$$P(\Delta\hat{\boldsymbol{f}}^*) = P(\boldsymbol{f}(\mathbf{a}) - \boldsymbol{f}^*) = P(\boldsymbol{f}(\mathbf{a})|\boldsymbol{f}^*) = \max \tag{3.8}$$

This function describes the probability of an error realization. The higher $P(\Delta\hat{\boldsymbol{f}}^*)$ the closer $\Delta\hat{\boldsymbol{f}}^*$ will be to the known statistical properties. Somewhere else it was shown that the Cramer-Rao inequality demonstrates that the solution obtained from this estimator is the solution with smallest variance, not only for each parameter individually but also for the ensemble of all retrieved parameters. Thus, it is very important to realize that the optimizations can be achieved for all parameters.

The PDF of the measurements is information that can be obtained from the experience, error modelization and appropriate statistical tools. The nature of the errors is very diverse and hardly can be

rigorously evaluated in direct analysis, therefore it is usually based on fundamental considerations. For example, the errors are considered to be formed as sum of a lot of independent errors of different origin. Under such conditions, the Central Limit Theorem (CLT) establishes that when independent random variables are added, their normalized sum tends to a Gaussian distribution. Thus, GRASP adapts the assumption that all the errors of all input datasets follow a normal distribution, which can be written as:

$$P(\boldsymbol{f}(\mathbf{a})|\boldsymbol{f}^*) = \sim\exp\left(-\frac{1}{2}(\boldsymbol{f}(\mathbf{a})-\boldsymbol{f}^*)^T\mathbf{C}_f^{-1}(\boldsymbol{f}(\mathbf{a})-\boldsymbol{f}^*)\right) \tag{3.9}$$

where $\mathbf{C}_f$ is the covariance matrix of the vector $\boldsymbol{f}^*$. Correspondingly, under the assumptions of the gaussian PDF, the general MML can be reduced to a more specific Least Square Method. The maximum of PDF and LSM correspond to the minimum of the gaussian exponent:

$$2\hat{\Psi}(\mathbf{a}) = (\boldsymbol{f}(\mathbf{a})-\boldsymbol{f}^*)^T\mathbf{C}_f^{-1}(\boldsymbol{f}(\mathbf{a})-\boldsymbol{f}^*) = \min \tag{3.10}$$

The minimum of the quadratic function $\hat{\Psi}(\mathbf{a})$ corresponds to a point which makes zero the gradient $\nabla\hat{\Psi}(\mathbf{a})$. This gradient can be defined in terms of partial derivatives as follows:

$$\nabla\Psi(\mathbf{a}) = \frac{\partial\Psi(\mathbf{a})}{\partial a_i} = \mathbf{0}, \qquad (i = 1,2,...,N_a) \tag{3.11}$$

Deriving eq. 3.11 from eq. 3.10 following common rules (process is not shown here), the gradients can be expressed as:

$$\nabla\Psi(\mathbf{a}) = \mathbf{K}_a^T\mathbf{C}_f^{-1}\boldsymbol{f}(\mathbf{a}) - \mathbf{K}_a^T\mathbf{C}_f^{-1}\boldsymbol{f}^* = \mathbf{K}_a^T\mathbf{C}_f^{-1}(\boldsymbol{f}(\mathbf{a})-\boldsymbol{f}^*) \tag{3.12}$$

Thus, combining equations 3.4 (assuming linear dependence of $\boldsymbol{f}(\mathbf{a})$, 3.11 and 3.12, one arrives to so-called Normal system of equations:

$$\mathbf{K}_a^T\mathbf{C}_f^{-1}\mathbf{K}_a\mathbf{a} = \mathbf{K}_a^T\mathbf{C}_f^{-1}\boldsymbol{f}^* \tag{3.13}$$

and using matrix inversion the rigorous LSM solution for linear case can be written as:

$$\hat{\mathbf{a}} = (\mathbf{K}_a^T\mathbf{C}_f^{-1}\mathbf{K}_a)^{-1}\mathbf{K}_a^T\mathbf{C}_f^{-1}\boldsymbol{f}^* \tag{3.14}$$

3.2.3 Non-linear Iterative solution: Newton-Gauss method + Levenberg-Marquardt

As it has been mentioned, the methodology showed above is constructed under the linearity assumption between the retrieved parameters and the measurements. However, this is rarely the case, highly complex dependencies with non-linear effects are expected in the processes involved in the interaction of radiation with the Atmosphere-surface system. At the same time, as discussed above, if the errors are minor, the first term in the Taylor series, relying on Jacobian K matrices, is dominant in the Taylor series of eq. 3.7. This consideration is a basis for a Newton-Gauss iterative method is applied to minimize eq. 3.10 that can we written as:

$$\begin{aligned}\mathbf{a}^{p+1} &= \mathbf{a}^p - \Delta\mathbf{a}^p \\ \mathbf{K}_p\Delta\mathbf{a}^p &\approx \boldsymbol{f}(\mathbf{a}^p) - \boldsymbol{f}^*\end{aligned} \tag{3.15}$$

Where superscript p is used to identify the iteration order. Thus, combining eq. 3.14 and eq. 3.15, we can replace eq. 3.15 by the following:

$$(\mathbf{K}_p^T\mathbf{C}_f^{-1}\mathbf{K}_p)\Delta\mathbf{a}^p = \mathbf{K}_p^T\mathbf{C}_f^{-1}\Delta\boldsymbol{f}^p \tag{3.16}$$

where

$$\Delta\boldsymbol{f}^p = \boldsymbol{f}(\mathbf{a}^p) - \boldsymbol{f}^* \tag{3.17}$$

Thus, the MML solution through a Newton-Gauss iterative method can be written as:

$$\begin{aligned}\mathbf{a}^{p+1} &= \mathbf{a}^p - (\mathbf{K}_p^T\mathbf{C}_{\boldsymbol{f}}^{-1}\mathbf{K}_p)^{-1}\nabla\Psi(\mathbf{a}) \\ &= \mathbf{a}^p - (\mathbf{K}_p^T\mathbf{C}_{\boldsymbol{f}}^{-1}\mathbf{K}_p)^{-1}\mathbf{K}_p^T\mathbf{C}_{\boldsymbol{f}}^{-1}(\boldsymbol{f}(\mathbf{a}^p) - \boldsymbol{f}^*)\end{aligned} \tag{3.18}$$

The matrix $((\mathbf{K}_p^T\mathbf{C}_{\boldsymbol{f}}^{-1}\mathbf{K}_p)^{-1})$ may suffer from other problems that can avoid its inversion in practical terms if the system of equations is degenerated, which implies that in some iteration points the determinant of the inversion matrix tends to zero ($\det(\mathbf{K}_p^T\mathbf{C}_{\boldsymbol{f}}^{-1}\mathbf{K}_p)^{-1} \approx 0$).

A common modification of the Newton-Gauss iteration is the Levenberg-Marquardt methodology:

$$\mathbf{a}^{p+1} = \mathbf{a}^p - \boldsymbol{t}_p(\mathbf{K}_p^T\mathbf{C}_{\boldsymbol{f}}^{-1}\mathbf{K}_p + \gamma\boldsymbol{D})^{-1}\mathbf{K}_p^T\mathbf{C}_{\boldsymbol{f}}^{-1}(\boldsymbol{f}(\mathbf{a}^p) - \boldsymbol{f}^*) \tag{3.19}$$

This method can also be considered as a generalization of the *steepest descendent method* (**?**). Indeed, the steepest descendent method can be derived from eq. 3.19 by assuming the matrix $\boldsymbol{D}$ as the unity matrix $\boldsymbol{I}$ and assume it is dominant.

In addition, the Levenberg-Marquardt is applied to assure convergence using the multiplier $\mathbf{t}_p$ that varies from: $0 < \mathbf{t}_p < 1$. This means a reduction of the step taken in each iteration since large correction step (obtained using linear approximation) prevent the convergence.

3.2.4 Constraints: Smoothness, apriori and Multipixel

Finally, this section is devoted to the description of the GRASP implementation of Multi-term LSM inversion and the use of several a priori constraints simultaneously. In this regard, in GRASP methodology, when the data from several different sources are inverted the following joint system of equations should be inverted:

$$\boldsymbol{f}_k^* = \boldsymbol{f}_k(\mathbf{a}) + \Delta\boldsymbol{f}_k^*, \qquad (k = 1, 2, ..., K) \tag{3.20}$$

or in matrix form: $\boldsymbol{f}^* = (\boldsymbol{f}_1^*, \boldsymbol{f}_2^*, ..., \boldsymbol{f}_k^*)$, where K is the total number of independent sources of data. Some examples of independent sources of information are: measurements of different instruments, different kinds of measurements of the same instruments, information from different climatologies, etc. This independence of the error distributions enables the expression of the total PDF of $\boldsymbol{f}^*$ just as a simple multiplication of the individual functions of each source:

$$P\big(\boldsymbol{f}(\mathbf{a})|\boldsymbol{f}^*\big) = P\big(\boldsymbol{f}_1(\mathbf{a}), \boldsymbol{f}_2(\mathbf{a}), ..., \boldsymbol{f}_k(\mathbf{a})|\boldsymbol{f}_1^*, \boldsymbol{f}_2^*, ..., \boldsymbol{f}_k^*\big) = \prod_{k=1}^{K} P\big(\boldsymbol{f}_k(\mathbf{a})|\boldsymbol{f}_k^*\big) \tag{3.21}$$

Under the previously gaussian shape assumption, the function to be minimized by the LSM is:

$$2\Psi(\mathbf{a}) = \sum_{k=1}^{K}(\boldsymbol{f}_k(\mathbf{a}) - \boldsymbol{f}_k^*)^T(\mathbf{C}_k)^{-1}(\boldsymbol{f}_k(\mathbf{a}) - \boldsymbol{f}_k^*) = \min \tag{3.22}$$

that can be derived from eq. 3.10 taking into account the following array structure of the covariance matrix of the total data set combined from K independent data sets:

$$\mathbf{C}_{\boldsymbol{f}^*} = \begin{pmatrix} \mathbf{C}_1 & \mathbf{0} & \mathbf{0} & \mathbf{0} \\ \mathbf{0} & \mathbf{C}_2 & \mathbf{0} & \mathbf{0} \\ ... & ... & ... & ... \\ \mathbf{0} & \mathbf{0} & \mathbf{0} & \mathbf{C}_K \end{pmatrix} \tag{3.23}$$

The practical implementation of the methodology can be illustrated by a specific case of three data sets shown by eq. 3.2, where k=1 corresponds to the measurements, k=2 to the a priori smoothness constraints, and k=3 to the a priori estimates. Thus, the complete set of equations can be described as:

$$\begin{cases} \boldsymbol{f}_1^* = & \boldsymbol{f}_1(\mathbf{a}) + \Delta\boldsymbol{f}_1^* \\ \boldsymbol{f}_2^* = & \boldsymbol{f}_2(\mathbf{a}) + \Delta\boldsymbol{f}_2^* \\ \boldsymbol{f}_3^* = & \boldsymbol{f}_3(\mathbf{a}) + \Delta\boldsymbol{f}_3^* \end{cases} \Rightarrow \begin{cases} \boldsymbol{f}^* = & \boldsymbol{f}(\mathbf{a}) + \Delta\boldsymbol{f}^* \\ \mathbf{0}^* = & \mathbf{S}_m + \Delta(\Delta^m\mathbf{a})^* \\ \mathbf{a}^* = & \mathbf{a} + \Delta\mathbf{a}^* \end{cases} \tag{3.24}$$

Smoothness constraints

Constraining inversions by a priori information is an essential tool for achieving a unique and stable solution of an ill-posed problem. It seems logical to filter out the solutions with non-physical characteristics from entire space of possible solutions. Among these undesired solutions, one can find characteristics which present unphysically strong oscillations. Indeed, the general behavior of nature tends to produce smooth characteristics and no sharp variations of these magnitudes are expected. The values of m-th derivatives, $\mathbf{g}_m$, of the function $\mathbf{a}(x)$ characterize the degree of their non-linearity and can be used as a measure of its smoothness. Some examples for $m = 1, 2$ and 3 can be found below:

$$\begin{aligned} g_1(x) = dy(x)/dx = 0 \;&\Rightarrow\; y_1(x) = C \\ g_2(x) = d^2y(x)/dx^2 = 0 \;&\Rightarrow\; y_2(x) = Bx + C \\ g_3(x) = d^3y(x)/dx^3 = 0 \;&\Rightarrow\; y_3(x) = Ax^2 + Bx + C \end{aligned} \tag{3.25}$$

These derivatives $\mathbf{g}_m$ can be approximated by differences between values of the fractions $a_i = y(x_i)$ in N_a discrete points x_i as:

$$\begin{aligned} \frac{dy(x_{i'})}{dx} &\approx \frac{\Delta^1 y(x_i)}{\Delta_1 x_i} = \frac{y(x_i + \Delta x_i) - y(x_i)}{\Delta_1 x_i} = \frac{y(x_{i+1} - y(x_i)}{\Delta_1 x_i} \\ \frac{d^2y(x_{i''})}{dx^2} &\approx \frac{\Delta^2 y(x_i)}{\Delta_2(x_i)} = \frac{\Delta^1 y(x_{i+1})/\Delta_1(x_{i+1}) - \Delta^1 y(x_i)/\Delta_1(x_i)}{(\Delta_1 x_i + \Delta_1 x_{i+1})/2} = ... \\ \frac{d^3y(x_{i'''})}{dx^3} &\approx \frac{\Delta^3 y(x_i)}{\Delta_3(x_i)} = \frac{\Delta^2 y(x_{i+1})/\Delta_2(x_{i+1}) - \Delta^2 y(x_i)/\Delta_2(x_i)}{(\Delta_2(x_i) + \Delta_2(x_{i+1}))/2} = ... \end{aligned} \tag{3.26}$$

where

$$\begin{aligned} \Delta_1(x_i) = x_{i+1} - x_i;\;\; \Delta_2(x_i) = (\Delta_1(x_i) + \Delta_1(x_{i+1}))/2; \\ \Delta_3(x_i) = (\Delta_2(x_i) + \Delta_2(x_{i+1}))/2 \\ x_{i'} = x_i + \Delta_1(x_i)/2;\;\; x_{i''} = x_i + (\Delta_1(x_i) + \Delta_2(x_i))/2; \\ x_{i'''} = x_i + (\Delta_1(x_i) + \Delta_2(x_i) + \Delta_3(x_i))/2; \end{aligned} \tag{3.27}$$

Thus, the limitations of the derivatives can be used as an additional source of input data:

$$\boldsymbol{f}_2^* = \boldsymbol{f}_2^*(\mathbf{a}) + \Delta\boldsymbol{f}_2^* \;\Rightarrow\; \boldsymbol{g}_m^* = \boldsymbol{g}_m(\mathbf{a}) + \Delta\boldsymbol{g}_m^* \;\Rightarrow\; \mathbf{0}^* = \boldsymbol{G}_m\mathbf{a} + \Delta_g^* \tag{3.28}$$

where $\mathbf{0}^*$ is the zero vector, $\boldsymbol{G}_m$ is the matrix corresponding to the derivative coefficients of m-th degree, and Δ_g^* represents the uncertainty of the deviations of the derivatives of real characteristic shape from the assumed ones. In a case, when a discrete representation of continues function is done using equidistant discretization of the nodal point ordinates, i.e. Δx=constant, the derivatives can be considered as differences:

$$\frac{d^m y(x)}{d^m x} \approx \frac{\Delta^m y(x_i)}{(\Delta x)^m} \;\Rightarrow\; \boldsymbol{G}_m = (\Delta x)^{-m}\boldsymbol{S}_m \tag{3.29}$$

Thus, the second equation of our system can be written as:

$$(\Delta^m \mathbf{a})^* = \mathbf{S}_m\mathbf{a} + \Delta(\Delta^m\mathbf{a})^* \;\Rightarrow\; \mathbf{0}^* = \mathbf{S}_m\mathbf{a} + \Delta_m^* \tag{3.30}$$

A priori constraints

This type of a priori constraints refers directly to the value of the characteristic $\mathbf{a}$ which is being retrieved. It is an optimal way, jointly with the smoothness constraint, to limit the possible solutions to values closer to the expected physical reality. As it can be seen in equation 3.24, in this case the matrix $\mathbf{K}$ is the unity, which means that the $\mathbf{K} = \frac{\partial \mathbf{a}}{\partial \mathbf{a}} = \mathbf{I}$. On the other hand, in this case the weighting matrix corresponds to the covariance matrix of the parameters.

In addition, since the absolute values of covariances are rarely known, the notation of weighting matrices ($\boldsymbol{W}_k$) and Lagrange multipliers is convenient to use in practical applications:

$$\boldsymbol{W}_k = \frac{1}{\epsilon_k^2} \text{ and } \boldsymbol{\gamma}_k = \frac{\epsilon_1^2}{\epsilon_k^2} \tag{3.31}$$

The value of the Lagrange multipliers are defined as the ratio of their error variance with respect to the first data set of measurements, i. e. $\gamma_1 = 1$.These multipliers γ_k determines the importance (weight) of corresponding input data set the retrieval.

Thus, taking all above assumptions in the consideration, the minimized function can be written as

$$2\Psi(\hat{\mathbf{a}}) = \sum_{k=1}^{N_{\boldsymbol{f}}} \gamma_k (\boldsymbol{f}(\hat{\mathbf{a}}) - \boldsymbol{f}^*)^T \mathbf{W}_k^{-1} (\boldsymbol{f}(\hat{\mathbf{a}}) - \boldsymbol{f}^*) + \gamma_{N_{\boldsymbol{f}}+1} \hat{\mathbf{a}}^T \boldsymbol{S}_m^T \boldsymbol{S}_m \mathbf{a} + \gamma_{N_{\boldsymbol{f}}+2} (\hat{\mathbf{a}} - \hat{\mathbf{a}}^*)^T \mathbf{W}_{\boldsymbol{a}^*}^{-1} (\hat{\mathbf{a}} - \hat{\mathbf{a}}^*) \tag{3.32}$$

and, the corresponding LSM iterative solution as:

$$\hat{\mathbf{a}} = (\mathbf{K}^T \mathbf{W}^{-1} \mathbf{K} + \gamma_{N_{\boldsymbol{f}}+1} \boldsymbol{S}_m^T \boldsymbol{S}_m + \gamma_{N_{\boldsymbol{f}}+2} \mathbf{W}_{\mathbf{a}^*}^{-1})^{-1} (\mathbf{K}^T \mathbf{W}^{-1} \boldsymbol{f}^* + \gamma_{N_{\boldsymbol{f}}+2} \mathbf{W}_{\mathbf{a}^*}^{-1} \mathbf{a}^*) \tag{3.33}$$

Where $\boldsymbol{K}$ and $\boldsymbol{W}_K$ matrices are defined:

$$\begin{gathered} \boldsymbol{K}_1 = \boldsymbol{K};\ \boldsymbol{K}_2 = \boldsymbol{S}_m \text{ and } \boldsymbol{K}_3 = \boldsymbol{I} \\ \boldsymbol{W}_1 = \boldsymbol{W} = (1/\epsilon_{\boldsymbol{f}^*})^2 \boldsymbol{C}_{\boldsymbol{f}^*};\ \boldsymbol{W}_2 = \boldsymbol{W}_{\Delta^*} = \mathbf{1} \text{ and } \boldsymbol{W}_3 = \boldsymbol{W}_{\boldsymbol{a}} = (1/\epsilon_{\boldsymbol{f}^*})^2 \boldsymbol{C}_{\boldsymbol{a}^*} \end{gathered} \tag{3.34}$$

3.2.4.1 Multipixel constraints

Hitherto, the idea of the retrieval has been presented as isolated datasets in terms of space and time. However, there is an important amount of knowledge about how the different properties of the elements forming the Atmosphere-Surface system spatially and temporally change. Therefore, the multipixel constraint strategy constitute a very valuable approach of adding more helpful constraints of the solution.

The term multipixel refers to link retrievals which correspond to different geographical points or different timestamps, with an expected common behavior between them. Some examples of the application of these constraints are the smooth horizontal change of aerosol properties, the quick change of clouds in time, the slow temporal variability of the surface...

The formal mathematical definition of these constraints is analogous to the definition of smoothness constraints for the parameters. However, in this case, the derivatives of the parameters are not referred to its functional shapes, but to their variability in the temporal-space coordinates: longitude, latitude, height and time:

$$\begin{gathered} \frac{\partial_i^m a(x,y,z,t,...)}{\partial x^m} \approx 0,\ \frac{\partial_i^m a(x,y,z,t,...)}{\partial y^m} \approx 0 \\ \frac{\partial_i^m a(x,y,z,t,...)}{\partial z^m} \approx 0,\ \frac{\partial_i^m a(x,y,z,t,...)}{\partial t^m} \approx 0 \end{gathered} \tag{3.35}$$

Thus, extra equations can be added following the same mathematical formalism as in the previously described data sets:

$$\begin{cases} \boldsymbol{f}_{k+1}^{a,*} = & \boldsymbol{f}_{k+1}^{a}(\mathbf{a}) + \Delta \boldsymbol{f}_{k+1}^{a,*} \\ \boldsymbol{f}_{k+2}^{a,*} = & \boldsymbol{f}_{k+2}^{a}(\mathbf{a}) + \Delta \boldsymbol{f}_{k+2}^{a,*} \\ \boldsymbol{f}_{k+3}^{a,*} = & \boldsymbol{f}_{k+3}^{a}(\mathbf{a}) + \Delta \boldsymbol{f}_{k+3}^{a,*} \\ \boldsymbol{f}_{k+4}^{a,*} = & \boldsymbol{f}_{k+4}^{a}(\mathbf{a}) + \Delta \boldsymbol{f}_{k+4}^{a,*} \end{cases} \Rightarrow \begin{cases} \mathbf{0}_x^* = & \mathbf{G}_{x,m_x} \mathbf{a} + \Delta_x^* \\ \mathbf{0}_y^* = & \mathbf{G}_{y,m_y} \mathbf{a} + \Delta_y^* \\ \mathbf{0}_z^* = & \mathbf{G}_{z,m_z} \mathbf{a} + \Delta_z^* \\ \mathbf{0}_t^* = & \mathbf{G}_{t,m_x} \mathbf{a} + \Delta_t^* \end{cases} \tag{3.36}$$

3.2.5 Further Aspects of Inversion Optimization: Non-negativity and data redundancy

The straightforward use of LSM-based constrained inversion could result in solutions with negative values for physically non-negative characteristics. The non-negativity constraints can be included in

the statistical estimation scheme by using an assumption of lognormal noise instead of normal in the retrieval optimization. This assumption of lognormal noise leads to the implementation of inversions in the logarithmic space, i.e., to employ a logarithmic transformation in the forward model:

$$\boldsymbol{f}^* = \boldsymbol{f}(\mathbf{a}) + \Delta\boldsymbol{f}^* \rightarrow \ln\boldsymbol{f}(\mathbf{a}) + \Delta\ln\boldsymbol{f}^* \tag{3.37}$$

The use of the log-normally distributed values presents several advantages. The values are positively-defined, and there are a number of theoretical and experimental reasons showing that for positively defined characteristics the log-normal curve is the best for modeling random deviations in non-negative values (Tarantola, 2005).

In addition, using the lognormal PDF for noise optimization does not require any revision of previously presented concepts for Gaussian distributions, and it can be implemented by simple direct transformation of the problem to the space of normally distributed logarithms.

Another possible issue is the the redundancy of the data. For example, an infinite enhancement of spectral or/and angular resolutions in remote sensing observations will not lead to accuracy improvements in the retrievals above a certain threshold. In a contrast, a simple increase in the number of observations, Nf, leads to an increase in the number of redundant measurements that do not help to improve the retrievals.

In the multi-source inversion shown here, an increase of the number of the observations in one of the several inverted datasets would lead to an increase in the weight of this data set. However, this weight increase of the added observations is not necessarily related with the amount of information provided by them. Thus, some degree of redundancy is introduced in the retrieval. Indeed, in the minimized quadratic form of equation 3.32, the higher the value of the k-th term Ψ_k, the stronger the contribution of k-th data set into the solution. In order to eliminate this obvious dependence of Ψ_k on N_k, Dubovik and King (2000) suggested that the accuracy of a single measurement degrades as $\frac{1}{N_k}$ for redundant observations if several measurements are taken simultaneously. Thus, a renormalization of the noise variance (and the corresponding Lagrange multipliers) by the number of elements it is performed:

$$\begin{aligned} \epsilon_k^2(\text{multiple}) &= N_k\epsilon_k^2(\text{single}) \\ \gamma_k &= \frac{N_1\epsilon_1^2(\text{single})}{N_k\epsilon_k^2(\text{single})} \end{aligned} \tag{3.38}$$

Where $\epsilon(\text{multiple})$ refers to measurements with a several elements with analogous characteristics.

3.3 Forward model

GRASP forward model is a highly generalized tool designed using different independent modules which simulate the measured properties of the different elements on the Atmosphere-Surface system. The main modules of GRASP forward model deals with aerosol single scattering based of spheroid scattering code (Dubovik et al., 2006); the surface reflectance models, modeling of the lidar vertical profiles (elastic and inelastic), mixing of scattering from several aerosol components, the radiative transfer and the gas absorption module. The three former modules have been expanded (radiative transfer and aerosol components) or completely changed (gas absorption) to fulfill the objectives of this thesis.

The spectral properties of gasses and aerosols are quite different in the complete electromagnetic spectrum. A representation of gas absorption and aerosol extinction can be appreciated in the following figure:

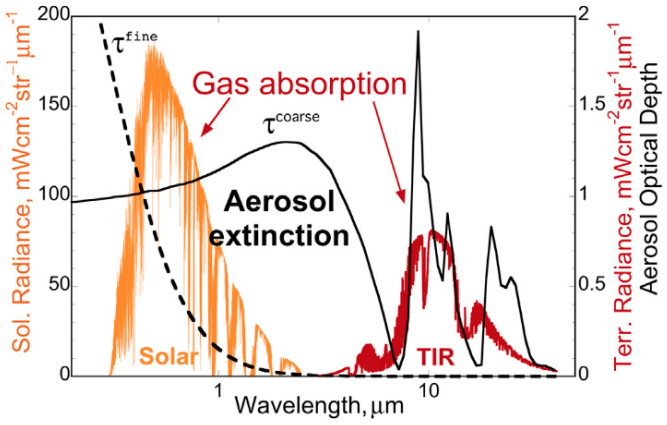

Figure 3.1: Spectral optical thickness characteristics of aerosols and gasses for Solar and Thermal Infrared parts of the spectrum.

Thus, in order to homogenize both behaviors and deal with the different technical issues arising from them, the connections between the GRASP forward model modules have been adapted for the new requirements of the objectives of this thesis, while keeping all the previous GRASP functionalities. In the following sections a description of these modules and its main characteristics will be discussed with the focus on the most related features to the work presented here. A visual representation of the different GRASP forward model and main modules can be seen below:

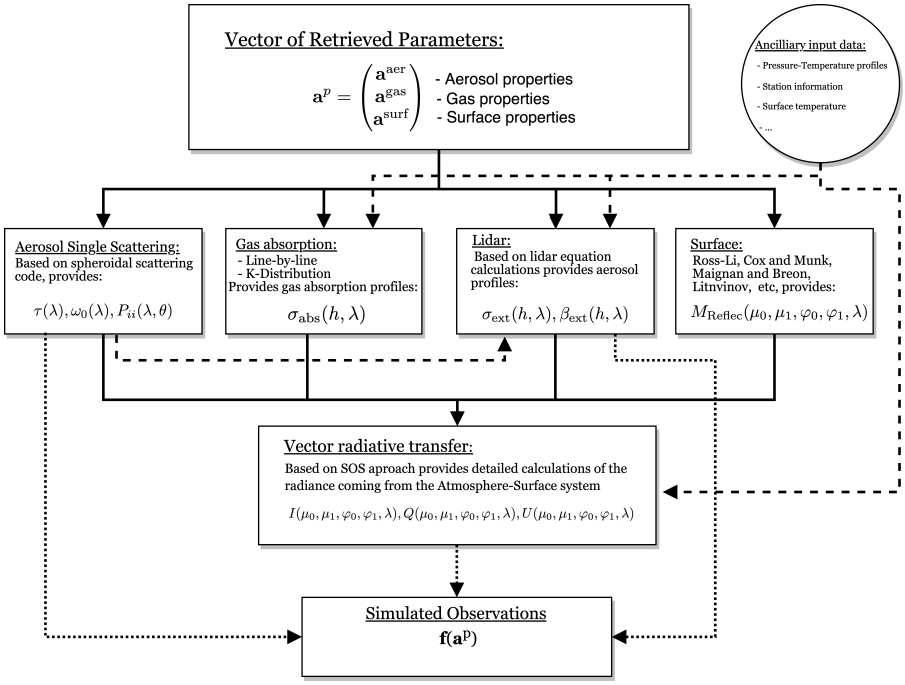

Figure 3.2: Scheme of GRASP modules conforming GRASP forward model.

3.3.1 Aerosol modeling: Single scattering properties

In this module it is established a link between the microphysical and optical characteristics of aerosols with its corresponding scattering properties. The single scattering code used in GRASP to obtain these properties is the randomly oriented spheroid kernel data base (Dubovik et al., 2006), whose description is out of the scope of this thesis. Despite the complexity of the scattering codes, generally the necessary input parameters are always the same: particle size, particle shape and complex refractive index. This scattering code provides all aerosol related information to perform radiative transfer calculations: Phase matrix and the scattering, absorption and extinction coefficients.

The calculation of scattering properties is a complex time consuming process that in practical

terms cannot be done “on the fly” if GRASP wants to be applied in a realistic manner. Thus, the link between the aerosol microphysical and optical characteristics and the corresponding particle scattering properties is done through the use of precalculated look-up-tables called “kernels”. The structure of kernels makes them easily expandable to satisfy new needs of the developments of the rest of the forward model, or to adapt them to the speed and accuracy requirements of any processing.

The large values of the complex refractive index of aerosols in thermal infrared arise the necessity to expand the kernels to bigger values. The size of the grids and shape characteristics of previous and extended kernels can be seen in the figure below.

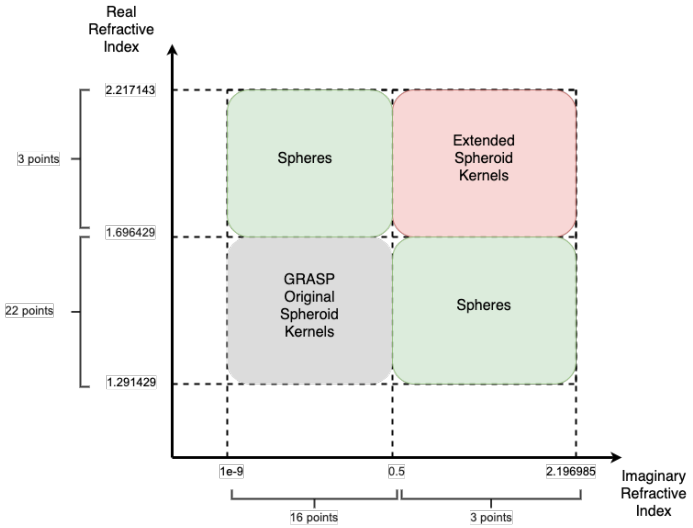

Figure 3.3: Schematic representation of the extended GRASP kernels developped for this thesis.

The spheroid calculations are especially time-consuming, for the required complex refractive limits (around 2.2 for both real and imaginary parts) the calculation will take up to several years. Thus, to fulfill the time constraints of this thesis, it was decided to complete some part of them with calculations obtained through Mie theory as it was done in (Legrand et al., 2014). Deeper analysis of the aerosol scattering properties in the thermal infrared range can be found in a latter chapter of this thesis called “Aerosol modeling complexity limits in Thermal infrared”.

Despite the input particle characteristics needed to perform the scattering calculations are fixed, the physical representation that can be done of them is very flexible, and it allows the code to be adapted to a wide variety of applications.

For many applications (not for all) the aerosols in GRASP forward model are assumed to be spheroids with a fixed axis ratio distribution (Dubovik et al., 2006):

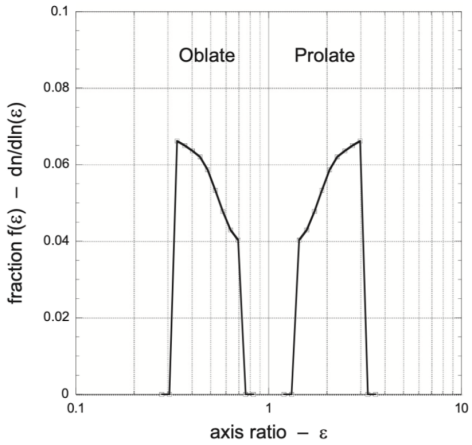

Figure 3.4: Reference spheriod axis ratio distribution used for the corresponding calculations of this work (Dubovik et al., 2006).

Thus, only the sphericity fraction, which is the percentage of spherical particles in the total aerosol concentration, can be retrieved. The kernels regions which correspond to spheroids are calculated with this axis ratio distribution.

On the other hand, the representation of aerosol size distribution in the GRASP forward model is much more flexible. The most complex model to represent particle size distribution is the Triangle bins characteristic, which is normally represented by one or several modes usually defined in 22 (or so) size bins. This model is used for the interpretation AERONET like observations. Other options such with reduced number of bins or using just one aerosol mode is also possible in GRASP.

Despite the high accuracy and representativity of the 22 triangle bin Particle size distribution, a very high content information in the input measurements is needed to properly retrieve this characteristic. Then, simplified representations of this characteristic are also available, such as the precalculated lognormal bins, or the bimodal lognormal size distribution. In the former example the PSD is represented by two gaussians, one for the coarse mode and one for the fine mode. Thus, only 3 parameters per mode are retrieved (norm, mean radius and standard deviation). These simplifications which increase the amount of assumed information are very useful to deal with retrievals in low information contexts.

The spectral values of the real and the imaginary parts of the complex refractive index can be directly retrieved. However, the component approach, which is the one selected for this thesis is based on the different representation of spectrally dependent complex refractive index. The volume fractions of different chemical components, which are normally found in atmospheric particles, are retrieved instead.

Finally, in order to simplify even more the physical representation of aerosol properties, GRASP forward model counts with the "models" approach. The main retrieved aerosol products of this approach are the fractions of the total aerosol concentration of precalculated aerosol models which are externally mixed. These precalculated models correspond to the main aerosol types established by previous experience (Ex: smoke, urban, oceanic and dust). Each of these models correspond to a fixed particle size distribution and refractive indices, containing the already calculated phase matrix, and the extinction and absorption cross-sections. The total aerosol retrieved characteristics can be obtained by weighting the characteristics used to calculate each of these models by its corresponding volume concentration. The absence of spheroid Kernels in the whole process makes this option by far the fastest of all. However, one of the main drawbacks of this methodology is the fact that the inversion is intrinsically constrained by the selected models. Notwithstanding, these models have been carefully selected to be suitable to cover almost all atmospheric situations. Moreover, they can be recalculated or extended in order to cover specific situations.

Further details about aerosol modeling and scattering calculations and sensitivity studies about the aerosol models in TIR are going to be described later in this thesis.

3.3.2 Lidar observations of aerosol vertical distribution

The most precise approach to derive aerosol vertical profiles in GRASP is through inversion of lidar measurements. Lidar, which stands for Light Detection and Ranging, is an active remote sensing technique which consists in the emission of pulsed laser to the atmosphere and its posterior measurement of the retro-dispersed radiance and its corresponding "flight time". A detailed description of this technique is out of the scope of this thesis. The lidar equation (limited to elastic processes) is a solution of the radiative transfer problem adapted to the particular geometry of these instruments:

$$L(\lambda,h) = A(\lambda)\beta(\lambda,h)\text{exp}\left(-2\int_0^h \sigma(\lambda,h')dh'\right) \tag{3.39}$$

Where$L(\lambda,h)$ is the backscattered radiance of the atmosphere, $A(\lambda)$ is the lidar calibration coefficient, $\beta(\lambda,h)$ is the backscatter coefficient and $\sigma(\lambda,h)$ is the extinction coefficient. The backscatter coefficient can be expressed in terms of single scattering albedo, the Phase function at 180° degrees and the extinction coefficient:

$$\beta(\lambda,h) = \frac{1}{4\pi}\sigma(\lambda,h)\omega_0(\lambda,h)P_{11}(180^\circ\lambda,h) \tag{3.40}$$

The total layer coefficients can be expressed in the following way:

$$\sigma(\lambda,h) = \sigma_{\text{gas}^{abs}}(\lambda,h) + \sigma_{\text{mol}^{scat}}(\lambda,h) + \sigma_{\text{aer}^{ext}}(\lambda,h) \tag{3.41}$$

Lidar instruments have a bottom limit, defined by its overlap region, and a top limit, defined by the power of the laser. However, GRASP forward model needs to complete the atmospheric profile from the surface to the TOA. Thus, in order to unify the radiative transfer and the lidar modules some assumptions are necessary. The aerosol properties of the bottom part are assumed to be constant and equal to the first measurement of the lidar, and for the top part, a linear decrease from the last point of the lidar to the TOA, where the aerosol concentration is zero, is assumed.

3.3.3 Surface

The surface in GRASP is represented by a reflectance matrix BRDM that is divided into a BRDF and a BPDF. Depending on the specific application, different models to represent these surface properties are available. In the case of the ground-based retrievals/simulations, the surface does not play a crucial role as it can in the case of satellite-like scenarios. Some examples of the semi-empirical models available at the moment in GRASP are: Cox and Munk model (Cox and Munk, 1954), the Ross-Li model (Ross (1981); Li et al. (1992); Wanner et al. (1995)), Maignan and Breon (Maignan et al. (2004); Maignan et al. (2009)) or the models of (Litvinov et al., 2010) and Litvinov et al. (2011).

3.3.4 Gaseous absorption

Despite gas absorption was already considered in GRASP code, the corresponding physical model was designed to cover needs of aerosol retrieval only in visible, i.e. taking into account only column and channel integrated values for a gas correction of the radiance. However, in the case of thermal infrared, the spectral width of the channels and the gas absorption lines and vertical profiles play a crucial role. Thus, the previous scheme of GRASP forward model is not enough to reach the objectives of this thesis.

Therefore, now GRASP forward model can account for monochromatic calculations for any gas in any spectral range for a maximum of ten different gaseous species simultaneously. The vertical profiles of atmospheric pressure and temperature have to be provided as an additional and necessary input for gas absorption calculations. Furthermore, the inclusion of these profiles are also necessary to account for the thermal emission in the radiative transfer as it will be shown.

In order to speed up the calculations, look-up-tables with the absorption spectral information for each considered gas species are needed. Indeed, all the calculations are expected to be done “on the fly”. However, obtaining the spectral absorption coefficients for each temperature and concentration value is a very time consuming process that significantly increases the retrieval/simulation time, up to an extent that the application to real datasets will be practically infeasible. Thus, these absorption values have been pre-calculated for a wide range of pressures, temperatures and wavelengths and stored into look-up-tables that are later called in the retrieval.

The implementation of this look-up-tables means that the shape of the vertical profile of gas concentration is assumed as fixed. Thus, only a renormalization to the required concentration and a simple interpolation to the defined pressure and temperature profile are needed to obtain the gas absorption profile. In order to obtain these precalculated values, the CGASA (Coefficient of GAS Absorption) line-by-line model (Doppler et al., 2014a) has been used. Notwithstanding, the look-up-table format is readable, easy to understand and it is open to the users to include their own look-up-tables which fulfill their requirements. Thus, the hyperspectral absorption calculations are now fully implemented and functional in GRASP.

However, direct spectral integration of line-by-line fine structure requires consideration of a very large number of lines with full accounting for multiple scattering for each one. Such direct implementation of the spectral integration has high accuracy but is very time consuming. Therefore, an alternative k-distribution approach has also been developed in parallel to speed up the integration time. As it has been previously described, the accuracy of this methodology is somewhat reduced compared to line-by-line procedure, but sufficient for most remote sensing applications. The k-distribution methodology assumes a smooth aerosol spectral behavior to reduce the number of multiple scattering runs for the spectral integration to about 10 or even less times instead of thousands. Specifically, the approach sorts the gaseous absorption coefficients “k” within spectral function to a limited set of bins (10) by the magnitude of the coefficients and then implements only a single multiple scattering run for each “k” bin.

The methodology involving the calculation of a k-distribution is complex and it requires expertise and experience in order to obtain successful results. For these reasons, at the current stage of the developments, it has been decided to prepare k-distribution information externally and then use it in the retrievals. Correspondingly, GRASP uses the k-distribution information including weights and bins for each gas as an input database. The selection of the format for all k-distribution related data is designed and implemented in concordance with GRASP philosophy, i.e., it is simple and as general as possible. Thus, it is compatible with the most common k-distribution methodologies.

The GRASP settings provide to the users the possibility to choose between both line-by-line and k-distribution spectral integration methods to adapt the retrieval to their needs. The user can select the corresponding methodology which better matches the specific requirements of each situation. Because of the high accuracy of this methodology and the significant reduction of the calculation time, K-Distribution technique presents evident advantages over line-by-line calculations.

In this case, for all the K-Distribution calculations presented in this thesis the "kbin" code kindly provided by the Free university of Berlin has been used (Doppler et al., 2014b).

3.3.5 Subchannel approach

As part of the new K-distribution implementation in GRASP forward model, the subchannel approach was a necessary development in order to deal with the strong aerosol spectral variations in the thermal infrared range. As it has been said, one of the basic assumptions of the K-distribution techniques is to assume that in the considered spectral range the aerosol properties are spectrally constant. Even in the thermal infrared spectral range, if the channel width is very reduced, the flat aerosol spectral behavior can be taken as an acceptable assumption. However, the thermal infrared instrument selected for this thesis, the CLIMAT radiometer (Legrand et al. (2000), Brogniez et al. (2003)), counts with an approximate spectral resolution of 1 μm.

The subchannel approach consists in the division of each channel in smaller parts where the aerosol properties can be taken as constant, and apply a different K-Distribution for each of them. Therefore, the single scattering module is called for the central wavelength of each of these smaller channels (from now on called "subchannels"), and then the radiative transfer is called for the different K-distribution of each subchannel. To obtain the final radiance corresponding to the full channel, the integral of the radiance calculated for each subchannel is performed in the following way:

$$I_{channel} = \sum_{i_s=1}^{N_{\text{Sub}}} \frac{\Delta\lambda_{i_s} I_{i_s}}{\sum_{i_s=1}^{N_{\text{Sub}}} \Delta\lambda_{i_s}} \quad \text{where} \quad I_{i_s} = \sum_{i_w=1}^{N_{w,i_s}} \omega_{i_w,i_s} I(k_{i_w,i_s}) \tag{3.42}$$

Where N_{sub} represent the number of subchannels in which the channels has been divided, $\Delta\lambda_{i_s}$ is the spectral width of each subchannel, I_{i_s} is the corresponding radiance obtained with the radiative transfer and the K-Distribution; and $N_{w,i_s}, \omega_{i_w,i_s}$ and k_{i_w,i_s} are correspondingly the number of bins, the weights and the extinction profiles of each K-distribution of each subchannel.

Further details of the optimization and necessary considerations to properly simulate CLIMAT radiance measurements will be provided later on in this thesis.

3.3.6 Radiative Transfer

An essential part of the GRASP forward model is the radiative transfer. It is based on the Successive Orders of Scattering technique originally proposed by Lenoble et al. (2007). Hitherto the possibilities of this scheme were limited to the Solar part of the electromagnetic spectrum, covering from the UV to the Shortwave infrared (SWIR). For this thesis an extension of the possibilities of this radiative transfer scheme has been developed, in which the Planck thermal emission has been added. With this modification and the corresponding temperature profiles development already mentioned in section 3.3.3, GRASP radiative transfer can accurately simulate radiance in the whole electromagnetic spectrum from UV to thermal infrared (TIR).

No more details about the GRASP radiative transfer are going to be provided here because the next chapter of this thesis is fully devoted to the detailed description of it.

3.4 Applications

In this section some description of different applications of GRASP is provided. GRASP presents a large range of possibilities and products, not only for the variety of instruments that can be used as input, but also for the synergies that arise from the combination of them. If measurements coming from different instruments are inverted at the same time, the available information can greatly increase, which can be translated into a decrease of the necessary assumptions and the improvement of the retrieved products.

On the other hand, if the content information of the available measurements is not very high, different methodological approaches can be taken in GRASP to overcome the related problems. One example of this kind of methodologies is the GRASP-AOD approach described in Torres et al. (2017) and Torres and Fuertes (2021). GRASP-AOD takes as input the information contained in the spectral aerosol optical depth measurements. Among the main advantages to restrict the GRASP input to direct measurements of the Sun radiation that have much larger amount of available data not contaminated by clouds compared to the sky radiance measurements are also used. However, the lack of angular information, which is provided by the sky radiance measurements, forces the use of simplified aerosol models and the increase of assumed a priori information. The information content in the spectral AOD measurements is not enough to retrieve the aerosol refractive indixes and information about particle shape. Consequently, these parameters need to be assumed. The values of the complex refractive index and particle sphericity are taken from monthly climatological values obtained by average of AERONET standard algorithm aerosol retrievals (which includes full sky radiances and τ measurements). The particle size distribution is represented as a bimodal lognormal function, whose characteristics have been already described. One key factor pointed out in these studies is the optimal selection of the initial guess. The latter has been achieved using multiple initial guesses (based on climatological values) and choosing the results with the best fitting. The validation of GRASP-AOD algorithm against the retrievals of AERONET standard algorithm for 3 million observations acquired over 20 years (1997– 2016) at 30 sites showed high correlations (r^2 around 0.75) in the retrieval of particle median radius and fine mode AOD discrimination. However, GRASP-AOD has special problems to deal with coarse mode dominated scenarios. In order to improve the characterization of it, the GRASP-AUR methodology adds to the direct measurements the radiance measurements near the Sun, azimuth angles between 3.5 and 10°. This extended information context increases the correlation coefficient of the particle median radius from 0.75 to 0.91.

The retrieval of aerosol vertical profiles is also possible with GRASP. The original developments by Lopatin et al. (2013) enabled the inclusion of multispectral lidar vertical profiles in order to retrieve aerosol properties resolved in the vertical direction. Even if the measurements of a multispectral lidar with backscatter and extinction channels are used as input for GRASP algorithm, there is not enough information for a complete aerosol characterization. Thus, the GRASP/GARRLiC scheme relies on the combination of the multiwavelength lidar profiles with the standard AERONET sunphotometer measurements (Spectral AOD and almucantar sky scans) to provide retrieval products which include a 22 triangle bins particle size distribution, complex refractive index for two aerosol modes, sphericity... In comparison with the AERONET standard strategy, the inclusion of the vertical profiles brings extra information about the minor mode, i.e., the mode with the smaller concentration. Furthermore, an increase in the precision of the retrieval is expected, because in the absence of the knowledge of the aerosol profiles this vertical distribution has to be assumed. Thus, if a correct information is provided about how the particles are vertically distributed a better modeling of the radiance can be done and most accurate results from then can be extracted. One of the main assumptions of this methodology is to assume all the aerosol properties of each mode, except the volume concentration, constant in the whole column. Therefore, it is assumed that for both considered aerosol modes only the amount of particles changes with the height. One example of the application of this methodology is the GRASP-pac scheme proposed by Román et al. (2018). Instead of a multiwavelength lidar the information about the vertical distribution of the aerosols is provided by a single wavelength ceilometer. Therefore, it is not possible to split the particles into two different modes.

Dubovik et al. (2019) and Chen et al. (2020) showed and validated the GRASP performance when applied to multi-angular measurements by space polarimeters, with a special focus in the retrieval of POLDER data. The studies presented by these authors are very extensive and detailed and it is out of the scoop of this thesis to provide a detailed description. However, it can be concluded that the polarimetric measurements provide valuable information to the retrieval and in the specific case of

POLDER. A high degree of agreement of POLDER/GRASP results was found with AERONET standard aerosol retrieval algorithm for the complete set of optical aerosol characteristics as it can be: AOD, aerosol absorption optical depth (AAOD) and single-scattering albedo (SSA) at six wavelengths, as well as Ångström exponent (AE), fine-mode AOD (AODF) and coarse-mode AOD (AODC).

The GRASP retrieval scheme selected for this thesis, the GRASP/Components approach originally proposed by Li et al. (2019), can be applied to any instrument configuration. However, it is especially interesting the application to the POLDER instrument presented in Li et al. (2019). The total radiance and polarization components of POLDER polarimeter were selected as input to retrieve in addition to the already mention aerosol microphysical properties, the aerosol components for two modes formed by a Maxwell-Garnett mixture of the following elements: Black carbon, brown carbon, fine mode non-absorbing insoluble, fine mode non-absorbing soluble, water, iron oxides, coarse-mode non-absorbing insoluble and coarse-mode non-absorbing soluble. The validation of the retrieval products against AERONET standard aerosol retrieval algorithm showed a high degree of agreement, with r^2 values of 0.9 for the AOD over the three analyzed sites. Furthermore, global seasonal climatologies of the volume fractions of the previously mentioned components were presented.

There are many more possible applications of GRASP, like: nephelometers, all-sky cameras, airborne sensors, other satellite instruments... (see Dubovik et al. (2021)). However, because of the time constraints of this thesis not all of them have been included in this document.

3.5 References

Brogniez, G., Pietras, C., Legrand, M., Dubuisson, P., and Haeffelin, M. (2003). A high-accuracy multiwavelength radiometer for in situ measurements in the thermal infrared. part ii: Behavior in field experiments. *Journal of Atmospheric and Oceanic Technology*, 20(7):1023–1033.

Chen, C., Dubovik, O., Fuertes, D., Litvinov, P., Lapyonok, T., Lopatin, A., Ducos, F., Derimian, Y., Herman, M., Tanré, D., et al. (2020). Validation of grasp algorithm product from polder/parasol data and assessment of multi-angular polarimetry potential for aerosol monitoring. *Earth System Science Data*, 12(4):3573–3620.

Cox, C. and Munk, W. (1954). Measurement of the roughness of the sea surface from photographs of the sun's glitter. *Josa*, 44(11):838–850.

Derimian, Y., Dubovik, O., Huang, X., Lapyonok, T., Litvinov, P., Kostinski, A. B., Dubuisson, P., and Ducos, F. (2016). Comprehensive tool for calculation of radiative fluxes: illustration of shortwave aerosol radiative effect sensitivities to the details in aerosol and underlying surface characteristics. *Atmospheric Chemistry and Physics*, 16(9):5763–5780.

Doppler, L., Carbajal-Henken, C., Pelon, J., Ravetta, F., and Fischer, J. (2014a). Extension of radiative transfer code momo, matrix-operator model to the thermal infrared–clear air validation by comparison to rttov and application to calipso-iir. *Journal of Quantitative Spectroscopy and Radiative Transfer*, 144:49–67.

Doppler, L., Preusker, R., Bennartz, R., and Fischer, J. (2014b). k-bin and k-ir: k-distribution methods without correlation approximation for non-fixed instrument response function and extension to the thermal infrared—applications to satellite remote sensing. *Journal of Quantitative Spectroscopy and Radiative Transfer*, 133:382–395.

Dubovik, O., Fuertes, D., Litvinov, P., Lopatin, A., Lapyonok, T., Doubovik, I., Xu, F., Ducos, F., Chen, C., Torres, B., Derimian, Y., Li, L., Herreras-Giralda, M., Herrera, M., Karol, Y., Matar, C., Schuster, G. L., Espinosa, R., Puthukkudy, A., Li, Z., Fischer, J., Preusker, R., Cuesta, J., Kreuter, A., Cede, A., Aspetsberger, M., Marth, D., Bindreiter, L., Hangler, A., Lanzinger, V., Holter, C., and Federspiel, C. (2021). A comprehensive description of multi-term lsm for applying multiple a priori constraints in problems of atmospheric remote sensing: Grasp algorithm, concept, and applications. *Frontiers in Remote Sensing*, 2:23.

Dubovik, O., Herman, M., Holdak, A., Lapyonok, T., Tanré, D., Deuzé, J., Ducos, F., Sinyuk, A., and Lopatin, A. (2011). Statistically optimized inversion algorithm for enhanced retrieval of aerosol properties from spectral multi-angle polarimetric satellite observations. *Atmospheric Measurement Techniques*, 4(5):975–1018.

Dubovik, O. and King, M. D. (2000). A flexible inversion algorithm for retrieval of aerosol optical properties from sun and sky radiance measurements. *Journal of Geophysical Research: Atmospheres*, 105(D16):20673–20696.

Dubovik, O., Lapyonok, T., Litvinov, P., Herman, M., Fuertes, D., Ducos, F., Lopatin, A., Chaikovsky, A., Torres, B., Derimian, Y., et al. (2014). Grasp: a versatile algorithm for characterizing the atmosphere. *SPIE Newsroom*, 25.

Dubovik, O., Li, Z., Mishchenko, M. I., Tanre, D., Karol, Y., Bojkov, B., Cairns, B., Diner, D. J., Espinosa, W. R., Goloub, P., et al. (2019). Polarimetric remote sensing of atmospheric aerosols: Instruments, methodologies, results, and perspectives. *Journal of Quantitative Spectroscopy and Radiative Transfer*, 224:474–511.

Dubovik, O., Sinyuk, A., Lapyonok, T., Holben, B. N., Mishchenko, M., Yang, P., Eck, T. F., Volten, H., Munoz, O., Veihelmann, B., et al. (2006). Application of spheroid models to account for aerosol particle nonsphericity in remote sensing of desert dust. *Journal of Geophysical Research: Atmospheres*, 111(D11).

Legrand, M., Dubovik, O., Lapyonok, T., and Derimian, Y. (2014). Accounting for particle nonsphericity in modeling of mineral dust radiative properties in the thermal infrared. *Journal of Quantitative Spectroscopy and Radiative Transfer*, 149:219–240.

Legrand, M., Pietras, C., Brogniez, G., Haeffelin, M., Abuhassan, N. K., and Sicard, M. (2000). A high-accuracy multiwavelength radiometer for in situ measurements in the thermal infrared. part i: Characterization of the instrument. *Journal of atmospheric and oceanic technology*, 17(9):1203–1214.

Lenoble, J., Herman, M., Deuzé, J., Lafrance, B., Santer, R., and Tanré, D. (2007). A successive order of scattering code for solving the vector equation of transfer in the earth's atmosphere with aerosols. *Journal of Quantitative Spectroscopy and Radiative Transfer*, 107(3):479–507.

Li, L., Dubovik, O., Derimian, Y., Schuster, G. L., Lapyonok, T., Litvinov, P., Ducos, F., Fuertes, D., Chen, C., Li, Z., et al. (2019). Retrieval of aerosol components directly from satellite and ground-based measurements. *Atmospheric Chemistry and Physics*, 19(21):13409–13443.

Li, X., Strahler, A. H., et al. (1992). Geometric-optical bidirectional reflectance modeling of the discrete crown vegetation canopy: Effect of crown shape and mutual shadowing. *IEEE transactions on Geoscience and Remote Sensing*, 30(2):276–292.

Litvinov, P., Hasekamp, O., and Cairns, B. (2011). Models for surface reflection of radiance and polarized radiance: Comparison with airborne multi-angle photopolarimetric measurements and implications for modeling top-of-atmosphere measurements. *Remote Sensing of Environment*, 115(2):781–792.

Litvinov, P., Hasekamp, O., Cairns, B., and Mishchenko, M. (2010). Reflection models for soil and vegetation surfaces from multiple-viewing angle photopolarimetric measurements. *Journal of Quantitative Spectroscopy and Radiative Transfer*, 111(4):529–539.

Lopatin, A., Dubovik, O., Chaikovsky, A., Goloub, P., Lapyonok, T., Tanré, D., and Litvinov, P. (2013). Enhancement of aerosol characterization using synergy of lidar and sun-photometer coincident observations: the garrlic algorithm. *Atmospheric Measurement Techniques*, 6(8):2065–2088.

Lopatin, A., Dubovik, O., Fuertes, D., Stenchikov, G., Lapyonok, T., Veselovskii, I., Wienhold, F. G., Shevchenko, I., Hu, Q., and Parajuli, S. (2021). Synergy processing of diverse ground-based remote sensing and in situ data using the grasp algorithm: applications to radiometer, lidar and radiosonde observations. *Atmospheric Measurement Techniques*, 14(3):2575–2614.

Maignan, F., Bréon, F.-M., Fédèle, E., and Bouvier, M. (2009). Polarized reflectances of natural surfaces: Spaceborne measurements and analytical modeling. *Remote Sensing of Environment*, 113(12):2642–2650.

Maignan, F., Bréon, F.-M., and Lacaze, R. (2004). Bidirectional reflectance of earth targets: Evaluation of analytical models using a large set of spaceborne measurements with emphasis on the hot spot. *Remote Sensing of Environment*, 90(2):210–220.

Román, R., Benavent-Oltra, J. A., Casquero-Vera, J. A., Lopatin, A., Cazorla, A., Lyamani, H., Denjean, C., Fuertes, D., Pérez-Ramírez, D., Torres, B., et al. (2018). Retrieval of aerosol profiles combining sunphotometer and ceilometer measurements in grasp code. *Atmospheric Research*, 204:161–177.

Ross, J. (1981). *The radiation regime and architecture of plant stands*. Number 3. Springer Science & Business Media.

Tarantola, A. (2005). *Inverse problem theory and methods for model parameter estimation*. SIAM.

Torres, B., Dubovik, O., Fuertes, D., Schuster, G., Cachorro, V. E., Lapyonok, T., Goloub, P., Blarel, L., Barreto, A., Mallet, M., et al. (2017). Advanced characterisation of aerosol size properties from measurements of spectral optical depth using the grasp algorithm.

Torres, B. and Fuertes, D. (2021). Characterization of aerosol size properties from measurements of spectral optical depth: a global validation of the grasp-aod code using long-term aeronet data. *Atmospheric Measurement Techniques*, 14(6):4471–4506.

Wanner, W., Li, X., and Strahler, A. (1995). On the derivation of kernels for kernel-driven models of bidirectional reflectance. *Journal of Geophysical Research: Atmospheres*, 100(D10):21077–21089.

Chapter 4

Thermal emission in the Successive Orders of Scattering (SOS) radiative transfer approach.

Todo depende del tiempo.

Fernando Calvo Pastor

The Successive Orders of Scattering (SOS) approach (Lenoble et al., 2007) is one of the well known methods for solving the Radiative Transfer (RT) problem. Its efficiency in terms of speed and accuracy of computation was already demonstrated for scattering and absorbing atmospheres in Solar spectrum. Although there are no principle limitations to account for the emission processes, the application of the SOS method for atmospheres with thermal emission is not widely used yet. In this chapter we present a SOS-based RT approach accounting for the full source function, which enables its application from the UV to the TIR parts of the electromagnetic spectrum. The atmospheric vertical discretization in this extended SOS scheme is a key point in order to properly retain the scattering and emission processes. An analysis of different methodologies to perform this vertical discretization is presented. The numerical implementation has been included in GRASP (Generalized retrieval of Atmosphere and Surface Properties) RT code (Dubovik et al., 2021). In comparison with the widely used code DISORT (DIScrete-ORdinatemethod for Radiative Transfer) (Stamnes et al., 1988), the developed SOS scheme achieves a mean accuracy of radiance calculation of -0.005 K (-0.003%) expressed in terms of brightness temperature. Under the same vertically inhomogeneous atmospheric conditions, GRASP SOS RT is approximately eight times faster than DISORT. The analysis of the sensitivity of GRASP TIR SOS scheme to the number of layers and the effect of polarization are also investigated in this chapter.

4.1 Introduction

The analytical solution of the RT equation does not exist for a particulate medium representing all complexity of Earth's atmosphere. There are several efficient and accurate numerical techniques for solving the RT problem (Lenoble et al. (2007), Hansen and Travis (1974), Hovenier et al. (2004)). In this chapter we consider the implementation of atmosphere and surface thermal emission into the SOS method for the RT standard problem: plane-parallel vertically inhomogeneous particulate layer atmosphere, which is representative for a vast variety of remote sensing applications. Although there are no principle limitations to account for the emission processes, the existing numerical implementations of the SOS method (e.g. Lenoble et al. (2007), Kotchenova et al. (2006), Zhai et al. (2009)) do not include thermal emission sources in the radiative transfer scheme. Hitherto, the SOS RT at TIR domain is not widely used yet. This is related to the fact that the radiative transfer in thermal infrared spectral range deals with problems which are not common at the Solar range. For example, the refractive index of atmospheric aerosol particles can produce scattering resonance effects at TIR range, while their

spectral dependence in UV, VIS, and NIR/SWIR range is rather smooth (Sokolik et al. (1998), Sokolik and Toon (1999)). The resonances result in an essential growth of the required number of expansion terms for accurate calculations of optical characteristics of aerosol (Van de Hulst (1963), Bohren and Huffman (2008)) and strongly affect the computation speed of SOS RT. Moreover, accounting for thermal emission together with gas absorption (Rothman et al., 2009) and multiple scattering requires a reliable procedure of discretisation for temperature, gases and aerosol vertical profiles ensuring an accurate RT solution.

This chapter describes the application of RT SOS method for atmospheres with thermal emission and tests it through the inter-comparison with another existent RT scheme accounting for the thermal emitted component. The series of case studies are performed to analyze different approaches for vertical discretisation of temperature and aerosol properties in atmospheres for a wide range of optical thickness. Other minor effects, such as, the influence of polarization in the long-wave radiative transfer calculations are also discussed.

Presently, there is a number of RT codes based on different techniques accounting for thermal radiation emission, scattering and absorption in the atmosphere: the Matrix Operator Model (MOMO) (Fell and Fischer (2001), Doppler et al. (2014)), RTTOV (Saunders et al. (1999a), Saunders et al. (1999b)) FASDOM (Dubuisson et al., 2005), or DISORT (DIScrete-ORdinate-method for Radiative Transfer) (Stamnes et al., 1988). DISORT has already been widely used by the scientific community to validate radiative transfer methodologies, as for example in Kotchenova et al. (2006) and Rozanov et al. (1997). In this work the $C\#$ implementation (cdisort-2.1.3) of DISORT technique is used to test the developed SOS RT in TIR domain. In addition to the original developments of (Stamnes et al., 1988), cdisort-2.1.3 also includes the δ–M method (Wiscombe, 1977), the correction to the intensity field (Buras et al., 2011) and the solution for a general source term (Kylling and Stamnes, 1992).

The chapter is organised as follows: first the basic general radiative transfer equations are presented (Section 4.2). In Section 4.3 the implementation of the SOS in the thermal infrared spectral range is discussed. A comparison of the performance of different methodologies to unify the optical depth and the temperature vertical discretization as well as the details about the implementation of the SOS approach in GRASP code can be found in the Section 4.4. The Section 4.5 is devoted to the validation and testing of the developed methodology and SOS code against DISORT. Analysis of the polarization effects in TIR is included in the Section 4.6.

4.2 The radiative transfer equation in TIR

For a plane-parallel layer of particulate sparse medium with an arbitrary optical thickness, the directions of the scattered and incident light can be represented by the vectors **k** and $\mathbf{k}_0$. In the right handed coordinate system with axis z perpendicular to the boundaries of the medium, these directions are described by azimuth and zenith angles (φ, θ) and (φ_0, θ_0) for the scattered and incident directions correspondingly. For the sake of clarity, here the zenith angle in this is always expressed in terms of its cosine ($\mu = cos(\theta)$). Thus, $\mu > 0$ stands for upward direction, $\mu < 0$ for downward direction. Therefore, $\mu_0 < 0$ in the chosen coordinate system. The vertical dimension is expressed in terms of the optical depth τ. Thus, a value of $\tau = 0$ corresponds to the TOA and a value of $\tau = \tau^*$ to the bottom of the atmosphere (BOA), where the boundary surface is located.

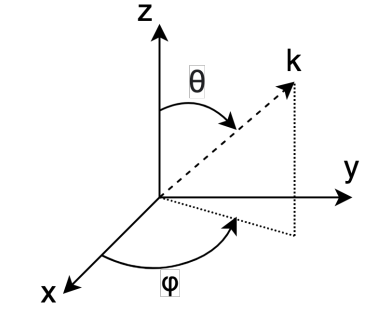

Figure 4.1: Spherical coordinates which define radiative transfer viewing geometry.

In general terms, the monochromatic vector radiative transfer equation can be expressed as follows

(Chandrasekhar, 1960):

$$\mu \frac{d\mathbf{L}(\tau,\mu,\varphi)}{d\tau} = \mathbf{L}(\tau,\mu,\varphi) - \mathbf{S}(\tau,\mu,\varphi). \tag{4.1}$$

Here the subscripts corresponding to the wavelength are omitted because the interactions of radiation with different frequencies are not going to be considered. $\mathbf{L}(\tau,\mu,\varphi)$ in eq. 4.1 corresponds to the vector radiance in the direction $\mathbf{n}$ defined by Stokes parameters vector (Van de Hulst, 1957):

$$\mathbf{L}(\tau,\mu,\varphi) = (I,Q,U,V)^T. \tag{4.2}$$

where I represents the total intensity, Q, U and V are the Stokes parameters describing linear and circular polarization (Lenoble et al. (2007), Liou (2002), Mishchenko et al. (2006)). $\mathbf{S}(\tau,\mu,\varphi)$ in eq. 4.1) is the vector source function. If scattering and emission is taken into account it can be generally defined as follows:

$$\begin{aligned}\mathbf{S}(\tau,\mu,\varphi) =& \frac{\omega(\tau)}{4\pi}\mathbf{P}(\tau,\mu,\varphi,\mu_0,\varphi_0)\mathbf{E}_0 \exp(\frac{\tau}{\mu_0}) \\ &+ \frac{\omega(\tau)}{4\pi}\int_0^{2\pi}\int_{-1}^{+1}\mathbf{P}(\tau,\mu,\varphi,\mu',\varphi')\mathbf{L}(\tau,\mu',\varphi')d\mu',d\varphi' \\ &+ \epsilon_\lambda(\tau)B_\lambda(T(\tau)),\end{aligned} \tag{4.3}$$

where ω represents Single Scattering Albedo (SSA) of scatterers in the medium, $\mathbf{P}(\tau,\mu,\varphi,\mu,\varphi)$ is the phase matrix of the scatterers, and B_λ is the Planck function describing thermal emission of particles with temperature $T(\tau)$ and emissivity $\epsilon_\lambda(\tau)$. In other words, the first term on the right hand side of the equation stands for the single scattering, the second one accounts for the multiple scattering processes and the third one describes the thermal emission. Since the natural Sun radiation is unpolarized, incident irradiance to the atmosphere can be expressed as: $\mathbf{E}_0 = (E_0,0,0,0)^T$.

Eq. 4.1 can be written in the integral form normally used for numerical solutions of the RT problem:

$$\mathbf{L}(\tau,\mu,\varphi) = -\int_0^\tau \mathrm{e}^{-(\tau'-\tau)/\mu}\mathbf{S}(\tau',\mu,\varphi)d\tau'/\mu \quad \forall \ \ \mu<0 \tag{4.4}$$

$$\mathbf{L}(\tau,\mu,\varphi) = \mathbf{L}(\tau^*,\mu,\varphi)\mathrm{e}^{-(\tau^*-\tau)/\mu} + \int_\tau^{\tau^*}\mathrm{e}^{-(\tau'-\tau)/\mu}\mathbf{S}(\tau',\mu,\varphi)d\tau'/\mu \quad \forall \ \ \mu>0 \tag{4.5}$$

The integro-differential nature of eq. 4.1 resulting in the inter-dependencies of $\mathbf{S}(\tau,\mu,\varphi)$ and $\mathbf{L}(\tau,\mu,\varphi)$ in eqs. 4.4 and 4.5 complicates general analytical solutions of the RT problem, especially when both scattering and emission processes are accounted. In order to avoid the complex numerical solution of the double integrals over azimuth and zenith angles in RT equations, expansions in Fourier series of the azimuthally dependent characteristics are used. In this way, the RT equations can be written as a system of linear independent integral equations for Fourier components independent of azimuth angle.

The Phase Matrix, $\mathbf{P}$, is the optical characteristic which describes the directional distribution of Stokes parameters of the polarized light scattered by a particle. For random media the phase matrix in eq. 4.3 is averaged over particle orientations and microphysical properties (size distribution, nonsphericity, etc). If Stokes parameters of the incident and scattered light are defined in the same scattering plane, the averaged over ensemble phase matrix for chaotically oriented and mirror symmetric particles depends only on the scattering angle Θ, and it can be represented by a 4x4 matrix with only 8 non-zero elements:

$$\mathbf{P}(\Theta) = \begin{pmatrix} p_{11}(\Theta) & p_{12}(\Theta) & 0 & 0 \\ p_{21}(\Theta) & p_{22}(\Theta) & 0 & 0 \\ 0 & 0 & p_{33}(\Theta) & p_{34}(\Theta) \\ 0 & 0 & p_{43}(\Theta) & p_{44}(\Theta) \end{pmatrix} \tag{4.6}$$

where

$$cos(\Theta) = -[cos(\theta)cos(\theta_0) + sin(\theta)sin(\theta_0)cos(\varphi - \varphi_0)] \tag{4.7}$$

For isotropic particles only six of the eight phase matrix elements are independent ($p_{21} = p_{12}$ and $p_{43} = -p_{34}$). This change between scattering and radiative transfer viewing angle can be expressed in matrix form as:

$$\mathbf{P}(\tau, \mu, \varphi, \mu_\mathbf{0}, \varphi_\mathbf{0}) = \mathbf{T}(-\chi)\mathbf{P}(\mathbf{\Theta})\mathbf{T}(\chi') \tag{4.8}$$

where

$$\mathbf{T}(\chi') = \begin{pmatrix} 1 & 0 & 0 & 0 \\ 0 & cos(2\chi') & sin(2\chi') & 0 \\ 0 & -sin(2\chi') & cos(2\chi') & 0 \\ 0 & 0 & 0 & 1 \end{pmatrix} \tag{4.9}$$

The angles χ and χ' refer to the angles between the scattering and the meridian planes for the scattered and incident radiance directions correspondingly. After some trigonometric transformations (Hovenier et al., 2004), these rotation angles can be written as:

$$\cos(\chi') = \frac{\cos(\theta) + \cos(\theta_0)\cos(\Theta)}{\sin(\theta_0)\sin(\Theta)} \tag{4.10}$$

$$\cos(\chi) = \frac{\cos(\theta_0) + \cos(\theta)\cos(\Theta)}{\sin(\theta)\sin(\Theta)} \tag{4.11}$$

The numerical solution of radiative transfer equation requires the expansion of the phase matrix elements in Legendre polynomials :

$$p_{ij}(\Theta) = \sum_{l=0}^{L} \xi_l^{i,j} P_l(cos(\Theta)). \tag{4.12}$$

Where $p_{ij}(\Theta)$ are the different elements of $\mathbf{P}(\Theta)$, and $\xi_l^{i,j}$ are the corresponding expansion coefficients in the Legendre polynomials $P_l(cos(\Theta))$ series:

$$\xi_l^{i,j} = \frac{1}{2(l+1)} \int_0^\pi p_{i,j}(\Theta) P_l(cos(\Theta)) sin(\Theta) d\Theta \tag{4.13}$$

This expansion decouples complex angular dependencies and crucially simplifies the numerical solutions of RT equations over angular integrals.

In addition to this Legendre polynomial expansion, the necessary simplifications to solve the angular integrals appearing in the radiative transfer equation require a Fourier azimuth decomposition of the radiance and Phase matrix. The radiance can be written as:

$$\mathbf{L_n}(\tau, \mu, \varphi) = \sum_{\mathbf{s=0}}^{\mathbf{S}} (\mathbf{2} - \delta_{\mathbf{0s}})[\cos[\mathbf{s}(\varphi - \varphi_\mathbf{0})]\mathbf{L}^{\mathbf{s}}_{\mathbf{n},\cos}(\tau, \mu) + \sin[\mathbf{s}(\varphi - \varphi_\mathbf{0})]\mathbf{L}^{\mathbf{s}}_{\mathbf{n},\sin}(\tau, \mu)] \tag{4.14}$$

with

$$\mathbf{L}^s_{n,\cos}(\tau, \mu) = (I^s_n, Q^s_n, 0, 0) \text{ and } \mathbf{L}^s_{n,\sin}(\tau, \mu) = (0, 0, U^s_n, V^s_n) \tag{4.15}$$

where

$$\begin{aligned} I_n(\tau,\mu,\varphi) &= \sum_{s=0}^{S}(2-\delta_{0s})\cos(s(\varphi-\varphi_0))I_n^s(\tau,\mu) \\ Q_n(\tau,\mu,\varphi) &= \sum_{s=0}^{S}(2-\delta_{0s})\cos(s(\varphi-\varphi_0))Q_n^s(\tau,\mu) \\ U_n(\tau,\mu,\varphi) &= \sum_{s=1}^{S}2\sin(s(\varphi-\varphi_0))U_n^s(\tau,\mu) \\ V_n(\tau,\mu,\varphi) &= \sum_{s=1}^{S}2\sin(s(\varphi-\varphi_0))V_n^s(\tau,\mu) \end{aligned} \tag{4.16}$$

On the other hand, the Phase Matrix is expressed as:

$$\mathbf{P}(\mu,\varphi,\mu',\varphi') = \sum_{\mathbf{s=0}}^{\mathbf{S}}(\mathbf{2}-\delta_{\mathbf{0s}})[\cos[\mathbf{s}(\varphi-\varphi')]\mathbf{P}^{\mathbf{s}}_{\cos}(\mu,\mu') + \sin[\mathbf{s}(\varphi-\varphi')]\mathbf{P}^{\mathbf{s}}_{\sin}(\mu,\mu')] \tag{4.17}$$

with

$$\begin{pmatrix} P_{11} & c'P_{12} & 0 & 0 \\ cP_{12} & cc'P_{22}+ss'P_{33} & 0 & 0 \\ 0 & 0 & ss'P_{22}+cc'P_{33} & -cP_{43} \\ 0 & 0 & c'P_{43} & P_{44} \end{pmatrix} = \sum_{s=0}^{S}(2-\delta_{0s})\cos(s(\varphi-\varphi'))\mathbf{P}^s_{\cos}(\mu,\mu') \tag{4.18}$$

$$\begin{pmatrix} 0 & 0 & s'P_{12} & 0 \\ 0 & 0 & cs'P_{22}-sc'P_{33} & sP_{43} \\ sP_{12} & sc'P_{22}-cs'P_{33} & 0 & 0 \\ 0 & -s'P_{43} & 0 & 0 \end{pmatrix} = \sum_{s=1}^{S}2\sin(s(\varphi-\varphi'))\mathbf{P}^s_{\sin}(\mu,\mu') \tag{4.19}$$

where c stands for cos(2χ), s for sin(2χ), and similarly for c' and s' with χ'.

The source function in first order approximation and multiple scattering can be expressed as:

$$\mathbf{S}_1(\tau,\mu,\varphi) = \frac{\omega(\tau)}{4\pi}\sum_{s=0}^{S}(2-\delta_{0s})[\cos[s(\varphi-\varphi_0)]\mathbf{P}^s_{\cos}(\mu,\mu_0)\mathbf{E}_0 e^{\tau/\mu_0} \tag{4.20}$$

$$\begin{aligned} \mathbf{S}_{n>1}(\tau,\mu,\varphi) = \frac{\omega(\tau)}{2}\sum_{s=0}^{S}(2-\delta_{0s})\Bigg[&\cos[s(\varphi-\varphi_0)]\int_{-1}^{+1}(\mathbf{P}^s_{\cos}\mathbf{L}^s_{n-1,\cos}-\mathbf{P}^s_{\sin}\mathbf{L}^s_{n-1,\sin})d\mu' \\ &+\sin[s(\varphi-\varphi_0)]\int_{-1}^{+1}(\mathbf{P}^s_{\sin}\mathbf{L}^s_{n-1,\cos}+\mathbf{P}^s_{\cos}\mathbf{L}^s_{n-1,\sin})d\mu'\Bigg] \end{aligned} \tag{4.21}$$

A more detailed description of the expansion techniques as well as the numerical solutions can be found elsewhere (Lenoble et al. (2007), Wiscombe (1977), Plass et al. (1973)).

The next Section briefly revisits the numerical approach used in SOS method to solve RT equations for scattering media and extends it to the case when TIR emission is taken into account.

4.3 The SOS RT method accounting for thermal emission

The interaction of light with the atmosphere includes scattering, absorption and emission processes with its own methodological differences. The SOS RT approach is based on the method of successive approximation implemented via consequent solution of linear equations. Specifically, the solution is represented by an infinite series of "orders of scattering (approximation)" which represents different approximation terms in the series:

$$L(\tau,\mu,\varphi)=\sum_{n=1}^{N}L_n(\tau^*,\mu,\varphi), \tag{4.22}$$

where the term with $n=1$ corresponds to the First order approximation term. If thermal emission is accounted, it includes both emission and single scattering terms. The terms $n>2$ represents multiple scattering contributions.

4.3.1 First order approximation

The usual way to account for thermal emission in the medium is based on the assumption that the particles can be modelled as a grey body in Local Thermodynamic Equilibrium (LTE) (Stamnes et al. (1988), Doppler et al. (2014)). According to Kirchhoff's law (Kirchhoff, 1978) particles emissivity at a certain wavelength corresponds directly to their absorptivity at the same wavelength. Therefore, the emission term of source function in eq. 4.3 at each optical depth τ can be expressed via single scattering albedo (ω) as the following:

$$\mathbf{S}_{1,emis}(\tau)=(1-\omega(\tau))B_\lambda(T(\tau)). \tag{4.23}$$

For a horizontally isotropic atmosphere, the emission does not depend on azimuth angle φ.

The total source function in the first order approximation is a sum of the emission and single scattering parts expressed as follows:

$$\mathbf{S}_1(\tau,\mu,\varphi)=\mathbf{S}_{1,emis}(\tau)+\mathbf{S}_{1,scat}(\tau,\mu,\varphi), \tag{4.24}$$

where

$$\mathbf{S}_{1,scat}(\tau,\mu,\varphi)=\frac{1}{4\pi}\omega(\tau)\mathbf{P}(\tau,\mu,\varphi,\mu_0,\varphi_0)E_0\mathrm{e}^{\tau/\mu_0}. \tag{4.25}$$

Thus, from the eqs. 4.4 and 4.5 the scattering and emission parts of the radiation in the first order approximation can be calculated independently for the upward and downward directions:

$$\mathbf{L}_{1,i}(\tau,\mu,\varphi)=-\int_0^\tau \mathrm{e}^{-(\tau'-\tau)/\mu}\mathbf{S}_{1,i}(\tau',\mu,\varphi)d\tau'/\mu \quad \forall \ \ \mu<0 \tag{4.26}$$

$$\mathbf{L}_{1,i}(\tau,\mu,\varphi)=\mathbf{L}_{1,i}(\tau^*,\mu>0,\varphi)\mathrm{e}^{-(\tau^*-\tau')/\mu}+\int_\tau^{\tau^*} \mathrm{e}^{-(\tau'-\tau)/\mu}\mathbf{S}_{1,i}(\tau',\mu,\varphi)d\tau'/\mu \quad \forall \ \ \mu>0, \tag{4.27}$$

where i stands for 'emis' or 'scat'.

At the boundary level, $\tau=\tau^*$, the upwelling ($\mu>0$) radiance in the first order approximation is defined by the surface scattering and emission:

$$\mathbf{L}_{1,scat}(\tau^*,\mu,\varphi)=-\frac{\mu_0}{\pi}\mathbf{R}(\mu,\varphi,\mu_0,\varphi_0)E_0\mathrm{e}^{\tau^*/\mu_0} \quad \forall \ \ \mu>0 \tag{4.28}$$

$$\mathbf{L}_{1,emis}(\tau^*,\mu,\varphi)=\epsilon_{sur}B_\lambda(T_{sur}). \quad \forall \ \ \mu>0 \tag{4.29}$$

Here $\mathbf{R}$ is the surface reflection matrix (Lenoble et al. (2007), Litvinov et al. (2012), Snyder and Wan (1998)) and ϵ_{sur} is the surface emissivity at a given wavelength. Similarly to the consideration of

the atmospheric layers, the surface emission is modelled as the emission of a grey body in LTE with a temperature T_{sur}. If the surface is optically thick, the transmitted radiation through the surface is negligible in comparison to the scattering and absorption. In these conditions, the surface emissivity can be directly related to the surface albedo a_{sur}:

$$\epsilon_{sur} = 1 - a_{sur}. \tag{4.30}$$

The total radiance in the first order approximation:

$$\mathbf{L}_1(\tau) = \mathbf{L}_{1,emis}(\tau) + \mathbf{L}_{1,scat}(\tau). \tag{4.31}$$

4.3.2 Multiple Scattering

In eq. 4.22 the terms with $n > 1$ describe the multiple scattering of the radiation in the medium. The total source function for the multiple scattering terms is expressed as the following:

$$\mathbf{S_n}(\tau,\mu,\varphi) = \frac{\omega(\tau)}{\mathbf{4\pi}} \int_{\mathbf{0}}^{\mathbf{2\pi}} \int_{\mathbf{-1}}^{\mathbf{+1}} \mathbf{P}(\tau,\mu,\varphi,\mu',\varphi')\mathbf{L_{n-1}}(\tau,\mu',\varphi')\mathbf{d}\mu',\mathbf{d}\varphi' \quad \forall \quad \mathbf{n > 1} \tag{4.32}$$

The corresponding upward and downward radiation can be calculated following once again equations 4.4 and 4.5:

$$\mathbf{L_n}(\tau,\mu,\varphi) = -\int_0^{\tau} \mathrm{e}^{-(\tau'-\tau)/\mu}\mathbf{S}_n(\tau',\mu,\varphi)d\tau'/\mu \quad \forall \quad \mu < 0 \tag{4.33}$$

$$\mathbf{L_n}(\tau,\mu,\varphi) = \mathbf{L_n}(\tau^*,\mu,\varphi)\mathrm{e}^{-(\tau^*-\tau)/\mu} + \int_{\tau}^{\tau^*} \mathrm{e}^{-(\tau'-\tau)/\mu}\mathbf{S_n}(\tau',\mu,\varphi)\mathbf{d}\tau'/\mu \quad \forall \quad \mu > \mathbf{0} \tag{4.34}$$

At the bottom border of the medium, the radiance for the multiple scattering term can be written as follows:

$$\mathbf{L}_n(\tau^*,\mu,\varphi) = \int_0^{2\pi} \int_{-1}^{0} (-\mu')\mathbf{R}(\tau,\mu,\varphi,\mu',\varphi')\mathbf{L}_{n-1}(\tau^*,\mu',\varphi')d\mu' d\varphi'/\pi \quad \forall \quad n > 1 \ , \ \mu > 0 \tag{4.35}$$

A simple fact can be noted from eqs. 4.23-4.35: accounting for the thermal emission in RT affects only the equation for the source function in the first order of approximation, whereas the equations for higher orders remain unchanged. Nevertheless, the accurate accounting for thermal emission, scattering and absorption in SOS solution faces some principle challenges in numerical implementation, such as the identification of a reliable procedure of discretisation for temperature, gases and aerosol vertical profiles.

4.4 Vertical discretization: scattering, absorption and temperature profiles

One of the most important factors for an accurate numerical solving of RT equations is the definition of an adequate vertical discretization of the atmosphere to account for the vertical variability of atmospheric scattering, absorption and emission properties. It is especially crucial for the SOS RT method, where the integral over source function should be calculated correctly for each discrete layer l (with optical thickness $\Delta\tau_l$) in both first order and multiple scattering approximations. Indeed, the atmosphere is divided into optically thin layers ranging from 1 to L_{max} (which corresponds to levels ranging from 0 to L_{max}), where the optical properties are averaged.

Thus, the radiance corresponding to an arbitrary level $\tau = \tau_L$ is expressed as:

$$\mathbf{L}(\tau_{\mathbf{L}}, \mu, \varphi) = -\sum_{l=1}^{L} \mathrm{e}^{-(\tau_l - \tau_L)/\mu} \int_0^{\Delta\tau_l} \mathrm{e}^{(\tau_l' - \Delta\tau_l)/\mu} \mathbf{S}(\tau_{l-1} + \tau_l', \mu, \varphi) d\tau_l'/\mu \quad \forall \quad \mu < 0 \tag{4.36}$$

$$\mathbf{L}(\tau_{\mathbf{L}}, \mu, \varphi) = \mathbf{L}(\tau^*, \mu > 0, \varphi)\mathrm{e}^{-(\tau^* - \tau_L)/\mu} + \sum_{l=L+1}^{L_{max}} \mathrm{e}^{-(\tau_{l-1} - \tau_L)/\mu} \int_0^{\Delta\tau_l} \mathrm{e}^{-\tau_l'/\mu} \mathbf{S}(\tau_{l-1} + \tau_l', \mu, \varphi) d\tau_l'/\mu, \quad \forall \quad \mu > 0 \tag{4.37}$$

where $\tau^* = \tau_{L_{max}}$, $\Delta\tau_l = \tau_l - \tau_{l-1}$ and $\mathbf{S}_n(\tau_{l-1} + \tau_l', \mu, \varphi)$ is the source function defined in the in the layer l:

$$\mathbf{S}(\tau_{l-1} + \tau_l', \mu, \varphi) = \frac{1}{4\pi} \int_0^{2\pi} \int_{-1}^{+1} \omega(\tau_{l-1} + \tau_l') \mathbf{P}(\tau_{l-1} + \tau_l', \mu, \varphi, \mu', \varphi') \mathbf{L}(\tau_{l-1} + \tau_l', \mu', \varphi') d\mu', d\varphi' \tag{4.38}$$

In addition to the scattering and absorption, accounting for the thermal emission in the atmosphere also requires a correct representation of the temperature profile in each layer l (eq. 4.22-4.38). In general, a correct vertical discretisation of the atmosphere with scattering, absorption and thermal emission can be done by increasing the number of atmospheric vertical layers. In practice, this may essentially increase the computation time and make the SOS method less efficient for a number of applications. Therefore, this section is devoted to the analysis of optimal discretization of the temperature, as well as, the scattering and absorption profiles.

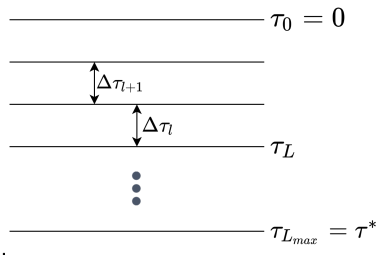

Figure 4.2: Schematic representation of the levels and layers discretisation.

First of all, the current section presents a description of how the atmospheric layers are defined in the GRASP SOS RT code for optimum accounting for vertical variations of scattering properties in the presence of several optically distinct components. Then, the effect of vertical discretization over scattering and emission processes are independently analysed in detail.

4.4.1 Atmospheric Layer definition

Finding a numerical solution for the SOS RT equations at a certain location of the observations requires the subdivision of the integrals over optical thickness eqs. 4.4 and 4.5 into optically thin layers eqs. 4.36 and 4.37. The scattering and absorption properties within each of such layers can be represented by the layer average phase matrix and single scattering albedo. In case of presence of several scattering and absorbing atmospheric components these quantities can be calculated as follows:

$$\omega(\Delta\tau_l) = \frac{\sum_{i=1}^{N_c} \omega_i(\Delta\tau_l)\Delta\tau_l^{(i)}}{\sum_{i=1}^{N_c} \Delta\tau_l^{(i)}}, \tag{4.39}$$

$$\omega(\Delta\tau_l)\mathbf{P}(\Delta\tau_l) = \frac{\sum_{i=1}^{N_c} \omega_i(\Delta\tau_l)\mathbf{P}_i(\Delta\tau_l)\Delta\tau_l^{(i)}}{\sum_{i=1}^{N_c} \Delta\tau_l^{(i)}}, \tag{4.40}$$

where N_c is the total number of components in each layer (aerosol, gases, molecules or clouds).

The scattering source functions for each layer l can be written as follows:

$$S_{1,scat}(\Delta\tau_l, \mu, \varphi) = \frac{1}{4\pi}\omega(\Delta\tau_l)\mathbf{P}(\Delta\tau_l)E_0 \mathrm{e}^{\tau/\mu_0} \tag{4.41}$$

As previously mentioned, the layers in the approach described here are considered to be in LTE conditions which requires all atmospheric components within the same layer to be at the same average temperature. Thus, each layer is represented just by one single Planck function. However, temperature variation through different layers is allowed. Consequently, the emission source term in the layer l and in the first order approximation represented in eq. 4.23 is expressed in terms of $\omega(\Delta\tau_l)$ as the following:

$$S_{1,emis}(\Delta\tau_l) = (1 - \omega(\Delta\tau_l))B_\lambda(T(\Delta\tau_l)). \tag{4.42}$$

The representation of $T(\Delta\tau_l)$ in each layer l is described in the next sections.

4.4.2 GRASP SOS RT in high TOD conditions

Hitherto, the performance of GRASP SOS radiative transfer has only been tested for moderate TOD values normally existing for visible and SWIR spectral range applications. If strong gas absorption lines are accounted for, then the conditions can be far from those in visible and SWIR domains. For example, TOD can reach more than one order of magnitude higher. If a high enough number of layers is selected, the SOS RT approach can be successfully used under any TOD condition. However, as already mentioned the calculations with a high number of layers can be computationally expensive. The thermal part, in general, does not present special problems once that the discretization of temperature vertical variability has been properly resolved. In this section we therefore focus on the calculation of the scattering processes solely.

In order to explore the limits of GRASP SOS RT accuracy under high TOD conditions, a reference simulation of 600 layers is going to be compared with simulations performed with a smaller number of layers. In order to avoid the effects of temperature vertical discretization, four different scenarios with a high TOD based on an isothermal atmosphere at 250 K (including the surface) have been designed. The single scattering albedo has been set to a value around 0.5 in all layers. This high single scattering albedo condition may not be very realistic in comparison with the zero value of this magnitude of pure gas absorption lines. However, in this analysis we want to assure that the scattering part plays a significant role in the calculations. The extreme characteristics of the atmospheric scenarios designed for this comparison mark a good reference for the accuracy limit of GRASP SOS RT to resolve scattering processes, because the real atmospheric situations present more favourable conditions to perform these calculations.

Figure 4.3 shows the average radiance difference between the reference simulation using 600 layers and the calculation with a smaller number of layers calculated by GRASP SOS RT. This average radiance difference includes a complete set of upward and downward geometries including the full azimuth range and a zenith range from 10° to 70° (it can be visualized in figure 4.6). Hereafter, the radiance results presented in this study will be expressed in terms of Brightness Temperature (BT).

In the case of ground-based observations, there is no significant change in the final radiance even for a reduced number of layers. On the contrary, in the case of calculations for satellite geometries, the convergence is reached only with a higher number of layers (around 300). This dependency seems to be fully associated with multiple scattering effects, because if the same simulations are performed restricting the code to a first order approximation regime (not shown), the effect of the increase of the number of layers totally vanishes; only numerical noise around 1e-6 K is obtained without any significant tendency. The complete isothermal nature of the atmosphere and surface selected for this test shows that the origin of this observed dependency of multiple scattering on satellite measurements is purely geometrical, arising from the involved scattering angles. Therefore, even in the thermal infrared spectral range, where the non-directional nature of the Planck function dominates, the multiple scattering effects cannot be neglected, especially in modeling observations with the satellite-like geometries.

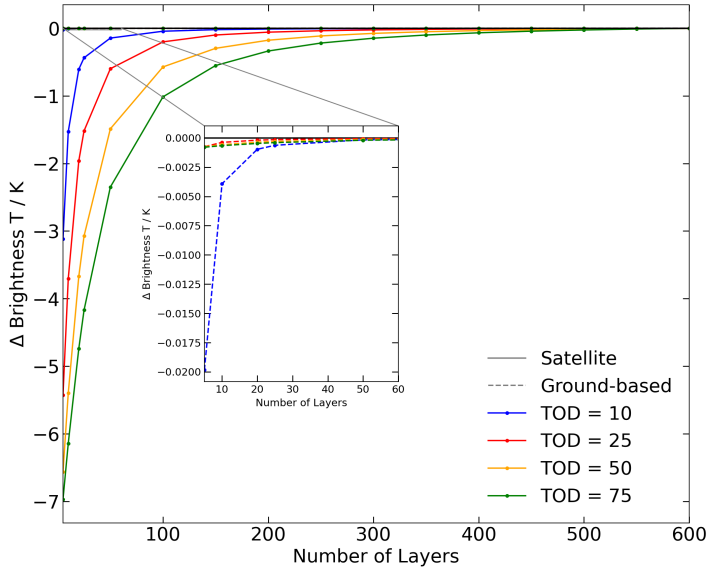

Figure 4.3: Radiance difference, expressed in brightness temperature, as a function of the number of layers used compare to the reference scenario with 600 layers for satellite (thick line) and ground-based (dashed line) geometries for four high TOD situations assuming a fully isothermal atmosphere at 250.0 K. Each point corresponds to the average radiance over upward and downward geometries including the full azimuth range, and a zenith range from 10° to 70°.

4.4.3 Emission source function and temperature vertical discretization: from levels to layers

Once the limits to adequately account scattering processes have been investigated in the previous section, the current section discusses the temperature vertical discretization and the calculation of the thermal source function within the layers. The re-gridding of the radiative magnitudes from levels to layers is not a trivial task. There are different approaches focused on the calculation of the most representative temperature of the layer to directly obtain the corresponding source function, while others take the source function of the levels as the starting point, in order to assume certain variation between them.

The GRASP SOS RT vertical discretization is based on the division of the full atmospheric column in thin layers of equal optical depth. No particular issues were observed for this methodology at the solar spectral range. However, at the thermal-infrared, the lack of a specific temperature discretization can raise some uncertainty when the vertical derivatives of the temperature and optical depth differ significantly. In order to illustrate the undesired interactions between the temperature profile and the TOD discretization, a TOD of 75 has been exponentially distributed along the atmospheric column in a US Standard atmosphere. This combination of atmospheric profile and optical depth distribution produces a fast temperature variation near the TOA which is not accompanied by an optical depth variation of the same magnitude, as it can be seen in fig. 4.4.

The blue line in fig. 4.4 represents the temperature (T_{pl}) in the original grid discretized in pressure levels but expressed in terms of TOD (τ'). The GRASP vertical discretisation of equal TOD levels (τ) is marked with an orange line. No particular issues can be seen in most part of the profile, however, it is clear that in the last levels from a TOD of 0.5 to TOA the temperature variation is not adequately retained by the TOD levels.

Furthermore, figure 4.4 shows two different approaches to assign a temperature value to the center of the layers. In one case only a linear variation of temperature between layer limits (green) is assumed. Whereas in the other approach, the final layer temperature is calculated by a TOD weighted integration (T_{wt}, marked in red) of all intermediate levels of the original pressure grid between each level of the GRASP TOD grid:

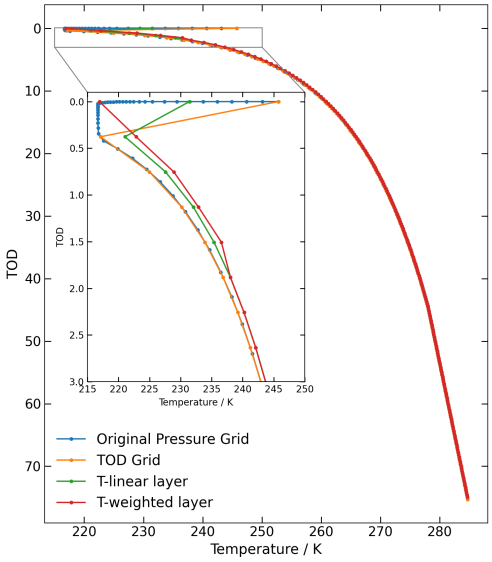

Figure 4.4: Comparison of pressure (blue) and GRASP SOS RT equal TOD (orange) vertical discretizations for a US-Standard like atmosphere with a TOD value of 75 exponentially distributed over it. Linear temperature variation between levels (green) and TOD weighted calculations (red) to obtain layer temperatures are also shown.

$$T_{\text{wt}}(\Delta\tau_l) = \frac{\int_{\tau_{l-1}}^{\tau_l} T(\tau')d\tau'}{\Delta\tau_l}. \tag{4.43}$$

However, it is common to perform this change from level to layer grid on the emission source function instead of applying it directly on the temperature profile, like in the case of Doppler et al. (2014), Dubuisson et al. (2005), Kylling and Stamnes (1992) and Saunders et al. (2018). A nalogously to the case of temperature, different assumptions of the source function variation between the levels can be used. Therefore, a linear variation from top of the layer and a TOD weighted integration of both temperature and emission source function will be also analysed here. The objective of such analysis is the comparison of the performance of the different methodologies to obtain thermal layer source function. A smaller change in the radiance values with the increase of the number of layers used in the radiative transfer calculations is considered as a sign of better correspondence between temperature and TOD discretizations. Thus, the methodology which presents a smaller sensitivity to the size of the step in the vertical discretization can be taken as more desirable. Figure 4.5 shows the change in average radiance, expressed as brightness temperature, of all geometries presented in figure 4.6 for a US-Standard atmosphere with an exponentially distributed TOD of 25. The reference radiance calculation corresponds to the calculation using 600 layers. This TOD value has been selected to minimize the effects of multiple scattering inconsistencies which have already been shown in figure 4.3

From the analysis of the fig. 4.5 it can be concluded that ground-based measurements almost do not present any sensitivity to the number of layers. This can be explained by the fact that the possible disagreement between derivatives is located near the TOA. Therefore, in the case of the ground-based geometry the radiation reaching the ground level from layers near the TOA is very attenuated. On the other hand, in the case of the satellite geometry the problematic TOA layers are just in front of the sensor. Thus, much stronger sensitivity to discretization methodology is expected. Thus, in the ground-based case, the assumptions in the temperature discretization has a minor effect, i.e., the differences in radiance disappear with a very reasonable amount of layers (between 100 and 150).

From the curves corresponding to satellite geometry (figure 4.5), it is clear that the methodologies assuming linear variations present a higher dependency with the number of layers. Whereas in the case of the TOD weighted methodologies the convergence is achieved much earlier. No special difference, in this test, can be seen between the calculations based on temperature or on source function.

Thus, figure 4.5 serves also as a proof of the performance of the GRASP SOS RT approach to deal with elevated TOD values. At the same time, these results correspond to a specific scenario, while the peak performance of each methodology can vary among different applications.

GRASP framework enables the possibility to add extra information that is very valuable to choose between the different methodologies presented above. If only columnar information is available, then the sensitivity tests like the presented in figure 4.5 can be used to assess the retrieval performance. At the same time, LIDAR or another kind of vertical resolved observations (extinction, depolarization, attenuation, etc) can be used in GRASP as discussed by Lopatin et al. (2021). In such situations, the amount of necessary assumptions is reduced and the TOD weighted methodologies should be more consistent.

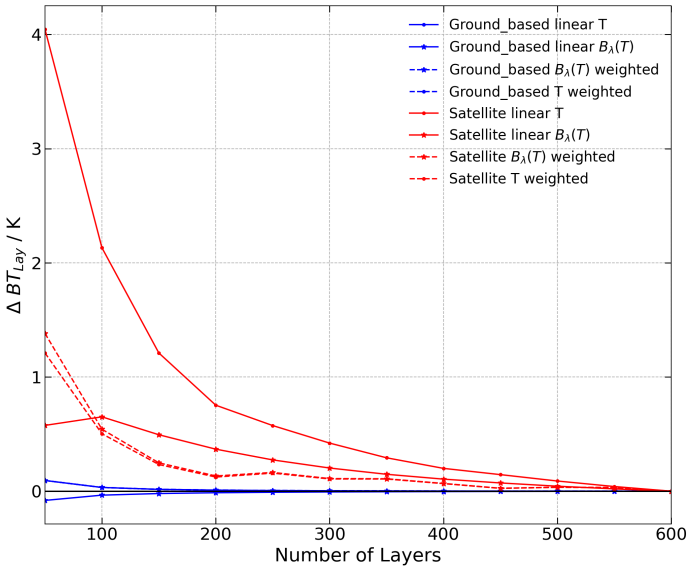

Figure 4.5: Radiance difference, expressed in brightness temperature, for different methodologies to obtain layer emission source function, compare to the reference the scenario with 600 layers shown as a function of the number of layers. Red lines show calculation for satellite-like geometry, blue lines correspond to ground-based like geometry. All the calculations are realized for a US-Standard atmosphere with a TOD of 25. Each point represents the average radiance of all geometries present in fig. 4.6.

4.5 Tests and comparisons against DISORT

This section presents the efforts on testing and validating the radiance calculations by GRASP SOS RT code at the thermal-infrared electromagnetic spectrum. As mentioned earlier, the DISORT (Stamnes et al., 1988) community code will be used as the established reference. GRASP SOS and DISORT approaches have several similar features that makes direct inter-comparison of the codes performance rather transparent. For example, both codes provide RT simulation for a vertically inhomogeneous non-isothermal plane parallel atmosphere. Furthermore, the phase matrix is expressed in a Legendre polynomial expansion in both approaches. Nonetheless, despite these similarities, the radiative transfer equation solving principles are different. Some of these fundamental differences will be discussed and analyzed below.

The selected DISORT implementation is restricted to the scalar radiative transfer equation, while a full development of the vector equation has been realized in GRASP RT code. Therefore, henceforth, only total radiances will be compared without accounting for polarization effects. The calculations of atmospheric radiance were realized for a US-Standard atmosphere using one hundred atmospheric levels and a lambertian surface model at a temperature of 303.15 K. The Sun irradiance has been modeled as a perfect black body at 5250.0 K, solar direction is defined at 60° zenith angle and at azimuth

angle of $\varphi = 0^{\circ}$. These atmospheric conditions are used in all the tests presented in this section with no modifications.

The absolute difference in brightness temperature between GRASP RT and DISORT (ΔBT $=$ GRASP $-$ DISORT) for all geometries at TOA and BOA can be found in figure 4.6. The upper part of each of the polar plots in this figure corresponds to observations with ground-based geometry, i.e. downward radiation. The lower part shows calculations for a satellite like geometry, i.e. upward radiation. The different panels in figure 4.6: A), B) and C) correspond to different amounts of total optical depth (TOD); 1.5, 0.15 and 0.015 correspondingly for each one. Each panel shows calculations at several wavelengths: 7, 8, 10, and 12 μm.

The mean difference for downward radiance averaging all selected scenarios shown in fig. 4.6 is -0.008 K (-0.005%), and for upward radiance the value of the difference is -0.002 K (-0.001%). The total mean difference for all considered wavelengths, TOD values and geometries between GRASP and DISORT is -0.005 K (-0.003%). These values can be compared with the commonly expected levels of noise of the remote sensing instruments operating in the thermal infrared range, e.g.: the average accuracy for IASI observations (Blumstein et al. (2004), Hilton et al. (2012)) of $\sim$0.1 K, for AIRS Garnier et al. (2012) is around 0.2 K, for CALIPSO IIR instrument measurements Garnier et al. (2012) is within 0.11 K, or for ground based observations by CLIMAT instrument (Legrand et al. (2000), Brogniez et al. (2003)) within 0.5 K. Thus, considering these levels of observation accuracy, it can be concluded that the discrepancies between GRASP RT and DISORT are notably below of their limits of detection.

The conducted comparisons did not reveal any noticeable systematic deviation tendency or bias for any of the scenarios presented above for the diverse aerosol loads and for the different selected zenith or azimuth angles. However, in the case of downward radiation, where the influence of the phase matrix is more important, small differences in the azimuth angle can be found. This is an expected known behaviour, because in this geometry the directional nature of Sun irradiance becomes more important. However, for upward radiance, where the surface is the major contributor in this spectral range, a high degree of homogeneity in each scenario can be appreciated for all wavelengths.

Some very minor tendencies can be seen in respect to TOD variations if the radiance difference is analyzed in detail. Specifically, in the case of downward radiance, a slight shift to positive values of ΔBT is observed. The averaged difference of ΔBT at 10 μm changes from -0.013 K for the lowest TOD, to -0.004 K in the highest TOD case. The maximum change with respecto to TOD for this geometry can be found at 8 μm, where the change in ΔBT with TOD ranges from -0.001 K to 0.023 K. If an analogous comparison is performed for upward radiance, the tendency is opposite to the case of downward observations. Thus, the increase of TOD tends to slightly shift ΔBT to smaller values. At 7 μm, the change in ΔBT with TOD ranges from 0.041 K to -0.021 K. And at 8 μm, ΔBT varies from 0.043 K to 0.011 K. Despite the presence of these tendencies, its small value and the change of the sign of ΔBT between different wavelengths and geometries avoid the assessment of any significant bias in the radiance comparison.

The differences found between both RT models can be partially attributed to intrinsic characteristics of their numerical implementations. For example, these small differences can be originated by differences in the numerical rounding between FORTRAN90 and $C\#$, the double precision of this DISORT implementation in comparison with the single precision of GRASP RT code, or the inconsistencies arising from the different analytical schemes used to solve the radiative transfer equation. Nonetheless, there are other factors that are interesting to be analyzed in detail in relation with the differences observed above. Specifically, our studies are focused on the thermal-infrared spectrum, thus the focus will be on the calculation of the Planck function of the source term for the different layers.

It has been shown that due to the non-isothermal nature of the atmosphere considered here, multiple possible implementations can be used to describe the temperature, the Planck function and the change of both magnitudes in the vertical dimension. In this respect, one of the main differences to calculate emission source function between GRASP RT and DISORT is that DISORT works with a spectrally integrated Planck function whereas GRASP calculates this magnitude in one single line. As a result, despite the smooth spectral behavior of Planck function, the differences between the two approaches are noticeable. Another main difference in the implementation of the two codes relates with how the vertical variation of temperature and Planck function is accounted for. Namely, DISORT operates with the exponential-linear interpolation method by Kylling and Stamnes (1992) to calculate the corresponding $B_{\lambda}(\tau)$ of each layer, whereas the GRASP RT numerical approximation used in this comparison is based on assuming linear variation of the temperature profile between the levels for

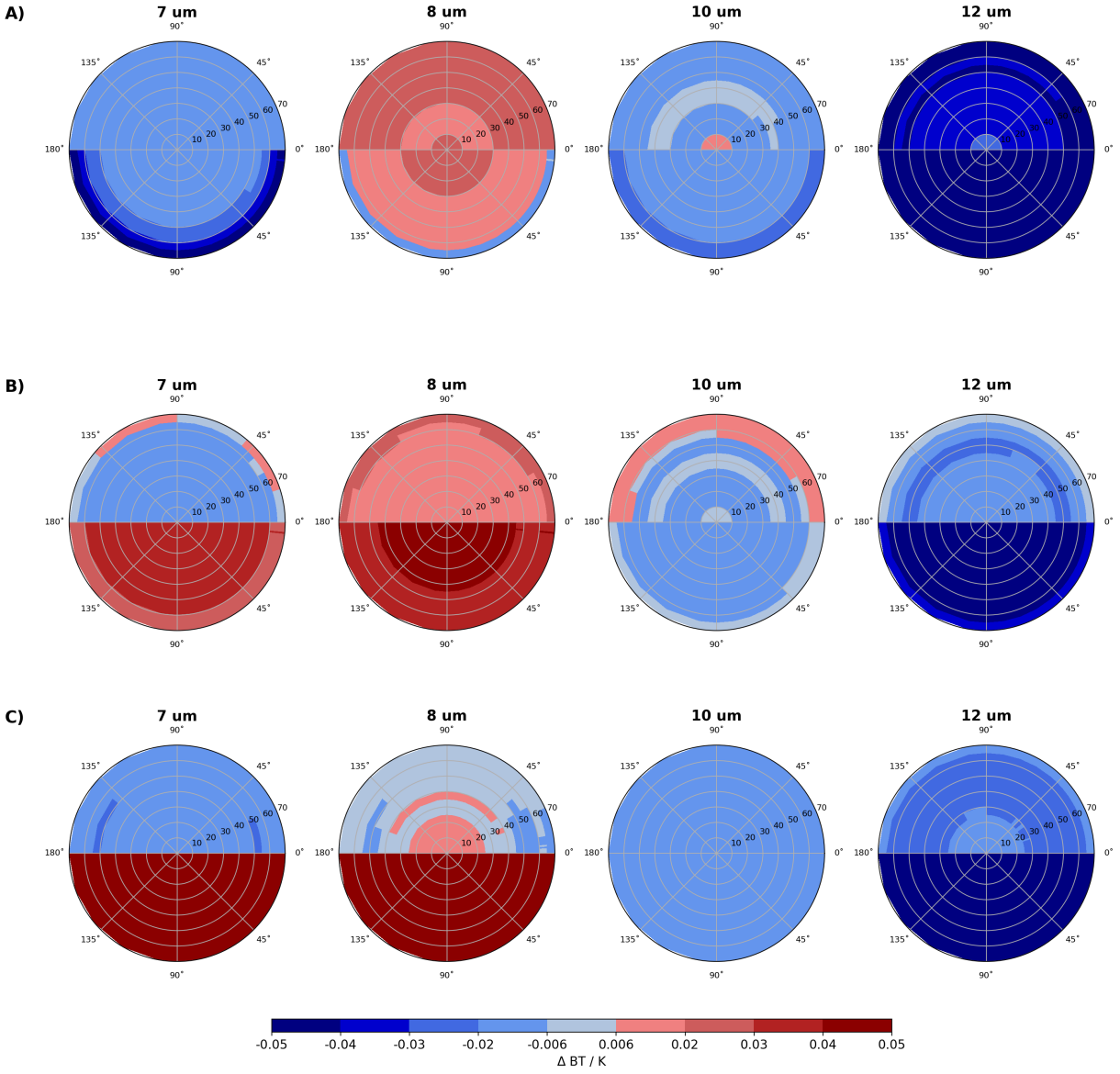

Figure 4.6: Absolute difference in brightness temperature between GRASP RT and DISORT (ΔBT $=$ GRASP $-$ DISORT), for downward radiation (upper part of polar plots) and upward radiation (lower part of polar plots) at 7, 8, 10 and 12 μm. The Sun is located at a zenith angle of 60°, and at an azimuth angle of 0°. The different panels A), B) and C) correspond to different amounts of TOD, 1.5, 0.15 and 0.015 correspondingly.

obtaining thermal layer source function.

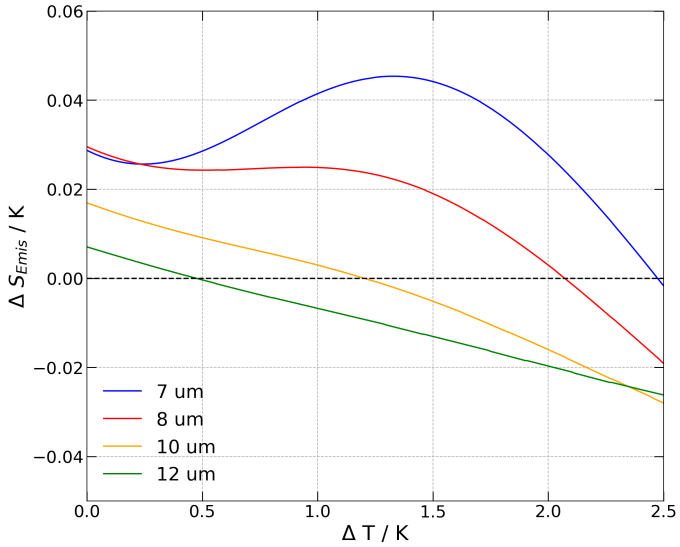

Figure 4.7: Absolute differences in layer emission source function between GRASP RT-like and DISORT-like methodologies shown as a function of the temperature difference between the top and the bottom limits of a layer at 270 K at four different wavelengths: 7, 8, 10 and 12 μm.

In order to quantify these methodological differences between GRASP RT and DISORT, the $S_{\text{Emis}}(T(\tau))$ calculated by the two methodologies for the layers have been generated and extracted out of their respective complete radiative transfer schemes. Their absolute difference, $\Delta S_{\text{Emis}} = S_{\text{Emis,GRASP}}(T(\tau)) - S_{\text{Emis,DISORT}}(T(\tau))$, is shown in fig. 4.7 at four wavelengths for different increases of temperature between the top and bottom limits of a single layer at a temperate around 270 K. Despite the comparison cannot be taken as an absolute reference, since both codes used other algorithmic adjustments and corrections in addition to the ones shown here, fig. 4.7 is evidently useful for explaining some of the observed features of the radiance comparison shown in fig. 4.6.

The temperature difference between levels in the selected US-standard atmosphere used for all the comparisons shown in fig. 4.6 ranges between 0.5 and 1.5 K. Looking at the mean values of ΔS_{Emis} in this temperature range, it can be noted that at 7 and 8 μm the GRASP RT methodology tends to overestimate the results of DISORT; in the case of 10 μm the differences are rather well centered around zero, and a slight underestimation can be seen at 12 μm. As fig. 4.6 shows very close tendencies as the differences in the calculations of $S_{\text{Emis}}(T(\tau))$ in the layers, it can be considered as one of the major sources of discrepancy between models. It is worth noting that even in fully isothermal conditions (ΔT = 0.0 K), still small differences between GRASP and DISORT can be found due to the spectrally integrated nature of DISORT Planck function calculation, as it has been previously mentioned. Notwithstanding, there are some other minor features in the observed radiance difference that remain unexplained by the factors discussed above, for example, the differences related to the azimuth variation, or to changes of the surface reflectance.

Computation time efficiency

In order to access the computation efficiency of the developed code, the calculation speed of GRASP RT SOS radiative transfer was compared to that of DISORT. The radiances were calculated by both codes for the same scenarios and geometries as those used above illustrated in fig. 4.6. The execution time of all the scenarios and wavelengths have been averaged for each code for a different number of streams or guassian quadratures for Fourier expansion coefficients correspondingly for DISORT and GRASP. Figure 4.8 illustrates the comparison of the average execution times for GRASP RT SOS and DISORT. It is important to note that for this comparison the same configuration has been used in both RT codes including the same number of vertical layers. However, the amount of necessary

atmospheric layers to achieve the same accuracy may be different between both schemes. Thus, the results shown here are an orientation.

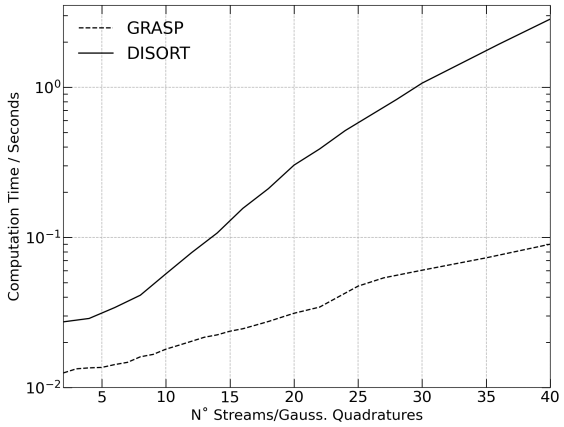

Figure 4.8: Computation time in seconds as a function of the number of streams or gaussian quadratures of GRASP RT SOS and DISORT radiative transfer codes.

From the conducted comparison, it can be concluded that the GRASP code is significantly faster than DISORT in the whole considered range of streams. On average, the GRASP code computation time is around 8 times smaller than DISORT. It can be noted that the calculation time difference increases with the number of streams. Indeed, when less than 10 streams are used for the radiative transfer calculations, GRASP SOS runs in about 2 to 3 times faster than DISORT. These differences increase significantly when the number of streams increases. For example, for 40 streams, the GRASP SOS RT calculations are more than 30 times faster than calculations by DISORT.

4.6 Effect of polarization and multiple scattering in TIR

At present, there is only a limited number of studies discussing the effects of polarization at TIR spectral range in the context of atmospheric remote sensing. For example, the analysis of polarimetric effects in TIR surface reflectance and in the observations of cirrus clouds can be found in Snyder and Wan (1998), or in Takano and Liou (1992) respectively.

As mentioned earlier, the comparisons against DISORT have been limited to solving the scalar radiative transfer equation because of the chosen version of DISORT does not account for polarization effects. In general, the contribution of polarization into total radiances at TIR is not significant and the scalar approximation provides sufficiently accurate results. Indeed, the emitted light by the sun, atmosphere and surface in this spectral range is unpolarized. Therefore, in the first order approximation (eq. 4.7) the radiance is unaffected by polarimetric effects and the degree of polarization (defined by the Stokes parameters ration Q/I and U/I) is close to zero if the emission from the Sun is negligible in comparison to the emission from the atmosphere and surface. However, due to multiple scattering in the atmosphere some polarization effect on the radiance and non-zero Q and U Stokes parameters of the scattered light still can arise. Although the conditions for the manifestation of the polarization seem to be quite specific, we have performed some analysis of the polarization effect in TIR for typical atmospheric aerosol conditions.

In this analysis, the TIR radiation was simulated for an scenario corresponding to a US-Standard atmosphere with a reference TOD value of 1.5 with different relative contributions of dust aerosol (AOD) and gas absorption (GOD). Figure 4.9 presents the absolute difference in radiance, expressed in terms of brightness temperature, calculated by GRASP SOS RT code using only the scalar equation and the complete one accounting for full polarization ($\Delta \mathrm{BT}_{\mathrm{Pol}} = \mathrm{Scalar} - \mathrm{Vector}$). Upper parts of the polar plots correspond to a ground-based up-looking geometries, and the lower part is for satellite down-looking geometries. Panel A) corresponds to a gas dominated atmosphere (AOD=0.5 and GOD = 1.0) and panel B) to an aerosol dominated atmosphere (AOD=1.0 and GOD=0.5). The situations with less aerosol are not shown because the differences between the calculations of the two different ra-

diative transfer schemes were hardly noticeable. Even in the situation where aerosol optical depth reaches 33% of total optical depth (panel A)), the average radiance difference for all geometries and the two selected wavelengths is only 3.09e-5 K, with a maximum difference of 2.06e-3 K. Whereas in the case where AOD is twice the GOD value (panel B)), the effects of polarization for some geometries can reach the same order of magnitude as the differences between GRASP and DISORT, with a maximum value of 1.02e-2 K. However, even in this case the average difference is 1.00e-4 K, which is far below the accuracy limits of common observations. Therefore, it can be concluded that accounting for the polarization effects in total radiances calculations at TIR is not significant for both satellite and ground-based observations.

The lack of azimuth dependence in the manifestation of polarimetric effects is related to the fact that the emission from the atmosphere and surface is dominant over the Sun incident radiation at TIR and there is no a predefined incident direction. At the same time, a dependence on the viewing zenith angle is noticeable. Namely, there is a slight increase of the radiance for smaller zenith angles if the scalar approximation is used in comparison with the values corresponding to higher angles. However, these observations can hardly be considered as a general tendency because this effect is strongly dependent on the structure of aerosol scattering matrix, aerosol vertical profile and the presence of the atmospheric gases. Thus, significant differences in this angular distribution could be found in another atmospheric scenario.

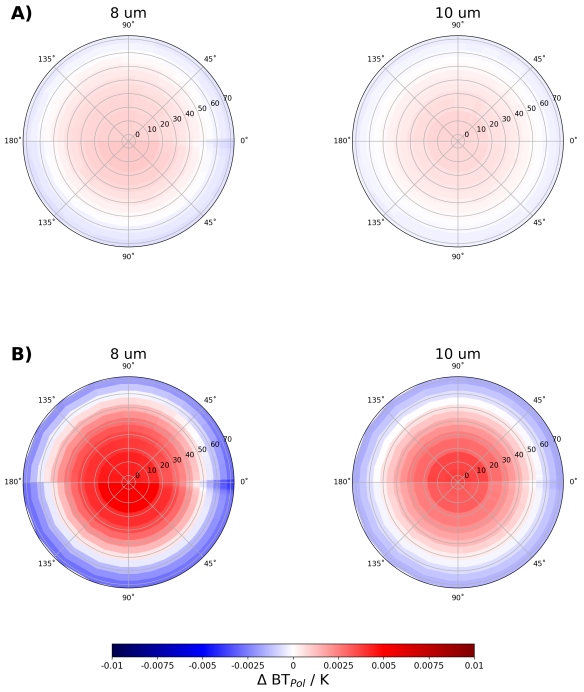

Figure 4.9: Absolute difference of radiance expressed in terms of brightness temperature calculated with and without polarization effects (ΔBT_{Pol} = Scalar − Vector) at 8 and 10 μm, for a solar zenith angle of 60°. Panel A) corresponds to a gas dominated atmosphere (AOD=0.5 and GOD = 1.0) and panel B) to an aerosol dominated atmosphere (AOD=1.0 and GOD=0.5). Upper part of the polar plots corresponds to downward radiation (ground-based like geometry) and the lower part to upward radiation (satellite-like geometry).

The results in fig. 4.9 suggest that only in the situations with a considerable load of aerosol particles and with low gaseous absorption the polarization may contribute noticeably to the total radiances at TIR spectral range.

Figure 4.10 shows the Q and U components of the radiance, both normalized by I, calculated for different aerosol loads. Panels A), B) and C) correspond to AOD of 1.0, 0.5 and 0.05 for a common GOD=0.5. In all the scenarios presented here the Q component is significantly more important than U, which is only noticeable at 8 μm and for medium with high aerosol loads. The azimuth structure that can be appreciated in this figure comes from the small influence of the solar radiance in TIR

range. This also explain the more noticeable azimuth dependence at 8 μm. In contrary to VIS, NIR and SWIR spectral range, the degree of polarization in TIR appears predominately in the multiple scattering terms of RT solution which describes scattering of radiation emitted by atmosphere and surface. However, in all scenarios of fig. 4.10 both components of polarization at the spectral range considered here are very low.

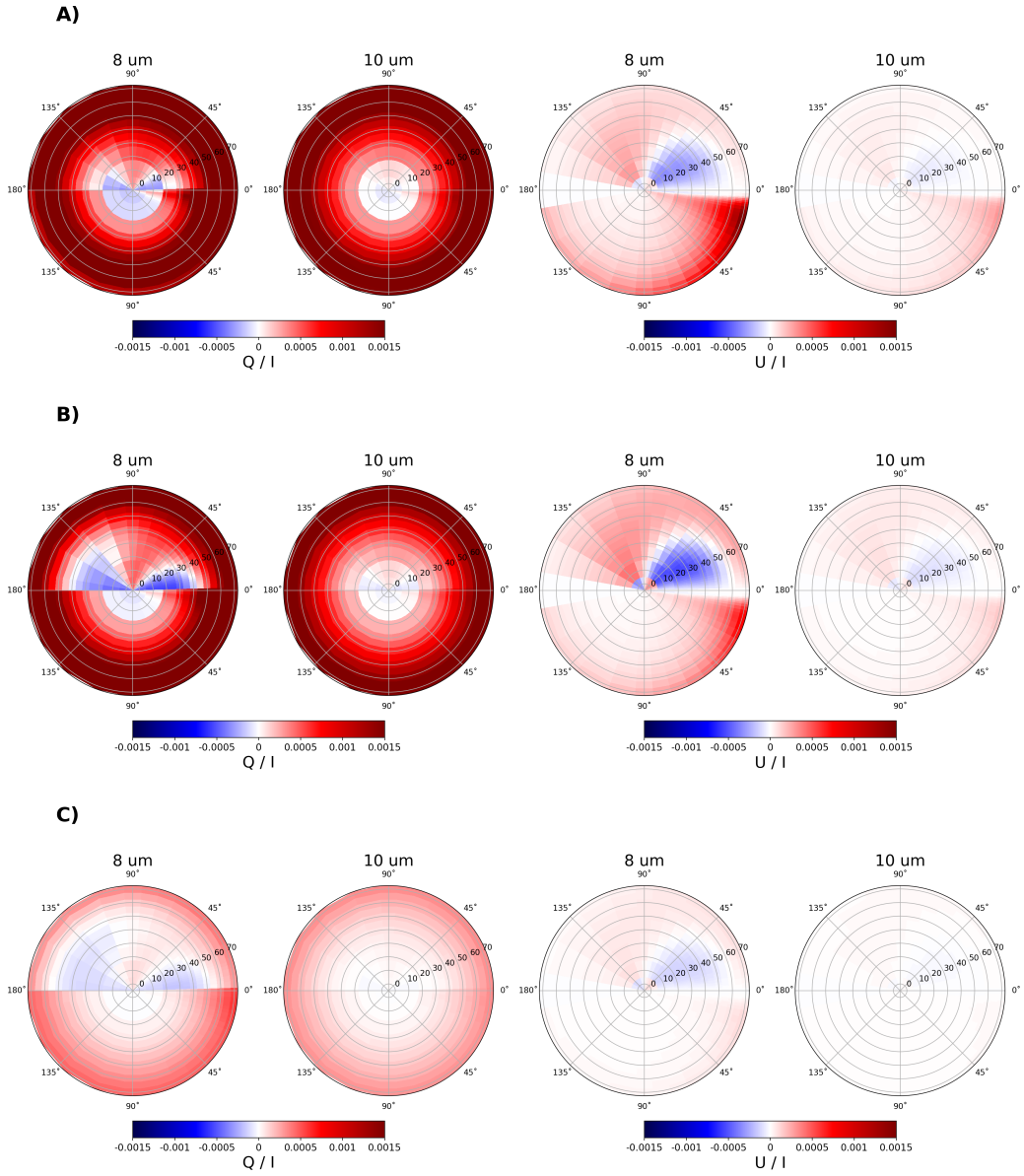

Figure 4.10: Q and U radiance components normalized by I at 8 and 10 μm for different aerosol loads. Panels A), B) and C) corresponds to AOD equal to 1.5, 0.5 and 0.05, in this example the GOD is fixed to 0.5 for all of them. Upper part of the polar plots corresponds to downward radiation (ground-based like geometry) and lower part to upward radiation (satellite-like geometry).

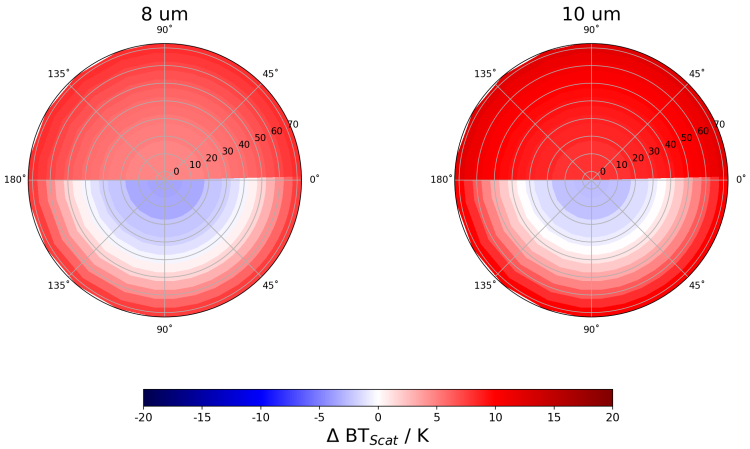

Figure 4.11: Absolute difference of radiance, expressed in terms of brightness temperature, for full GRASP SOS RT solution and the solution in first order approximation (ΔBT_{Scat} = Full RT − SS) at 8 and 10 μm, for an atmosphere with medium aerosol load (AOD=0.5 and GOD = 0.5) and a solar zenith angle of 60°. Upper part of the polar plots corresponds to downward radiation (ground-based like geometry) and lower part to upward radiation (satellite-like geometry).

Figure 4.11 shows the brightness temperature differences obtained in the full RT solution and in the first order approximation (ΔBT_{Scat} = Full RT − SS). Here the calculations were done for an atmosphere with equal aerosol and gas optical depths (AOD = 0.5 and GOD = 0.5). As it can be appreciated, despite the emission is originated in first order approximation of RT solution, the multiple scattering effects cannot be neglected for an accurate radiance computation. This multiple scattering effect is much more noticeable in ground-based geometries, where a maximum difference of 20 K can be found; whereas in the case of satellite, the strong influence of the surface diminishes these differences.

4.7 References

Blumstein, D., Chalon, G., Carlier, T., Buil, C., Hebert, P., Maciaszek, T., Ponce, G., Phulpin, T., Tournier, B., Simeoni, D., et al. (2004). Iasi instrument: Technical overview and measured performances. In *Infrared Spaceborne Remote Sensing XII*, volume 5543, pages 196–207. International Society for Optics and Photonics.

Bohren, C. F. and Huffman, D. R. (2008). *Absorption and scattering of light by small particles*. John Wiley & Sons.

Brogniez, G., Pietras, C., Legrand, M., Dubuisson, P., and Haeffelin, M. (2003). A high-accuracy multiwavelength radiometer for in situ measurements in the thermal infrared. part ii: Behavior in field experiments. *Journal of Atmospheric and Oceanic Technology*, 20(7):1023–1033.

Buras, R., Dowling, T., and Emde, C. (2011). New secondary-scattering correction in disort with increased efficiency for forward scattering. *Journal of Quantitative Spectroscopy and Radiative Transfer*, 112(12):2028–2034.

Chandrasekhar, S. (1960). Radiative transfer.

Doppler, L., Carbajal-Henken, C., Pelon, J., Ravetta, F., and Fischer, J. (2014). Extension of radiative transfer code momo, matrix-operator model to the thermal infrared–clear air validation by comparison to rttov and application to calipso-iir. *Journal of Quantitative Spectroscopy and Radiative Transfer*, 144:49–67.

Dubovik, O., Fuertes, D., Litvinov, P., Lopatin, A., Lapyonok, T., Doubovik, I., Xu, F., Ducos, F., Chen, C., Torres, B., Derimian, Y., Li, L., Herreras-Giralda, M., Herrera, M., Karol, Y., Matar, C., Schuster, G. L., Espinosa, R., Puthukkudy, A., Li, Z., Fischer, J., Preusker, R., Cuesta, J., Kreuter, A., Cede, A., Aspetsberger, M., Marth, D., Bindreiter, L., Hangler, A., Lanzinger, V., Holter, C., and Federspiel, C. (2021). A comprehensive description of multi-term lsm for applying multiple a priori constraints in problems of atmospheric remote sensing: Grasp algorithm, concept, and applications. *Frontiers in Remote Sensing*, 2:23.

Dubuisson, P., Giraud, V., Chomette, O., Chepfer, H., and Pelon, J. (2005). Fast radiative transfer modeling for infrared imaging radiometry. *Journal of Quantitative Spectroscopy and Radiative Transfer*, 95(2):201–220.

Fell, F. and Fischer, J. (2001). Numerical simulation of the light field in the atmosphere–ocean system using the matrix-operator method. *Journal of Quantitative Spectroscopy and Radiative Transfer*, 69(3):351–388.

Garnier, A., Pelon, J., Dubuisson, P., Faivre, M., Chomette, O., Pascal, N., and Kratz, D. P. (2012). Retrieval of cloud properties using calipso imaging infrared radiometer. part i: effective emissivity and optical depth. *Journal of Applied Meteorology and Climatology*, 51(7):1407–1425.

Hansen, J. E. and Travis, L. D. (1974). Light scattering in planetary atmospheres. *Space science reviews*, 16(4):527–610.

Hilton, F., Armante, R., August, T., Barnet, C., Bouchard, A., Camy-Peyret, C., Capelle, V., Clarisse, L., Clerbaux, C., Coheur, P.-F., et al. (2012). Hyperspectral earth observation from iasi: Five years of accomplishments. *Bulletin of the American Meteorological Society*, 93(3):347–370.

Hovenier, J. W., Van der Mee, C. V., and Domke, H. (2004). *Transfer of polarized light in planetary atmospheres: basic concepts and practical methods*, volume 318. Springer Science & Business Media.

Kirchhoff, G. (1978). Über das verhältnis zwischen dem emissionsvermögen und dem absorptionsvermögen der körper für wärme und licht. In *Von Kirchhoff bis Planck*, pages 131–151. Springer.

Kotchenova, S. Y., Vermote, E. F., Matarrese, R., and Klemm Jr, F. J. (2006). Validation of a vector version of the 6s radiative transfer code for atmospheric correction of satellite data. part i: Path radiance. *Applied optics*, 45(26):6762–6774.

Kylling, A. and Stamnes, K. (1992). Efficient yet accurate solution of the linear transport equation in the presence of internal sources: The exponential-linear-in-depth approximation. *Journal of Computational Physics*, 102(2):265–276.

Legrand, M., Pietras, C., Brogniez, G., Haeffelin, M., Abuhassan, N. K., and Sicard, M. (2000). A high-accuracy multiwavelength radiometer for in situ measurements in the thermal infrared. part i: Characterization of the instrument. *Journal of atmospheric and oceanic technology*, 17(9):1203–1214.

Lenoble, J., Herman, M., Deuzé, J., Lafrance, B., Santer, R., and Tanré, D. (2007). A successive order of scattering code for solving the vector equation of transfer in the earth's atmosphere with aerosols. *Journal of Quantitative Spectroscopy and Radiative Transfer*, 107(3):479–507.

Liou, K.-N. (2002). *An introduction to atmospheric radiation*. Elsevier.

Litvinov, P., Hasekamp, O., Dubovik, O., and Cairns, B. (2012). Model for land surface reflectance treatment: Physical derivation, application for bare soil and evaluation on airborne and satellite measurements. *Journal of Quantitative Spectroscopy and Radiative Transfer*, 113(16):2023–2039.

Lopatin, A., Dubovik, O., Fuertes, D., Stenchikov, G., Lapyonok, T., Veselovskii, I., Wienhold, F. G., Shevchenko, I., Hu, Q., and Parajuli, S. (2021). Synergy processing of diverse ground-based remote sensing and in situ data using the grasp algorithm: applications to radiometer, lidar and radiosonde observations. *Atmospheric Measurement Techniques*, 14(3):2575–2614.

Mishchenko, M., Travis, and L Lacis, A. (2006). *Radiative transfer and coherent backscattering*. Cambridge: Cambridge University Press.

Plass, G. N., Kattawar, G. W., and Catchings, F. E. (1973). Matrix operator theory of radiative transfer. 1: Rayleigh scattering. *Applied Optics*, 12(2):314–329.

Rothman, L. S., Gordon, I. E., Barbe, A., Benner, D. C., Bernath, P. F., Birk, M., Boudon, V., Brown, L. R., Campargue, A., Champion, J.-P., et al. (2009). The hitran 2008 molecular spectroscopic database. *Journal of Quantitative Spectroscopy and Radiative Transfer*, 110(9-10):533–572.

Rozanov, V. V., Diebel, D., Spurr, R., and Burrows, J. (1997). Gometran: A radiative transfer model for the satellite project gome, the plane-parallel version. *Journal of Geophysical Research: Atmospheres*, 102(D14):16683–16695.

Saunders, R., Hocking, J., Turner, E., Rayer, P., Rundle, D., Brunel, P., Vidot, J., Roquet, P., Matricardi, M., Geer, A., et al. (2018). An update on the rttov fast radiative transfer model (currently at version 12). *Geoscientific Model Development*, 11(7):2717–2737.

Saunders, R., Matricardi, M., and Brunel, P. (1999a). *A fast radiative transfer model for assimilation of satellite radiance observations-RTTOV-5*. ECMWF Reading, UK.

Saunders, R., Matricardi, M., and Brunel, P. (1999b). An improved fast radiative transfer model for assimilation of satellite radiance observations. *Quarterly Journal of the Royal Meteorological Society*, 125(556):1407–1425.

Snyder, W. C. and Wan, Z. (1998). Brdf models to predict spectral reflectance and emissivity in the thermal infrared. *IEEE Transactions on Geoscience and remote Sensing*, 36(1):214–225.

Sokolik, I. N. and Toon, O. B. (1999). Incorporation of mineralogical composition into models of the radiative properties of mineral aerosol from uv to ir wavelengths. *Journal of Geophysical Research: Atmospheres*, 104(D8):9423–9444.

Sokolik, I. N., Toon, O. B., and Bergstrom, R. W. (1998). Modeling the radiative characteristics of airborne mineral aerosols at infrared wavelengths. *Journal of Geophysical Research: Atmospheres*, 103(D8):8813–8826.

Stamnes, K., Tsay, S.-C., Wiscombe, W., and Jayaweera, K. (1988). Numerically stable algorithm for discrete-ordinate-method radiative transfer in multiple scattering and emitting layered media. *Applied optics*, 27(12):2502–2509.

Takano, Y. and Liou, K.-N. (1992). Infrared polarization signature from cirrus clouds. *Applied optics*, 31(12):1916–1919.

Van de Hulst, H. (1957). Light scattering by small particles john wiley & sons. *Inc., New York*, 470.

Van de Hulst, H. (1963). A new look at multiple scattering, techn. *Rept, Inst. Space Studies, NASA, New York*.

Wiscombe, W. (1977). The delta–m method: Rapid yet accurate radiative flux calculations for strongly asymmetric phase functions. *Journal of the atmospheric sciences*, 34(9):1408–1422.

Zhai, P.-W., Hu, Y., Trepte, C. R., and Lucker, P. L. (2009). A vector radiative transfer model for coupled atmosphere and ocean systems based on successive order of scattering method. *Optics express*, 17(4):2057–2079.

Chapter 5

Aerosol dust modeling complexity limits for remote sensing in TIR spectral range

Bueno, pues ya soy CAE mastera.

Fernando Martínez García

The aerosol model representation in remote sensing algorithms has a high importance and can be a complex procedure that involves numerous parameters. Depending on the measurement technique or the application, different approaches can be taken to represent particles and their properties. The scattering codes, as the ones based on Mie theory or T-Matrix, enable to link the optical and microphysical properties (particle size distribution, shape, refractive index, etc.) of the aerosols with their corresponding scattering properties (extinction, absorption, Single Scattering Albedo (SSA), etc.). How to properly account for the optical and microphysical properties of aerosols to obtain scattering properties representative enough of the real particles has been extensively studied for applications in the solar spectrum. However, the important differences between the main interactions related to the solar and thermal infrared spectra lead to changes in the importance of the different elements involved in the modeling. This chapter presents the efforts on adapting and optimizing the aerosol optical and microphysical modeling in the solar spectrum to the requirements of the thermal infrared range in terms of accuracy and computational efficiency.

5.1 Aerosol Refractive Index in Thermal Infrared

The refractive index is the aerosol optical characteristic in the TIR spectral range most present in the scientific literature. The data corresponding to refractive indexes of a wide variety of materials is publicly available in different spectroscopic databases as: GEISA (Gestion et Étude des Informations Spectroscopiques Atmosphériques) (Jacquinet-Husson et al., 2011), OPAC (Optical Properties of Aerosols and Clouds) (Hess et al., 1998), ARIA (Aerosol Refractive Index Archive) (Grainger D, 2021), GADS (Global Aerosol Data Set) (Koepke et al., 1997) or HITRAN (HIgh-resolution TRANsmission molecular absorption database) (Massie (1994), Massie and Goldman (2003), Rothman and Gordon (2013)). Most of the examples cited here cover a wide spectral range, in some cases from UV to the end of TIR. However, in general, they do not present a high spectral resolution.

The spectroscopic databases mentioned above contain a vast amount of information corresponding to different species, authors and measurements techniques. This information is valuable for a large range of applications. It is possible to find optical characteristics of chemical components related to: metals, rocks and conglomerates, or even components related to specific industrial processes (like diesel, acids, or different organic compounds). Sometimes it is very important to analyze the characteristics of each dataset in order to properly adapt it to a specific purpose. For some species there is crucial information that must be carefully treated, for example: the origin, the formation processes or the thermodynamic conditions of the material. In our case, this detailed data, which normally corre-

sponds to laboratory conditions, presents a variability far beyond the detection limit of remote sensing. In fact, if inversion algorithms are provided with measurements whose sensitivity is not enough, serious problems in terms of finding satisfactory solutions can be encountered. Thus, the species present in the already mentioned spectroscopic databases should be rather regrouped by similar optical and chemical characteristics. However, the simplified representation of aerosol components does not only address the sensitivity requirements of the remote sensing applications, but may also generalize the methodology and results to match with interests of other fields.

TIR spectral range extends up to 40 μm. However, as the scope of the presented work is the remote sensing of aerosols, only the wavelengths of the atmospheric window between 9 and 14 μm are considered here. Although the atmospheric aerosols present quite a large variability of microphysical and spectral characteristics, the long-wave TIR radiation is more sensitive to coarse mode particles. One of the major contributors to global aerosol coarse mode is desert dust (Textor et al. (2006), Tsigaridis et al. (2006), Gassó et al. (2010), Yu et al. (2012)). Thus, the refractive index of mineral dust is therefore in the scope hereafter.

Despite the high variability of the aerosol mineral dust composition over the globe (Claquin et al. (1999), Journet et al. (2014), Di Biagio et al. (2017)), there are only a few species that present main dust fractions in the vast majority of cases. Moreover, several species present similarity in terms of spectral complex refractive index. A summary of references reporting the refractive index of the main species conforming atmospheric aerosols can be found in table 5.1.

Specie	References
Quartz	Spitzer and Kleinman (1961)
	Longtin et al. (1988)
	Henning and Mutschke (1997)
	Zolotarev (2009)
Silicate clays	Querry (1987)
	Glotch and Rossman (2009)
Calcite	Long et al. (1993)
	Lane (1999)
	Posch et al. (2007)
Iron Oxides	Querry (1987)
	Marra et al. (2005)
	Glotch and Rossman (2009)
Water	Volz (1972)
	Ray (1972)
	Downing and Williams (1975)
	Kou et al. (1993)
	Warren and Brandt (2008)
Ammonium Sulfate	Toon et al. (1976)
	Longtin et al. (1988)
	Earle et al. (2006)
Soot	Shettle and Fenn (1979)
	Querry (1987)
	Chang and Charalampopoulos (1990)
	Bond and Bergstrom (2006)
Brown Carbon	Shettle and Fenn (1979)
	Sun et al. (2007)
Brown Carbon	Volz (1972)
	Volz (1973)
	Shettle and Fenn (1979)

Table 5.1: References for the refractive index of some of the main atmospheric aerosol components.

The refractive indices of the aerosol components considered in this work can be found in figure 5.1. Left panel of figure 5.1 presents the atmospheric aerosol species that can be retrieved by GRASP components algorithm in the solar spectrum (Li et al., 2019), while the right panel shows an extension of refractive indices of the same species for the TIR spectral range. It should be emphasized that the refractive indices of different aerosol mineral dust components (Quartz, clays and Calcite) in TIR are clearly distinguishable, while nearly identical in solar spectrum. The possibility of distinguishing and

retrieval of aerosol components, except for the different elements of mineral dust, was tested in detail in the work of Li et al. (2019). The current work is now focused on a deep analysis of the dust components retrievals in order to find a balance between complexity and applicability to the proposed retrieval scheme.

Quartz (figures 5.2 and 5.3, panels top-left) is a uniaxial birefringent material that normally is found in the atmosphere in crystalline form. Some studies suggest that depending on the processes suffered by the Quartz particles when they are injected in the atmosphere, it is also possible to find it in amorphous form (Reed et al., 2017). However, the expected ratio between amorphous and crystalline forms is not significant for the applications of interest here. Thus, here only crystalline form will be assumed from now on. The birefringent nature of the Quartz raises a similar question about the ratio between the ordinary and the extraordinary parts that is present in this material. The ordinary/extraordinary ratio depends on multiple factors, origins and conditions. Inside the remote sensing community, there is a standard assumed ratio which consists in 2/3 of ordinary Quartz and 1/3 of the extraordinary part (Hudson et al. (2008), Alexander et al. (2013), Reed et al. (2017)). From now on, the term "Quartz" will be used to refer to this volume weighted internal mixture of the two parts (Querry, 1987).

Some examples of the refractive indexes of silicate clay materials can be seen in figure 5.2 and 5.3 (panels top-right): Kaolinite, Illite and Montmorillonite. In other contexts, these clay materials are perfectly distinguishable, because of their chemical properties or the geographical different soils which are sources of these materials (Journet et al., 2014). Despite the relatively high differences in refractive index between them that can be found in specific spectral bands (like around 11 μm), here from now on, these three species will be accounted as a single volume weighted internal mixture referred to as "clays". The refractive index of clays that will be referred from now on can be seen in figure 5.1. This internal mixture is formed by a combination of three species with the following volume fractions: 40% Kaolinite, 40% Illite and 20% Montmorillonite. These proportions are based on climatological studies (Caquineau et al. (1998), Claquin et al. (1999)).

There is plenty of information about water (figure 5.2 and 5.3, panels bottom-left) at different temperature conditions in the spectroscopic databases. However, the temperature introduces only relatively small differences to the refractive index. Therefore, a fixed model for water is assumed here. In addition, it should be noted that the vertical distribution of aerosol water and its corresponding temperature is not well known to be properly considered. Furthermore, the pure water as an aerosol component practically does not exist in the atmosphere. Water soluble components are defined by a vast variety of chemical elements, as for example: Ammonium Nitrate, Ammonium Sulfate or other different salts. However, here all of them are grouped as a single aerosol group which will represent the mixture of pure water and the soluble components. It will be referred to as "solubles". The full spectral range from solar to TIR has been covered using data corresponding to Volz (1972), Volz (1973) and Shettle and Fenn (1979).

Carbon-like and soot particles (figure 5.2 and 5.3, panels bottom-left) cover an extremely wide range of chemical components that leads to important differences in the refractive index. However, the origin of these differences can be also related to extremely specific factors, as for example the thermodynamic formation conditions of these particles. The vast variety of aerosol types and atmospheric conditions measured in remote sensing contexts lead one to consider more general components usually called "Black Carbon" or "Brown Carbon". Despite the loss of accuracy implied in these simplifications which gather an extensive group of different chemical components, this methodology enables a much broader range of application. However, in the scientific community it is not clear how to classify these species and what optical properties should be attributed to them (Kirchstetter et al. (2004), Sun et al. (2007), Moosmüller et al. (2009), Andreae and Gelencsér (2006), Chen and Bond (2010)). Here, the Brown Carbon refractive index for solar spectrum is taken from Sun et al. (2007), and for the thermal infrared the organic insoluble species from Shettle and Fenn (1979) were selected. For Black Carbon, the values provided by Bond and Bergstrom (2006) are taken for the solar spectrum, and a mixture of three kinds of Diesel and one of soot in equal parts from Querry (1987) and Shettle and Fenn (1979) have been selected to complete the TIR part of the spectrum.

Calcite is a calcium carbonate material which is commonly found as a component of aerosol mineral dust. As in the case of Quartz, Calcite also presents a birefringent behavior. However, the impact of this birefringence on the refractive index is much smaller than in the case of Quartz. The values of Posch et al. (2007) were selected to represent Calcite in this work as an internal volume weighted mixture of equal proportions of the ordinary and extraordinary parts.

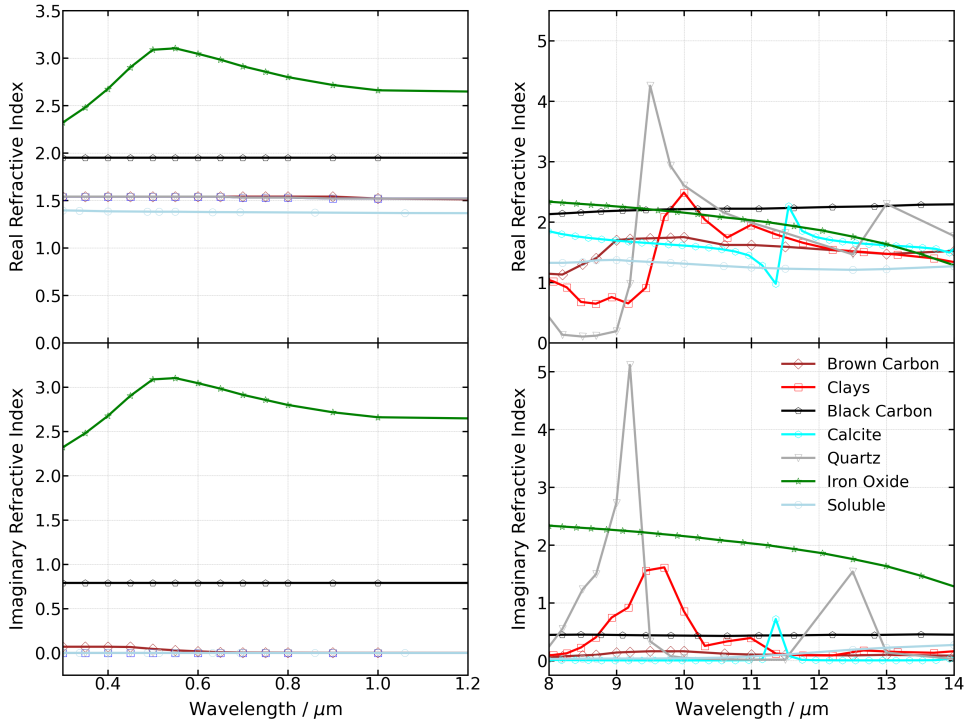

Figure 5.1: Refractive index of aerosol components retrieved by GRASP components approach for solar (left panel, Li et al. (2019)) and thermal infrared (right panel) spectral ranges.

The strategy employed for the iron oxides refractive index selection is similar to the case of selection for clays and carbonaceous aerosols. That is, several chemical species with close optical characteristics are represented by one value, while the variety represents the uncertainty. Specifically, among iron oxides are: Hematite, Goethite and Magnemite ((Lafon et al., 2006), Lázaro et al. (2008), Kandler et al. (2009), Shi et al. (2011)) and while in another application they could be distinguishable, the spectral resolution considered here is a limiting factor. The iron oxide in this work is represented by Hematite (Querry, 1987) as it is one of the most common species for this component in atmospheric studies (Journet et al., 2014).

5.2 Aerosol Scattering properties in Thermal Infrared

The main factors driving the modeling of the interaction between radiation and the atmosphere in the solar and thermal infrared spectra present significant differences. The Sun position geometry establishes a privileged direction for light propagation, which is the reference to define the scattering angles. Thus, the directional behavior is a crucially important factor in the studies of solar light scattering. Therefore, a lot of effort is devoted to the understanding and modelization of Phase Matrix and Scattering coefficients in studies centered around interactions in the solar spectrum (Koepke and Hess (1988), Mishchenko et al. (1997), Dubovik et al. (2002)). On the other hand, the TIR radiation has significantly lower influence of the scattering signal and angular dependence. The main source of radiation is the Earth's surface and the atmosphere itself. In realistic conditions, the three-dimensionality of the atmosphere could also introduce privileged directions of scattering, mainly due to clouds, because aerosols and gasses tend to be more homogeneous. However, in remote sensing, especially if it is orientated to aerosols, the assumption of horizontal homogeneity is almost universal within the scientific community. Thus, under this assumption, the directional behavior that has importance in TIR is mainly related to the zenith angle or basically to the air mass. The optical path is thus directly related to the zenith angle and the relative weight of each atmospheric component in the total radiance

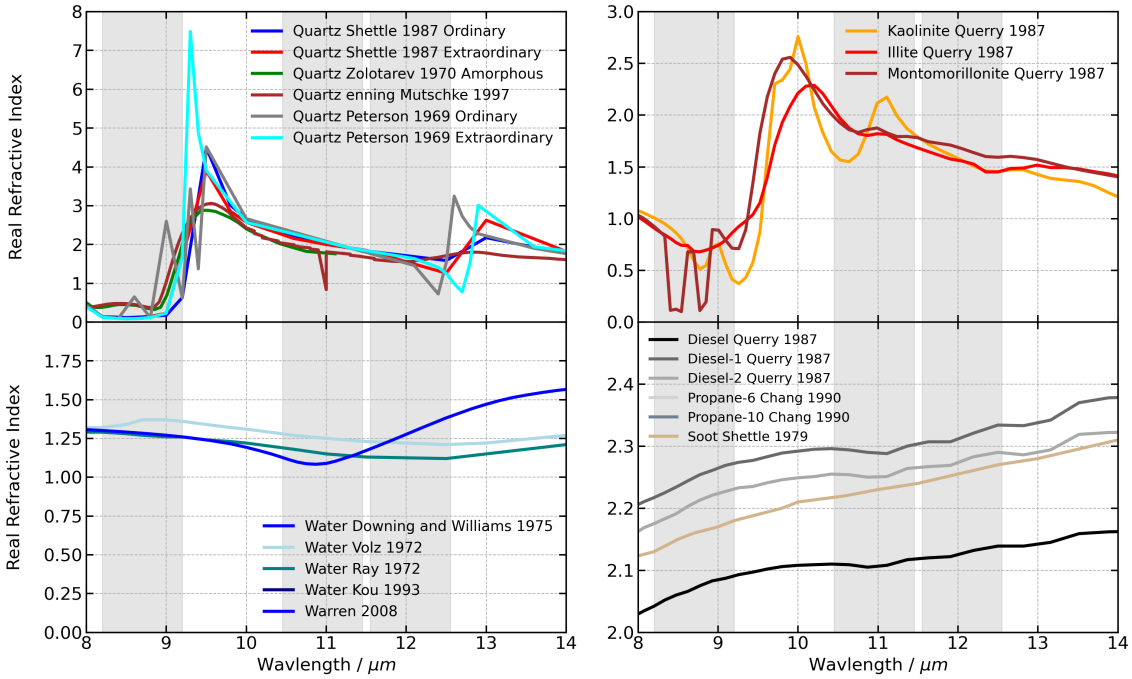

Figure 5.2: Comparison of the real refractive index of aerosol mineral dust of some of the main references found in the literature. The shaded grey areas indicate the most common spectral bands of remote sensing instruments at low spectral resolution.

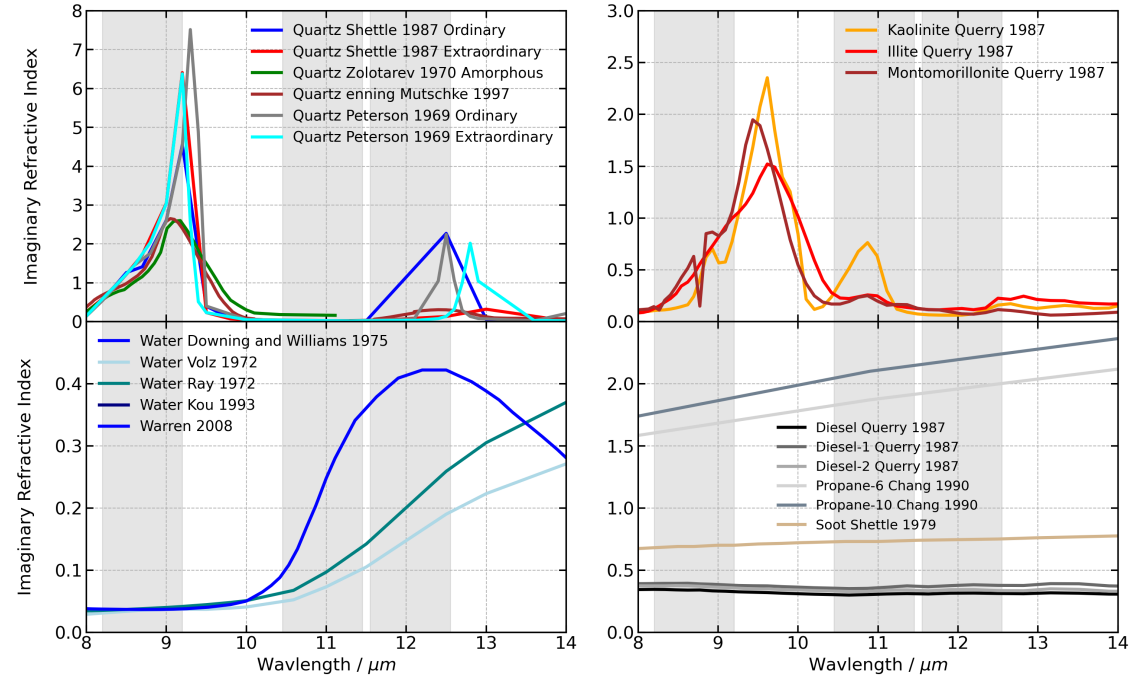

Figure 5.3: Comparison of the imaginary refractive index of aerosol mineral dust of some of the main references found in the literature. The shaded grey areas indicate the most common spectral bands of remote sensing instruments at low spectral resolution.

will change depending on their vertical distribution. It is important to note that this lack of directionality of radiation in TIR does not mean that multiple scattering effects could be neglected, as it also has been shown in the previous chapter of this thesis. Nevertheless, for the aerosol remote sensing purposes, the main attention has to be dedicated to the extinction and absorption coefficients.

Numerous examples on the characterization and modeling of mineral dust extinction coefficients are available in the literature (Hudson et al. (2008), Kleiber et al. (2009), Alexander et al. (2013), Klüser et al. (2015), Reed et al. (2017)). Some of them are focused on specific studies of mineral dust components (Hudson et al. (2008), Klüser et al. (2015), Reed et al. (2017)), while others take a more general approach analyzing real dust samples corresponding to different geographical areas (Alexander et al., 2013). Methodological differences can be appreciated in the aforementioned studies, such as different particle size distribution models, in-situ instrumentation, spectral bands or inversion algorithms to fit the non-measured aerosol properties. However, all of them focus on the discussion about the effect of aerosol shape as the most crucial element to properly reproduce the experimental measurements. The special accent that these studies put on the aerosol shape can be explained by the fact that the rest of the aerosol properties are better characterized, or present a lesser degree of complexity

In Hudson et al. (2008) different shape parameterizations like spheroids, needles or disks are analyzed. In that study it was concluded that the spheroid approach presents a better performance over the rest of the considered shapes. A similar conclusion was obtained in Nousiainen et al. (2006). On the other hand, Mogili et al. (2008) showed that whereas a spheroid like approximation was more appropriate to reproduce Quartz extinction features, the small clay particles are better approximated by a disk based model. However, due to the broader range of applicability with proper precision and its wider extension inside the scientific community, from now on this thesis will be restricted to work with spheroids.

The differences in the mineral dust extinction spectrum between spheres and spheroids present a complex behavior. While for many atmospheric aerosol chemical species the performance of Mie approximation in TIR is very satisfactory (Mie (1908), van de Hulst (1958), Wiscombe (1980), Bohren and Huffman (2008)), some significant differences can be found for some minerals in specific spectral regions. For example, this is the case of the Quartz Mass Extinction coefficient between 8 and 13 μm, e.g., see figure 8 of Reed et al. (2017). Common characteristics between Mie and spheroids can be observed in some parts of the spectrum, however, important overestimations of spheres extinction can be appreciated around 9 μm, where the spheroidal particles model is much better in comparison to the reference measurements. Similar results for pure Quartz can be found in Klüser et al. (2015). Moreover, in the former study, a slight positive bias in the spheroid extinction can be also observed over the complete considered spectral range. Even in the real dust samples studied by Alexander et al. (2013), figures 1, 2 and 3, it is clear to see that spheres present a shift to shorter wavelengths (higher wavenumbers) of the maximum extinction peak situated again around 9 μm (1100 cm^{-1}). For clay materials (as Kaolinite, Illite or Montmorillonite) the differences in observations also exist, however, are more attenuated compared to Quartz. Nevertheless, important differences for clays can appear in other spectral regions.

A common feature is that the extinction maximums and spheres-spheroids differences found in these spectra are related to increases in the refractive index. However, it should be clarified that the differences are not related to the refractive index peaks themselves, but with the phenomenon called "resonance" that appears for specific combinations of the real and imaginary refractive indices, e.g. see (Bohren and Huffman (2008), Chapter 12). The origin of resonance is related to the internal structure of the materials. For example, in the case of Quartz, its extinction maximum around 9 μm is originated by the fundamental asymmetric stretching vibrations of the Si–O bonds (Spitzer and Kleinman (1961), Reed et al. (2017)). A deep analysis of these processes is out of the scope of this work. However, in the following sections some general implications of these resonance phenomena will be addressed in the framework of the Mie theory.

In the case of spheroids, the description of resonances became significantly more complicated. As it was shown by Kostinski and Derimian (2020), for particles with an axial ratio different than 1, resonances can suppose increases of extinction up to two orders of magnitude for small changes in refractive index or shape parameter. However, the prediction of these resonances is complex and very dependent on the shape and size of the considered particles.

As it has been reported in the references discussed above, computations employing the nonspherical particles model is a common problem for both solar and TIR spectral range. In fact, the T-matrix

codes, normally used to calculate aerosol scattering properties for non-spherical particles, have convergence problems in the regime of large radius, which explains why some of the aforementioned studies are limited to a small particle range (Hudson et al. (2008), Mogili et al. (2008), Kostinski and Derimian (2020)). Moreover, these T-matrix methodologies present similar problems while dealing with high values of refractive index, which is the case for minerals in TIR.

Legrand et al. (2014) studied an alternative to overcome these problems optimizing the precision to correctly reproduce Quartz, Kaolinite and Illite extinction spectra in TIR, in addition to other scattering properties as the asymmetry factor and the SSA. These authors showed that it is possible to fill the problematic computational regimes of the T-matrix code using the Mie calculations with a margin error of 0.3%. At the same time, a more recent development of the T-matrix methodology (Bi et al., 2013) complemented with the geometrical optics approximation (Yang and Liou, 1996) may resolve the code convergence shortcoming for performing the scattering calculations in the full range of sizes, axis ratios or refractive indices needed for remote sensing applications.

Hitherto, all the scattering properties discussed here refer to a relatively wide integrated range of particle sizes. However, the approach of Hansell Jr et al. (2011) is slightly different. These authors are focused on the variation of extinction coefficients for the main mineral dust components as a function of the particle size. In the considered range of particle Volume Mean Diameter by Hansell Jr et al. (2011), which covers from 2 to 12 μm, it can be clearly appreciated that the changes in wavelength present a much higher influence on the extinction than changes in particle size. In order to properly interpret these results, it is important to note that a variation of wavelength implies both changes in size parameter and changes in refractive index. Thus, in general this higher dependency with the wavelength is expected. Attending the wavelength dependencies, abrupt changes of tendency in scattering properties can be found, like in the case of Quartz (around 9.2, 9.8, or 11.1 μm) or Gypsum (around 9.7 μm). However, for most of the scenarios considered in Hansell Jr et al. (2011), even significant increases in the particle diameter produce very smooth changes of extinction. Muscovite and Illite are the elements with the largest changes with Volume Mean Diameter. Therefore, the smooth dependency of dust extinction with particle size presented by Hansell Jr et al. (2011) enables us to extend the results shown by the previous authors to all bins of the corresponding particle size mode that they belong to. However, as it will be shown later, crucial differences can be appreciated between the behavior of fine and coarse particles.

An extension of some results offered by the aforementioned authors is going to be exposed in the next section. The objective of the following section is to provide complete support for the final results of this thesis, and for the methodological assumptions about aerosol modeling in the thermal infrared that have to be made to achieve them.

5.3 Aerosol modeling optimization in Thermal Infrared

The studies presented in the former section are purely theoretical or focused on the characterization of the materials in laboratory conditions with high resolution procedures (Spectrometers, particle counters, FTIR, etc.). These studies belong to high information content cases where aerosol modeling can be performed accurately using laboratory conditions providing nearly complete information on the aerosol/material microphysics and optics. However, even under these high information situations some of the applications need an inversion procedure in order to obtain aerosol characteristics such as the refractive index.

In lower information content cases, like often happens in remote sensing, the sensitivity to aerosol models significantly decreases. The over representation of aerosols in simulations can lead to excessive computation resources, which are very accentuated if non-spherical calculations are involved. In addition, for the aerosol properties, the knowledge of the aerosol characteristics with a significant sensitivity is crucial to optimize an already ill-posed problem as it is the remote sensing inversion. As it has been already said, comprehensive information to guide this optimization of aerosol modeling for inversion at UV, VIS and SWIR can extensively be found in the scientific literature (Yang and Liou (1996), Mishchenko et al. (1996), Mishchenko et al. (1997), Dubovik et al. (2002), Dubovik et al. (2006)).

This section aims to provide insights into the sensitivity to aerosol model characteristics in remote sensing contexts at the TIR spectral range. Three essential aspects will be covered such as the size, from fine to coarse mode, the effects of non-sphericity and the sensitivity to the mixing rule of aerosol

components. The final objective is to guide the optimization of the aerosol retrievals involving this spectral range and to optimize the calculation time of aerosol models for non-spherical particles. The models and techniques that are going to be used here are described in a lot of detail in studies particularly focused on each of them. However, the approach taken here is more specific, because it is going to be centered around the case of aerosol mineral dust modeling for remote sensing applications. This means that the focus is not going to be over the link and explanations between the observed behaviors and the mathematical formalism responsible for them. But rather it will be on the implications of the specific characteristics of mineral dust particles in the relation between the particle scattering properties and the aerosol model characteristics used to represent them.

The scattering calculations shown in this chapter have been done using a T-Matrix code called Invariant Imbedding T-Matrix IITM (Bi et al., 2013). This code will be used to perform all calculations to obtain the aerosol scattering properties starting from the corresponding microphysical and refractive index information.

5.3.1 Size. Influence over bins of AERONET Particle Size Distribution

Efficiency of radiation interaction with particles is highly influenced by the size parameter. In the Mie theory the relation between the scattering efficiency and the size parameter is well described and illustrated in literature. This section is focused on how an ensemble of sizes and integration over size bins influence the optical properties over solar and TIR spectral range.

The starting point will be the well established aerosol model characteristics used in AERONET retrievals (Dubovik and King (2000), Dubovik et al. (2002), Dubovik et al. (2006) and the GRASP algorithm (Dubovik et al. (2014), Lopatin et al. (2013), Li et al. (2019), Dubovik et al. (2021)) in the solar/SWIR spectrum. The sensitivity to the 22 bins particle size distribution in TIR has to be analyzed now for employing solar-TIR spectrum synergy. That is, extra bins in the coarse mode can be potentially included expecting higher sensitivity of TIR to large particles, e.g. extension up to 30 μm.

Figure 5.4 shows the extinction cross sections for pure Quartz and clays corresponding to each size bin calculated for three different axial ratios (ϵ = 1, 2 and 3) and at 4 different wavelengths, one at the solar spectrum and three at the TIR: λ = 0.5, 9.1, 11, 12 and 13 μm. As it was expected, the TIR wavelengths present a higher efficiency to interact with coarse mode particles in comparison with the chosen reference wavelength in the solar spectrum. However, the fine mode bins are almost totally invisible for these long wavelengths, but present a high sensitivity at 0.5 μm. Thus, it is clear that the solar wavelength presents a broader range of sensitivity to the particle size. At the same time, in comparison with the solar wavelengths which present a maximum efficiency around 1 or 2 μm in the coarse mode, the extinction cross sections calculated at the TIR range present these maximums around 3 or 4 μm. Thus, the inclusion of longer wavelengths could improve the information that can be obtained from the aerosol coarse mode. Nevertheless, the extinction efficiency of the TIR wavelengths at the last bins of the standard 22-bin particle size distribution remains low indicating that the current range of sizes accounts for the measurements sensitivity limits even if the TIR is included. Later in this thesis, a deeper study in terms of radiance of this sensitivity will be done. As it will be shown, the lack of a directional nature of TIR radiation in the atmosphere minimizes the particle size information that can be inferred from it.

It has to be clarified that figure 5.4 cannot be directly compared with the cross section as a function of the size parameter that is commonly presented in literature (e.g., Figure B1 of Kudo et al. (2021)). The reason is first of all, the width of the size bins that has been calculated logarithmically, this means that the bins centered in a bigger radius are broader than the bins corresponding to smaller particles. Thus, the tendencies introduced by the size parameter are more averaged compared to single particle calculations. On the other hand, here a change in the wavelength does not mean only a change in the size parameter, but also a change in the refractive index. Normally this kind of representations are done taking a constant value of the refractive index for all the considered wavelengths. Thus, it is possible that the changes in both parameters could compensate their effect over the extinction cross section. As it has been shown previously in this chapter, the refractive index of Quartz and clays is highly variable in TIR range. Thus, more complex tendencies are expected if both parameters (refractive index and size parameter) are changing at the same time.

It is to note that Quartz and clays do not present significant differences. In general, Quartz presents a higher extinction cross section in all sizes and axial ratios, with the exception of fine mode at 9.1 μm

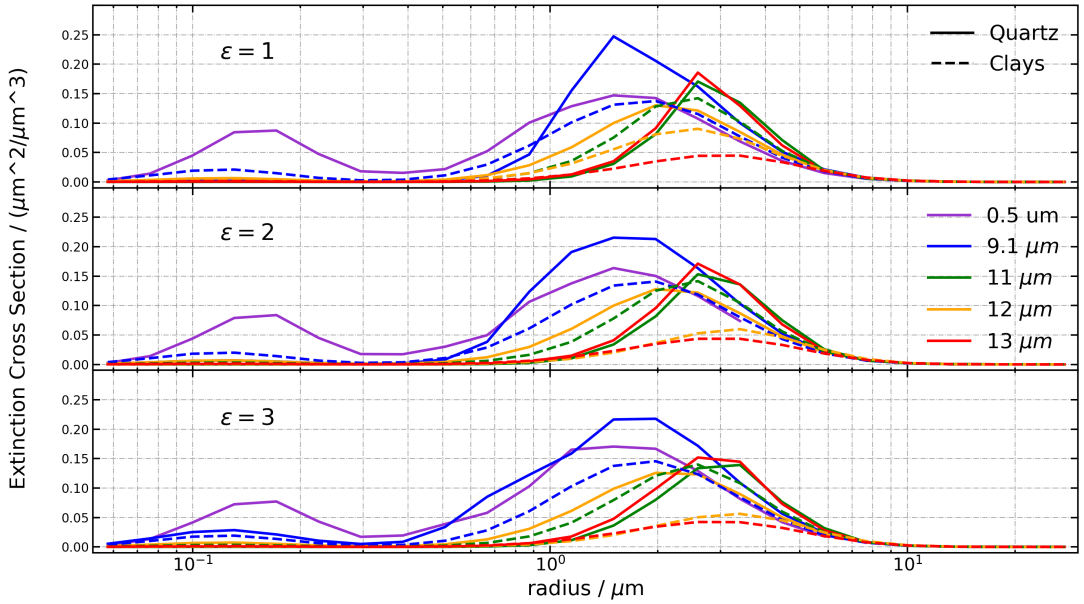

Figure 5.4: Quartz (solid line) and Clays (dashed line) Extinction cross section as a function of AERONET radius bins (plus 3 extra bins extended until 30 μm) at 4 wavelengths of TIR spectral range (9.1, 11, 12 and 13 μm) and one in visible (0.5 μm) for 3 different axial ratios (1,2,3).

for ϵ = 1 and 2, where clays have a higher extinction coefficient. The other remarkable difference between the two species is that the extinction maximums of Quartz are slightly shifted to bigger particles in comparison with clays. In the real atmosphere always a mixture of both species (among others not considered in this section) is going to be found, it is very rare to find atmospheric aerosols conformed purely by only one of these species. Thus, these observed differences are not very significant.

The variable refractive index of other species conforming atmospheric aerosols could present some important specific features which may affect the results shown above. The study of these aerosol components remains open for the future. However, the results corresponding to this section can be reasonably extrapolated to all aerosol mineral dust because of the elevated predominance of Quartz and clays in the global aerosol dust composition.

5.3.2 Shape. Influence of axis ratio

Different behavior of particle scattering properties as a function of the shape have been mentioned previously. More detailed description of the shape dependence features is presented hereafter.

Aerosol shape is a crucial factor to take into account because of two reasons: the complexity that it introduces and the extreme computation time increase that is associated with it. Thus, it is very important to know what limit of detail for particle shape should be achieved in order to reach a proper balance between accuracy and computing resources. The significant differences already shown between aerosol properties at solar and TIR spectra will also affect the requirements for proper accounting for particle shape.

Figure 5.5 shows the derivative of particle extinction cross sections as a function of axial ratio ($\frac{\Delta Ext}{\Delta \epsilon}$) for each of the bins of the particle size distribution shown in the previous section. This derivative has been obtained from the data in figure 5.4, i.e, the Y-axis of figure 5.5 has been calculated performing a linear interpolation between the extinction and the axial ratio corresponding to each bin of the panels of figure 5.4. Note that these derivatives represent only the selected particle shapes and the linear assumptions are taken to obtain a rough approximation of the behavior of the dependency of extinction with axial ratio. Nevertheless, this methodology is useful to compare the visible wavelength, for which the shape modeling has been deeply studied, with the behavior of this magnitude at the thermal in-

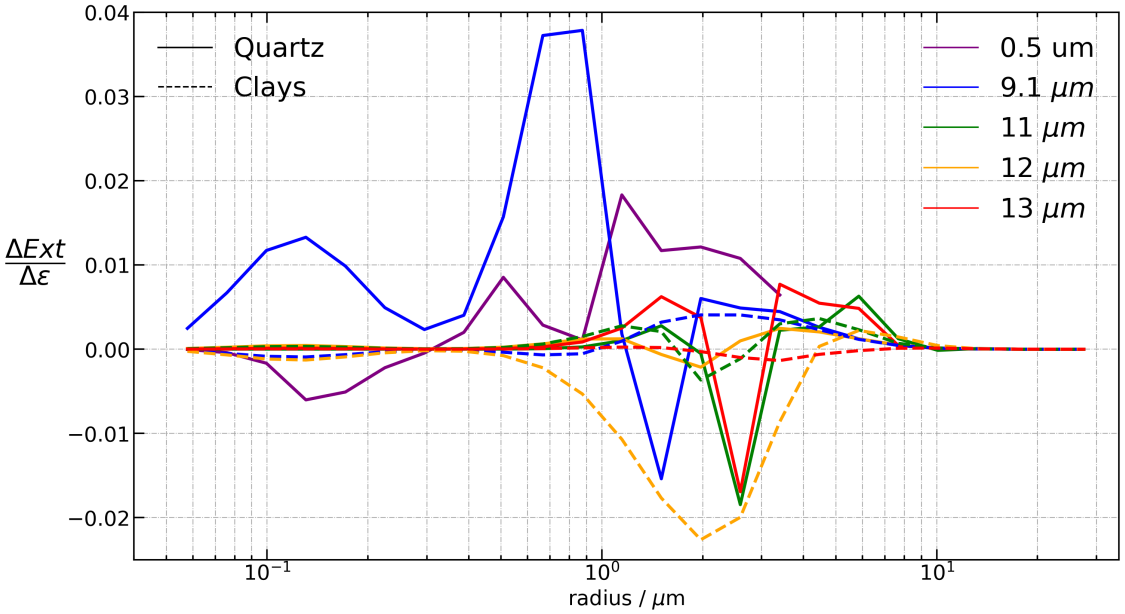

Figure 5.5: Extinction cross section derivative of axial ratio as a function of the particle size for the bins of the standard 22-bins AERONET like size distribution. The different colors correspond to wavelength (0.5, 9.1, 11, 12 and 13 μm), solid lines correspond to Quartz refractive index and the dashed lines to clays. The derivatives have been calculated performing a linear interpolation between the extinction and the corresponding axial ratio values of figure 5.4 for each size bin, the slope of this fitting is identified as the extinction derivative with respect to the axial ratio.

frared wavelengths. Thus, some general guidance is provided about the dependency of the extinction with a reasonable amount of calculations. However, in order to properly interpret this figure, it should be noted that geometrical factors implied in the increase of particle size are also present. Thus, the observed behavior cannot be fully attributed to shape.

The axial ratios ϵ = 1, 2 and 3, were used for this illustration. Note that an axis ratio of 3 is near the maximum assumed in the shape distributions more commonly used in the remote sensing community as proposed in Dubovik et al. (2006). These particle shape distributions are defined assuming that all possible orientations are equally represented. In addition to the illustration presented here where only prolates ($\epsilon \geqslant 1$) are used, it is also usually assumed that there are the same amount of oblate and prolate particles. Nevertheless, even if differences are expected between oblate and prolate particles, the simplification used here is not critical as aims only the illustration of the shape effect in TIR compared to solar wavelengths.

In the case of the chosen solar wavelength, coarse mode particles are more affected by the change of aerosol shape. It is clear to see how the increase of the axial ratio of the prolate spheroids studied here has an opposite effect in the particles of fine and coarse mode. In the case of fine mode, an increase of the axial ratio of aerosol prolate particles produces a decrease of the extinction. However, in the case of the dust coarse mode an increase in the axial ratio is also accompanied by an increase of the radiance for almost all size bins.

In the case of the thermal infrared wavelengths a different behavior can be observed. The wavelengths 11, 12 and 13 μm present common tendencies. The small changes in the fine mode of the extinction can be seen in its nearly zero dependence on the particle shape for the small size bins. In general the sensitivity to shape of coarse mode is neither very high. However, it can be clearly seen that for each wavelength there is a specific bin where the extinction presents a strong dependence on shape. Clays at 12 μm present by far the strongest dependence of extinction with axial ratio in the coarse mode among all considered cases.

Remarkable are the curves for the 9.1 μm wavelength. That is, the case of clays is significantly different from the case of Quartz and is quite different from the rest of the examples shown. The high

extinction dependence of shape and an important change of this dependence with the different size bins can be explained by the resonance effects of Quartz around this wavelength, as was earlier presented in this chapter. As it can be seen, Quartz extinction at 9.1 μm is much more sensitive to particle shape changes. Specially remarkable is the strong dependence of the fine mode, with an absolute magnitude that is not visible in any other proposed example. Furthermore, the effect of shape over the extinction even changes its sign for the bins centered around 1 μm.

At the sight of the strong simplifications done in this analysis the detailed behavior of the species accounted here should not be taken as a reference. However, it is reasonable to conclude that in thermal infrared spectral range mainly the coarse mode particles will present a significant extinction dependence with axial ratio. On the other hand, in resonance regions the effect of particle non-sphericity can be significant for all sizes and a more detailed description of the shape must be done in order to properly model aerosol scattering properties in these conditions.

5.3.3 Components mixing rule. Resonance effects

Hitherto in this section, the relation between aerosol microphysical characteristics with the corresponding scattering properties have been studied. However, there is another element in terms of aerosol modeling that has been previously mentioned but has not been analyzed in detail yet, the aerosol components mixing rule. Atmospheric aerosols are heterogeneous particles formed by the combination of different species. Very different approaches can be taken to model the combination of elements. In this section, the focus will be on the differences in the scattering properties introduced by the selection of different mixing rules. Three different methodologies have been selected: Maxwell-Garnett and Volume-Weighted internal mixtures, and External mixture. The mathematical details of each of these methods can be found elsewhere (Bohren and Huffman (2008), Li et al. (2019)). The Maxwell-Garnett and Volume-Weighted methodologies are employed to model internal mixtures, which means that a particle is constituted from different components and the effective refractive index of this particle is resulted from refractive indices of each component. In general, an often used assumption is that the particles in each aerosol mode have the same composition and only the size is different. However, in the approach taken in this thesis, following previous developments and sensitivity tests (Li et al., 2019), a different composition is allowed for particles corresponding to different size modes. In the case of the Volume-Weighted linear mixture, a weighted sum of the refractive indices of each component by its corresponding volume fraction is performed to obtain the effective value for the whole particle. The Maxwell-Garnett approach is more complex, in this case some species are considered to be the host and the rest of the components are taken as inclusions inside of it. The equation to obtain the refractive index is not based directly on a weighted sum of the refractive index but of the dielectric functions of the components:

$$\epsilon_m = \epsilon_h \left[1 + \frac{3 \sum_{i=1}^{N} f_i \frac{(\epsilon_i - \epsilon_h)}{(\epsilon_i + 2\epsilon_h)}}{1 - \sum_{i=1}^{N} f_i \frac{(\epsilon_i - \epsilon_h)}{(\epsilon_i + 2\epsilon_h)}} \right] \tag{5.1}$$

Where ϵ_h and ϵ_i are correspondingly the dielectric functions of the host and the inclusions, and f_i are the volume fractions of each component. Once, the average dielectric function for the mixture has been obtained, the corresponding refractive index can be calculated as follows:

$$\begin{aligned} m_r &= \sqrt{\frac{\sqrt{\epsilon_r^2 + \epsilon_i^2} + \epsilon_r}{2}} \\ m_i &= \sqrt{\frac{\sqrt{\epsilon_r^2 + \epsilon_i^2} - \epsilon_r}{2}} \end{aligned} \tag{5.2}$$

On the other hand, the assumed particle properties in the external mixture approach are different. In this case each particle is constituted from only one component. The amount of particles corresponding to each specie depends on the volume fractions. For the external mixture the volume fractions are applied directly over the scattering magnitudes, which means to perform a volume weighted linear sum over the phase matrix and the scattering, absorption and extinction coefficients, instead of doing it over the refractive index. In this kind of procedure the effective refractive index of the mixture remains unknown.

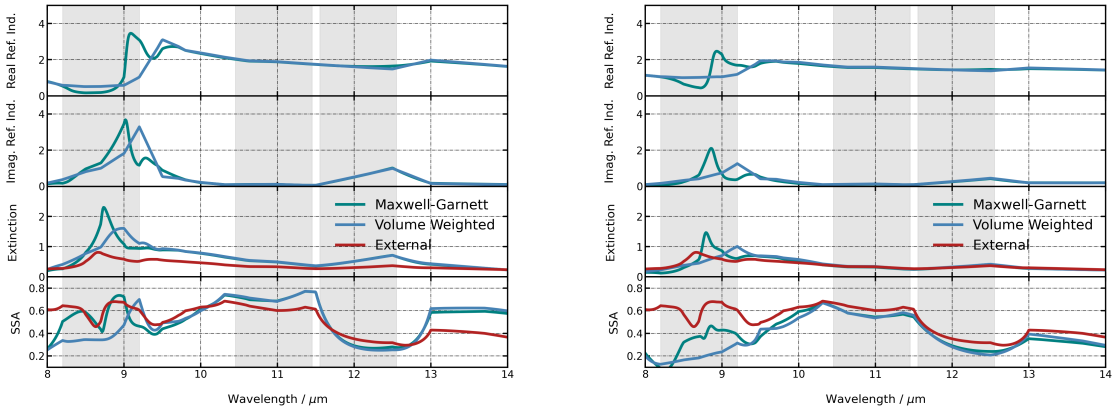

Figure 5.6: Comparison for the refractive indexes, extinction and Single Scattering Albedo for three different aerosol components mixing rules. Right panel corresponds to a dust-like mixture with a high Quartz content, the left panel corresponds to a low Quartz dust-like mixture.

In the previous section it was concluded that despite the effect of non-sphericity and outside of the resonance regions, the Mie theory can be indeed used for studies of aerosol characteristics at the thermal infrared spectral range. Thus, due to the amount of calculations needed for this analysis, all the results shown in this section are restricted to spheres. However, one has to keep in mind that some of the behaviors of the Mie regime are different from the non-spherical aerosol models.

Figure 5.6 shows the comparison of the refractive index, the Extinction cross section and the SSA of a dust-like aerosol model whose components have been mixed following the three aforementioned procedures. This means that the volume fractions of the different components and the particle size distributions are exactly the same, but the methodology used to obtain the effective refractive index (or the extinction in the case of the external mixture) is different. The effective refractive index of the external mixture is not shown in this figure, because the calculations to obtain the scattering properties with this mixture methodology are done directly with the scattering properties of each component, and there is no effective refractive index corresponding to this mixture procedure. The left panel corresponds to a dust-like model with a high amount of Quartz, and the right one to a mixture with a low amount of this component. The particle size distribution of both is the same, following the Solar-Village sample presented in Dubovik et al. (2002). The grey bands represent the three channels of the CLIMAT TIR radiometer.

In general, at the spectral range considered in figure 5.6, there are no significant differences among the three studied mixing methodologies, either in the refractive indexes or in the scattering properties. Namely, from 10 to 14 μm the refractive indices obtained by Maxwell-Garnett or by the internal Volume-Weighted methodology are almost identical. In terms of extinction or SSA similar conclusions can be done. At this spectral range the external mixture is the only methodology which presents significant discrepancies with the other two, especially for the SSA. While in the case of the low-Quartz mixture (right panel), an overestimation of this magnitude can be seen in comparison with the Volume-Weighted and the Maxwell-Garnett, when the amount of Quartz is increased (left panel), the SSA of the external mixture tends to underestimate the other two procedures.

However, these differences are very minor in comparison with what can be observed between 8 and 10 μm. At this spectral range dramatic differences can be observed among the three methodologies in the refractive index, extinction and SSA. However, these differences are attenuated in the case of the low-Quartz mixture. The maximums of both real and imaginary refractive index are shifted to higher wavelengths for the Volume-Weighted mixture in both panels, and an analogous behaviour can be appreciated in the case of extinction. For the SSA, in general a higher value is obtained for the Maxwell-Garnett methodology.

At the sight of figure 5.6 it is clear that the importance of the mixing methodology is not the same in the full TIR spectrum. Moreover, some significant differences can be found depending on the amount of Quartz contained in the mixture. In general the scattering properties obtained for the Maxwell-Garnett and the Volume-Weighted mixture are closer in comparison to the External one. However,

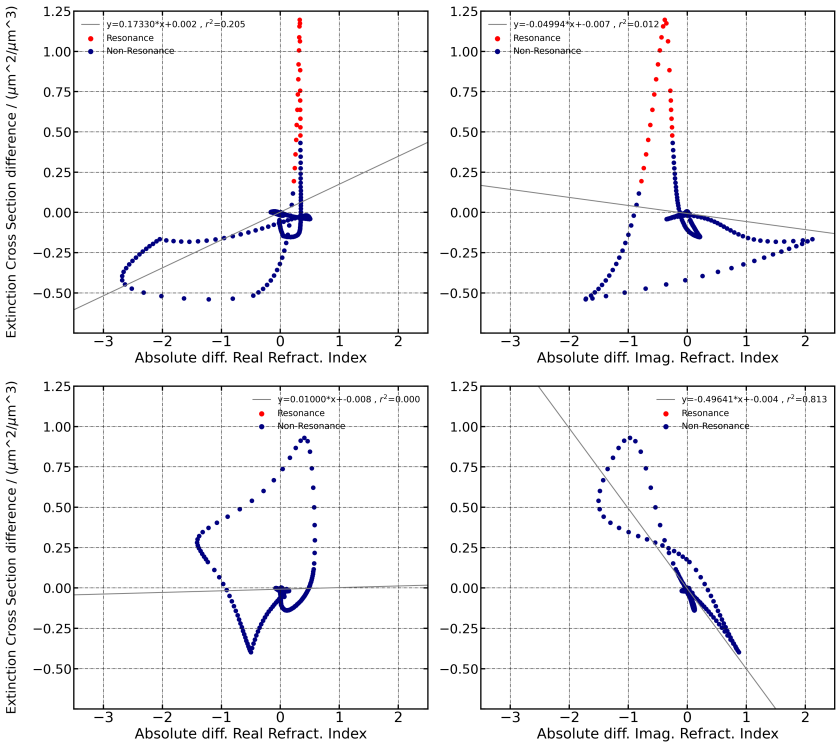

Figure 5.7: Differences in extinction cross sections obtained between Volume Weighted and Maxwell-Garnett aerosol components methodologies as a function of the corresponding differences in the real or imaginary refractive indexes. Top panels correspond to a high Quartz dust-like mixture and the bottom panels to low Quartz dust-like mixture.

there are two features that need to be analyzed in detail: the high variability of the scattering properties between 8 and 10 μm and why the reduction of Quartz means also a reduction of these differences. One could think about the high variability of the Quartz refractive index at this spectral range as the responsible for this behavior. However, the correlation between the variability of the refractive index of the different species forming the aerosol mixtures and the observed difference between the corresponding extinction (not shown) is almost zero. Furthermore, figure 5.7 shows the correlation between the extinction differences of Maxwell-Garnett and the Volume-Weighted mixtures as a function of the absolute differences between the effective refractive index obtained for each mixing methodology. Upper panels correspond to the high-Quartz mixture and the lower ones to the low-Quartz model. As it can be seen these correlations are also almost zero, except for the correlation between the imaginary part for the low-Quartz mixture. Thus, this means that the pure difference in the refractive index coming from the mixture methodologies are not enough to explain the observed differences in the extinction.

The Quartz resonances around 9 μm are responsible for these significant changes of extinction which are not associated with very large changes in the refractive index. Inside the resonance regions, small changes of the refractive index lead to strong changes in extinction. Thus, when the refractive index of the mixture is close to fall in this region, the small changes produced by the different mixing rules can cause crucial changes of the scattering properties due to the non-linearities introduced by the resonance.

In figure 5.7 the points inside these resonance regions are marked with a red dot. These points of resonance are clearly manifested for the mixture with a high amount of Quartz. The pronounced peaks in the two upper panels, which correspond to very moderated differences of both real and imaginary refractive index, are most of it inside the resonance region. Moreover, it is clear to see that when this phenomenon does not play a role, the difference between the extinction of the two mixing methodologies are very well explained by the differences of the imaginary refractive index (lower right panel). The real part of the refractive index appears to have almost no correlation with the extinction differences.

To establish the limits of the refractive index regions considered as resonances, the full range of possible refractive index for dust-like aerosols in this spectral range has been used to calculate the

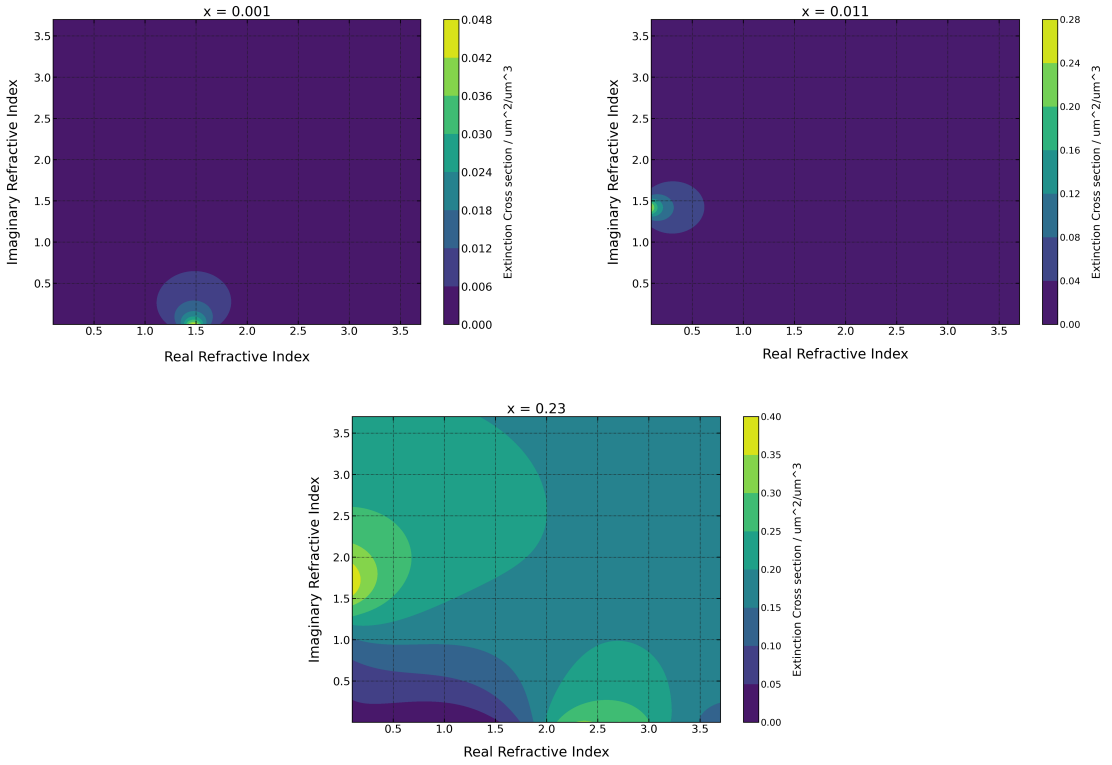

Figure 5.8: Particle extinction cross section for spheres as a function of the real and imaginary parts of the refractive index for a Rayleigh like regime (upper left panel), fine mode like particle (upper right panel) and coarse mode like particle (lower panel).

corresponding extinction. These extinction calculations can be seen in figure 5.8, where three different particle sizes have been selected: Rayleigh (upper left panel), fine (upper right panel) and coarse mode (lower panel).

The upper left corresponds to the Rayleigh regime, this means to consider really small particles in comparison with the wavelength. In this case a size parameter (χ) of 0.001 has been selected. For this particular example the extinction cross section has not been calculated with the Mie code directly, but following the approximation of Bohren and Huffman (2008) for this small particle regime. In particular the equations 5.7 and 5.8, which are the following:

$$Q_{\text{ext}} = 4x\text{Im}\left\{\frac{m^2-1}{m^2+2}\left[1+\frac{x^2}{15}\left(\frac{m^2-1}{m^2+2}\right)\frac{m^4+27m^2+38}{2m^2+3}\right]\right\}+\frac{8}{3}x^4\text{Re}\left\{\left(\frac{m^2-1}{m^2+2}\right)^2\right\} \tag{5.3}$$

$$Q_{\text{sca}} = \frac{8}{3}x^4\left\|\frac{m^2-1}{m^2+2}\right\|^2 \tag{5.4}$$

These equations are much more simple than the full Mie theory, but they can be very useful to understand some dependencies of this complex theory. However, in order to have precise enough results for bigger particles the full scattering theory for spherical particles has to be used. Comparing the three panels in figure 5.8, it can be seen that the three regimes count with a region of resonance. The case of fine mode is especially clear because this region is concentrated around a small range of refractive index values and with a significant increase of extinction. However, in the case of Rayleigh and coarse particles, despite the limits not so clear, the resonance regions can also be identified.

Remarkable is the change of position that the resonance region suffers between the Rayleigh and the other two regimes. In the top panel this resonance region is approximately centered around a value of the real part of the refractive index of 1.5 and a value of 0.1 for the imaginary part. While for the fine and coarse particles, we can find it centered around a value of 0.2 for the real part and 1.7 for the imaginary part.

In order to provide a deeper characterization of the dust scattering properties in the TIR spectral

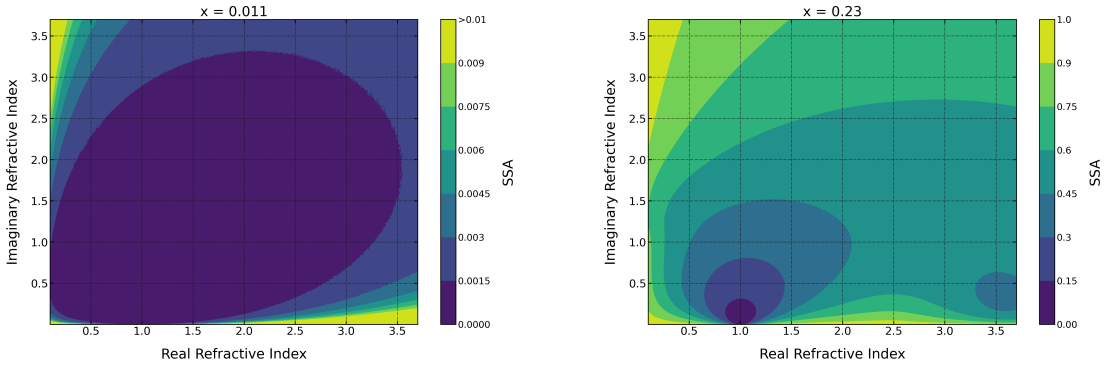

Figure 5.9: Single Scattering Albedo for spherical particles as a function of the real and imaginary parts of the refractive index for two size parameters x = 0.011 (left panel) and 0.23 (right panel) which can be associated with aerosol fine and coarse modes correspondingly in the TIR spectral range.

range, figure 5.9 shows the SSA corresponding to the calculations shown in figure 5.8 for the fine and coarse modes. In the case of the fine mode it is clear to see that the extinction is totally dominated by the absorption, and very small differences in SSA can be found even for high variations of refractive index. For the coarse mode particles this magnitude presents a much higher range of variability. There are regions dominated also by the absorption as the one centered in a real part of 1.0 and an imaginary part of 0.1. But there are others with a really elevated contribution to the scattering. However, none of the tendencies observed here can be associated with the resonance regions identified in figure 5.8.

As it can be seen in figure 5.8 there are some other tendencies and behaviors that cannot be explained because of the resonance phenomenon. Mie and mixing rules methodologies are complex and further analysis can be done to fully characterize the observed features. Nevertheless, the analysis sheds light on the reasons and possible discrepancies related to the aerosol mixing rule assumption for aerosol properties modeling in TIR.

5.4 References

Alexander, J. M., Laskina, O., Meland, B., Young, M. A., Grassian, V. H., and Kleiber, P. D. (2013). A combined laboratory and modeling study of the infrared extinction and visible light scattering properties of mineral dust aerosol. *Journal of Geophysical Research: Atmospheres*, 118(2):435–452.

Andreae, M. O. and Gelencsér, A. (2006). Black carbon or brown carbon? the nature of light-absorbing carbonaceous aerosols. *Atmospheric Chemistry and Physics*, 6(10):3131–3148.

Bi, L., Yang, P., Kattawar, G. W., and Mishchenko, M. I. (2013). Efficient implementation of the invariant imbedding t-matrix method and the separation of variables method applied to large nonspherical inhomogeneous particles. *Journal of Quantitative Spectroscopy and Radiative Transfer*, 116:169–183.

Bohren, C. F. and Huffman, D. R. (2008). *Absorption and scattering of light by small particles*. John Wiley & Sons.

Bond, T. C. and Bergstrom, R. W. (2006). Light absorption by carbonaceous particles: An investigative review. *Aerosol science and technology*, 40(1):27–67.

Caquineau, S., Gaudichet, A., Gomes, L., Magonthier, M.-C., and Chatenet, B. (1998). Saharan dust: Clay ratio as a relevant tracer to assess the origin of soil-derived aerosols. *Geophysical research letters*, 25(7):983–986.

Chang, H.-c. and Charalampopoulos, T. (1990). Determination of the wavelength dependence of refractive indices of flame soot. *Proceedings of the Royal Society of London. Series A: Mathematical and Physical Sciences*, 430(1880):577–591.

Chen, Y. and Bond, T. (2010). Light absorption by organic carbon from wood combustion. *Atmospheric Chemistry and Physics*, 10(4):1773–1787.

Claquin, T., Schulz, M., and Balkanski, Y. (1999). Modeling the mineralogy of atmospheric dust sources. *Journal of Geophysical Research: Atmospheres*, 104(D18):22243–22256.

Di Biagio, C., Formenti, P., Balkanski, Y., Caponi, L., Cazaunau, M., Pangui, E., Journet, E., Nowak, S., Caquineau, S., Andreae, M. O., et al. (2017). Global scale variability of the mineral dust long-wave refractive index: a new dataset of in situ measurements for climate modeling and remote sensing. *Atmospheric Chemistry and Physics*, 17(3):1901–1929.

Downing, H. D. and Williams, D. (1975). Optical constants of water in the infrared. *Journal of Geophysical Research*, 80(12):1656–1661.

Dubovik, O., Fuertes, D., Litvinov, P., Lopatin, A., Lapyonok, T., Doubovik, I., Xu, F., Ducos, F., Chen, C., Torres, B., Derimian, Y., Li, L., Herreras-Giralda, M., Herrera, M., Karol, Y., Matar, C., Schuster, G. L., Espinosa, R., Puthukkudy, A., Li, Z., Fischer, J., Preusker, R., Cuesta, J., Kreuter, A., Cede, A., Aspetsberger, M., Marth, D., Bindreiter, L., Hangler, A., Lanzinger, V., Holter, C., and Federspiel, C. (2021). A comprehensive description of multi-term lsm for applying multiple a priori constraints in problems of atmospheric remote sensing: Grasp algorithm, concept, and applications. *Frontiers in Remote Sensing*, 2:23.

Dubovik, O., Holben, B., Eck, T. F., Smirnov, A., Kaufman, Y. J., King, M. D., Tanré, D., and Slutsker, I. (2002). Variability of absorption and optical properties of key aerosol types observed in worldwide locations. *Journal of the atmospheric sciences*, 59(3):590–608.

Dubovik, O. and King, M. D. (2000). A flexible inversion algorithm for retrieval of aerosol optical properties from sun and sky radiance measurements. *Journal of Geophysical Research: Atmospheres*, 105(D16):20673–20696.

Dubovik, O., Lapyonok, T., Litvinov, P., Herman, M., Fuertes, D., Ducos, F., Lopatin, A., Chaikovsky, A., Torres, B., Derimian, Y., et al. (2014). Grasp: a versatile algorithm for characterizing the atmosphere. *SPIE Newsroom*, 25.

Dubovik, O., Sinyuk, A., Lapyonok, T., Holben, B. N., Mishchenko, M., Yang, P., Eck, T. F., Volten, H., Munoz, O., Veihelmann, B., et al. (2006). Application of spheroid models to account for aerosol particle nonsphericity in remote sensing of desert dust. *Journal of Geophysical Research: Atmospheres*, 111(D11).

Earle, M., Pancescu, R., Cosic, B., Zasetsky, A., and Sloan, J. (2006). Temperature-dependent complex indices of refraction for crystalline (nh4) 2so4. *The Journal of Physical Chemistry A*, 110(48):13022–13028.

Gassó, S., Grassian, V. H., and Miller, R. L. (2010). Interactions between mineral dust, climate, and ocean ecosystems. *Elements*, 6(4):247–252.

Glotch, T. D. and Rossman, G. R. (2009). Mid-infrared reflectance spectra and optical constants of six iron oxide/oxyhydroxide phases. *Icarus*, 204(2):663–671.

Grainger D, Peters D, C. L. H. H. (2021). Aria: introduction.

Hansell Jr, R., Reid, J., Tsay, S., Roush, T., and Kalashnikova, O. (2011). A sensitivity study on the effects of particle chemistry, asphericity and size on the mass extinction efficiency of mineral dust in the earth's atmosphere: from the near to thermal ir. *Atmospheric chemistry and Physics*, 11(4):1527–1547.

Henning, T. and Mutschke, H. (1997). Low-temperature infrared properties of cosmic dust analogues. *Astronomy and Astrophysics*, 327:743–754.

Hess, M., Koepke, P., and Schult, I. (1998). Optical properties of aerosols and clouds: The software package opac. *Bulletin of the American meteorological society*, 79(5):831–844.

Hudson, P. K., Young, M. A., Kleiber, P. D., and Grassian, V. H. (2008). Coupled infrared extinction spectra and size distribution measurements for several non-clay components of mineral dust aerosol (quartz, calcite, and dolomite). *Atmospheric Environment*, 42(24):5991–5999.

Jacquinet-Husson, N., Crepeau, L., Armante, R., Boutammine, C., Chédin, A., Scott, N., Crevoisier, C., Capelle, V., Boone, C., Poulet-Crovisier, N., et al. (2011). The 2009 edition of the geisa spectroscopic database. *Journal of Quantitative Spectroscopy and Radiative Transfer*, 112(15):2395–2445.

Journet, E., Balkanski, Y., and Harrison, S. P. (2014). A new data set of soil mineralogy for dust-cycle modeling. *Atmospheric Chemistry and Physics*, 14(8):3801–3816.

Kandler, K., Schütz, L., Deutscher, C., Ebert, M., Hofmann, H., Jäckel, S., Jaenicke, R., Knippertz, P., Lieke, K., Massling, A., et al. (2009). Size distribution, mass concentration, chemical and mineralogical composition and derived optical parameters of the boundary layer aerosol at tinfou, morocco, during samum 2006. *Tellus B: Chemical and Physical Meteorology*, 61(1):32–50.

Kirchstetter, T. W., Novakov, T., and Hobbs, P. V. (2004). Evidence that the spectral dependence of light absorption by aerosols is affected by organic carbon. *Journal of Geophysical Research: Atmospheres*, 109(D21).

Kleiber, P., Grassian, V., Young, M., and Hudson, P. K. (2009). T-matrix studies of aerosol particle shape effects on ir resonance spectral line profiles and comparison with an experiment. *Journal of Geophysical Research: Atmospheres*, 114(D21).

Klüser, L., Banks, J., Martynenko, D., Bergemann, C., Brindley, H., and Holzer-Popp, T. (2015). Information content of space-borne hyperspectral infrared observations with respect to mineral dust properties. *Remote Sensing of Environment*, 156:294–309.

Koepke, P. and Hess, M. (1988). Scattering functions of tropospheric aerosols: the effects of nonspherical particles. *Applied Optics*, 27(12):2422–2430.

Koepke, P., Hess, M., Schult, I., and Shettle, E. P. (1997). Global aerosol data set.

Kostinski, A. B. and Derimian, Y. (2020). Minimum principles in electromagnetic scattering by small aspherical particles: Extension to differential cross-sections. *Journal of Quantitative Spectroscopy and Radiative Transfer*, 241:106720.

Kou, L., Labrie, D., and Chylek, P. (1993). Refractive indices of water and ice in the 0.65-to 2.5-μm spectral range. *Applied optics*, 32(19):3531–3540.

Kudo, R., Diémoz, H., Estellés, V., Campanelli, M., Momoi, M., Marenco, F., Ryder, C. L., Ijima, O., Uchiyama, A., Nakashima, K., et al. (2021). Optimal use of the prede pom sky radiometer for aerosol, water vapor, and ozone retrievals. *Atmospheric Measurement Techniques*, 14(5):3395–3426.

Lafon, S., Sokolik, I. N., Rajot, J. L., Caquineau, S., and Gaudichet, A. (2006). Characterization of iron oxides in mineral dust aerosols: Implications for light absorption. *Journal of Geophysical Research: Atmospheres*, 111(D21).

Lane, M. D. (1999). Midinfrared optical constants of calcite and their relationship to particle size effects in thermal emission spectra of granular calcite. *Journal of Geophysical Research: Planets*, 104(E6):14099–14108.

Lázaro, F. J., Gutiérrez, L., Barrón, V., and Gelado, M. D. (2008). The speciation of iron in desert dust collected in gran canaria (canary islands): Combined chemical, magnetic and optical analysis. *Atmospheric Environment*, 42(40):8987–8996.

Legrand, M., Dubovik, O., Lapyonok, T., and Derimian, Y. (2014). Accounting for particle nonsphericity in modeling of mineral dust radiative properties in the thermal infrared. *Journal of Quantitative Spectroscopy and Radiative Transfer*, 149:219–240.

Li, L., Dubovik, O., Derimian, Y., Schuster, G. L., Lapyonok, T., Litvinov, P., Ducos, F., Fuertes, D., Chen, C., Li, Z., et al. (2019). Retrieval of aerosol components directly from satellite and ground-based measurements. *Atmospheric Chemistry and Physics*, 19(21):13409–13443.

Long, L., Querry, M., Bell, R., and Alexander, R. (1993). Optical properties of calcite and gypsum in crystalline and powdered form in the infrared and far-infrared. *Infrared Physics*, 34(2):191–201.

Longtin, D. R., Shettle, E. P., Hummel, J. R., and Pryce, J. D. (1988). A wind dependent desert aerosol model: Radiative properties. Technical report, OPTIMETRICS INC BURLINGTON MA.

Lopatin, A., Dubovik, O., Chaikovsky, A., Goloub, P., Lapyonok, T., Tanré, D., and Litvinov, P. (2013). Enhancement of aerosol characterization using synergy of lidar and sun-photometer coincident observations: the garrlic algorithm. *Atmospheric Measurement Techniques*, 6(8):2065–2088.

Marra, A., Blanco, A., Fonti, S., Jurewicz, A., and Orofino, V. (2005). Fine hematite particles of martian interest: absorption spectra and optical constants. In *Journal of Physics: Conference Series*, volume 6, page 013. IOP Publishing.

Massie, S. (1994). Indices of refraction for the hitran compilation. *Journal of Quantitative Spectroscopy and Radiative Transfer*, 52(3-4):501–513.

Massie, S. and Goldman, A. (2003). The infrared absorption cross-section and refractive-index data in hitran. *Journal of Quantitative Spectroscopy and Radiative Transfer*, 82(1-4):413–428.

Mie, G. (1908). Beiträge zur optik trüber medien, speziell kolloidaler metallösungen. *Annalen der Physik*, 330(3):377–445.

Mishchenko, M. I., Travis, L. D., Kahn, R. A., and West, R. A. (1997). Modeling phase functions for dustlike tropospheric aerosols using a shape mixture of randomly oriented polydisperse spheroids. *Journal of Geophysical Research: Atmospheres*, 102(D14):16831–16847.

Mishchenko, M. I., Travis, L. D., and Mackowski, D. W. (1996). T-matrix computations of light scattering by nonspherical particles: A review. *Journal of Quantitative Spectroscopy and Radiative Transfer*, 55(5):535–575.

Mogili, P. K., Yang, K., Young, M. A., Kleiber, P. D., and Grassian, V. H. (2008). Extinction spectra of mineral dust aerosol components in an environmental aerosol chamber: Ir resonance studies. *Atmospheric Environment*, 42(8):1752–1761.

Moosmüller, H., Chakrabarty, R., and Arnott, W. (2009). Aerosol light absorption and its measurement: A review. *Journal of Quantitative Spectroscopy and Radiative Transfer*, 110(11):844–878.

Nousiainen, T., Kahnert, M., and Veihelmann, B. (2006). Light scattering modeling of small feldspar aerosol particles using polyhedral prisms and spheroids. *Journal of Quantitative Spectroscopy and Radiative Transfer*, 101(3):471–487.

Posch, T., Mutschke, H., Baier, A., and Henning, T. (2007). Ir properties of calcite and dolomite at low temperatures. *Astronomische Nachrichten*, 328(7):648.

Querry, M. R. (1987). *Optical constants of minerals and other materials from the millimeter to the ultraviolet*. Chemical Research, Development & Engineering Center, US Army Armament ....

Ray, P. S. (1972). Broadband complex refractive indices of ice and water. *Applied optics*, 11(8):1836–1844.

Reed, B. E., Peters, D. M., McPheat, R., Smith, A. J., and Grainger, R. (2017). Mass extinction spectra and size distribution measurements of quartz and amorphous silica aerosol at 0.33–19 μm compared to modelled extinction using mie, cde, and t-matrix theories. *Journal of Quantitative Spectroscopy and Radiative Transfer*, 199:52–65.

Rothman, L. S. and Gordon, I. E. (2013). The hitran molecular database. In *AIP Conference Proceedings*, volume 1545, pages 223–231. American Institute of Physics.

Shettle, E. P. and Fenn, R. W. (1979). *Models for the aerosols of the lower atmosphere and the effects of humidity variations on their optical properties*, volume 79. Air Force Geophysics Laboratory, Air Force Systems Command, United States ....

Shi, Z., Krom, M. D., Bonneville, S., Baker, A. R., Bristow, C., Drake, N., Mann, G., Carslaw, K., McQuaid, J. B., Jickells, T., et al. (2011). Influence of chemical weathering and aging of iron oxides on the potential iron solubility of saharan dust during simulated atmospheric processing. *Global Biogeochemical Cycles*, 25(2).

Spitzer, W. and Kleinman, D. (1961). Infrared lattice bands of quartz. *Physical Review*, 121(5):1324.

Sun, H., Biedermann, L., and Bond, T. C. (2007). Color of brown carbon: A model for ultraviolet and visible light absorption by organic carbon aerosol. *Geophysical Research Letters*, 34(17).

Textor, C., Schulz, M., Guibert, S., Kinne, S., Balkanski, Y., Bauer, S., Berntsen, T., Berglen, T., Boucher, O., Chin, M., et al. (2006). Analysis and quantification of the diversities of aerosol life cycles within aerocom. *Atmospheric Chemistry and Physics*, 6(7):1777–1813.

Toon, O. B., Pollack, J. B., and Khare, B. N. (1976). The optical constants of several atmospheric aerosol species: Ammonium sulfate, aluminum oxide, and sodium chloride. *Journal of Geophysical research*, 81(33):5733–5748.

Tsigaridis, K., Krol, M., Dentener, F., Balkanski, Y., Lathiere, J., Metzger, S., Hauglustaine, D., and Kanakidou, M. (2006). Change in global aerosol composition since preindustrial times. *Atmospheric Chemistry and Physics*, 6(12):5143–5162.

van de Hulst, H. C. (1958). Light scattering by small particles. *Quarterly Journal of the Royal Meteorological Society*, 84(360):198–199.

Volz, F. E. (1972). Infrared refractive index of atmospheric aerosol substances. *Applied Optics*, 11(4):755–759.

Volz, F. E. (1973). Infrared optical constants of ammonium sulfate, sahara dust, volcanic pumice, and flyash. *Applied Optics*, 12(3):564–568.

Warren, S. G. and Brandt, R. E. (2008). Optical constants of ice from the ultraviolet to the microwave: A revised compilation. *Journal of Geophysical Research: Atmospheres*, 113(D14).

Wiscombe, W. J. (1980). Improved mie scattering algorithms. *Applied optics*, 19(9):1505–1509.

Yang, P. and Liou, K. (1996). Geometric-optics–integral-equation method for light scattering by nonspherical ice crystals. *Applied Optics*, 35(33):6568–6584.

Yu, F., Luo, G., and Ma, X. (2012). Regional and global modeling of aerosol optical properties with a size, composition, and mixing state resolved particle microphysics model. *Atmospheric Chemistry and Physics*, 12(13):5719–5736.

Zolotarev, V. (2009). Study of quartz glass by differential fourier transform ir reflection spectroscopy: Bulk and surface properties. *Optics and Spectroscopy*, 107(5):754–767.

Chapter 6

Enhanced Dust Retrieval

Y recuerda: ¡tiempo anticiclónico significa buen tiempo!

Pablo Álvarez Zapatero

This chapter is devoted to the description, sensitivity analysis, application and validation of the enhanced dust retrieval by means of the synergic combination of solar and thermal infrared measurements in GRASP algorithm. First of all, a general description of the algorithm, including input, output and ancillary information is provided. In addition, tests to prove the accuracy of the proposed assumptions and methodology to model the CLIMAT measurements will be presented. Then, a series of synthetic tests are performed in order to: exposed the sensitivity to the different aerosol characteristics of the CIMEL sunphotometer and the CLIMAT TIR radiometer measurements, and to understand the accuracy of the retrieval and how the measurement noise and the uncertainty in the ancillary input information affect the results. Finally, the developed retrieval scheme is applied to real data corresponding to the AERONET site of Dakar Belair for the months of November 2020, January 2021 and April 2021. A validation of the output characteristics against the corresponding AERONET retrieved products in the same station has also been done.

6.1 Retrieval scheme description

GRASP (Dubovik et al., 2021) retrieval algorithm is going to be applied to a combination of Solar and Thermal Infrared measurements in order to provide an aerosol mineral dust composition characterization based on the original GRASP/Components retrieval (Li et al., 2019). The measurements in the solar spectrum provide sensitivity to dust particles size distribution, non-sphericity and fraction of iron oxides. However, these measurements are less affected by the changes in dust mineralogical composition because the refractive index of different species at solar wavelengths tends to be spectrally flat, except for iron oxides. On the other hand, TIR radiance is less sensitive to changes in aerosol microphysics, but due to the more accentuated spectral changes of the refractive index, these longwave measurements present a high sensitivity to the aerosol mineralogical composition. Thus, as it will be demonstrated, the combination of radiances in both parts of the spectrum as the input of GRASP algorithm will enhance the aerosol composition retrieval. Furthermore, due to the synergic combination, in addition to all previous aerosol properties and the extended information about aerosol mineral dust composition, the total column concentration (TCC) of water vapor is also retrieved. The objective to perform a combined retrieval of aerosol plus gas concentration seemed quite ambitious for the time constraints of the thesis, this is why the synthetic sensitivity tests were performed assuming that the total column water vapor concentration is a fixed input parameter and it is not part of the retrieved characteristics. However, during the real data application and the validation process, the high sensitivity of the TIR measurements to this parameter lead to the inclusion of water vapor as part of the retrieved products. The high agreement of the obtained values with the AERONET precipitable water product (Smirnov et al. (2004), Pérez-Ramírez et al. (2014)) seems to confirm the validity of this

Input Measurements	
$I_{\text{Solar}}(\mu_0, \mu, \varphi_0, \varphi, \lambda)$	AERONET almucantar at 440, 675, 870 and 1020 nm
$\tau_{\text{Solar}}(\lambda)$	AERONET TOD
$I_{\text{TIR}}(\mu_0, \mu)$	CLIMAT radiance at 8.7, 11 and 12 μm
Ancillary Input Information	
Temperature vertical profile	ECMWF ERA5 hourly reanalysis
Surface Temperature	ECMWF ERA5 hourly reanalysis
Surface emissivity at TIR	ECMWF ERA5 hourly reanalysis
BRDF at Solar wavelengths	MODIS climatology
$CO_2, CH_4, N_2O, NO_2, O_3$	TCC of ECMWF CAMS reanalysis
Retrieved Characteristics	
Cv_i	Volume concentration of aerosol for fine and coarse
C_{sph}	Sphericity fraction
$dV(r_i)/dlnr$	Normalized 22-bins bimodal PSD
Frac(F_i)	Volume fractions of aerosol fine mode
Frac(C_i)	Volume fractions of aerosol coarse mode
h_0	Aerosol mean height
H_2O	Total column water vapor

Table 6.1: List of input and output parameters in the proposed GRASP retrieval scheme.

parameter inversion.

The input measurements selected to accomplish the pursued objectives are: the AERONET sun-photometer almucantar and TOD (Total Optical Depth) at four wavelengths: 440, 675, 870 and 1020 nm; and the CLIMAT radiances at three different channels: 8.7, 11 and 12 μm. More detailed information about the measurement geometries and technical details of these instruments can be found in a previous chapter of this thesis. However, these measurements are not the only input information necessary for the retrieval scheme proposed here. There is also a set of fixed, assumed as true, information that is essential to perform the retrieval: the total column concentration of CO_2, CH_4, N_2O, NO_2 and O_3; the atmospheric temperature vertical profiles and the surface temperature, BRDF and emissivity. The surface BRDF at solar wavelengths is provided by the MODIS database (Schaaf et al., 2011) following (Román et al., 2018) for the climatological calculations. The surface emissivity at TIR range was taken from LP DAAC reanalysis database (Hook, 2017). The rest of the ancillary data was taken from ECMWF ERA5 hourly reanalysis (Hersbach, 2016) and ECMWF CAMS reanalysis (Inness et al., 2019). More details about the modeling of these characteristics will be provided in the following sections.

The output characteristics of the retrieval scheme outlined above include aerosol microphysics, aerosol composition, aerosol mean height and total column water vapor concentration. The aerosol microphysics are represented by a 22-bins bimodal particle size distribution and the sphericity fraction. The former indicates the percent of the total particles that are not spherical, the shape distribution is assumed to be fixed as the reference of Dubovik et al. (2006). The aerosol composition is represented by a linear Volume Weighted mixture. The assumed fine mode components are: Black Carbon, Brown Carbon, soluble, Quartz and clays; whereas in the coarse mode the selected species are: Iron oxide, soluble, Quartz and clays.

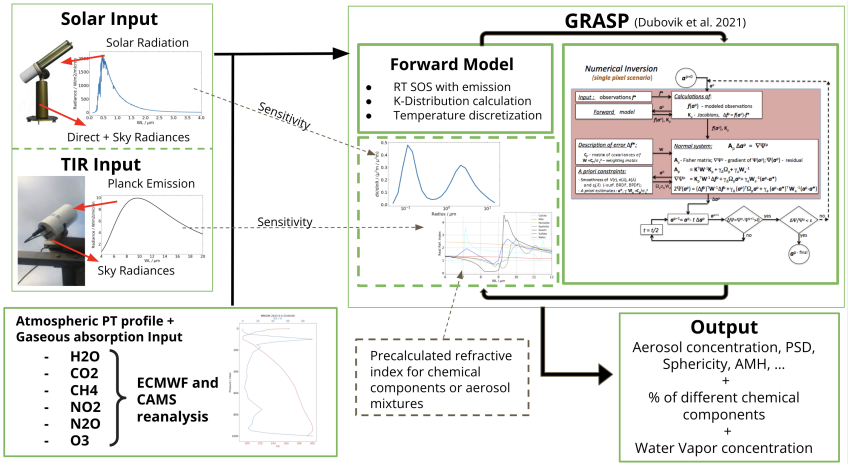

Figure 6.1: GRASP retrieval scheme of the developed inversion strategy for this thesis.

6.1.1 Forward Modelling of TIR radiometer measurements

The modeling of radiance measurements at the solar spectral range in the GRASP framework has been extensively described and validated in a number of studies about the development of GRASP algorithm and about its different applications, among others. Here will be provided a general description of the new implementations to simulate TIR radiance.

The details about the simulation of the temperature profiles, in the vertically inhomogeneous atmospheres that are considered here, can be found in the chapter of this thesis related to the thermal emission inclusion in the SOS RT scheme. At the sight of the results shown in that chapter, the extinction weighted methodology is the selected approach to perform the retrieval calculations presented here. As no lidar or vertical aerosol profile information is part of the input of this retrieval scheme (which is open for the future perspectives), aerosols are supposed to be vertically distributed following a gaussian distribution shape with a fixed standard deviation of 500 meters and a center which corresponds to the AMH (Aerosol Mean Height) retrieved parameter.

Information about the vertical distribution of the gaseous species is scarce in the reanalysis databases. Only total column integrated concentration values can be found with a proper temporal and spatial resolution. Thus, the vertical distribution of all the species considered here is assumed as fixed following a US standard atmosphere as the reference. The only exception is the water vapor. An average gas concentration profile based on the mean relative humidity profile over Dakar is the constant vertical shape assumed for this specie.

As it has been mentioned, the FWHM of the CLIMAT channels is 1 μm, which is significantly larger than the spectral width of the channels of the instruments normally used as GRASP input. Thus, using a single spectral value of aerosol single scattering properties to represent these large channels may lead to significant errors caused by the highly varying spectral behavior of aerosols at this spectral interval. The previously described subchannel methodology is the solution to this problem. The optimal number of subchannels in which each CLIMAT channel should be divided is presented in the following section. On the other hand, the 10 nm FWHM of the sun photometer channels and the smooth spectral behavior of aerosol optical properties at the solar spectral range do not require the subdivision of the channels of this instrument. In addition, the subchannel methodology enables the application of K-distribution methodologies in all channels independently of their spectral characteristics. As it has been previously mentioned, the CGASA (Doppler et al., 2014a) line-by-line model was used to calculate gas absorption lines, and the "kbins" methodology (Doppler et al., 2014b) was employed to perform the K-Distribution calculations. An independent K-Distribution was obtained for each sun photometer channel and for each subchannel of each channel of CLIMAT radiometer. However, in order to reduce the computation time required to calculate these K-Distributions, climatological values of the temperature and gaseous absorption profiles were used to calculate a reference K-Distribution for Dakar. Thus, for each atmospheric situation, or for each iteration of the water vapor retrieval, the absorption profiles provided for this methodology are renormalized by the new total column concentration values. This methodology assumes a linear relation between the gas absorption and its concentration.

6.2 Synthetic Sensitivity tests

This section is meant to provide quantitative support and accuracy estimates for the retrieved parameters of the proposed inversion scheme. First of all, the effect of the different simulation assumptions over the radiance measured by the CLIMAT radiometer will be analyzed. The simplifications of aerosol single scattering properties at TIR range with the number of subchannels and the new representation of the shape distribution at this spectral range will be exposed. Then, quantitative estimates of the effect over radiance of the variation of aerosol size and composition at the different spectral ranges will be shown.

Once that the radiance uncertainties and sensitivity have been analyzed, the complete retrieval algorithm will be tested. Synthetic scenarios covering a wide range of atmospheric situations (including different aerosol loads, PSD, and compositions) will be used jointly with GRASP forward model to generate simulated measurements, with and without added noise, to perform retrievals whose solution is known. This methodology is applied in order to evaluate the accuracy of the output products

under different situations and to analyze the effect of the measurement noise. Finally, the effect of the uncertainties in the ancillary input information is going to be exposed. Note that the previous synthetic tests have been performed assuming a perfect knowledge of all of these parameters. In this final part, the analysis is focused on the errors introduced in the retrieved output characteristics by the inconsistencies between each of these fixed parameters and the real atmospheric situation.

6.2.1 Measurement sensitivity

General insights have been provided in previous chapters on the influence of the aerosol optical characteristics in TIR. A more detailed analysis is provided at this stage. The current section is devoted to the analysis of the measurement sensitivity of both instruments, accounting for the particular technical characteristics and measurement geometries of each of them. The objective is to understand the uncertainties introduced by the numerical implementation in the modeling of each measurement, and to illustrate the different sensitivity in both spectral ranges to the main aerosol characteristics, as they are the PSD, the sphericity and the mineralogical composition.

6.2.1.1 TIR radiometer measurements sensitivity to the number of subchannels and the particle shape

The most precise methodology to simulate the CLIMAT measurements is to apply a line-by-line methodology where the aerosol optical properties and the gas absorption values are accounted with a high spectral resolution precision. However, both the integration of the gas lines and the aerosol scattering calculations in all of these small spectral steps is highly time and computer resources consuming. The K-Distribution and the subchannels division methodologies constitute a proper alternative to crucially speed up and lighten the required calculations. In order to optimize the amount of subchannel divisions required to accurately simulate the radiance of CLIMAT channels, a typical aerosol dust scenario was selected to perform calculations with a different number of subchannels. The relative differences in the radiance introduced by the decrease of the number of subchannels in comparison to the reference simulations (25 subchannels) for each CLIMAT channel can be seen in figure 6.2.

As it can be seen in the results shown in figure 6.2, for simulations performed with a number of subchannels smaller than 5, significant differences can be found in the three channels of CLIMAT radiometer. These differences are especially accentuated in the channel around 11 µm where values up to a 7% can be observed. On the other hand, the 8.7 μm channel is the least affected. When the simulations are obtained with a number of subchannels higher than 5, the convergence to the reference is achieved and no significant differences can be observed.

As the results shown in figure 6.2 can present differences in other atmospheric scenarios, a value of 10 subchannels have been selected in order to assure the minimization of the uncertainties introduced by this approximation. All the results shown from now on have been done dividing the CLIMAT channels in 10 subchannels.

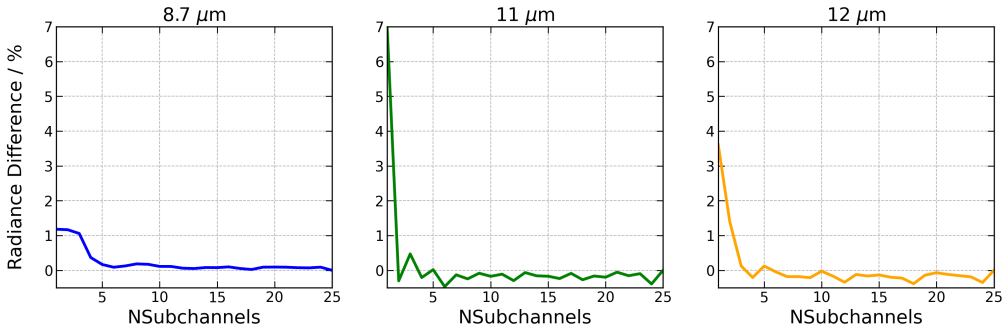

Figure 6.2: Relative radiance difference, expressed in percent, as a function of the number of subchannels used compared to the reference simulation made with 25 subchannels for the three CLIMAT channels (8.7, 11 and 12 μm).

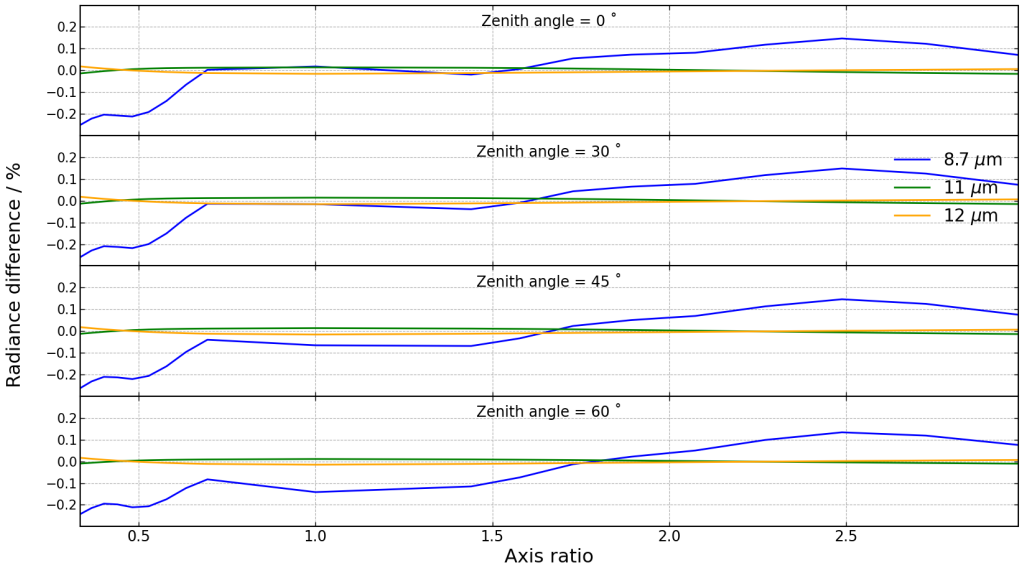

Figure 6.3: Relative radiance difference, expressed in percent, as a function of the used particle axis ratio compared to the reference simulation made with the complete shape distribution (Dubovik et al., 2006) for the three CLIMAT channels (8.7, 11 and 12 μm) for three different measurement geometries (zenith angles: 0°, 30°, 45° and 60°).

In a previous chapter of this thesis it was shown the importance of the aerosol shape in the extinction calculations. The effect of varying axis ratio on radiances over the CLIMAT channels will be analyzed here. Figure 6.3 shows the relative differences of radiance between a reference calculation performed with the complete shape distribution presented in (Dubovik et al., 2006) and radiance simulations accounting for one single axis ratio.

The 8.7 μm channel is the most affected by the changes in the aerosol shape. As it was shown in the previous chapter about aerosol scattering at TIR, this strong dependence can be mainly attributed to the Quartz scattering resonance in this spectral band. The other two channels are barely affected by the aerosol shape. These observed differences grow when the viewing zenith angle of the measurement increases. This tendency is mainly explained by the vertical distribution of aerosols. A significant part of the total aerosol load is situated near the surface, thus, when the zenith angle is increased the weight of the aerosols and their effect over the total radiance is increased. From the comparisons corresponding to an axis ratio of 1 in figure 6.3, the effect of considering just spherical particles in the calculations can be seen. The highest difference, -0.1%, can be found at 8.7 μm for a measurement zenith angle of 60°. Thus, it can be concluded that the simplifications in the kernels calculations made for this thesis do not present a major source of error.

6.2.1.2 Differences in sensitivity of Solar and TIR radiance to aerosol composition and particle size

The basic principle of the GRASP retrieval scheme presented here is built on the synergic combination of the high sensitivity of solar radiance measurements to the particle size and the enhanced sensitivity of the TIR measurements to the aerosol mineralogical composition. This section is meant to provide quantitative illustrations of the different effects of these two aerosol characteristics over the radiance measured by the sun photometer and the CLIMAT radiometer.

The reference atmospheric climatological situation taken for these tests is based on the Solar Village case from Dubovik et al. (2006) for the coarse mode dominated scenarios and an USA urban aerosol model for the fine mode dominated scenarios. The gaseous concentrations were selected from mean values over Dakar of the above mentioned reanalysis databases. The reference for the aerosol volume fraction components have been defined based on Sokolik et al. (1998), Sokolik and

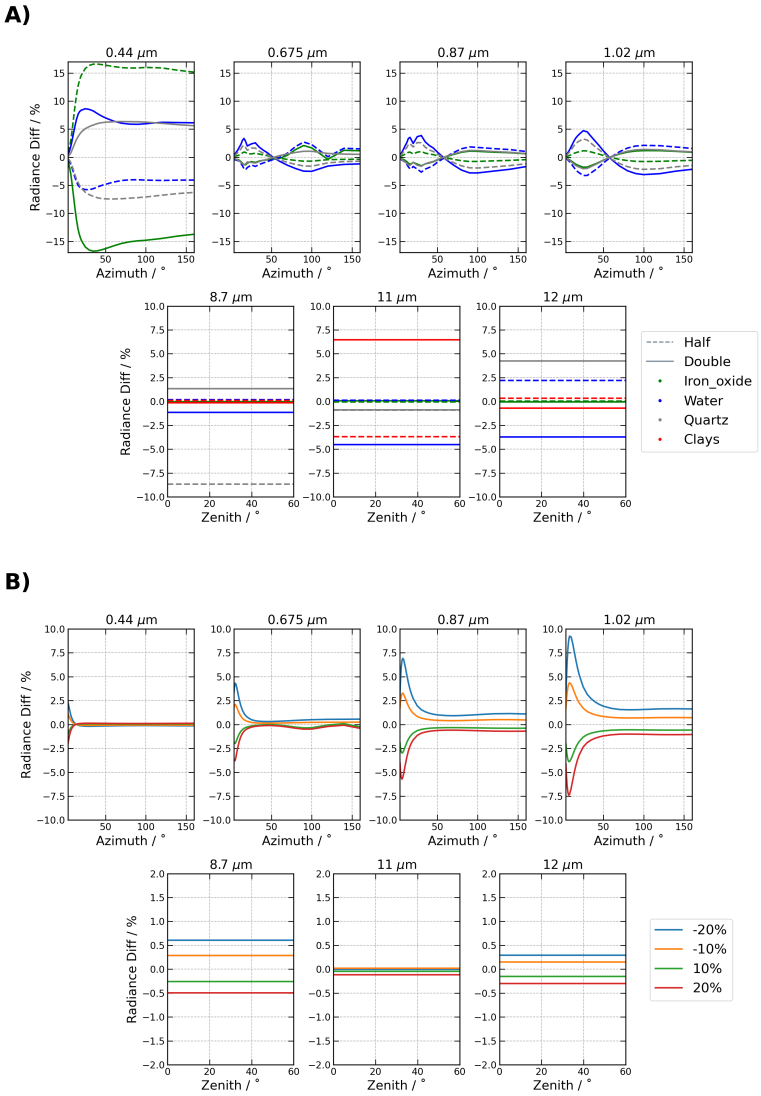

Figure 6.4: Relative radiance difference, expressed in percent, between a climatological mineral dust scenario and variations of: each aerosol component concentrations (Panel A) for double (dashed lines) and half (solid lines) values from climatology; and for different variations of the mean radius of the coarse mode bimodal lognormal size distribution (Panel B). The radiance has been calculated for all channels and geometries of the sunphotometer and the CLIMAT radiometer.

Toon (1999), Claquin et al. (1999), Journet et al. (2014) and Di Biagio et al. (2017). GRASP forward model was used to obtain the radiance coming from these reference situations for the typical measurement geometry of the sunphotometer and the CLIMAT radiometer. The relative difference introduced in all the channels by the individual variations of each aerosol parameter, maintaining fixed all the rest, will be analyzed here.

Figure 6.4 shows the relative radiance differences for each channel of both instruments in a coarse mode dominated scenario. Panel A) shows the effect of the doubling (solid line) and decreasing by half (dashed line), with respect to the reference, the volume fractions of each component considered in the coarse mode. Each component is represented by a different color. In the case of the sunphotometer channels the maximum radiance variations can be seen at 440 nm. In this channel the Iron Oxide variations introduce a 15% of radiance difference, whereas the rest of the species produce changes smaller than 5%. The sunphotometer channels at 675, 870 and 1020 nm present a very similar structure with variations also lower than 5% for all species. The red line corresponding to clays cannot be seen in the plots of the sun photometer because at this spectral range clays and Quartz have an identical refractive index. Thus, both lines are totally overlapped. A very different situation appears at the TIR channels of CLIMAT radiometer. The differences introduced by Quartz and clays are perfectly distinguishable

in the three channels. The maximum differences in Quartz can be seen at 8.7 μm with a maximum difference around 10%, whereas for clays the maximum differences are located at 11 µm with a 7.5% of change. In this case, there is no angular behavior in the radiance differences.

In the case of panel B) of figure 6.4, the aerosol mineralogical composition has been fixed and the changes in the PSD over the radiance have been represented. For these tests a bimodal lognormal size distribution to represent the PSD has been selected. Variations of 10% and 20% over the mean radius of the coarse mode distribution are represented by the different colors. Both solar and TIR channels present the expected behavior from the particle size variations. The sunphotometer channels at longer wavelengths are more sensitive to changes in coarse mode particle sizes, as they are the measurements corresponding to smaller azimuth angles, where variations up to 10% can be seen at 1020 nm. On the other hand, TIR channels present a very reduced sensitivity to this aerosol parameter with maximum radiance variations of 5% at 8.7 μm and 12 μm.

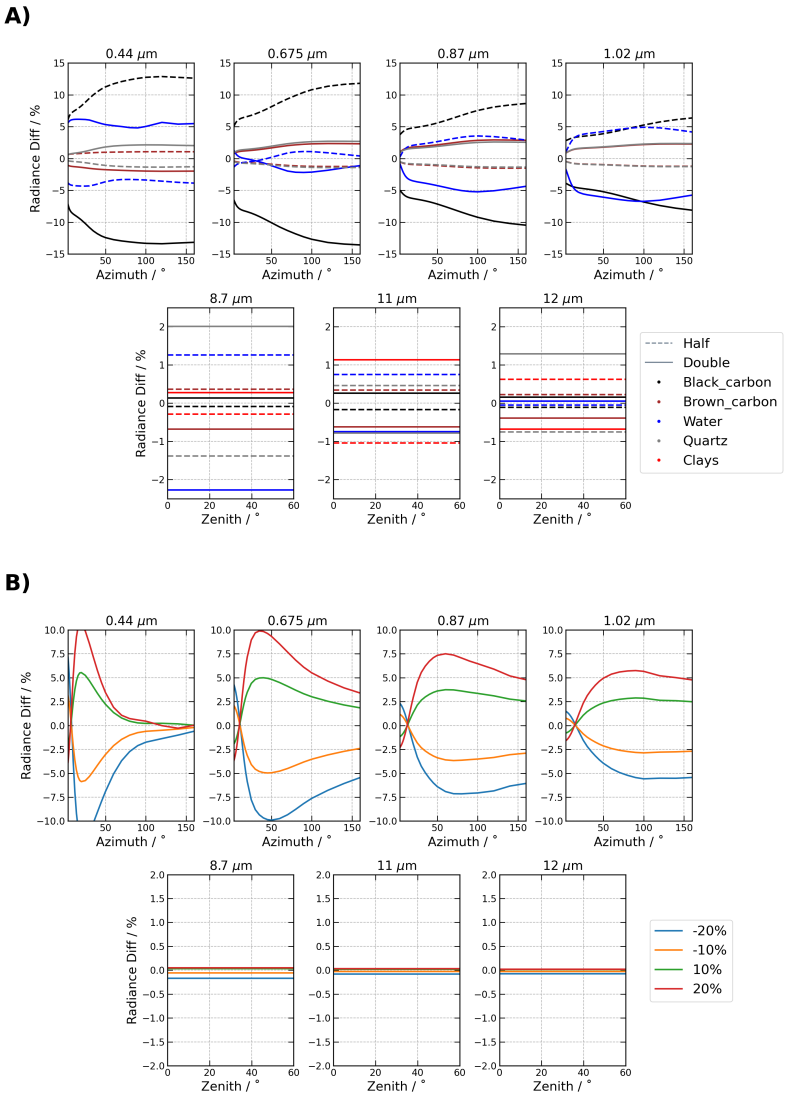

Figure 6.5: Relative radiance difference, expressed in percent, between a climatological biomass burning scenario and variations of: each aerosol component concentrations (Panel A) for double (dashed lines) and half (solid lines) values from climatology; and for different variations of the mean radius of the fine mode bimodal lognormal size distribution (Panel B). The radiance has been calculated for all channels and geometries of the sunphotometer and the CLIMAT radiometer.

A similar comparison has been made in figure 6.5, but in this case all the radiance simulations correspond to a fine mode dominated escenario. In panel A) of figure 6.5 the radiance differences due to the changes in the volume fractions of the aerosol components of fine mode can be appreciated.

In this case the Black Carbon is the specie which produces the larger changes in the radiance of the sunphotometer channels, up to 12% at 440 nm. Very similar patterns can be seen for the rest of the components in all channels, with differences up to 5%. In comparison with the coarse mode simulations, the changes in the mineralogical composition of fine mode particles seems to provide higher radiance differences. On the other hand, if in this case clays and Quartz can also be distinguished in all CLIMAT channels, but now the differences are smaller with a maximum value of 2% at 8.7 μm. These low values can be explained by the low extinction cross sections that these small particle sizes present at the TIR spectral range. Panel B) of figure 6.5 shows the radiance difference induced by the changes in particle size of the aerosol fine mode. At 440 nm differences higher than 10% can be observed. However, all sunphotometer channels present a higher sensitivity to this aerosol mode in comparison with the coarse case, with changes up to 7.5% and 10% in all solar wavelengths. As it was shown in the previous chapter about the aerosol scattering properties at TIR, aerosol fine mode particles are almost invisible at this spectral range. Thus, any significant change of radiance can be appreciated in CLIMAT channels for fine mode radius changes even up to a 20%.

The results presented in this section constitute a consistent proof that the sunphotometer radiance measurements at the solar spectrum and CLIMAT radiances at TIR can be synergically combined to complete the information about the particle size distribution and an extended mineralogical composition. The next section shows how the suggested algorithm is able to retrieve the corresponding aerosol characteristics from the radiance sensitivity.

6.2.2 Synthetic retrieval

This section presents an estimation of the accuracy of the retrieved products of the proposed GRASP retrieval scheme. Three different scenarios for the aerosol particle size distribution have been selected: coarse mode dominated, fine mode dominated and a mixture case. These three scenarios are going to be considered under two different situations of aerosol load: a high turbidity case, with an AOD at 440 nm of 0.4; and a low aerosol concentration case, with an AOD at 440 nm of 0.1. With these fixed aerosol concentration and PSD characteristics, the rest of the retrieved parameters, components volume fractions, AMH, and sphericity, have been randomly varied inside climatology based ranges of each of them to create sets of 30 different cases for each combination of PSD and aerosol concentration. The gas concentrations of all the species considered here are fixed to the already mentioned mean values over Dakar.

Once the atmospheric scenarios have been defined, the GRASP forward model has been used to generate the corresponding radiance measurements and TOD. Then, starting from a common initial guess of all retrieved parameters, the GRASP algorithm is applied to obtain the output parameters from these synthetic measurements. Thus, a direct comparison between the output retrieved characteristics and the original parameters defining each scenario can be made. However, this procedure does not account for the instrument measurement noises. Thus, a second set of tests has therefore been done but with the addition of random noise to each measurement, based on the knowledge of the performance of the real instruments. In the case of the sunphotometer TOD values, each wavelength has been perturbed with random noise following a gaussian distribution with a standard deviation of 0.01. This value is the standard reference uncertainty normally attributed to this AERONET product. The case of the radiance is slightly different, for both the sunphotometer and CLIMAT, the addition of random noise has been done with relative values. Which means to add to each radiance measurement a random value obtained from a gaussian distribution with a standard deviation of 3% of the value of the measurement itself.

For these analyses all the non-retrieved characteristics (e.g.: gas concentrations, temperature profiles, surface, etc.) are the same in the forward simulations and in the retrieval, the effect of this ancillary data in the retrieval will be analyzed in the following sections.

6.2.2.1 Noise free conditions

As it has been said, this part of the analysis of the synthetic retrieval will be conducted for noise free measurements. Thus, a high agreement between the reference parameters and the retrieved characteristics is expected.

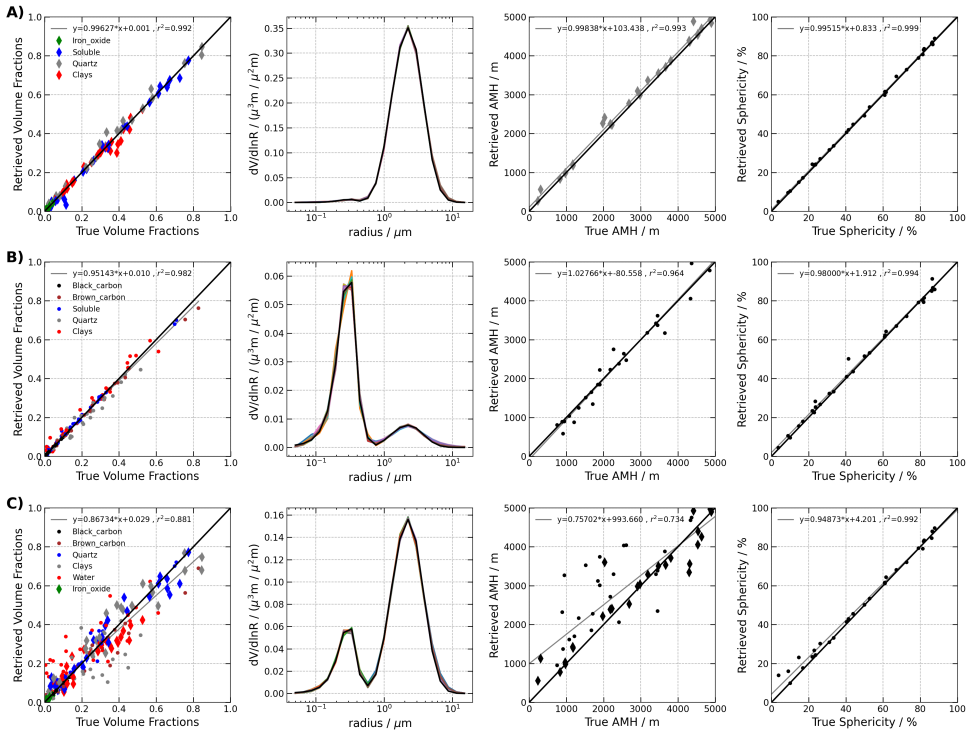

Figure 6.6: Comparison of the GRASP output characteristics of the synthetic retrieval tests in noise free conditions for a high aerosol load (AOD_{440nm} = 0.4). Each panel corresponds to different aerosol dominated scenarios: coarse (Panel A), fine (Panel B) and a mixture scenario (Panel C). The points represented as a dot correspond to the fine mode, the diamonds to the coarse mode and the different colors to the different aerosol components of each mode.

Figure 6.6 shows the comparisons of the GRASP outputs for synthetic retrievals corresponding to the high aerosol load scenarios (AOD = 0.4 at 440 nm). Panels A), B) and C) represent correspondingly the coarse and the fine mode dominated scenarios and the mixture case. In all of them the circles correspond to aerosol properties of the fine mode and the diamonds to the coarse mode. In the plots where the volume fractions are compared, each color represents a different component. In the case of the comparisons of the PSD, the thick black line is the reference for each escenario and each retrieved output is represented with a line of a different color. As it can be appreciated from figure 6.6, all the results are in a very good agreement with the reference values. For the coarse and fine dominated escenarios all characteristics are retrieved without any significant uncertainty. In the case of the mixture scenario (Panel C), the PSD and the sphericity is perfectly retrieved in all the examples. However, a higher dispersion can be found for the coarse mode fractions of Quartz and Clays and the AMH of both aerosol modes.

The retrieved volume fractions corresponding to a lower aerosol load (figure 6.7 where only coarse and fine dominated cases are shown) present a significant degradation. However, even in this less favorable situation, the correlation coefficients are higher than 0.9 and 0.8 correspondingly for coarse and fine mode scenarios. The PSD and sphericity ($r^2 > 0.96$) are also well retrieved in these conditions of low aerosol load. While the AMH parameter is still in a proper agreement for the coarse mode scenario with a correlation coefficient of 0.945, in the fine mode case this information is almost lost and a very poor correlation can be found. The result is expected due to low sensitivity of TIR to small size particles.

6.2.2.2 Realistic noise conditions

Figures 6.8 and 6.9 show the results of analogue tests for high and low aerosol load scenarios but with the measurement noise addition, as previously described. In general, coarse mode scenarios present a higher agreement with the reference than the fine mode dominated cases. In the former scenarios, the aerosol load also plays a significant role. Coarse mode dominated scenarios do not present any special dependency on the aerosol load, the correlation of the retrieved volume fraction is always

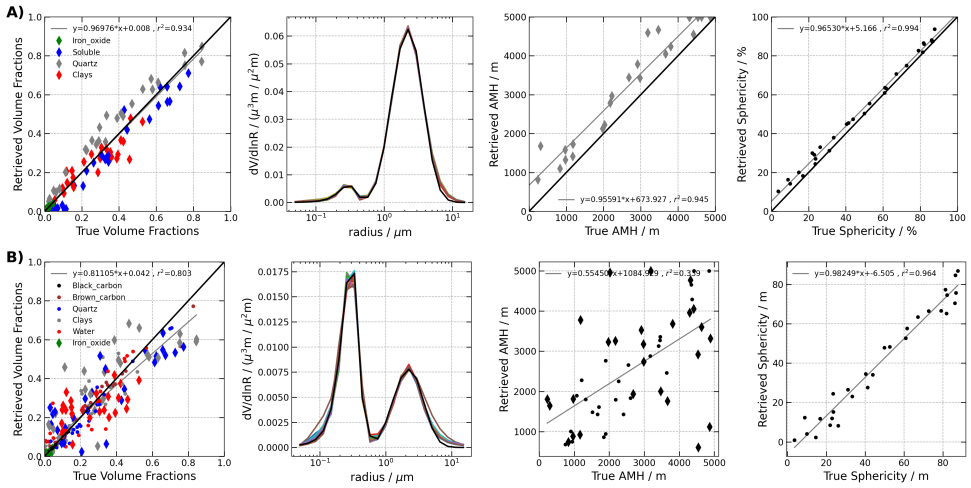

Figure 6.7: Comparison of the GRASP output characteristics of the synthetic retrieval tests in noise free conditions for a low aerosol load (AOD_{440nm} = 0.1). Each panel corresponds to different aerosol dominated scenarios: coarse (Panel A) and fine (Panel B). The points represented as a dot correspond to the fine mode, the diamonds to the coarse mode and the different colors to the different aerosol components of each mode.

over 0.9. However, a value of AOD at 440 nm of at least 0.4 is necessary in order to have a proper characterization of the fine mode volume fractions. For lower aerosol loads, in realistic noise conditions, the correlation coefficient for the fine mode volume fractions falls lower than 0.6. The PSD and sphericity products do not present a significant loss of accuracy due to the measurement noise and both retrieved characteristics are in a very high agreement for all proposed situations.

The sunphotometer radiance measurements provide some degree of sensitivity to the AMH because the multiple scattering contribution depends on the vertical structure of the atmosphere. However, the main contribution to the sensitivity to the AMH is provided by the CLIMAT measurements. The temperature of aerosols, and correspondingly their thermal emission, crucially depends on their altitude. Thus, it is expected to find a better agreement in the AMH of the coarse particles than in the case of the aerosols of smaller size. Indeed, a correlation coefficient of 0.897 is obtained in the coarse mode case in comparison with the 0.657 corresponding to the fine particles.

A summary of the median of the retrieved volume differences (expressed in percent) with respect to the reference simulations corresponding to the high aerosol load synthetic tests in realistic noise conditions shown above is also reported in table 6.2.

	Fine mode					Coarse mode			
	Black Carbon	Brown Carbon	Water	Quartz	Clays	Iron Oxides	Water	Quartz	Clays
Fine Dom. Sce.	0.0 (0.6)	1.5 (7.9)	-3.6 (13.9)	2.5 (11.5)	2.6 (10.4)	-0.3 (5.7)	6.1 (24.8)	-10.6 (25.0)	7.3 (22.7)
Coarse Dom. Sce.	0.9 (4.4)	11.2 (21.2)	1.5 (27.2)	0.51 (18.4)	-11.9 (24.0)	0.0 (0.3)	0.3 (5.8)	-1.31 (5.8)	-0.1 (4.9)
Mixture Sce.	0.24 (1.4)	-0.3 (25.4)	1.0 (10.7)	4.7 (17.7)	-4.9 (22.0)	0.1 (1.4)	-3.9 (13.8)	-0.8 (13.2)	2.4 (8.7)

Table 6.2: Median of the volume fraction differences (expressed in percent) between the synthetic retrievals and the reference simulations corresponding to a high aerosol load and realistic noise conditions. The corresponding standard deviation values are in parenthesis.

6.2.2.3 Comparison of the results using only Sunphotometer measurements

In order to better illustrate the enhancement that brings to the retrieval the inclusion of the TIR radiometer measurements, the same synthetic tests presented above have been repeated but using solely the sun photometer TOD and almucantars as the input measurements in GRASP. The results for the noise free measurements for a high aerosol load can be seen in figure 6.10 (the results for the low aerosol case are not shown). Particle size distribution and aerosol sphericity are once again in a very satisfactory degree of agreement with the reference. However, as it can be appreciated, the main differences in the retrieval results are: the worse retrieval of the AMH and the total loss of correlation for the retrieved fractions of Quartz and clays in the three particle size escenarios. On the other hand,

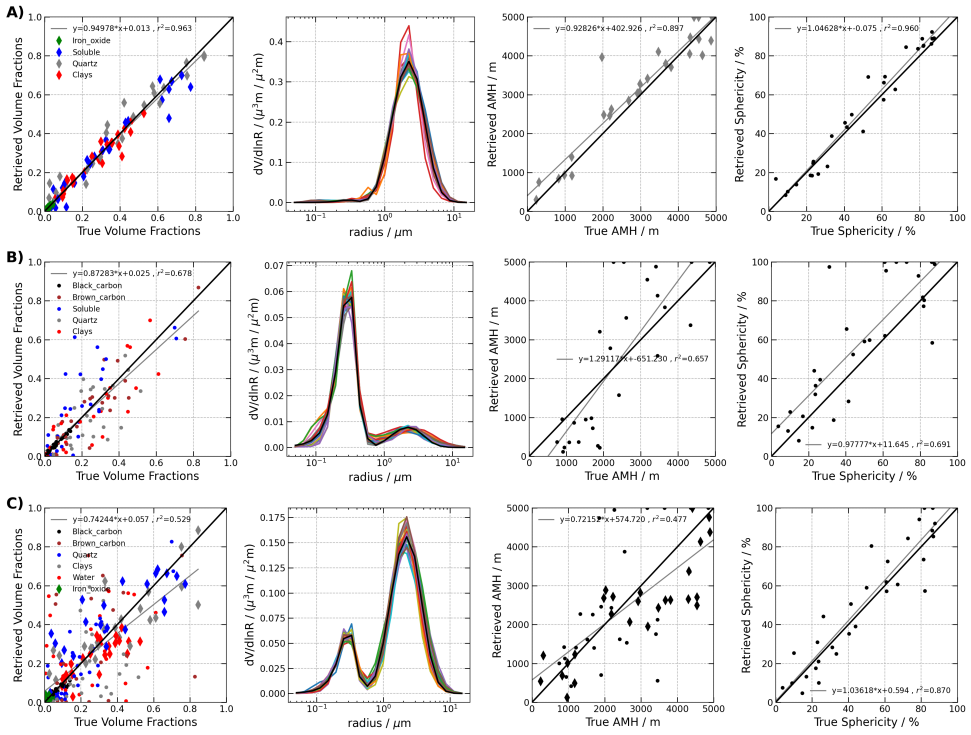

Figure 6.8: Comparison of the GRASP output characteristics of the synthetic retrieval tests in realistic noise conditions for a high aerosol load (AOD_{440nm} = 0.4). Each panel corresponds to different aerosol dominated scenarios: coarse (Panel A), fine (Panel B) and a mixture scenario (Panel C). The points represented as a dot correspond to the fine mode, the diamonds to the coarse mode and the different colors to the different aerosol components of each mode.

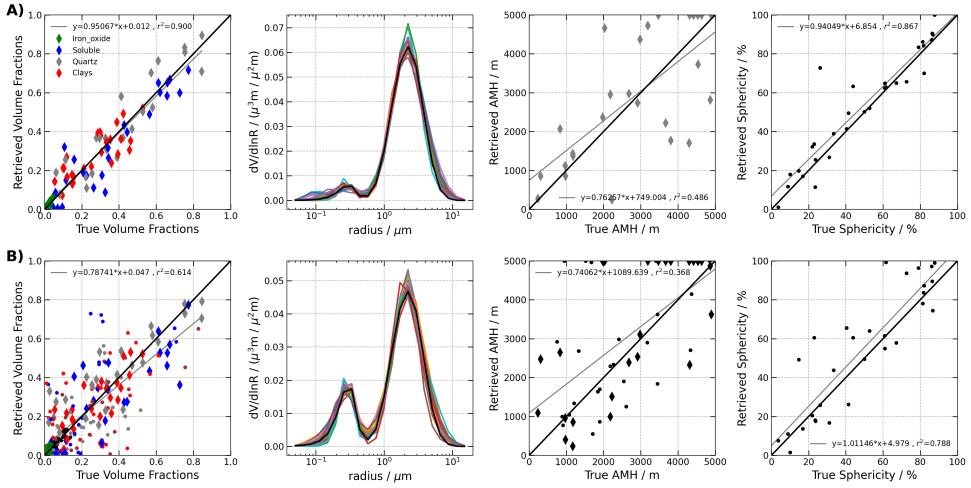

Figure 6.9: Comparison of the GRASP output characteristics of the synthetic retrieval tests in realistic noise conditions for a low aerosol load (AOD_{440nm} = 0.1). Each panel corresponds to different aerosol dominated scenarios: coarse (Panel A) and fine (Panel B). The points represented as a dot correspond to the fine mode, the diamonds to the coarse mode and the different colors to the different aerosol components of each mode.

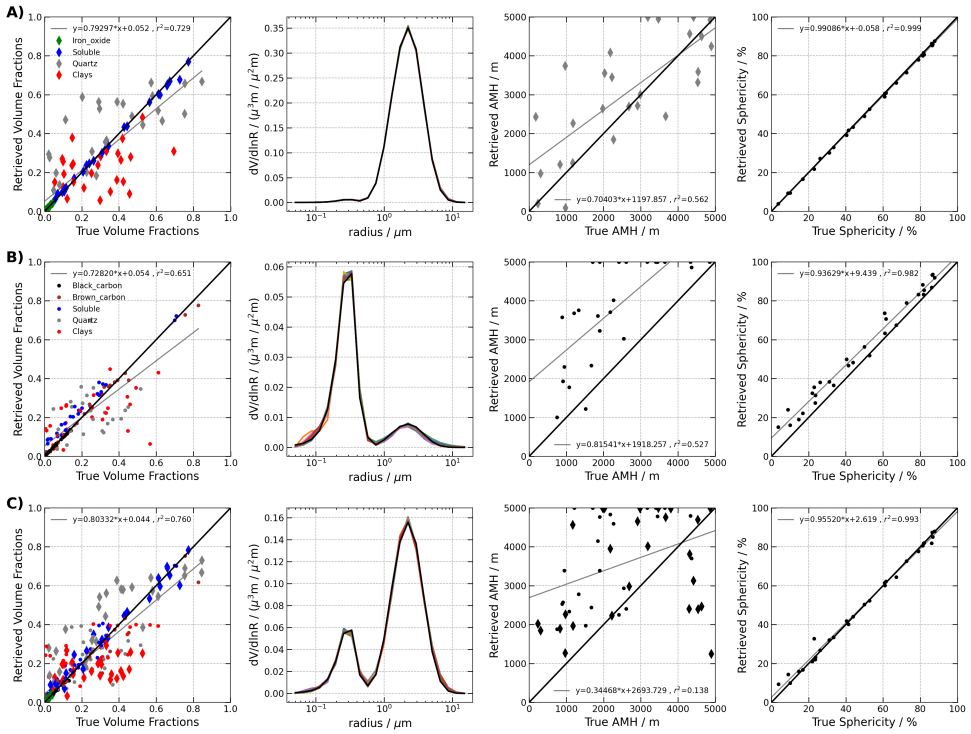

Figure 6.10: Same results as in figure 6.6 but the only input measurements of GRASP corresponds to the sunphotometer.

the species which were part of the previous GRASP Components retrievals proposed by Li et al. (2019) are retrieved quite reasonably in this example. Note that the lack of sensitivity to Quartz and clays still perturbe the components retrievals as it is formulated here. Also, as expected, the fractions of Quartz and clays do not present any kind of correlation. Furthermore, while the AMH correlations for the high aerosol load scenarios when the CLIMAT measurements are part of the GRASP input range from 0.73 to 0.99, in this case significantly lower values ranging from 0.14 to 0.56 are obtained.

The synthetic retrievals for a high aerosol load corresponding to the GRASP inversions using only sunphotometer measurements with the addition of random noise are shown in figure 6.11. Clays and Quartz fractions are again out of any correlation as well as the AMH parameter, which in comparison with the free noise tests has been crucially degraded. No major inconsistencies can be appreciated in the case of PSD or sphericity characteristics.

From all the results presented in this section it can be concluded that a proper degree of accuracy is achieved in all the output retrieved characteristics. The sunphotometer measurements constitute the main source of information for the PSD and the particle sphericity. However, for the component volume fractions considered here and the AMH, the measurements at the solar spectrum are not enough to provide a satisfactory retrieval. The inclusion of the CLIMAT radiance measurements at the TIR ranges synergically enhance the volume fractions characteristics, specially for Quartz and clays, and significantly improves the AMH retrieved values.

6.2.3 Sensitivity to the uncertainties in the retrieval assumptions

This section is meant to take a step further in the characterization of the accuracy of the proposed retrieval scheme and to achieve a better understanding of its interpretation in the application to real data. The following tests are designed to provide insights about the uncertainty introduced in the retrieved volume fractions by the ancillary input information.

As it has been mentioned, the previous synthetic retrieval results have been done assuming a perfect knowledge of all the ancillary information. However, this is not going to be the case in the retrieval of real data because of different reasons: the accuracy of the measurements of these parameters, the temporal and spatial resolution, atmospheric inhomogeneities, etc.

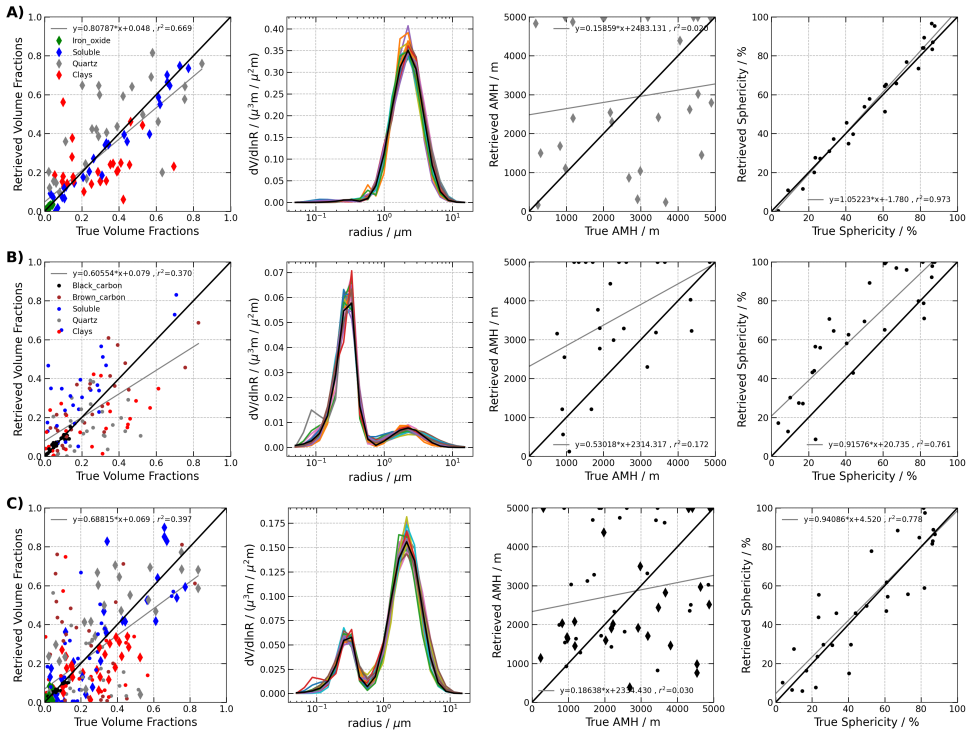

Figure 6.11: Same results as in figure 6.8 but the only input measurements of GRASP corresponds to the sunphotometer.

All gas concentrations and temperature vertical profiles have been obtained from different realysis databases. The ERA5 reanalysis provides the temperature profiles with an hourly temporal resolution and for a horizontal grid of 0.25°. These profiles cover from 1000 hPa to 1 hPa, which means that there is no information for approximately the first 100 meters. However, the CAMS reanalysis for the gas concentrations and relative humidity profiles present lower resolutions with a horizontal grid of 0.75° each 3 hours. In the case of the surface emissivity grid provided by NASA LP DAAC database, a high resolution daily grid of 0.05° was used. The global coverage of these reanalysis products and the wide range of information provided by them make these tools very useful for our purposes. However, the accuracy loss due to the interpolations in the spatial and temporal grids and the assumptions to complete the vertical information in the case of the temperature introduce a non-negligible degree of uncertainty in the retrieval which must be carefully analyzed.

Other important assumptions which can introduce significant uncertainty are: the aerosol vertical distribution and the mixing rule. In the previous examples, although the AMH is well retrieved, the aerosol distribution shape is taken as a gaussian function in both the simulations and the retrievals. However, in the real cases the aerosol vertical distribution shape is more complex and may differ significantly from this simplification. Thus, the effect of this mismatching of vertical profiles will be analyzed. An analogous situation can be found for the aerosol mixing rule. Although here it is always supposed a linear volume weighted mixture for aerosol components, the real atmospheric aerosols can present very different internal structures.

The following tests present the volume fractions differences for the previous high aerosol load scenarios in realistic noise measurement conditions, but introducing extra uncertainties in the retrievals for each parameter of the ancillary data set or in the aerosol modeling assumptions. In order to isolate the uncertainty introduced by each parameter/assumption, in each test only one of them will be modified, while the rest will remain as known. Maximum variation values based on different criteria are selected for each of them. These changes introduced in each parameter are meant to provide a limit of the retrieval error because more favorable situations are expected in the application to real cases.

6.2.3.1 Uncertainties of gas concentration variability

This section is devoted to the analysis of the uncertainty introduced by the gas concentration variability in the retrieved volume fractions of the different aerosol components. For each gaseous specie, the average maximum daily variability over Dakar has been selected as the uncertainty criteria of this set of characteristics. The maximum relative daily concentration variability corresponds to the NO_2 concentration with a 95% of daily variation, and the most stable specie is the CO_2 with a value of 0.1%.

The degree of uncertainty introduced by each specie is defined by two elements: the variability of its concentration and its absorption at the CLIMAT channels. Gas species with high values of daily variability but low absorption or, on the contrary, low daily variabilities with higher absorption values are not going to represent an important source of error in the retrieval. Thus, both elements have to be considered in order to make a correct interpretation of the results.

Figures 6.12 to 6.14 represent the volume fraction differences between the synthetic retrievals and the corresponding references. The green boxes correspond to retrievals where the same gas concentration was assumed in the retrievals and in the simulations, and blue and red boxes represent, correspondingly, the minimum and maximum daily concentration values assumed for the retrievals but a mean daily value was taken in the simulations. Each figure corresponds to a different specie: water vapor, CO_2, N_2O, CH_4, NO_2 and Ozone. The left part of the panels corresponds to the aerosol components considered in the fine mode, the right part corresponds to the aerosol elements in the coarse mode, and from top to bottom the panels represent the different aerosol scenarios already used in the previous tests: coarse and fine mode dominated scenarios and the mixture case. The line in each box represents the median of the volume fraction differences with respect to the reference, the box limits mark the 25 and 75 percentiles, the whiskers represent the maximum and minimum values to consider outliers and with diamonds are marked all outliers of each case. The introduced uncertainties sometimes produce too large errors that GRASP is not able to fit. Thus, in these box plots only the retrievals with a sunphotometer radiance residual smaller than 10% are included. The same methodology and structure described for these box plots is going to be used in all the following tests of this section, but with different meanings of the color boxes.

All the tests for the different gasses present some common characteristics. The dominant mode is by far much better retrieved than the volume fractions belonging to the mode with the smaller concentration. This is an expected behavior because as higher is the concentration, higher is the impact over the measurements and higher the corresponding information content. However, as it has been shown, the long wavelengths of the CLIMAT channels present more sensitivity to the coarse mode particles, which is translated in an improved performance of the retrievals of the fractions of this mode, with no dependence on which gas concentration has been perturbed.

In general, when the gas concentrations are different between the simulations and the retrievals, the dispersion of the results are higher. However, despite the case of water vapor, there is not a significant degradation of the correlation coefficients, and no significant bias can be addressed. This can be explained because despite the high variability of some species such as CH_4 (40%) or NO_2 (95%), its absorption values in all the channels of the selected instruments are not very elevated. For the mean gas concentrations of Dakar, a maximum absorption value of 0.6E-03 at 8.7 μm can be found for CH_4. NO_2 presents a higher absorption in the visible channels, specially at 440 nm where a value of 0.1E-01 can be found; however, in the rest of the channels is also low enough to barely affect the retrieved fractions. In the case of CO_2, even if more significant gas absorption can be found at the CLIMAT channels with mean values of 0.4E-02, its daily variability is so small (0.1%), that there is no significant effect on the retrieval.

The case of water vapor is totally different. Because of its high absorption (0.4E-01 on average for CLIMAT channels) and its 50% daily variability, the degradation of the retrieved volume fractions significantly increases with differences of about 40% in the worst case (water fraction of coarse mode for the mixture scenario). The most absorbing species, Black Carbon and Iron Oxides, are barely affected. On the other hand, a reduction of the assumed amount of water vapor induces a positive bias of around 25% in the Brown Carbon fractions for fine mode dominated and the mixture scenarios. On the other hand, an increase of the water vapor introduces negative bias in the retrieved Brown Carbon fractions. In the case of the retrieved fractions of water, an opposite behavior between the fine and coarse mode can appear. Whereas for the fine mode a decrease of the water vapor amount implies a negative bias and an increase induces a positive mean deviation; for the coarse mode, the water

fractions are inversely proportional to the variations of the water vapor concentration. The retrieved Quartz volume fractions behave in the same way in both modes, with negative bias for the decrease of water vapor and positive bias for the increase of this gas concentration. However, in the case of clays, once again opposite behaviors are found between the fractions of the different aerosol modes.

These extreme effects observed in the volume fraction differences introduced by the water vapor absorption led the authors to think that the water vapor concentration could also be part of the retrieved characteristics.

6.2.3.2 Uncertainties of atmospheric temperature variability

The temperature vertical profile is one of the most important magnitudes in the remote sensing at TIR spectral range. Despite the ECMWF reanalysis provides an hourly temporal resolution, temperature can change due to very local phenomena and significant differences could be found with the real atmospheric situation. The most optimal methodology to characterize the errors introduced by these reanalysis products is the direct comparisons with in situ radiosonde profiles. However, here a simpler approach has been taken. For the closest lat-lon grid point to the Dakar station, the daily mean maximum and minimum temperature for each point of the profile has been selected as the uncertainty reference for this test. The mean, maximum and minimum temperature profiles for Dakar can be seen in figure 6.15. A maximum temperature difference of 11.0 K can be found at 113 m, which is one of the first points of the profile situated very close to the CLIMAT sensor; and a minimum temperature difference of 1.2 K at 2525 m.

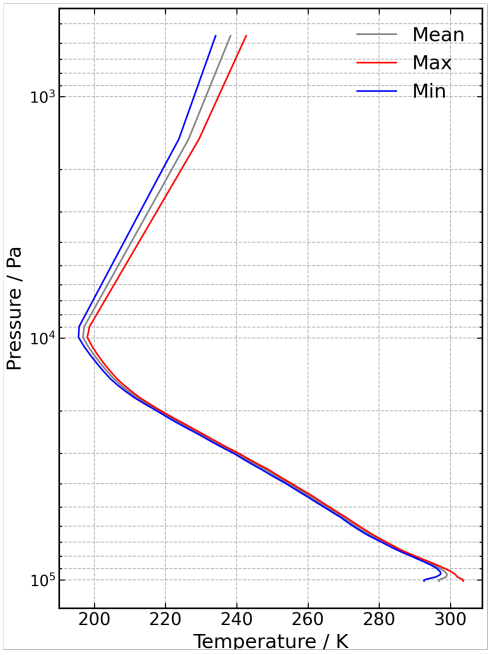

Figure 6.15: Daily temperature mean and the maximum and minimum values for each profile height obtained for March of 2015 in MBOUR. Data obtained from ECMWF reanalysis.

The effect of these variations in the temperature profile over the retrieved aerosol component volume fractions can be seen in figure 6.16. In this case the green boxes correspond to retrievals were the mean temperature profile of Dakar has been taken in the simulations and in the synthetic retrievals, the blue and red boxes represents the retrievals where the mean temperature profile of Dakar has been used in the simulations but correspondingly the minimum and maximum profiles of figure 6.15 have been assumed in the synthetic retrievals.

As it can be appreciated, the changes in this magnitude, in general, do not constitute a significant

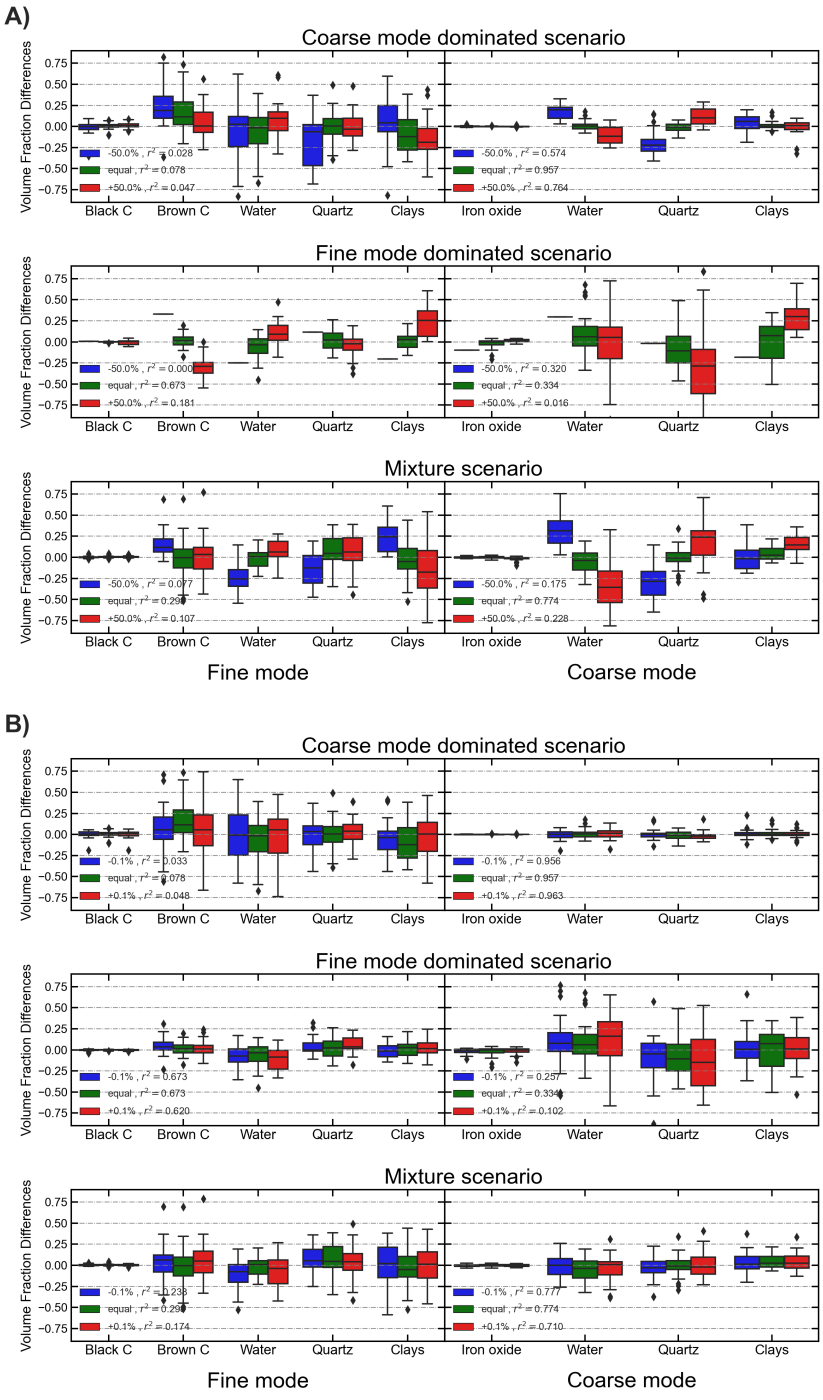

Figure 6.12: Volume fraction differences of aerosol components for scenarios with realistic noisy measurements and a high aerosol load ($AOD_{440nm} = 0.4$). The different color boxes represent retrievals performed assuming the same water vapor concentration (green) in the simulations and in the retrievals, for the blue and red the minimum and maximum climatological daily variations of H_2O concentration (top panel) and CO_2 (bottom panel) for Dakar has been taken in the retrievals in comparison with the mean daily values taken in the simulations. Each panel from top to bottom corresponds to a coarse, fine or mixture dominated scenario. The horizontal line in the boxes represents the median, the color box limits the 25 and 75 percentiles of the difference distribution, the whiskers mark the maximum and minimum limits to consider outliers and the diamonds represent the outliers.

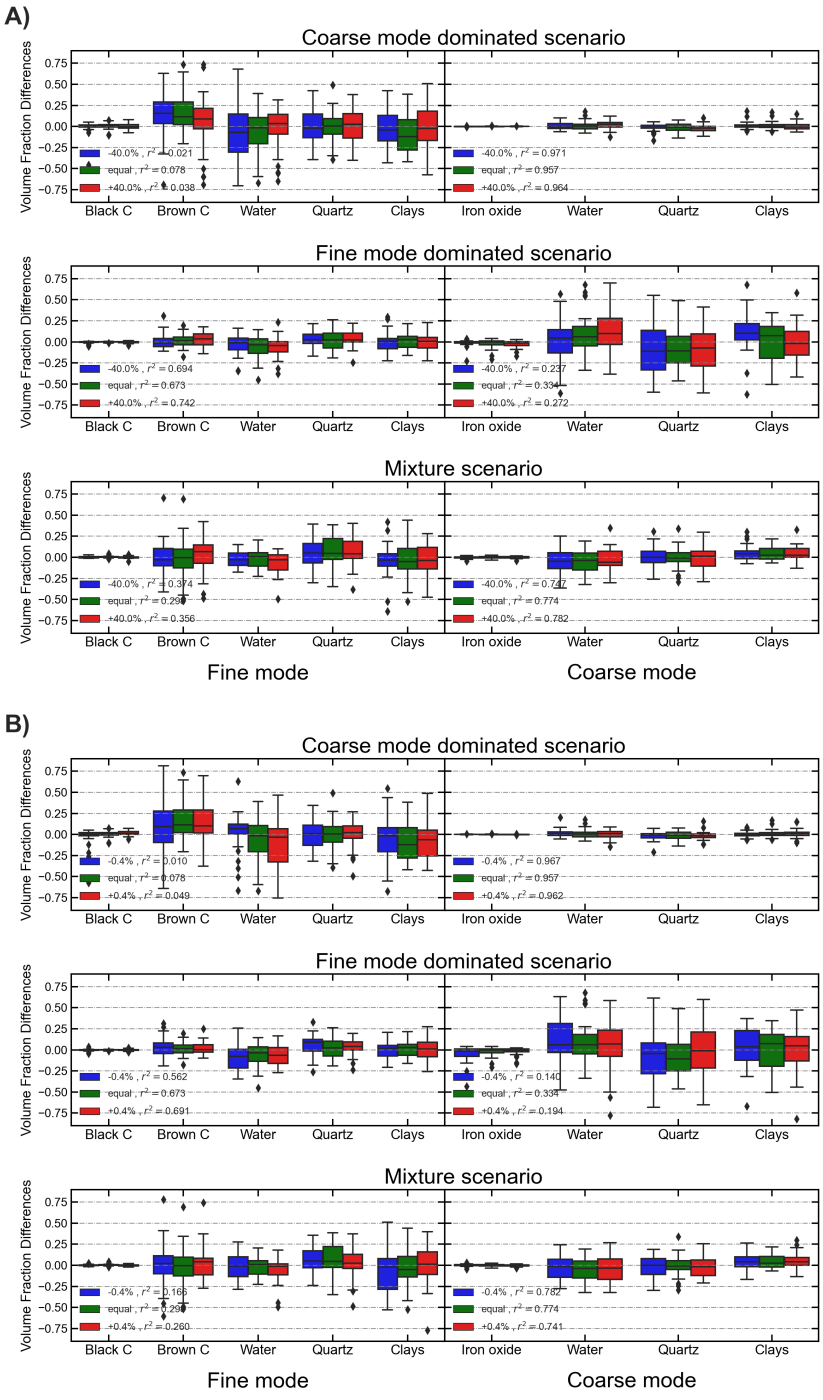

Figure 6.13: Volume fraction differences of aerosol components for scenarios with realistic noisy measurements and a high aerosol load (AOD_{440nm} = 0.4). The different color boxes represent retrievals performed assuming the same water vapor concentration (green) in the simulations and in the retrievals, for the blue and red the minimum and maximum climatological daily variations of N_2O concentration (top panel) and CH_4 (bottom panel) for Dakar has been taken in the retrievals in comparison with the mean daily values taken in the simulations. Each panel from top to bottom corresponds to a coarse, fine or mixture dominated scenario. The horizontal line in the boxes represents the median, the color box limits the 25 and 75 percentiles of the difference distribution, the whiskers mark the maximum and minimum limits to consider outliers and the diamonds represent the outliers.

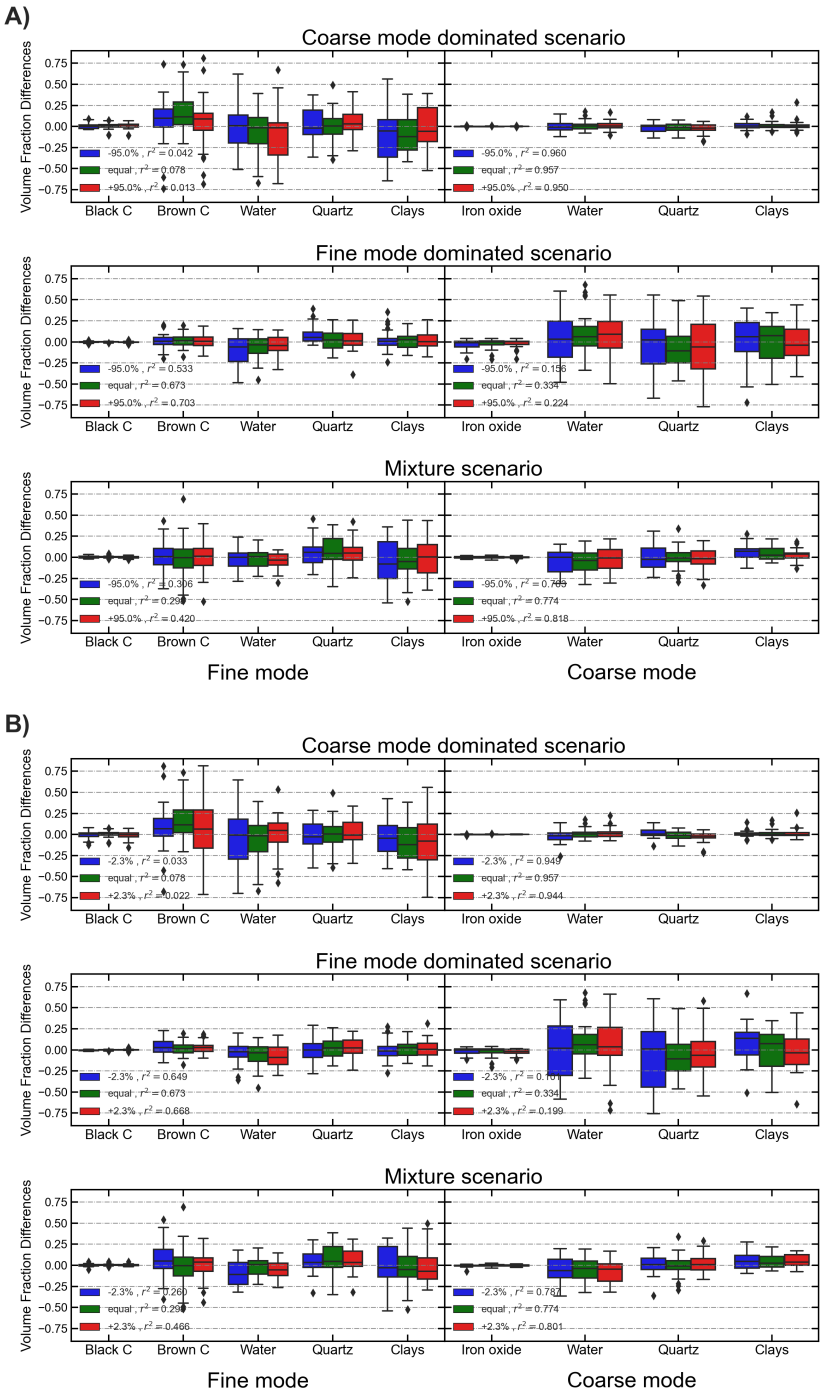

Figure 6.14: Volume fraction differences of aerosol components for scenarios with realistic noisy measurements and a high aerosol load (AOD_{440nm} = 0.4). The different color boxes represent retrievals performed assuming the same water vapor concentration (green) in the simulations and in the retrievals, for the blue and red the minimum and maximum climatological daily variations of NO_2 concentration (top panel) and O_3 (bottom panel) for Dakar has been taken in the retrievals in comparison with the mean daily values taken in the simulations. Each panel from top to bottom corresponds to a coarse, fine or mixture dominated scenario. The horizontal line in the boxes represents the median, the color box limits the 25 and 75 percentiles of the difference distribution, the whiskers mark the maximum and minimum limits to consider outliers and the diamonds represent the outliers.

source of uncertainty in the retrieved volume fractions. The dominant modes of each scenario are barely affected by these changes in the temperature vertical profile. The coarse mode fractions of the coarse mode dominated scenario do not present almost any degradation. On the other hand, the fine mode fractions of Brown Carbon and Quartz of the fine mode dominated scenario present small biases of around 5%. In the case of the mixture scenario, no significant bias is appreciated, however a slight increase of the dispersion of the results can be observed.

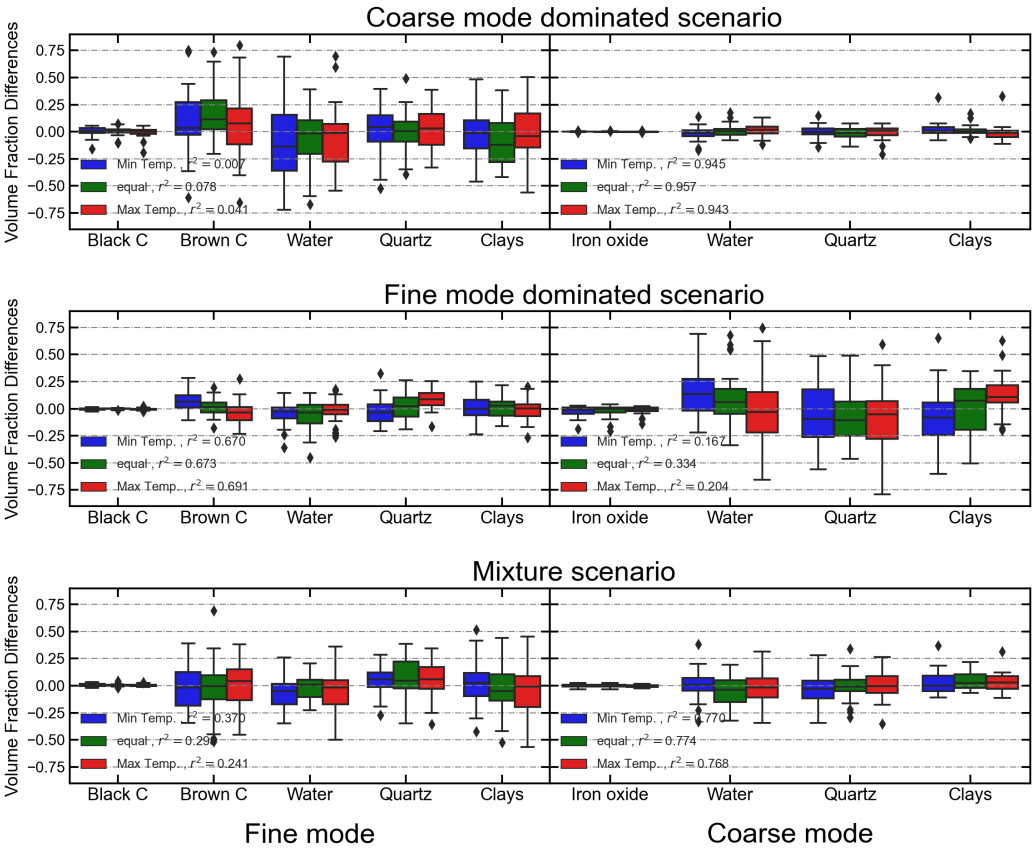

Figure 6.16: Volume fraction differences of aerosol components for scenarios with realistic noisy measurements and a high aerosol load (AOD_{440nm} = 0.4). The different color boxes represent retrievals performed assuming the same temperature vertical profile (green) in the simulations and in the retrievals, for the blue and red the minimum and maximum climatological daily variations of temperature vertical profile for Dakar has been taken in the retrievals in comparison with the mean daily values taken in the simulations. Each panel from top to bottom corresponds to a coarse, fine or mixture dominated scenario. The horizontal line in the boxes represents the median, the color box limits the 25 and 75 percentiles of the difference distribution, the whiskers mark the maximum and minimum limits to consider outliers and the diamonds represent the outliers.

At the sight of the results of these tests, for aerosol loads with an AOD at 440 nm of 0.4, the precision of the ECMWF reanalysis databases is enough to achieve a proper accuracy in the retrieved volume fractions.

6.2.3.3 Uncertainties of aerosol vertical distribution

Aerosol vertical profiles can be complex and multilayer distributions are not rare. GRASP enables the use of lidar profile measurements as input of the retrieval, this added information will synergically improve the results because a more accurate relation could be established between the aerosol load of each level and its corresponding temperature. However, the time constraints of this thesis have limited the current study to the use of sunphotometer and CLIMAT measurements as the input of the retrieval scheme. On the other hand, the simplified gaussian or exponential vertical distributions

have been proved to be useful in aerosol retrievals. Hitherto, all the GRASP retrievals made without lidar data as part of the input follow this methodology. However, as the temperature is a significant magnitude in aerosol retrievals at the TIR spectral range, the uncertainties introduced by the assumed aerosol vertical profile shapes need to be more carefully evaluated.

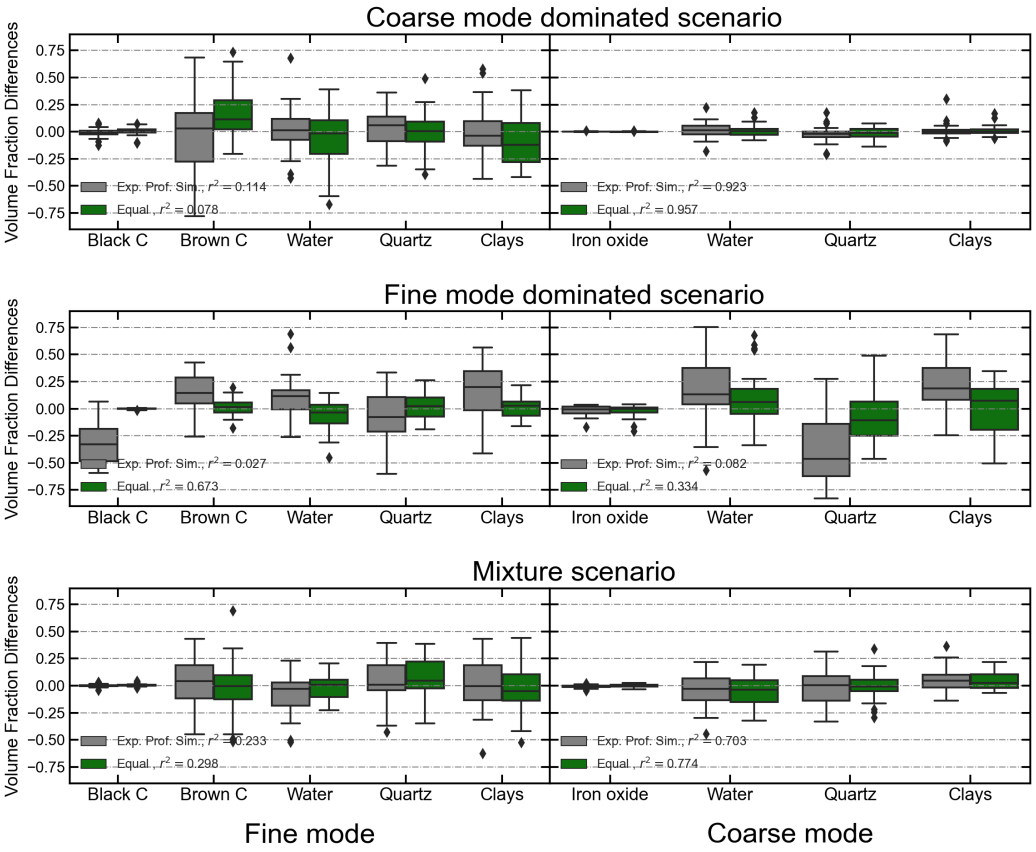

Figure 6.17: Volume fraction differences of aerosol components for scenarios with realistic noisy measurements and a high aerosol load (AOD_{440nm} = 0.4). The different color boxes represent retrievals performed assuming the same aerosol vertical profile shape (green) in the simulations and in the retrievals, but the grey boxes represent comparisons assuming a gaussian aerosol vertical profile shape in the simulations and an exponential gaussian aerosol vertical profile shape in the retrievals. Each panel from top to bottom corresponds to a coarse, fine or mixture dominated scenario. The horizontal line in the boxes represents the median, the color box limits the 25 and 75 percentiles of the difference distribution, the whiskers mark the maximum and minimum limits to consider outliers and the diamonds represent the outliers.

Figure 6.17 shows the volume fractions differences for synthetic retrievals with respect to the reference simulations, where the green boxes represent comparisons in which a gaussian vertical shape has been selected in both simulations and retrievals. On the other hand, the grey boxes represent comparisons where the simulations have been done with an aerosol load vertically distributed following an exponential shape and a gaussian shape has been assumed for the retrievals.

The coarse mode is in general not affected by the uncertainty in the shape of the aerosol vertical profile for scenarios with a significant load of this mode, only a higher dispersion of the retrieved fractions can be appreciated.

However, the aerosol shape is clearly a crucial factor for the retrieval of fine mode fractions. Not only the dispersion of these retrieved fractions is increased, but also a significant loss of correlation in the fine mode dominated scenario can be seen. In this case, the correlation coefficient diminishes from 0.673, when the aerosol profile is known, to 0.027. The Black Carbon is by far the more degraded fraction, with a crucial increase of the dispersion and a negative bias which reaches 30%. The rest of the fine mode fractions of this fine mode dominated scenario also present important biases ranging

from 10% to 20%. The results corresponding to the mixture scenario do not present any significant loss of accuracy in the coarse mode fractions. However, the dispersion of the comparisons corresponding to the fine mode presents a clear increase.

The results shown by these tests clearly remark the importance of the inclusion of lidar measurement profiles as input of this retrieval scheme in order to crucially improve the fine mode retrieved fractions.

6.2.3.4 Uncertainties of surface properties

In aerosol retrievals at the solar spectral range which include only upward looking instruments, the effect of the surface is not crucial. However, a correct characterization of the surface BRDF provides an enhancement of the retrieval accuracy. At TIR, the surface and atmospheric thermal emission are the main sources of radiance. Thus, even with the upward looking measurement geometries considered in this retrieval scheme, the surface temperature and emissivity may play a significant role in the retrieved volume fractions. As it has been said before, at the TIR range the surface is going to be considered as lambertian. Thus, these two parameters are enough to model it.

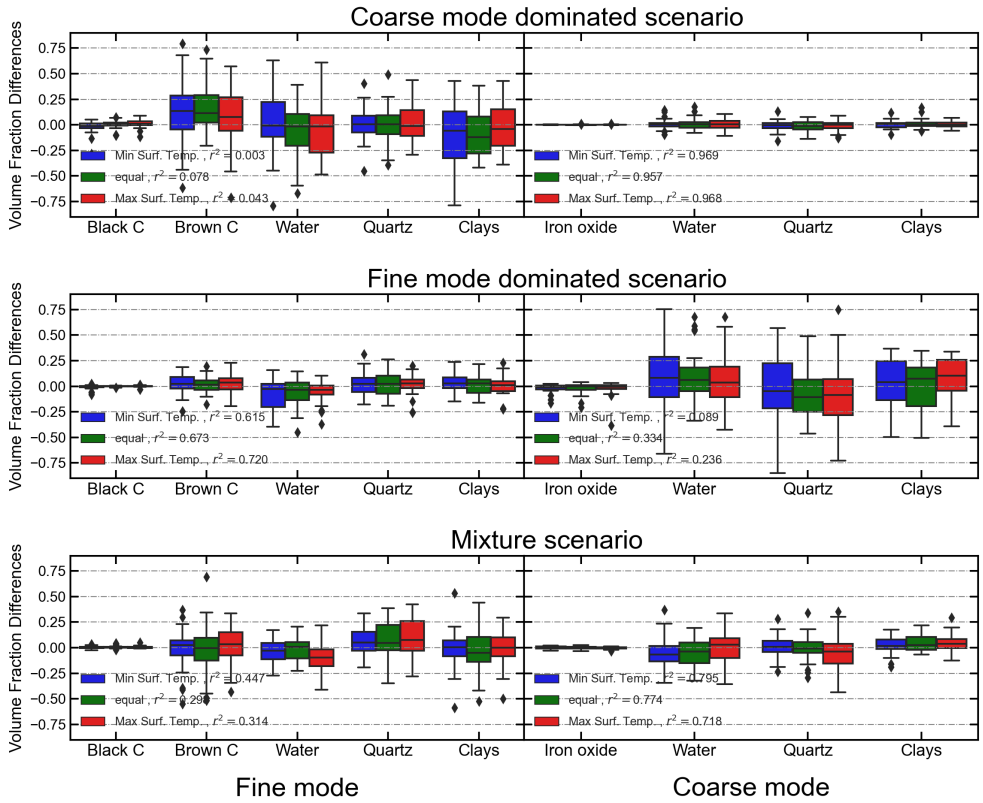

Figure 6.18: Volume fraction differences of aerosol components for scenarios with realistic noisy measurements and a high aerosol load (AOD_{440nm} = 0.4). The different color boxes represent retrievals performed assuming the same surface temperature (green) in the simulations and in the retrievals, for the blue and red the minimum and maximum climatological daily variations of surface temperature for Dakar has been taken in the retrievals in comparison with the mean daily values taken in the simulations. Each panel from top to bottom corresponds to a coarse, fine or mixture dominated scenario.

Figure 6.18 shows the volume fraction differences between the reference simulations and the synthetic retrievals, where the green boxes represent comparisons in which the mean daytime surface temperature of Dakar (296.57 K) has been taken for the simulations and the retrievals, the blue and red boxes represent correspondingly comparisons where the simulations were done with a mean daytime surface temperature but the retrievals correspond to mean minimum (293.97 K) and maximum (299.61 K) daytime surface temperatures. Any special uncertainty is introduced by this parameter. As

in the previous tests, the coarse mode is in general less affected, and a higher dispersion of the fine can be appreciated in the retrievals where the surface temperature has been perturbed. Any bias can be addressed.

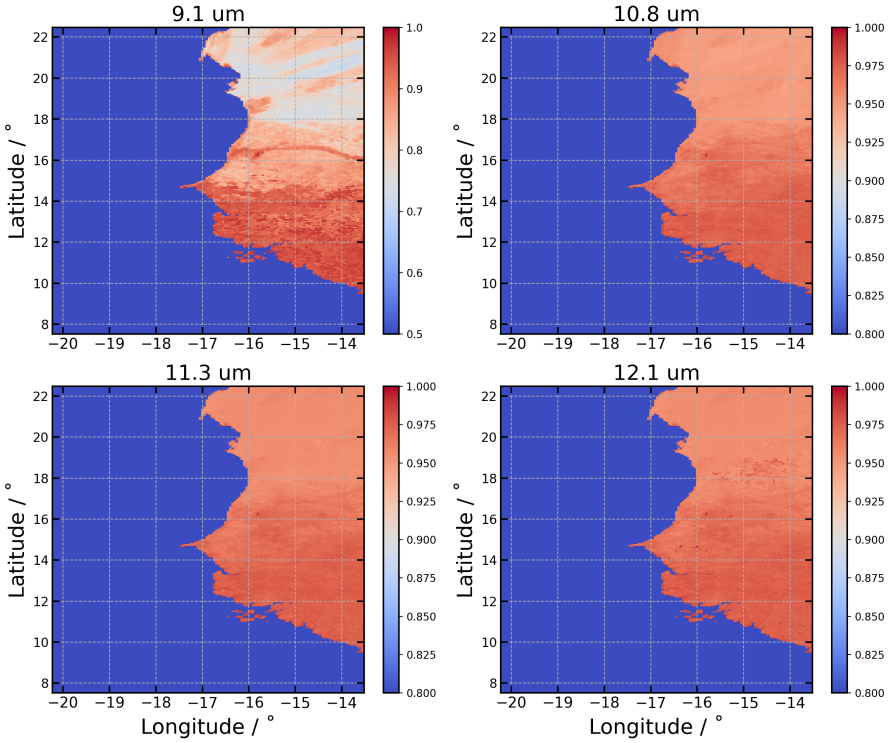

Figure 6.19: Average surface emissivity around Dakar area of LP DAAC NASA database at the closest wavelengths to CLIMAT channels.

The average emissivity of the Dakar area of the closest wavelengths of CAMEL database to the CLIMAT channels can be seen in figure 6.19. The surface of this region presents a high emissivity with a mean value around 0.95 at these TIR wavelengths for the pixels around Dakar area. The surface emissivity closer to the 8.7 μm CLIMAT channel is by far the most variable in temporal or spatial terms. However, even for this channel a mean temporal variability of 0.01 and a mean spatial variability (taking the neighbor pixels) of 0.019 is obtained. The uncertainties introduced in the retrieved volume fractions by this surface emissivity variability can be seen in figure 6.20. The effect of these variations of temperature emissivity do not introduce any significant error or bias in the retrieval.

6.2.3.5 Uncertainties due to mixing rule methodology

The effect of the different mixing rules in the aerosol scattering properties at TIR range has already been exposed in a previous chapter of this thesis. This section is devoted to the analysis of the differences introduced on the retrieved volume fractions by the different methodologies to obtain the total refractive index. In order to provide some insights about the uncertainty produced by the assumption of the aerosol internal structure, the purple boxes in figure 6.21 represent the volume fraction differences corresponding to comparisons of synthetic retrievals made assuming a volume weighted linear mixture but whose corresponding simulations have been done following a Maxwell-Garnett methodology. On the other hand, the green boxes in figure 6.21 correspond to comparisons in which both the synthetic retrievals and the simulations have been done according to a volume weighted linear mixture methodology. Black Carbon, Brown Carbon, Iron Oxides and clays are almost not affected by the changes introduced by the mixing rule for either fine or coarse mode fractions. In the case of water fractions, whereas the fine mode does not present any significant deviation, a positive bias of almost 25% can be observed in the case of the coarse mode fractions. A similar behavior can be observed in the case of Quartz, whereas the fine mode fractions of this component are almost unperturbed, a negative bias of around -20% can be appreciated for the coarse mode fractions.

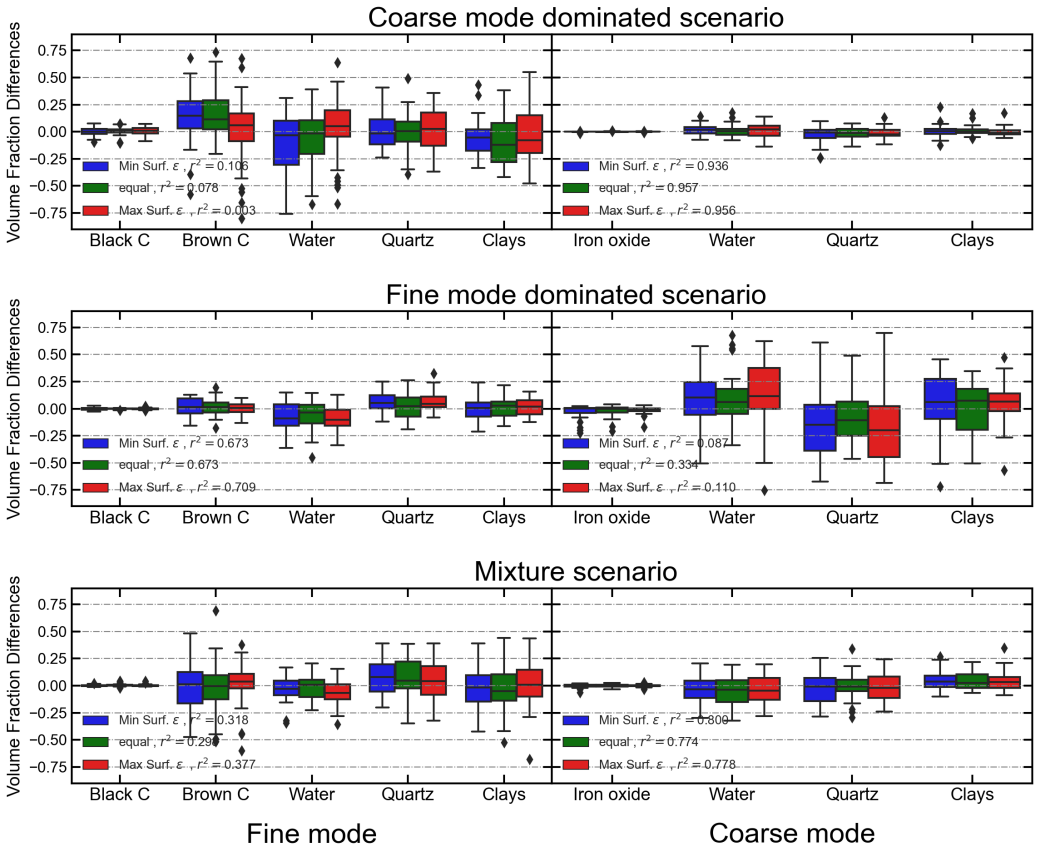

Figure 6.20: Volume fraction differences of aerosol components for scenarios with realistic noisy measurements and a high aerosol load (AOD_{440nm} = 0.4). The different color boxes represent retrievals performed assuming the same surface emissivity (green) in the simulations and in the retrievals, for the blue and red the minimum and maximum climatological daily variations of surface emissivity for Dakar has been taken in the retrievals in comparison with the mean daily values taken in the simulations. Each panel from top to bottom corresponds to a coarse, fine or mixture dominated scenario. The horizontal line in the boxes represents the median, the color box limits the 25 and 75 percentiles of the difference distribution, the whiskers mark the maximum and minimum limits to consider outliers and the diamonds represent the outliers.

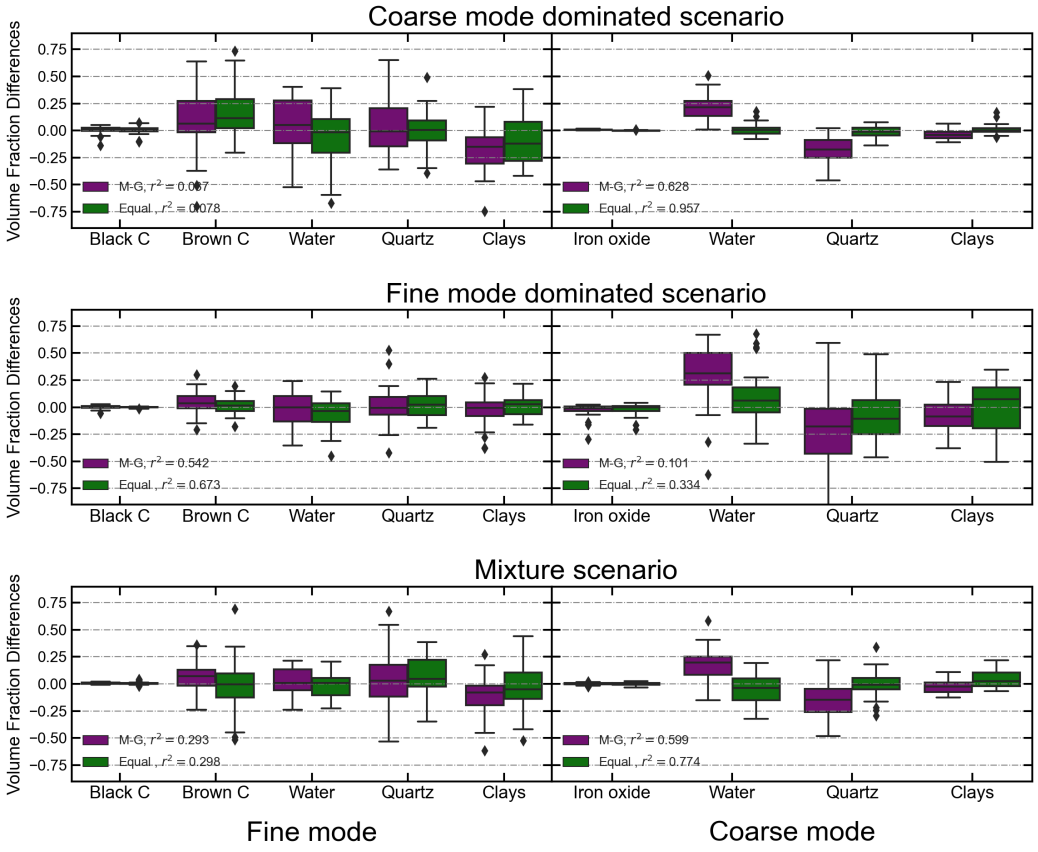

Figure 6.21: Volume fraction differences of aerosol components for scenarios with realistic noisy measurements and a high aerosol load (AOD_{440nm} = 0.4). The different color boxes represent retrievals performed assuming the same aerosol mixing rule (green) in the simulations and in the retrievals, and the purple boxes represent comparisons assuming a Maxwell-Garnett mixture in the simulations and a Volume Weighted mixture in the retrievals. Each panel from top to bottom corresponds to a coarse, fine or mixture dominated scenario. The horizontal line in the boxes represents the median, the color box limits the 25 and 75 percentiles of the difference distribution, the whiskers mark the maximum and minimum limits to consider outliers and the diamonds represent the outliers.

In general, the different mixing rule methodologies considered here do not seem to introduce significant changes in the retrieved fractions despite the coarse mode fractions of water and Quartz. Further analysis of the accuracy of these methodologies and the inclusion of new approaches (e.g. Core-Shell) are necessary to be made in future steps.

6.2.3.6 Uncertainties due to components definition

As it has been shown in previous chapters of this thesis, the components which normally form aerosol particles present a vast range of variability. Indeed, all the retrieved component fractions correspond to groups of species with similar optical and chemical properties. However, despite these kind of classifications being useful, following this grouping methodology can introduce significant uncertainties because of different reasons. For example, not all species are always present in the real particles. However, the lower volume fraction limits allowed in the retrieval for all species is very close to zero. Thus, this is not going to be considered as an important source of error. Particularly, this section is focused on the analysis of the errors introduced by the simplifications made in the definition of the "clays" fractions. As it has been said, here "clays" refers to a volume weighted internal mixture of Kaolinite (40%), Illite (40%) and Montmorillonite (20%). Thus, the clay material in the real atmospheric particles could highly differ from these assumed fractions that are fixed.

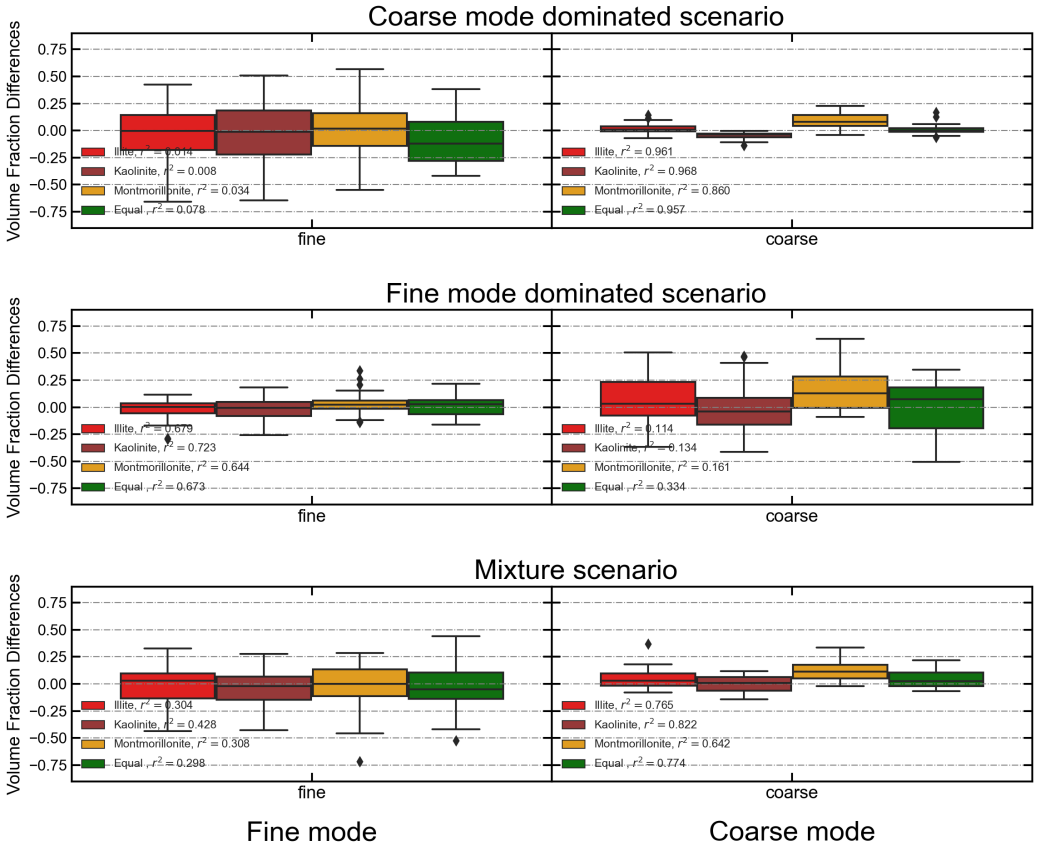

Figure 6.22: Volume fraction differences of aerosol components for scenarios with realistic noisy measurements and a high aerosol load (AOD_{440nm} = 0.4). The different color boxes represent retrievals performed assuming the same clays aerosol component (green) in the simulations and in the retrievals, the rest of the colors represent comparisons where the retrievals have been done exchanging the clays mixture assumed in the simulations by the pure components forming the mixture, correspondingly Ilite, Kaolinite and Montmorillonite. Each panel from top to bottom corresponds to a coarse, fine or mixture dominated scenario. The horizontal line in the boxes represents the median, the color box limits the 25 and 75 percentiles of the difference distribution, the whiskers mark the maximum and minimum limits to consider outliers and the diamonds represent the outliers.

The different color boxes in figure 6.22 show the volume fraction differences for comparisons of synthetic retrievals where clays fractions have been substituted by the pure components, whereas the corresponding simulations have been done with the clays mixture assumed until now. In the case of the green box, in both the simulations and in the synthetic retrievals the same clays mixture has been used. As it can be appreciated the optical characteristics of the different clay species taken here are similar enough to avoid any important deviation or bias.

6.3 Application to measurements in Dakar

Dakar is a densely populated city (1.000.000 inhabitants) situated on the west coast of the African continent (14.70170° North, 17.42560° West) with a mean elevation of almost 0.0 meters above the sea level. In particular, the instrumentation selected for the application of the retrieval scheme proposed above is situated in the facilities of IRD (Institut de Recherche et Développement, Dakar Belair AERONET site). This station is elevated around 15.0 Meters above the sea level, and it is located at 300 m from the coast. The site is thus affected by urban population to some degree. However, the site is mainly known as influenced by local and transported from Sahara and Sahel region mineral dust. The atmospheric dust in Senegal is present practically all year long with picks that appear mainly from spring to fall; the winter months are influenced by biomass burning aerosol transported from the Sa-

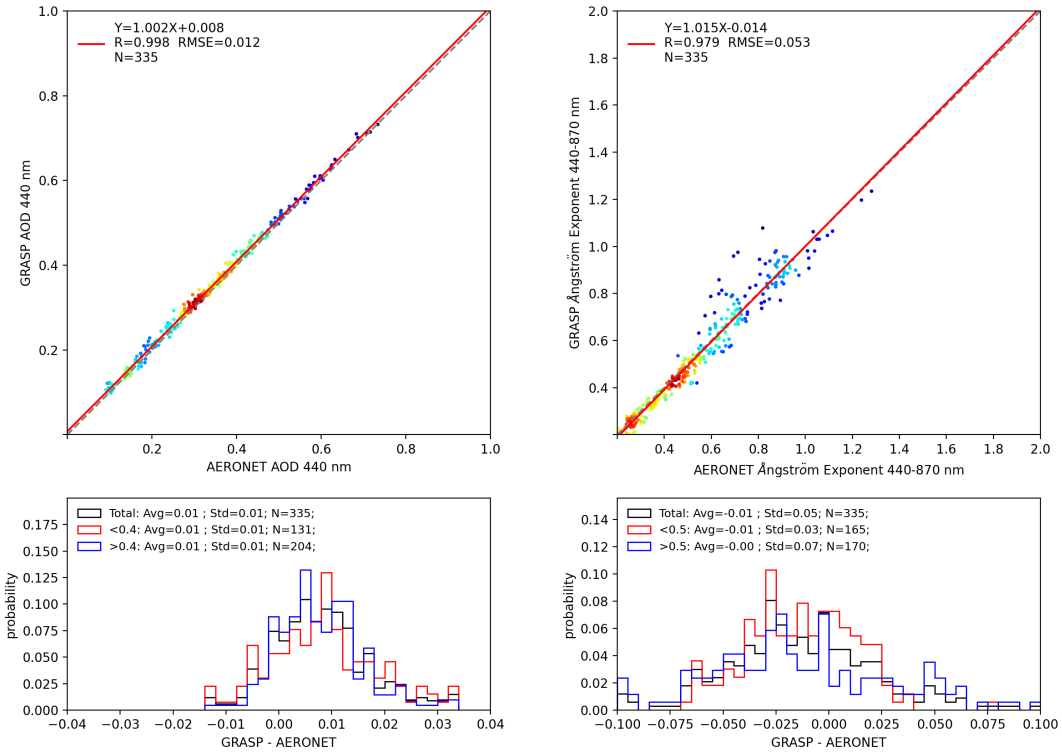

Figure 6.23: Intercomparison of AOD at 440 nm (left panel) and Angstrom Exponent 440-870 nm (right panel) between GRASP enhanced dust retrieval and AERONET inversion at Dakar Belair station for the complete months of November 2020, January 2021 and April 2021. In the bottom part of the panels the probability distributions of the differences between both algorithms for each product can be found.

hel region (**?**, **?**).

The observation platform at the roof level height counts with a sunphotometer, a fluxmeter station, a CLIMAT TIR radiometer and a MicroLidar at 532 nm. Thus, a very complete information context is available in order to make a correct interpretation of the measurements and retrievals. The location of Dakar Belair station in a coastal region of south west of the Saharan desert enables the observation of aerosol mineral dust, biomass burning and marine particles. AERONET database counts with a vast measurements record, the aerosol monitoring started in a very close site called Dakar station in 1996. Unfortunately, CLIMAT measurements at this place started only recently. The consistent record of TIR measurements in Dakar (practically the MBour city located 80 km south from Dakar) had started in February of 2014. However, as explained before, the extended calibration of the TIR radiometer for the pursued here objectives had reduced the data availability. Thus, the months of November 2020, January 2021 and April 2021 have been selected as the reference periods of time to perform the retrievals and the corresponding validation against AERONET inversion products.

Figure 6.23 shows the intercomparison of the AOD at 440 nm and the Angstrom Exponent 440-870 nm (left and right panel respectively) between the corresponding retrievals of the proposed GRASP retrieval scheme and the AERONET products for the three selected months. In the bottom part of each panel the probability distributions of the differences between GRASP and the references can be observed. Both products present a very high correlation with r^2 values of 0.998 and 0.979 for AOD and Angstrom exponent respectively. While the dispersion of the AOD values is not significant, higher values can be appreciated in the case of the Angstrom exponent with a RMSE (Root Mean Square Error) of 0.053. A slight overestimation of the GRASP AOD at 440 nm of 0.005 can be observed in comparison with the AERONET reference. However, it should be noted that the standard AERONET AOD uncertainty is 0.01, and the methodologies to account for gas absorption in both algorithms are

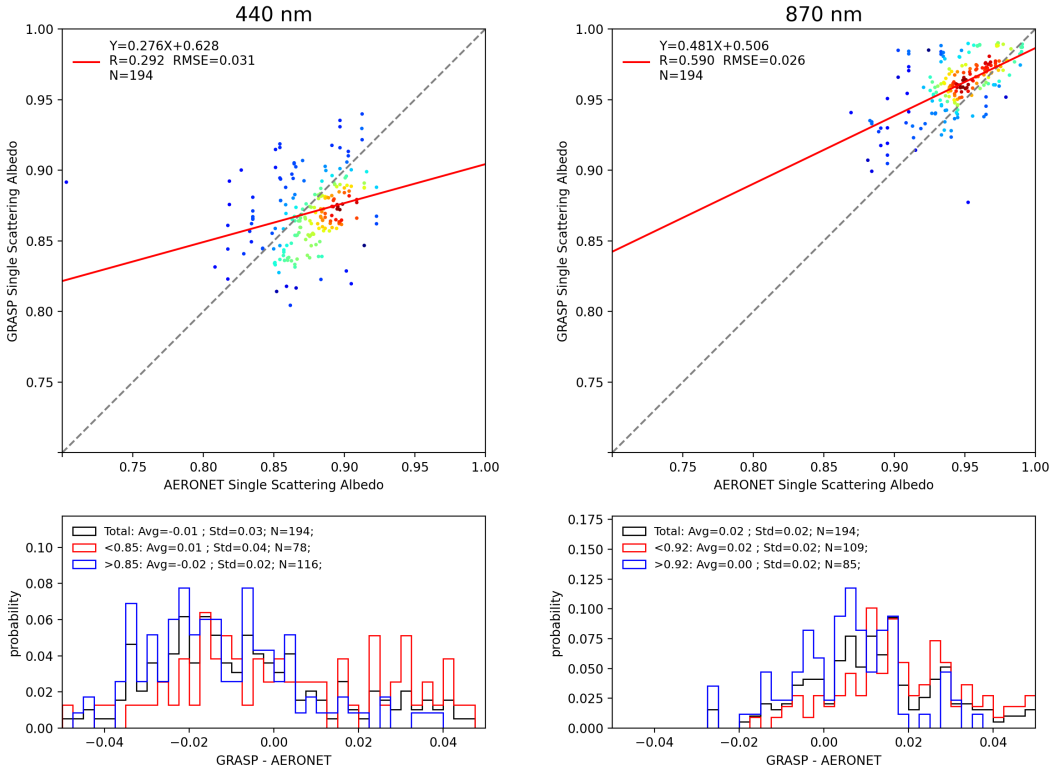

Figure 6.24: Intercomparison of Single Scattering Albedo at 440 nm (left panel) and at 870 nm (right panel) between GRASP enhanced dust retrieval and AERONET inversion at Dakar Belair station for the complete months of November 2020, January 2021 and April 2021. In the bottom part of the panels the probability distributions of the differences between both algorithms for each product can be found.

totally different. Thus, this small bias and dispersion cannot be taken as significant. On the other hand, the Angstrom exponent derived from GRASP retrieval is slightly biased to smaller values. A visual inspection of the PSD retrieved by both methodologies (not shown) confirms this deviation. In general, GRASP coarse mode particle size distributions tend to be centered around a larger radius. However, this is taken as an expected behavior because of the small value of these deviations and the enhanced sensitivity to this radius range introduced by CLIMAT measurements.

The intercomparison corresponding to the Single Scattering Albedo (SSA) at two wavelengths, 440 and 870 nm, can be seen in figure 6.24. The correlation of this optical magnitude is significantly lower compared with the two previous cases, which can be partially explained by the low range of the SSA values in the whole considered period, around only 10%. While the SSA at 440 nm is slightly biased to negative values, an opposite behavior of this optical magnitude can be appreciated at 870 nm. However, these uncertainties are always smaller than 6%.

The temporal evolution of the AMH for all inverted periods can be seen in figure 6.25. A high stable behavior can be observed for the three months, with a mean value of approximately 500 meters for November 2020 and January 2021, with maximum values of around 1500 meters. On the other hand, a higher height can be observed in April 2021, with mean values around 1000 meters. A qualitative comparison of the obtained heights with the simultaneous lidar measurements offer a good agreement. On average, the main part of the aerosol load of Dakar is located at the Planetary Boundary Layer, which presents an extension of around 1000 meters in the winter months of 2020-2021 and a clear expansion can be noted in April that is consistent with a possibly higher boundary layer in this season.

In order to provide some insights about the dust components in Dakar Belair site, the mean volume fractions for the fine and coarse modes can be seen in figure 6.26, where each panel corresponds

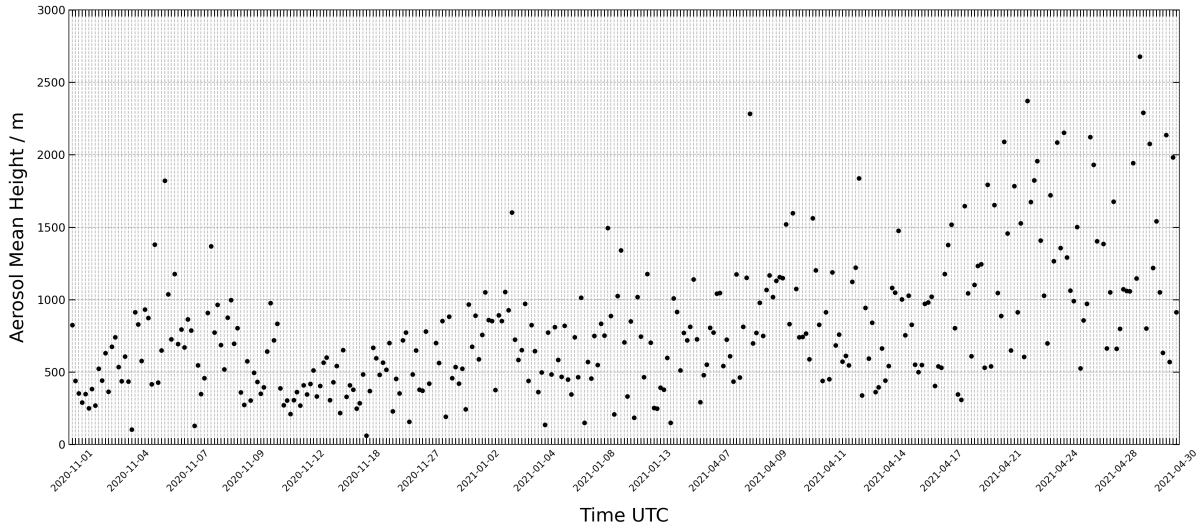

Figure 6.25: Temporal evolution of the Aerosol Mean Height product expressed in meters retrieved by GRASP enhanced dust retrieval at Dakar Belair station for the complete months of November 2020, January 2021 and April 2021 (note that the abscissa is not in real time scale).

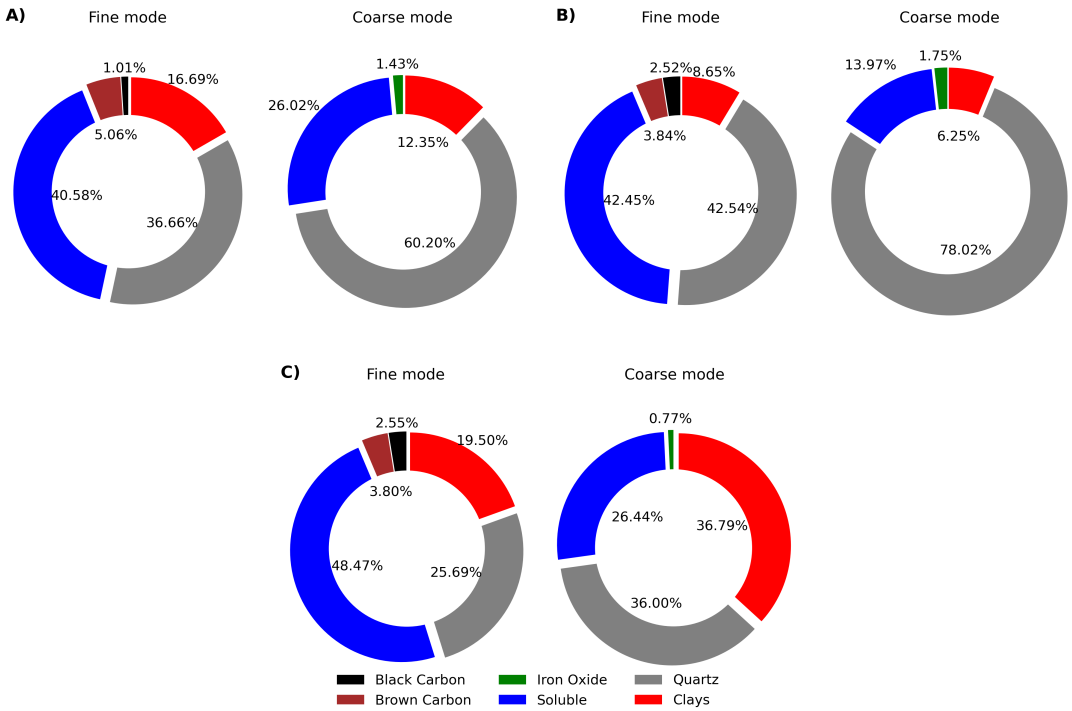

Figure 6.26: Mean volume fractions for fine and coarse mode retrieved by GRASP enhanced dust approach for the months of November 2020 (Panel A), January 2021 (Panel B) and April 2021 (Panel C).

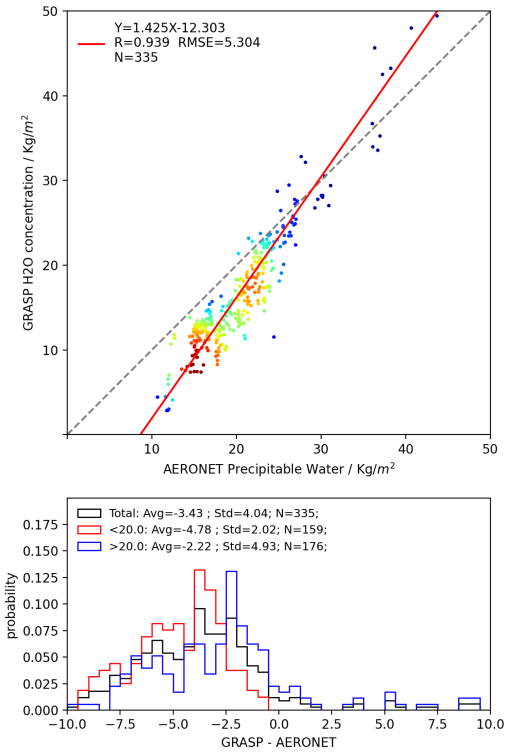

Figure 6.27: Mean volume fractions for fine and coarse mode retrieved by GRASP enhanced dust approach for the months of November 2020 (Panel A), January 2021 (Panel B) and April 2021 (Panel C).

to a different month. In general, the variation of dust components within a day time period was found as not significant and a very stable behavior has been found for all the different fractions of both particle size modes. However, when longer time periods are averaged, some differences in the aerosol components become appreciable.

Water soluble and Brown Carbon are the most stable especies. In the case of water soluble, almost no variability from month to month either in the coarse or the fine mode are observed for the given data sample. While it is remarkable that the fine mode water soluble fraction is larger (∼43% on average) then the coarse mode (∼22% on average), which is consistent with generally more hydrophobic coarse dust. A larger concentration of highly absorbing components can be found in the fine mode (∼2% for Black Carbon and ∼4% for Brown Carbon) in comparison with the coarse mode (∼1 to ∼2% of iron oxides). A clear dominance of the Quartz fraction over clays is found for November 2020 and January 2021, where 3 to 12 times more Quartz than clays are observed. However, a clear change of tendency is appreciated in April 2021, where aerosols present a similar fraction of Quartz and clays for both fine and coarse modes. Overall, the retrieved aerosol components and AMH present a seasonal variability that is in line with possible physical expectations.

However, for the moment there is no available direct validation of the obtained components fractions against an independent source. For the future steps of this work it is planned to add alternative sources of information, such as reanalysis comparisons, in situ measurements or analysis of HYSPLIT (Stein et al., 2015) backtrayectories, which help to support the validity of the presented results about aerosol components volume fractions.

Nevertheless, one of the retrieved parameters can be directly validated. That is, can be done the intercomparisons (figure 6.27) of the total column water vapor retrieved by the GRASP/Components synergy solar/TIR algorithm and the total column precipitable water of the AERONET product (Smirnov et al., 2004). As it was mentioned before, in the original plan of this thesis the water vapor was not expected to be retrieved, but rather be part of the fixed input information. However, the

validation results presented in figure 6.27 illustrate sufficient sensitivity of the TIR radiometer measurements for quite reasonable accuracy of the water vapor retrieval..

It is important to note that the methodology to obtain these parameters in both algorithms is totally different. Whereas in GRASP/Components synergy solar/TIR the total column concentration of water vapor is directly retrieved with the rest of aerosol properties, the AERONET precipitable water product is obtained a posteriori. That is, once the AERONET aerosol retrieval has been done, the AOD at 940 nm is interpolated to fit the remaining absorption of this channel to the corresponding water vapor concentration. Thus, the retrieval of both parameters is not performed in a simultaneous way.

While a high correlation between both magnitudes can be found with a r^2 of 0.939, a clear mean bias of approximately 3 kg/m^2 is also found. This value represents 14% of the average water concentration value (21 kg/m^2) in the considered time periods. According to Pérez-Ramírez et al. (2014), the mean uncertainty of the AERONET water vapor product can be established between 12 and 15%. Thus, the differences obtained here are within reasonable limits of accuracy. However, the AERONET product also presents a negative bias, between 6 and 9%, against independent products based on microwave radiometry and GPS signals. Thus, further studies and validation are needed to understand the degree of accuracy of this GRASP/Components synergy solar/TIR retrieved water vapor.

6.4 References

Claquin, T., Schulz, M., and Balkanski, Y. (1999). Modeling the mineralogy of atmospheric dust sources. *Journal of Geophysical Research: Atmospheres*, 104(D18):22243–22256.

Di Biagio, C., Formenti, P., Balkanski, Y., Caponi, L., Cazaunau, M., Pangui, E., Journet, E., Nowak, S., Caquineau, S., Andreae, M. O., et al. (2017). Global scale variability of the mineral dust long-wave refractive index: a new dataset of in situ measurements for climate modeling and remote sensing. *Atmospheric Chemistry and Physics*, 17(3):1901–1929.

Doppler, L., Carbajal-Henken, C., Pelon, J., Ravetta, F., and Fischer, J. (2014a). Extension of radiative transfer code momo, matrix-operator model to the thermal infrared–clear air validation by comparison to rttov and application to calipso-iir. *Journal of Quantitative Spectroscopy and Radiative Transfer*, 144:49–67.

Doppler, L., Preusker, R., Bennartz, R., and Fischer, J. (2014b). k-bin and k-ir: k-distribution methods without correlation approximation for non-fixed instrument response function and extension to the thermal infrared—applications to satellite remote sensing. *Journal of Quantitative Spectroscopy and Radiative Transfer*, 133:382–395.

Dubovik, O., Fuertes, D., Litvinov, P., Lopatin, A., Lapyonok, T., Doubovik, I., Xu, F., Ducos, F., Chen, C., Torres, B., Derimian, Y., Li, L., Herreras-Giralda, M., Herrera, M., Karol, Y., Matar, C., Schuster, G. L., Espinosa, R., Puthukkudy, A., Li, Z., Fischer, J., Preusker, R., Cuesta, J., Kreuter, A., Cede, A., Aspetsberger, M., Marth, D., Bindreiter, L., Hangler, A., Lanzinger, V., Holter, C., and Federspiel, C. (2021). A comprehensive description of multi-term lsm for applying multiple a priori constraints in problems of atmospheric remote sensing: Grasp algorithm, concept, and applications. *Frontiers in Remote Sensing*, 2:23.

Dubovik, O., Sinyuk, A., Lapyonok, T., Holben, B. N., Mishchenko, M., Yang, P., Eck, T. F., Volten, H., Munoz, O., Veihelmann, B., et al. (2006). Application of spheroid models to account for aerosol particle nonsphericity in remote sensing of desert dust. *Journal of Geophysical Research: Atmospheres*, 111(D11).

Hersbach, H. (2016). The era5 atmospheric reanalysis. In *AGU fall meeting abstracts*, volume 2016, pages NG33D–01.

Hook, S. (2017). Combined aster and modis emissivity database over land (camel) emissivity monthly global 0.05deg v002 [data set]. *NASA EOSDIS Land Processes DAAC*.

Inness, A., Ades, M., Agusti-Panareda, A., Barré, J., Benedictow, A., Blechschmidt, A.-M., Dominguez, J. J., Engelen, R., Eskes, H., Flemming, J., et al. (2019). The cams reanalysis of atmospheric composition. *Atmospheric Chemistry and Physics*, 19(6):3515–3556.

Journet, E., Balkanski, Y., and Harrison, S. P. (2014). A new data set of soil mineralogy for dust-cycle modeling. *Atmospheric Chemistry and Physics*, 14(8):3801–3816.

Li, L., Dubovik, O., Derimian, Y., Schuster, G. L., Lapyonok, T., Litvinov, P., Ducos, F., Fuertes, D., Chen, C., Li, Z., et al. (2019). Retrieval of aerosol components directly from satellite and ground-based measurements. *Atmospheric Chemistry and Physics*, 19(21):13409–13443.

Pérez-Ramírez, D., Whiteman, D. N., Smirnov, A., Lyamani, H., Holben, B. N., Pinker, R., Andrade, M., and Alados-Arboledas, L. (2014). Evaluation of aeronet precipitable water vapor versus microwave radiometry, gps, and radiosondes at arm sites. *Journal of Geophysical Research: Atmospheres*, 119(15):9596–9613.

Román, R., Benavent-Oltra, J. A., Casquero-Vera, J. A., Lopatin, A., Cazorla, A., Lyamani, H., Denjean, C., Fuertes, D., Pérez-Ramírez, D., Torres, B., et al. (2018). Retrieval of aerosol profiles combining sunphotometer and ceilometer measurements in grasp code. *Atmospheric Research*, 204:161–177.

Schaaf, C., Liu, J., Gao, F., and Strahler, A. H. (2011). Modis albedo and reflectance anisotropy products from aqua and terra. *Land Remote Sensing and Global Environmental Change: NASA's Earth Observing System and the Science of ASTER and MODIS*, 11:549–561.

Smirnov, A., Holben, B., Lyapustin, A., Slutsker, I., and Eck, T. (2004). Aeronet processing algorithms refinement. In *AERONET Workshop, El Arenosillo, Spain*, pages 10–14.

Sokolik, I. N. and Toon, O. B. (1999). Incorporation of mineralogical composition into models of the radiative properties of mineral aerosol from uv to ir wavelengths. *Journal of Geophysical Research: Atmospheres*, 104(D8):9423–9444.

Sokolik, I. N., Toon, O. B., and Bergstrom, R. W. (1998). Modeling the radiative characteristics of airborne mineral aerosols at infrared wavelengths. *Journal of Geophysical Research: Atmospheres*, 103(D8):8813–8826.

Stein, A., Draxler, R. R., Rolph, G. D., Stunder, B. J., Cohen, M., and Ngan, F. (2015). Noaa's hysplit atmospheric transport and dispersion modeling system. *Bulletin of the American Meteorological Society*, 96(12):2059–2077.

Conclusion and perspectives

Aerosols are one of the atmospheric constituents with a higher uncertainty in the effective Earth's radiative budget (Szopa et al., 2021). The vast variability of the chemical components which form these particles is one of the main reasons for this uncertainty. In addition, the composition of mineral particles and aerosols, in general, can have an impact on the environment, the air quality and even aviation safety. The aerosol components monitoring from ground-based and satellite measurements at the solar spectral range using GRASP algorithm has been formulated in Li et al. (2019). On the other hand, several studies showed the possibilities of aerosol retrievals from Thermal Infrared (TIR) spectral range (e.g.: DeSouza-Machado et al. (2010), Clarisse et al. (2013), Klüser et al. (2011), Klüser et al. (2012) and Klüser et al. (2015)). Retrievals restricted to work in this longwave part of the spectrum count with several appealing advantages such as: the possibility to measure both at day and night time, the satellite retrievals have less problems to deal with bright surfaces, and a higher sensitivity to coarse mode aerosols and mineral dust composition. However, only the TIR based retrievals have also obvious drawbacks as: the almost lack of sensitivity to fine mode aerosols, the lower sensitivity to particle size and shape, the important influence of gas absorption lines, and the influence of surface and atmospheric temperatures.

This thesis constitutes the framework for the synergy of solar and TIR measurements in the GRASP algorithm (GRASP stand for Generalized Retrieval of Atmosphere and Surface Properties) (Dubovik et al. (2011), Dubovik et al. (2014) and Dubovik et al. (2021)). The combination of measurements in both parts of the spectra provides complementary aerosol information. For instance, solar measurements provided by the AERONET (AErosol RObotic NETwork) (Holben et al., 1998) sunphotometer are highly sensitive to aerosol size distribution, refractive index and particle shape. Li et al. (2019) also showed how aerosol component information can be retrieved using the GRASP algorithm applied to remote sensing measurements in the solar part of the spectrum. An extension of this retrieval scheme up to TIR is suggested in the current work to enhance the sensitivity to aerosol coarse mode, enable the distinction between mineral species (e.g., quartz and clays) and provide a combined retrieval of the aerosol properties jointly with the total column water vapor and aerosol layer mean height.

In this thesis work, the corresponding necessary developments were dedicated to (i) the incorporation of thermal emission in radiative transfer code employed in GRASP forward calculations and (ii) accurate computation of radiances over spectral channels in any part of the electromagnetic spectrum. Thus, first of all, the original Successive Orders of Scattering radiative transfer of GRASP forward model, which is based on Lenoble et al. (2007), was expanded to include thermal emission. Moreover, different approaches to unify optical depth and temperature vertical profiles have been studied. In comparison with DISORT (DIScrete Ordinates Radiative Transfer) (Stamnes et al., 1988), the GRASP radiative transfer in TIR spectral range offered an accuracy of -0.005 K (0.003%) with a computation time around 8 times faster for the same configuration and vertically inhomogeneous conditions. As it has been said, the gas absorption lines are very important in TIR spectral channels. Even in the atmospheric windows where atmospheric transmissivity is very high, the absorption of some species as water vapor or CO_2 still plays a significant role in the total radiance. Thus, the column integrated gas absorption values used in GRASP for solar channels were not enough for this new TIR application. The line-by-line approach from CGASA (Coefficient of GAS Absorption) (Doppler et al., 2014a)has been included as GRASP input to precisely simulate gas absorption lines. Despite the high precision of this methodology, the demanding computation time required to perform retrievals exclude the line-by-

line approach. The K-distribution methodology "kbins" (Doppler et al., 2014b) was therefore adapted to make it part of GRASP input and speed up the calculations to make them feasible in terms of time. However, the highly varying refractive indexes of aerosol particles at TIR require to divide the channels at this spectral range in smaller parts where a flat aerosol spectral behavior can be assumed without a significant loss of accuracy. Thus, the methodology called "Subchannels" approach was also developed. In addition, a study was done on aerosol scattering properties at TIR, for a proper modeling and accounting for changes in shape and resonance effects.

Synthetic tests with and without measurement noise have been made to evaluate the capabilities of the proposed GRASP retrieval scheme to obtain a variety of aerosol characteristics. It included the particle size distribution, sphericity parameter, the aerosol mean height and the aerosol components volume fractions, including separation of Quartz and clays. Furthermore, the influence of the uncertainty in the ancillary fixed input information (e.g.: atmospheric temperature profiles, surface emissivity, gas concentration etc.) on the retrieved volume fractions of aerosol components was analyzed.

The application of the synergic combined retrieval of Solar and TIR measurements was done for the combination of an AERONET sunphotometer and a CLIMAT TIR radiometer (Legrand et al. (2000), Brogniez et al. (2003)) in the AERONET station of Dakar Belair, Senegal. The possibilities of CLIMAT radiometer for aerosol retrieval purposes were additionally explored in this study. A revision and extension of the calibration protocol of this instrument was made in order to satisfy the new required precision limits.

Finally an application to real data and a validation of the results against the corresponding products of the operational AERONET inversion was done for the months of November 2020, January 2021 and April 2021 at the Dakar Belair station; correlation values higher than 0.97 for AOD at 440 nm and Angstrom Exponent 440-870 nm were found. The derived volume fractions of aerosol components showed month to month variability consistent with physical expectations for this site. In addition, the simultaneously derived water vapor concentrations showed good agreement with the AERONET product and the mean aerosol layer height was in line with local lidar observations. It should be mentioned here that the possibility of the joint retrieval of aerosol properties and total column water vapor was identified only at the final stages of the work. Note that initially this characteristic was meant to be part of the fixed ancillary input information. Thus, the corresponding sensitivity tests were not conducted as it was done for the rest of the retrieved parameters. However, this parameter could be directly validated and the comparison with the AERONET precipitable water product (Smirnov et al. (2009), Pérez-Ramírez et al. (2014))showed an agreement within the expected uncertainty of AERONET, with a correlation of 0.94 and a bias of around -3 kg/m2.

The future steps of this work require efforts in two main directions. First of all, despite the aerosol optical and microphysical characteristics present high levels of correlation with AERONET reference, a deeper validation of the retrieved volume fractions is needed against independent external sources such as: reanalysis, soil composition analysis, in-situ measurements and correlation with HYSPLIT (Stein et al., 2015) backtrajectories to support the observed composition changes. Moreover, further understanding of the retrieved total column water vapor is necessary for potential correction of the observed negative bias. On the other hand, the main perspective of this work is in the application of the described framework of synergic and consistent retrievals using solar and TIR measurements for a longer time series of ground-based and spaceborne observations. The combination of 3MI (Multi-viewing, Multi-channel, Multi-polarisation Imager) (Marbach et al. (2015) and Fougnie et al. (2018)) and IASI (Infrared Atmospheric Sounding Interferometer) (Siméoni et al. (1997), Clerbaux et al. (2009))instruments, which will be flying on the same platform, seems to offer promising possibilities for the retrieval scheme developed here. The hyperspectral channels of the IASI instrument may enable the combined retrieval of other atmospheric gasses (in addition to water vapor) jointly with the enhanced aerosol products.

Brogniez, G., Pietras, C., Legrand, M., Dubuisson, P., and Haeffelin, M. (2003). A high-accuracy multiwavelength radiometer for in situ measurements in the thermal infrared. part ii: Behavior in field experiments. *Journal of Atmospheric and Oceanic Technology*, 20(7):1023–1033.

Clarisse, L., Coheur, P.-F., Prata, F., Hadji-Lazaro, J., Hurtmans, D., and Clerbaux, C. (2013). A unified approach to infrared aerosol remote sensing and type specification. *Atmospheric Chemistry and Physics*, 13(4):2195–2221.

Clerbaux, C., Boynard, A., Clarisse, L., George, M., Hadji-Lazaro, J., Herbin, H., Hurtmans, D., Pommier, M., Razavi, A., Turquety, S., et al. (2009). Monitoring of atmospheric composition using the thermal infrared iasi/metop sounder. *Atmospheric Chemistry and Physics*, 9(16):6041–6054.

DeSouza-Machado, S., Strow, L., Imbiriba, B., McCann, K., Hoff, R., Hannon, S., Martins, J., Tanré, D., Deuzé, J., Ducos, F., et al. (2010). Infrared retrievals of dust using airs: Comparisons of optical depths and heights derived for a north african dust storm to other collocated eos a-train and surface observations. *Journal of Geophysical Research: Atmospheres*, 115(D15).

Doppler, L., Carbajal-Henken, C., Pelon, J., Ravetta, F., and Fischer, J. (2014a). Extension of radiative transfer code momo, matrix-operator model to the thermal infrared–clear air validation by comparison to rttov and application to calipso-iir. *Journal of Quantitative Spectroscopy and Radiative Transfer*, 144:49–67.

Doppler, L., Preusker, R., Bennartz, R., and Fischer, J. (2014b). k-bin and k-ir: k-distribution methods without correlation approximation for non-fixed instrument response function and extension to the thermal infrared—applications to satellite remote sensing. *Journal of Quantitative Spectroscopy and Radiative Transfer*, 133:382–395.

Dubovik, O., Fuertes, D., Litvinov, P., Lopatin, A., Lapyonok, T., Doubovik, I., Xu, F., Ducos, F., Chen, C., Torres, B., Derimian, Y., Li, L., Herreras-Giralda, M., Herrera, M., Karol, Y., Matar, C., Schuster, G. L., Espinosa, R., Puthukkudy, A., Li, Z., Fischer, J., Preusker, R., Cuesta, J., Kreuter, A., Cede, A., Aspetsberger, M., Marth, D., Bindreiter, L., Hangler, A., Lanzinger, V., Holter, C., and Federspiel, C. (2021). A comprehensive description of multi-term lsm for applying multiple a priori constraints in problems of atmospheric remote sensing: Grasp algorithm, concept, and applications. *Frontiers in Remote Sensing*, 2:23.

Dubovik, O., Herman, M., Holdak, A., Lapyonok, T., Tanré, D., Deuzé, J., Ducos, F., Sinyuk, A., and Lopatin, A. (2011). Statistically optimized inversion algorithm for enhanced retrieval of aerosol properties from spectral multi-angle polarimetric satellite observations. *Atmospheric Measurement Techniques*, 4(5):975–1018.

Dubovik, O., Lapyonok, T., Litvinov, P., Herman, M., Fuertes, D., Ducos, F., Lopatin, A., Chaikovsky, A., Torres, B., Derimian, Y., et al. (2014). Grasp: a versatile algorithm for characterizing the atmosphere. *SPIE Newsroom*, 25.

Fougnie, B., Marbach, T., Lacan, A., Lang, R., Schlüssel, P., Poli, G., Munro, R., and Couto, A. B. (2018). The multi-viewing multi-channel multi-polarisation imager–overview of the 3mi polarimetric mission for aerosol and cloud characterization. *Journal of Quantitative Spectroscopy and Radiative Transfer*, 219:23–32.

Holben, B. N., Eck, T. F., Slutsker, I. a., Tanre, D., Buis, J., Setzer, A., Vermote, E., Reagan, J. A., Kaufman, Y., Nakajima, T., et al. (1998). Aeronet—a federated instrument network and data archive for aerosol characterization. *Remote sensing of environment*, 66(1):1–16.

Klüser, L., Banks, J., Martynenko, D., Bergemann, C., Brindley, H., and Holzer-Popp, T. (2015). Information content of space-borne hyperspectral infrared observations with respect to mineral dust properties. *Remote Sensing of Environment*, 156:294–309.

Klüser, L., Kleiber, P., Holzer-Popp, T., and Grassian, V. H. (2012). Desert dust observation from space–application of measured mineral component infrared extinction spectra. *Atmospheric environment*, 54:419–427.

Klüser, L., Martynenko, D., and Holzer-Popp, T. (2011). Thermal infrared remote sensing of mineral dust over land and ocean: a spectral svd based retrieval approach for iasi. *Atmospheric Measurement Techniques*, 4(5):757–773.

Legrand, M., Pietras, C., Brogniez, G., Haeffelin, M., Abuhassan, N. K., and Sicard, M. (2000). A high-accuracy multiwavelength radiometer for in situ measurements in the thermal infrared. part i: Characterization of the instrument. *Journal of atmospheric and oceanic technology*, 17(9):1203–1214.

Lenoble, J., Herman, M., Deuzé, J., Lafrance, B., Santer, R., and Tanré, D. (2007). A successive order of scattering code for solving the vector equation of transfer in the earth's atmosphere with aerosols. *Journal of Quantitative Spectroscopy and Radiative Transfer*, 107(3):479–507.

Li, L., Dubovik, O., Derimian, Y., Schuster, G. L., Lapyonok, T., Litvinov, P., Ducos, F., Fuertes, D., Chen, C., Li, Z., et al. (2019). Retrieval of aerosol components directly from satellite and ground-based measurements. *Atmospheric Chemistry and Physics*, 19(21):13409–13443.

Marbach, T., Riedi, J., Lacan, A., and Schlüssel, P. (2015). The 3mi mission: multi-viewing-channel-polarisation imager of the eumetsat polar system: second generation (eps-sg) dedicated to aerosol and cloud monitoring. In *Polarization science and remote sensing VII*, volume 9613, page 961310. International Society for Optics and Photonics.

Pérez-Ramírez, D., Whiteman, D. N., Smirnov, A., Lyamani, H., Holben, B. N., Pinker, R., Andrade, M., and Alados-Arboledas, L. (2014). Evaluation of aeronet precipitable water vapor versus microwave radiometry, gps, and radiosondes at arm sites. *Journal of Geophysical Research: Atmospheres*, 119(15):9596–9613.

Siméoni, D., Singer, C., and Chalon, G. (1997). Infrared atmospheric sounding interferometer. *Acta Astronautica*, 40(2-8):113–118.

Smirnov, A., Holben, B., Slutsker, I., Giles, D., McClain, C., Eck, T., Sakerin, S., Macke, A., Croot, P., Zibordi, G., et al. (2009). Maritime aerosol network as a component of aerosol robotic network. *Journal of Geophysical Research: Atmospheres*, 114(D6).

Stamnes, K., Tsay, S.-C., Wiscombe, W., and Jayaweera, K. (1988). Numerically stable algorithm for discrete-ordinate-method radiative transfer in multiple scattering and emitting layered media. *Applied optics*, 27(12):2502–2509.

Stein, A., Draxler, R. R., Rolph, G. D., Stunder, B. J., Cohen, M., and Ngan, F. (2015). Noaa's hysplit atmospheric transport and dispersion modeling system. *Bulletin of the American Meteorological Society*, 96(12):2059–2077.

Szopa, S., V. Naik, B. A., Artaxo, P., Berntsen, T., Collins, W., Fuzzi, S., Gallardo, L., Scharr, A. K., Klimont, Z., Liao, H., Unger, N., and Zanis, P. (2021). *Short-Lived Climate Forcers. In Climate Change 2021: The Physical Science Basis. Contribution of Working Group I to the Sixth Assessment Report of the Intergovernmental Panel on Climate Change*. Cambridge University Press.